

Micro and Macro Fluidic Effects in Cochlear Mechanics

by

Yizeng Li

A dissertation submitted in partial fulfillment
of the requirements for the degree of
Doctor of Philosophy
(Mechanical Engineering)
in the University of Michigan
2013

Doctoral Committee:

Professor Karl Grosh, Chair
Professor Charles R. Doering
Professor David R. Dowling
Professor Gregory M. Hulbert

© Yizeng Li 2013
All Rights Reserved

ACKNOWLEDGEMENTS

I would like to thank:

- My advisor Prof. Karl Grosh for everything;
- The committee members, Prof. Charles Doering, Prof. David Dowling, and Prof. Gregory Hulbert for their valuable time and all the supports;
- Dr. Lei Cheng and Dr. Julien Meaud for discussion;
- Prof. Tianying Ren for discussion and providing experimental data;
- “(T)hose who put together a nice L^AT_EX template for me to use” (quoted from the template).

This work was supported by National Institutes of Health Grant (Prof. Grosh).

TABLE OF CONTENTS

ACKNOWLEDGEMENTS	ii
LIST OF FIGURES	vii
LIST OF TABLES	xvii
LIST OF APPENDICESxviii
LIST OF ABBREVIATIONS	xix
ABSTRACT	xx
CHAPTER	
I. Introduction	1
1.1 Anatomy	1
1.1.1 The external, middle, and inner ears	1
1.1.2 The cochlea	2
1.2 Cochlear Function and Epiphenomenon	5
1.2.1 Sound	6
1.2.2 The hearing process	6
1.2.3 Otoacoustic emissions (OAEs)	7
1.3 Motivation	8
1.3.1 Modeling the macro-fluid shear viscosity in a pressure- field model	9
1.3.2 How is the stereocilia of the IHCs stimulated?	9
1.3.3 The difference between the cochlear base and the apex	9
1.3.4 The emitted wave type for energy generated inside the cochlear	10
1.3.5 Identifying multiple sources for BM responses	10
1.3.6 Evaluating the cochlear activity	11
1.4 Organization of the thesis	11

II. The mechano-electro-acoustical finite element cochlear model description	12
2.1 Fluid and the BM	12
2.2 Electrical environment	14
2.3 Kinematic model of microstructures	16
2.4 TM longitudinal coupling	19
2.5 Hair bundle conductance and OHC electromotility	19
2.6 Local governing equation	20
2.7 Finite elements	21
III. Including fluid shear viscosity in a structural acoustic finite element model using a scalar fluid representation	22
3.1 Introduction	22
3.2 Method	24
3.2.1 Viscous Boundary Layer Correction Theory	25
3.2.2 Strong form	28
3.2.3 Variational formulation	29
3.3 Results	33
3.3.1 Prediction from a 3-D model	34
3.3.2 Computational cost	37
3.4 Discussion and conclusion	38
IV. Micro fluid model in the reticular lamina-tectorial membrane gap with complex boundary conditions	41
4.1 Introduction	41
4.2 Modeling method	42
4.2.1 The TM model	43
4.2.2 The TM-RL fluid gap model	47
4.2.3 The sulcus fluid model	65
4.2.4 SV/ST fluid model	67
4.2.5 The overall FEM matrix and post-processing	69
4.3 Results	70
4.3.1 The motion of the OoC	72
4.3.2 Forces on the IHC HB	72
4.4 Discussion and conclusion	73
V. Direction of wave propagation in the cochlea for internally excited basilar membrane	76
5.1 Introduction	76
5.2 Model description	79
5.3 Results	80

5.3.1	Impulse responses	80
5.3.2	Spatial response	84
5.3.3	Variation of stimulus frequencies	87
5.3.4	Relative response at two locations	89
5.3.5	Apex excitation	90
5.4	Discussion	92
5.4.1	Reciprocity and traveling times	92
5.4.2	The response to internal force excitation is dominated by backward traveling waves	93
5.4.3	Forward traveling waves basal to the excitation location are possible	94
5.4.4	When does the non-negligible compression wave exist?	95
5.4.5	Implications on the DPOAE	96
5.5	Conclusion	97
VI. The coda of the transient response in a sensitive cochlea		98
6.1	Introduction	98
6.2	Method	99
6.3	Results	100
6.3.1	Unperturbed responses	100
6.3.2	Perturbed responses	102
6.4	Discussion	104
6.4.1	Compression wave in the cochlea	104
6.4.2	Passive initial response and one directional amplification	106
6.4.3	About roughness and scattering	107
6.4.4	Implication on the otoacoustic emissions	109
6.5	Conclusion	109
VII. Assessing the activity of the cochlea		111
7.1	Introduction	111
7.2	Assessment of cochlear activity via power flow	113
7.2.1	Method	113
7.2.2	Result	114
7.3	Assessment of cochlear activity via impedance	115
7.3.1	Pressure estimation via WKB	115
7.3.2	Pressure estimation via FEM	128
7.4	Application to the experimental data	133
7.4.1	WKB approximation	133
7.4.2	Frequency-space transformation	135
7.5	Discussion	137
7.5.1	Cross sectional power flow and the real part of the BM impedance	137
7.5.2	Wave number approximation	138

7.5.3	Impedance estimation	139
7.5.4	Pressure recovery by using the FEM	140
7.5.5	Transformation by using scaling symmetry	140
7.6	Conclusion	141
VIII.	Conclusion	143
8.1	Viscous boundary layer correction	143
8.2	Macro wave propagation in the cochlea	144
8.3	Micro fluid-structure interaction	145
8.4	Cochlear activity	146
8.5	Future work	147
APPENDICES	148
BIBLIOGRAPHY	171

LIST OF FIGURES

Figure

1.1	Schematic of the human ear. The ‘E’ denotes the external ear, the ‘M’ denotes the middle ear, and the ‘I’ denotes the inner ear. The tympanic membrane is also known as the eardrum. Malleus, incus, and the stapes are the three auditory ossicles which are the smallest bones in the human body. Cochlea is the spiral organ to the right of the drawing. Figure taken from: http://www.iurc.montp.inserm	2
1.2	Schematic of a cross section of the cochlear duct. White spaces indicate the fluid region. Supporting structures not relevant for modeling purposes are not shown. Ionic boundary between endolymph in the scala media and perilymph in the scala vestibuli is at the Reissner’s membrane and between endolymph in the scala media and perilymph in the scala tympani is at the reticular lamina in the organ of Corti. Figure taken from N. Deo’s dissertation (Fig. 2.2 in [28]).	3
1.3	Schematic of the top view of a cochlea turns. The BM width varying along the length of the cochlea. The BM is thick and narrow (tuned to high frequency) at the base and thin and wide (tuned to low frequency) at the apex. Figure taken from N. Deo’s dissertation (Fig. 2.3 in [28]). . .	4
1.4	Schematic of the Organ of Corti and the tectorial membrane. IP – Inner Pillar cells; OP – Outer Pillar cells; OHC – Outer Hair Cell; IHC – Inner Hair Cell. The reticular lamina is formed by the apical ends of the OHCs and other supporting cells. It forms a tight ionic junction that separates the endolymph in the scala media from the perilymph in the organ of Corti space. Figure modified from N. Deo’s dissertation (Fig. 2.4 in [28]).	5
2.1	Illustration of the model used for simulating the cochlea. Organ of Corti is only pictured at one cross-section. In the mathematical model it is included over the entire length of the basilar membrane. Figure taken from Ramamoorthy <i>et al.</i> [82] (Fig. 1).	13

2.2	Electrical network at a given cross-section of the cochlea. The SV, SM, and ST cables run longitudinally along the cochlea. The factor of three multiplying the apical and the basolateral membrane capacitance, and dividing the apical and the basolateral membrane resistance of the OHC is to account for the three OHCs in a cross-section. Figure taken from Ramamoorthy <i>et al.</i> [82] (Fig. 2).	15
2.3	Micromechanical model for the organ of Corti structures. The sketch is drawn for $\alpha = \beta$. BM – Basilar Membrane, TM – Tectorial Membrane, OHC – Outer Hair Cell, RL – Reticular Lamina. L_{Ro} is the distance between RL pivot point on the arch of Corti and the middle OHC, L_1 is the radial distance between OHCs along the RL, θ_1 is the acute angle between the inner pillar cell and the BM, θ_2 is the acute angle between the inner and outer pillar cell, L_{pc} is the distance along the BM between the left edge of the BM and the contact point of the outer pillar cell with the BM, L_o is the distance along the BM between the left edge of the BM and the contact point of the middle OHC with the BM, and L_{tm} is the length of the TM from its pivot to the attachment point of the middle row HBs with the TM. Figure taken from Ramamoorthy <i>et al.</i> [82] (Fig. 3).	17
3.1	Schematic of a generic fluid-structure coupled system. Ω is the interior of fluid filled duct. The boundary of the duct is denoted by $\partial\Omega$, and $\Gamma \subset \partial\Omega$ is the flexible structure on the $z = 0$ and $z = L_z$ surfaces.	24
3.2	Schematic of the 3-D coupling boundary layer correction. The elements on $z = 0$ are coupled to the elements on $z = L_z$ through a 2-D configuration.	32
3.3	The dimension of the duct and the structure (not to scale).	33
3.4	Comparison of the normalized structure displacements at the central line with respect to the input pressure among the N-S model (thin solid lines), the thin BL model (dashed lines), and the thick BL model (thick solid lines) on the $z = 0$ and $z = L_z$ surfaces with different duct heights ($L_z = 110\mu\text{m}$, $50\mu\text{m}$, and $15\mu\text{m}$). The three curves overlap in the $L_z = 110\mu\text{m}$ case.	34
3.5	Comparison of normalized (with respect to the input pressure) fluid longitudinal displacement u_x on the central-plane ($y = 0$) among the N-S model (thin solid lines), the thin BL model (dashed lines), and the thick BL model (thick solid lines, overlapped with dashed lines) on the $z = 0$ and $z = L_z$ surfaces. The numbers on each group of curves indicate the selected longitudinal locations in the duct. The duct height is $110\mu\text{m}$. . .	35

3.6	Central-line structural displacement normalized to the input pressure from the 3-D acoustic model. Thin solid lines: inviscid model. Thick solid lines: one thin BL correction on $z = 0$. Thick dashed lines: thick BL correction. Thin dashed lines: N-S solution. (a). $L_z = 110 \mu\text{m}$. $L_z/\delta = 9.12$. (b). $L_z = 15 \mu\text{m}$. $L_z/\delta = 1.24$	36
3.7	Variation of normalized longitudinal fluid velocity v_x (at $x = 30 \text{ mm}$) in the vertical direction in 3-D acoustic models. Thin solid lines: an inviscid model. Thick solid lines: one BL correction at $z = 0$. Thick dashed lines: thick BL correction. (a) $L_z = 110 \mu\text{m}$ ($L_z/\delta = 9.12$). The velocity is normalized to the velocity at $z = 5.5 \mu\text{m}$. (b) $L_z = 15 \mu\text{m}$ ($L_z/\delta = 1.24$). The velocity is normalized to the velocity at $z = 0.75 \mu\text{m}$	36
4.1	Schematic of an OoC cross section in the cochlea. x , s , and z are the longitudinal, radial, and vertical coordinates, respectively. The sub-TM microfluid between the TM and RL gap interacts with the OHC/IHC HBs, the HS, and the sulcus.	42
4.2	Schematic of the TM and the OoC model showing the microfluidic domains: Ω_1 between the OHC and the scala media (SM); Ω_2 between the IHC and OHC bundles; Ω_s the inner sulcus region. The TM is attached to a linear and a rotational spring at the spiral lamina. s and z are the radial and vertical coordinates, respectively. The positive direction of s points from OHC to IHC. The coordinates of the four nodes at $s_1 = 0$, $s_2 = L_{hb_2}$, $s_3 = L_{IHC}$, and $s_4 = L_{tm}$, represents respectively the free end of the TM, the location of the second-row OHC, the location of the IHC/Hessen stripe, and the spiral lamina. L_{pill} is the distance from $s = 0$ to the tip of the pill cells. Both OHC HB and IHC HB are denoted by arrows.	43
4.3	Schematic of the OHC HB configuration, viewed from the top of the RL plane (the $x - s$ plane as denoted in the bottom right corner of the figure). s and x are the global coordinates consistent with the coordinates indicated in Fig. 4.1. r and w are the local coordinates that describe the geometry relation between two adjacent OHC HBs in the longitudinal direction. The double arrow shows the direction of the displacement of the OHC HB (u_{HB}).	51
4.4	Schematic of the configuration in the surrounding region of the HS and IHC HB. s' is the local coordinate with the origin located at the middle line of the IHC HB. Loosely speaking, $s = s' + L_{IHC}$. The three vertical dashed lines have coordinates from left to right: $s' = -R_{IHB}$, $s' = R_{IHB}$, and $s' = a_{HS}$. The notations of the geometry are listed in Tab. 4.1. RL: reticular lamina. TM: tectorial membrane. HS: Hessen's stripe. IHC: inner hair cells. HB: hair bundles. IHB: a short cut for IHC HB.	55

4.5	Schematic of the configuration of the sulcus (see Ω_s in Fig. 4.2). The local coordinate y is in the same direction as s . The effective fluid velocity at the inlet of the sulcus is assumed to be \dot{Q}/H_s that uniformly extends over the entire height of the sulcus. The width of the sulcus L_s is defined as $L_s = L_{tm} - L_{IHC}$	65
4.6	Model prediction of the spectrum amplitudes (a) and phases (b) of the BM, TM shearing ($U^s _{s=L_{hb2}}$), TM bending ($W^b _{s=L_{hb2}}$), OHC compression, and the IHC HB displacement at $x = 4$ mm with respect to a unit force on the BM.	71
4.7	Model prediction of the spectrum forces (real part) per unit length on the IHC HB with respect to a unit force on the BM. Solid line: force on the IHC HB due to the pressure different across the IHC HB. Dashed line: force on the IHC HB due to the shear viscosity on the IHC HB tip. Both forces are small below and above the best frequency, and have larger values around the best place. The pressure difference has a phase change across the best frequency.	73
4.8	Model prediction of the spectrum vertically averaged fluid velocity (real part) in the TM-RL gap at $x = 4$ mm, $s = L_{IBC}$ with respect to a unit force on the BM. The averaged fluid velocity is small below and above the best frequency, and have a Dirac Delta function type response at the best frequency.	74
5.1	Schematic of the cochlear rectangular box model and an internal force excitation on the BM.	79
5.2	Impulse responses of the BM at 6.5 mm from the base under acoustic stimuli (thick solid lines) and the impulse responses of the stapes under internal force excitation (thin solid lines). Temporal resolution: 0.625 μ s. Each response is normalized to its own maximum value (normalization factors: passive acoustic, $4.887 \times 10^{-4} \mu$ m; passive internal force, $6.332 \times 10^{-3} \mu$ m; active acoustic, $6.455 \times 10^{-3} \mu$ m; active internal force, $2.833 \times 10^{-2} \mu$ m). (a) Long time scale responses of the passive model. (b) Long time scale responses of the fully active model. (c) Early temporal responses of the passive model. (d) Early temporal responses of the fully active model. The thin vertical dashed lines in (c) and (d) indicate the time for sound in water to travel from the stapes to the BM at 6.5 mm, or from the BM at 6.5 mm to the stapes. The result predicts the identical normalized passive responses under two excitation methods, and same traveling-wave arrival time for active response.	82

5.3	Difference between the stapes and the BM responses at 25 μm under internal force excitation. Thick solid lines: responses of the stapes. Thin solid lines: responses of the BM at 25 μm away from the stapes. Temporal resolution: 0.625 μs . Each displacement is normalized to its own maximum value (normalization factors: passive stapes, $6.332 \times 10^{-3} \mu\text{m}$; passive BM at 25 μm , 1.661 μm ; active stapes, $2.833 \times 10^{-2} \mu\text{m}$; active BM at 25 μm , 12.02 μm). (a) Prediction from the passive model. (b) Prediction from the fully active model. In both cases, the BM wave form leads the stapes response, indicating that the traveling wave propagates towards the base.	83
5.4	Schematic of the spatial mappings of 5 kHz and 20 kHz along with an idealization of the BM responses. The unit internal forcing is applied on the BM at 6.5 mm from the base. The best place for 5 kHz is ~ 10 mm, apical to the forcing location. The best place for 20 kHz is ~ 3 mm, basal to the forcing location.	84
5.5	BM responses at 5 kHz under acoustic and internal force inputs. The best place is around 10 mm. Both amplitudes and phases are normalized with respect to the stapes. Solid lines: responses under the BM excitation at 6.5 mm from the base. Dashed lines: responses under acoustic stimuli. For reference, mirror reflection of the phase under acoustic stimuli for locations basal to the force (< 6 mm) is shown with short dashed lines. (a) and (b): predictions from a passive model. (c) and (d): predictions from an active model. (a) and (c): BM amplitudes referenced to the stapes. (b) and (d): BM phases in cycles. A backward-traveling wave is predicted from the response under the internal BM excitation, while a forward-traveling wave dominates the response to acoustic stimulation.	85
5.6	BM responses at 20 kHz under acoustic and internal force inputs. The best place is around 3 mm. Both amplitudes and phases are normalized with respect to the stapes. Solid lines: responses under the BM excitation at 6.5 mm from the base. Dashed lines: response under acoustic stimuli. For reference, mirror reflection of the phase under acoustic stimuli for locations basal to the best place (< 2.8 mm) is shown with short dashed lines. (a) and (b): predictions from a passive model. (c) and (d): predictions from an active model. (a) and (c): BM amplitudes referenced to the stapes. (b) and (d): BM phases in cycles. A backward-traveling wave, along with an active forward-traveling region (enclosed by two vertical dashed lines), is predicted from the response under the internal BM excitation.	86

5.7	Active BM spatial responses under unit force excitation on the BM at 6.5 mm with different stimulus frequencies. The best places of 7 kHz, 9 kHz, 11 kHz, and 13 kHz excitations are, respectively, around 8.5 mm, 7.1 mm, 6.0 mm, and 5.3 mm (from our active model prediction). Both BM amplitudes (a) and phases (b) are normalized to the motion of the stapes. BM amplitude ‘notches’ from wave interaction in two directions are denoted by arrows; these ‘notches’ correspond to half-cycle phase jumps. Waves basal to the forcing place are dominated by backward-traveling waves, with the appearance of a forward-traveling region if the excitation frequency is higher than the best frequencies of the forcing place (e.g., for 11 kHz and 13 kHz).	88
5.8	The relative active BM amplitudes (a) and phases (b) at the 3.2 mm place relative to the 3.0 mm place under a unit internal force excitation on the BM at 6.5 mm (solid lines). The same relative response under an acoustic stimulation is plotted for comparison (dashed lines). The best frequencies at 3.0 mm and 3.2 mm are 20.3 kHz and 19.5 kHz (from our active model prediction), respectively. Negative phase values indicate that the wave travels forward, and conversely for positive phase.	89
5.9	Schematic of the cochlear apex excitation model.	90
5.10	Cochlear responses under the apex input. (a, b). Normalized impulse responses of the stapes under the apex excitation. Temporal resolution: 1 μ s. (a). Long time scale response of the active model. (b). A copy of (a) that emphasizes short time scale response of the active model. The thin vertical dashed line in (b) indicates the time (13 μ s) for sound in water to travel from the cochlear apex to the stapes. (c, d). The active steady-state spatial response of the BM referenced to the stapes under 20 kHz apex input. The best place is around 3 mm. (c). Amplitude in dB. (d) Phase in cycles. The motion of the stapes is induced by the compression wave, and the forward-traveling wave exists in the entire cochlea.	91
6.1	Schematic of the rectangular cochlear model. The internal pressure sources are denoted by solid dots pointed by arrows. OW: oval window. RW: round window. SV: Scala Vestibuli. ST: Scala Tympani. BM: basilar membrane.	99
6.2	Normalized active BM temporal responses at 4 mm under acoustic (a) and a pair of symmetric internal pressure sources (b). The gray curve in (b) is the acoustic response copied from (a) for easy comparison. The two responses has the same group delay of ~ 0.7 msec.	101

6.3	Normalized active BM temporal response at 4 mm under an internal point force on the BM at 4 mm.	102
6.4	Normalized BM temporal response at 4 mm under an internal pressure source beneath the BM at 4 mm ($p^- : p^+ = 1 : 0$) for different activity levels. The normalization ratio among the 100%, 90%, and 80% activity levels is 279.1 : 280.2 : 281.4, which is close to 1 : 1 : 1. (a) A prediction from a 100% active model. (b) A prediction from a 90% active model. (c) A prediction from a 80% active model. The three responses show a similar initial amplitude, but the relative amplitudes of the traveling waves decrease with decreasing activity levels.	103
6.5	Normalized active BM temporal response at 4 mm with 0.05% designed perturbation (Eq. 6.1) on the MET channel. (a) Acoustic simulation. (b) Internal force excitation at 4 mm. (c) Internal pressure sources with $p^- : p^+ = 1 : 0.98$. Extended ringings are observed. In (c), the group delays of ringings are approximately at $t_g, 3t_g, 5t_g, 7t_g, \dots$	104
6.6	Active BM spectrum response at 4 mm with 0.05% designed perturbation (Eq. 6.1) on the MET channel for internal pressure sources ($p^- : p^+ = 1 : 0.98$) excitation. (a) BM amplitude in dB with respect to the stapes. (b) BM phase in cycles with respect to the stapes. Two thin solid vertical lines enclose the region of the middle peak around the best frequency; two thin solid horizontal lines enclose the region corresponding to the intersection of the two vertical lines and the phase.	105
6.7	Normalized active BM temporal responses at 4 mm with 0.05% filtered perturbation on the MET channel under acoustic simulation. (a) Response under R1. (b) Response under R2.	106
6.8	Active BM spectrum response at 4 mm with 0.05% filtered perturbation on the MET channel under acoustic simulation. (a) and (b) Response under R1. (c) and (d) Response under R2. (a) and (c) BM amplitude in dB with respect to the stapes. (b) and (d) BM phase in cycles with respect to the stapes.	107
7.1	Illustration of the power flow through each cross section. The dashed rectangular box represents a control volume where the total power flow across all its boundaries is zero.	113

7.2	Predicted power flow at each cross section in the SV [in (b) and (d)] for both the active (thick solid lines) and passive (thick dashed lines) models. The BM amplitudes [in (a) and (c)] are plotted for reference. The vertical thin solid and dashed lines indicate the location of best places in an active and a passive model, respectively. (a) and (b), 10 kHz. (c) and (d), 20 kHz. The intracochlear pressure is predicted by the FEM model [82]. Decreasing and increasing power flow in x indicated power dissipation and injection, respectively, from the organ of Corti.	114
7.3	Results of wavenumber fitting on both the real and imaginary parts of the BM displacements by using the first order WKB BM approximation. The reference (ref.) displacements (considered as the given data) are the original BM displacements from the FEM model under 20 kHz acoustic simulation. (a) and (b), BM responses from a passive model. (c) and (d), BM responses from an active model. The initial displacements refer to the displacements given by the initial guess before the Levenberg-Marquardt algorithm is implemented [see (a) and (c)]. The fitted displacements refer to the BM displacements after the Levenberg-Marquardt algorithm is implemented [see (b) and (d)]. The data fitting gives accurate results in terms of the reproduction of the given displacements.	123
7.4	The value of ϵ [(a) and (c)] and the real part of the BM impedance [(b) and (d)] for an active model under acoustic simulations. Two orders of WKB BM approximation are compared. Dashed lines: first-order approximation. Dotted lines: second-order approximation. Solid lines: reference value from the FEM output. (a) and (b), 10 kHz. (c) and (d), 20 kHz. In (a) and (c), ϵ is obtained from the result of data fitting. In (b) and (d), the reference BM impedance (solid lines) comes from the direct output of the FEM model prediction. The BM impedances approximated by the WKB method are given by dashed (first-order) and dotted (second order) lines. $\epsilon \ll 1$ is mostly satisfied, and the tow orders of approximation almost give the same $k_x(x)$. The sign of $\Re\{Z_{BM}\}$ from the WKB BM approximation is consistent with the reference value from the FEM output.	125

- 7.5 The value of ϵ [(a) and (c)] and the real part of the BM impedance [(b) and (d)] for a passive model under acoustic simulations. The spatial span is the same as that in Fig. 7.4, which does not include the entire peak for the passive model. Two orders of WKB approximation are compared. Dashed lines: first-order approximation. Dotted lines: second-order approximation. Solid lines: reference value from the FEM output. (a) and (b), 10 kHz. (c) and (d), 20 kHz. In (a) and (c), ϵ is obtained from the result of data fitting. In (b) and (d), the reference BM impedance (solid lines) comes from the direct output of the FEM prediction. The BM impedances approximated by the WKB method are given by dashed and dotted lines. The sign of $\Re\{Z_{BM}\}$ from WKB approximation agrees with that of the reference value from the FEM output, but the amplitudes are different. For both ϵ and $\Re\{Z_{BM}\}$, the second order WKB BM approximation gives a different result compared to the first order WKB BM approximation. 126
- 7.6 The value of ϵ [(a) and (c)] and the real part of the BM impedance [(b) and (d)] for a passive model under acoustic simulations. The spatial span is such chosen that the best place is included. Two orders of WKB approximation are compared. Dashed lines: first-order approximation. Dotted lines: second-order approximation. Solid lines: reference value from the FEM output. (a) and (b), 10 kHz. (c) and (d), 20 kHz. In (a) and (c), ϵ is obtained from the result of data fitting. In (b) and (d), the reference BM impedance (solid lines) comes from the direct output of the FEM prediction. The BM impedances approximated by the WKB method are given by dashed and dotted lines. The sign of $\Re\{Z_{BM}\}$ from WKB approximation is inconsistent with the reference value from the FEM output. 127
- 7.7 Comparison between transformed data from the BM spectrum (dashed lines) and the original BM spatial response (solid lines). All the spectrum and spatial responses are obtained from an active incompressible cochlear model under acoustic simulation. For the spectrum response, the BM is taken at $x_0 = 3.1$ mm; for the spatial response, the simulation frequency is $f_0 = 20$ kHz. (a) BM amplitude. (b) and (c), BM phase in cycles. The insertions in (b) and (c) are the zoomed-in BM phases at the base. (b), $\alpha = 0.3796$. (c), $\alpha = 0.3983$. The transformation matches the width of the BM peaks and the slope of the phase slightly differently, but the overall transformed response is similar to the original BM spatial response. 131

7.8	Compression between the prediction from the transformed BM response (dashed lines) and the original values (solid lines) on the anti-symmetric intracochlear pressure and $\Re\{Z_{BM}\}$. The profiles of transformed BM response and the original response are shown in Fig. 7.7. (a) and (b), the anti-symmetric pressure is calculated from transformed BM response in Fig. 7.7 (a) and (b). The insertion in (a) shows the zoomed in response at $x = 0$. (c) and (d), the anti-symmetric pressure is calculated from transformed BM response in Fig. 7.7 (a) and (c). (a) and (c) show the real part of the anti-symmetric intracochlear pressure at the basal region. (b) and (d) show the normalized real part of the BM impedance. Normalization factors: 5.2943×10^3 for the original FEM output; 2.9201×10^4 for the transformation given by $\alpha = 0.3796$; 4.7503×10^4 for the transformation given by $\alpha = 0.3983$	132
7.9	First order WKB approximation for the value of ϵ (a) and the real part of the BM impedance (b) from the measured gerbil cochlear responses under various acoustic simulation levels at 16 kHz. Two terms of Fourier expansion are used in the data fitting. (a) $\epsilon \ll 1$ is almost satisfied. (b) the negative region of $\Re\{Z_{BM}\}$ basal to the best place (around 2.5 mm) indicates that the cochlea has activity there. The zeros move to the basal as the sound pressure level increases.	134
7.10	Frequency-spatial transformation based on the frequency-space mapping given in Eq. 7.48. The BM spectrum response (dashed lines) comes from Fig. 3 in [86]. The original spatial data (solid lines) comes from Fig. 4 in the same paper. SPL = 40 dB for both data. (a) The BM amplitude. Adjustment (see Eq. 7.46) is implemented. (b) The BM phase in cycles. No adjustment is implemented.	135
7.11	Frequency-spatial transformation based on the frequency-space mapping given in Eq. 7.49. Dashed lines: 60 dB BM spectrum response comes from Fig. 3 in [86]. Thin solid lines: BM spatial response under 60 dB 16 kHz acoustic stimulation [86]. Thick solid lines: BM spatial response under 60 dB 15 kHz acoustic stimulation [84]. The transformation mapping is matched for the phase in [84]. (a) The BM amplitude. Adjustment (see Eq. 7.46) is implemented. (b) The BM phase in cycles. No adjustment is implemented.	137
G.1	Schematic showing the boundary (denoted by dashed lines) of the intracochlear fluid.	168

LIST OF TABLES

Table

2.1	Symbols and units in Fig. 2.2	16
3.1	Material properties for the example problem	34
3.2	Root mean square errors of structural displacement for different L_z/δ ratios and models.	37
4.1	A list of geometry in Fig. 4.4.	55
4.2	Geometric parameters for the cross sectional model.	70
4.3	Material properties for the cross sectional model (x is in meters).	72
5.1	Material properties for the cochlear model (x is in meters).	81
7.1	Geometrical parameters used for the gerbil model.	133

LIST OF APPENDICES

Appendix

A.	Inclusion of in-plane structure motion in the shear viscous boundary layer correction	149
B.	Asymptotic analysis	151
C.	Derivation of longitudinal fluid velocity in the acoustic model	152
D.	Shape functions for the 1-D elements	154
E.	Extended derivations for a cross section	157
F.	Integral evaluation	164
G.	Derivation of the reciprocity in the passive cochlea	168

LIST OF ABBREVIATIONS

BL	Boundary layer
BM	Basilar membrane
DP	Distortion product
FEM	Finite element method
HB	Hair bundle
HS	Hensen's stripe
IHC	Inner hair cells
MET	Mechanoelectrical transducer
N-S	Navier-Stokes
OAE	Otoacoustic emission
OHC	Outer hair cells
OoC	Organ of Corti
OW	Oval window
RL	Reticular laminar
RMSE	Root mean square error
RW	Round window
SM	Scala Media
ST	Scala Tympani
SV	Scala Vestibuli
TM	Tectorial membrane
WKB	Wentzel-Kramers-Brillouin

ABSTRACT

Micro and Macro Fluidic Effects in Cochlear Mechanics

by

Yizeng Li

Chair: Karl Grosh

The cochlea is a fluid-filled organ with multiple structures. The scales of the structures in the cochlea range from millimeter (macro) to sub-micrometer (micro). In this work, both the micro and macro fluidic effects in cochlear mechanics are studied to understand the working mechanism of the cochlea. Topics include wave generation and propagation, fluid viscosity, complex boundary conditions for fluid-structure interactions, power flow, and inverse problems. In addition, a method is developed to bridge the gap for the modeling effort among different scales. This method is applicable to other fluid-structure coupling problems with multiple scales.

The entire work is based on a physiologically-based finite element cochlear model that couples mechanical, electric, and acoustic fields. On the macro scale, the direction of wave propagation is studied under various stimulation methods, including acoustic, bone conduction, internal force, and internal pressure sources excitations. In a passive cochlea, the reciprocity relation holds. The effect of structural (active component) perturbations on the wave propagation is also analyzed. Multiple sources are identified to the contribution of the extended ringings of the basilar membrane under an impulse response. The power dissipation and amplification are analyzed in the cochlear channels as well.

On the micro scale, the viscous flow in the sub-tectorial membrane region is modeled. The flow is coupled to the motion of surrounding micro structures. The micro fluid is also coupled to the macro fluid. The model combines both analytical solutions for the micro fluid-structure interaction and numerical solutions for the intermediate and macro scale fluid behaviors. The interactive usage of analytic and numerical solutions makes the multiscale model computationally efficient and physically interpretable. This model provides a tool to determine the spatial dependence of flow modality in the sub-tectorial

membrane region; determine the relative importance of motility (either outer hair cell somatic or hair bundle motility) on inner hair cell hair bundle stimulation; and analyze the role of the Hensen's stripe and the noise to signal ratio in the hearing.

CHAPTER I

Introduction

Sound and hearing process are two important parts in our daily life. A good understanding on how ears respond to sound will help with protecting hearing, preventing hearing loss, treating hearing diseases, designing hearing aid devices, and developing transducers based on biological hearing. This work focuses on cochlear mechanics which deals with the relationship between cochlear responses and acoustic/energy input. In this chapter, the anatomy and function of the cochlea will be introduced as the modeling basis of the physiologically-based cochlear model used/developed in this thesis.

1.1 Anatomy

The beautiful configuration and the remarkable sensitivity to sounds make the ear one of the most eminent structures in human body. Anatomically, the ear is divided into three parts: the external (E), the middle (M), and the inner ears (I) (Fig. 1.1). The structures and functions of each component are described next.

1.1.1 The external, middle, and inner ears

The external ear is composed of the pinna and the ear canal. The pinna is supported by a convoluted plate of flexible cartilage that extends a nearly closed tube one-third of the way down the ear canal. This one-third ear canal has small hairs that protect the ear for small animals. The inner two-thirds of the ear canal has a bony wall with thin and fragile skin. At the end of the ear canal is a stretched eardrum (tympanic membrane), which separates the external and the middle ear.

The middle ear is composed of the eardrum and an air-filled cavity. The eardrum is a circle of thin skin consisting of elastic fibers arranged in both radial and circumferential directions. Inside the cavity, there are three tiny bones (the malleus, the incus, and the

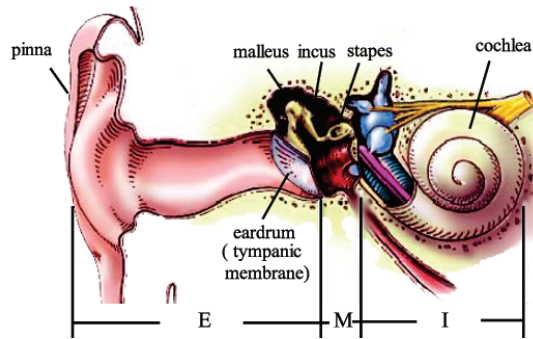


Figure 1.1: Schematic of the human ear. The ‘E’ denotes the external ear, the ‘M’ denotes the middle ear, and the ‘I’ denotes the inner ear. The tympanic membrane is also known as the eardrum. Malleus, incus, and the stapes are the three auditory ossicles which are the smallest bones in the human body. Cochlea is the spiral organ to the right of the drawing. Figure taken from: <http://www.iurc.montp.inserm>.

stapes) which form a mechanical chain that links the eardrum to the inner ear. The stapes footplate is attached to the oval window of the inner ear. The middle ear cavity is also connected to the nasal cavity through the Eustachian tube which is located at the bottom of the cavity.

The inner ear is a large fluid-filled chamber called vestibule, which is composed of semicircular canals (vestibular apparatus) and a snail shaped cochlea. In mammals, the vestibule is embedded in the hard and complex temporal bone within the skull. The semicircular canals control the balance of the body and are not related to the hearing process. The cochlea is the intricate part of the hearing process. The semicircular canals are connected to the cochlea at the very basal part (close to the stapes) of the scala vestibuli (see the next section for the explanation for scala vestibuli); hence they have the same inner fluid environment.

1.1.2 The cochlea

The mammalian cochlea is a snail-shaped duct with about 2 to 4 turns depending on species. For human beings the cochlea coils around the modiolus about 2.5 turns, and for guinea-pigs there are about 4 turns. When uncoiled, the total duct length also varies from species to species – 3.5 cm for human beings and 1.85 cm for guinea-pigs. The end of the spiral duct at where the stapes connects to is referred to as the base of the cochlea, while the top of the spiral is referred to as the apex. The cross section areas of the cochlear duct reduce from the base to the apex.

The whole cochlear duct contains three fluid-filled channels: the scala vestibuli (SV),

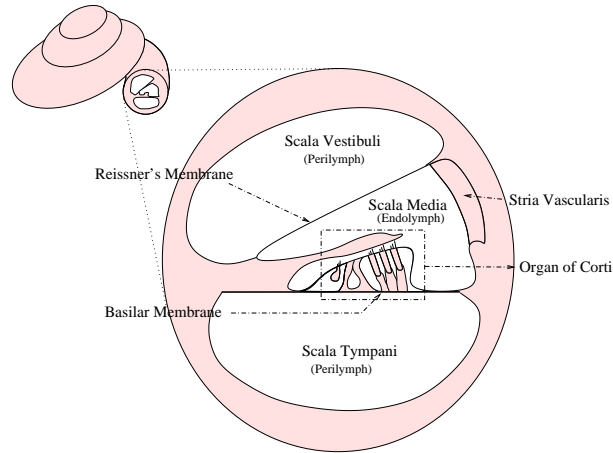


Figure 1.2: Schematic of a cross section of the cochlear duct. White spaces indicate the fluid region. Supporting structures not relevant for modeling purposes are not shown. Ionic boundary between endolymph in the scala media and perilymph in the scala vestibuli is at the Reissner's membrane and between endolymph in the scala media and perilymph in the scala tympani is at the reticular lamina in the organ of Corti. Figure taken from N. Deo's dissertation (Fig. 2.2 in [28]).

the scala tympani (ST), and the scala media (SM). The three channels can be visualized at a typical cochlear cross section (Fig. 1.2). An oval window and a round window are located at the very base of the SV and the ST channels, respectively. The two windows are part of the cochlear boundaries at the base. The SV and ST are filled with perilymph similar to cerebrospinal fluid while the SM is filled with endolymph similar to intracellular fluids. Perilymph and endolymph have different ionic concentrations, and thus have different electronic potentials. The SV and the SM are separated by a thin Reissner's membrane [RM, in memory of a Baltic German anatomist Ernst Reissner (1824-1878) who discovered it] while the SM and the ST are separated by the basilar membrane (BM). The SV and the ST are connected at the apex through the helicotrema (not shown), which is typically a round cavity that provides a continuous communication of the fluid in the SV and ST. Traveling inside the cochlea channel from the oval window towards the cochlear apex will spiral upwards several turns (the RM is the floor) and reach the helicotrema. Then one heads into the ST side and spirals downwards (the BM is the roof), and finally reaches the round window. The BM is a highly orthotropic material with high stiffness in the radial direction and low stiffness in the longitudinal direction. The thickness and width of the BM decreases and increases, respectively, from the base to the apex (Fig. 1.3).

On the BM sits the organ of Corti complex [OoC, in memory of an Italian anatomist Alfonso Corti (1822-1888) who discovered it] (Figs. 1.2 and 1.4) which contains both

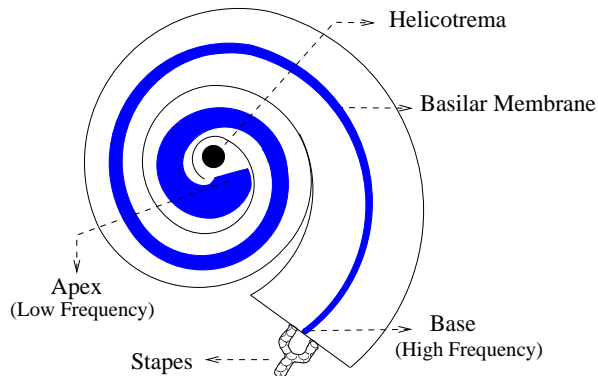


Figure 1.3: Schematic of the top view of a cochlea turns. The BM width varying along the length of the cochlea. The BM is thick and narrow (tuned to high frequency) at the base and thin and wide (tuned to low frequency) at the apex. Figure taken from N. Deo’s dissertation (Fig. 2.3 in [28]).

sensory and supporting cells, and is the right organ that converts acoustic signals to electronic signals. The OoC is sealed at its top by the reticular lamina (RL) which separates endolymph and perilymph. Hair cells are arranged in two groups depending on their spatial locations. There is a single row of inner hair cells (IHCs), which lie closer to the core of the cochlea (modiolus), and three to four rows of outer hair cells (OHCs), which are further away from the modiolus. In a healthy young human ear there are about 3,500 IHCs and about 12,000 OHCs [15]. Each hair cell has a cluster of hairs (stereocilia) which project from the cell’s thicker upper surface into the fluid region between the RL and the tectorial membrane (TM). This fluid region is also called the sub-TM region or the TM-RL gap. The stereocilia are typically arranged in rows of 3 or 4 in a “V” or a “W” configuration. The highest row of stereocilia in the OHCs are embedded into the lower surface of the TM, and all the other rows have free ends in the sub-TM region. All the stereocilia in IHCs have free ends in the sub-TM region. At the inner end between the TM and the top of the OoC, there is a relative large space called sulcus. In addition to communicating with the fluid in the sub-TM region, the sulcus also forms a small fluid channel that run longitudinally and spirals up with the OoC. Between the sulcus and IHCs, a small soft structure called Hensen’s stripe (HS) is located at the lower surface of the TM.

OHCs are thin and cylindrically shaped, and are supported by multiple cells. One of the supporting cells are Deiters’ cells [DCs, in memory of a German neuroanatomist Otto Friedrich Deiters (1834-1863) who discovered it], which attach to the BM and encase the bottom end of OHCs where nerve fibers running through. Between the IHCs and OHCs

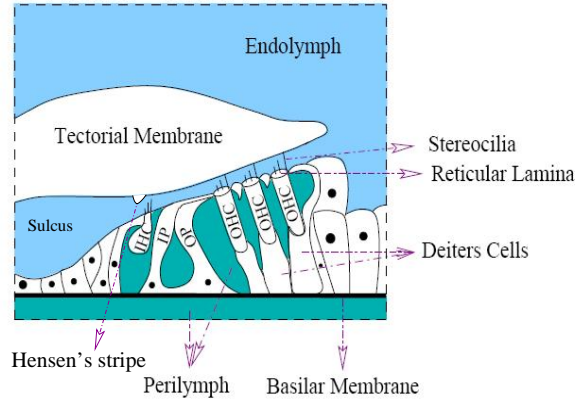


Figure 1.4: Schematic of the Organ of Corti and the tectorial membrane. IP – Inner Pillar cells; OP – Outer Pillar cells; OHC – Outer Hair Cell; IHC – Inner Hair Cell. The reticular lamina is formed by the apical ends of the OHCs and other supporting cells. It forms a tight ionic junction that separates the endolymph in the scala media from the perilymph in the organ of Corti space. Figure modified from N. Deo’s dissertation (Fig. 2.4 in [28]).

is the important supporting structure called the pillar cells. According to the spatial locations, pillar cells are divided into inner pillar (IP) cells and outer pillar (OP) cells. The two groups of pillar cells are joined at their base and apex, forming a triangular tunnel (Corti’s tunnel) running parallel to the BM. Pillar cells are much stiffer than the other cells in the OoC, and thus serve as a major supporting structures and maintain the stability of the OoC. Numerous nerve fibres run through Corti’s tunnel and between the rows of DCs. These nerve fibres will eventually run through the cochlear modiolus along with blood vessels before they enter the brain.

1.2 Cochlear Function and Epiphenomenon

This section gives a brief introduction to the cochlear function and its epiphenomenon. The function of the cochlea is to process sounds and act as a real-time time-frequency analyzer. Normal cochlea are active in that they possess some form of mechanical amplification. In addition to improving our ability to process low level sound, this mechanical amplification manifests an epiphenomenon, namely the emission of sound from the cochlea known as otoacoustic emission (OAE). Before the introduction of the cochlea function and its epiphenomenon, a brief description of sound is presented.

1.2.1 Sound

Sound is the vibration of molecules in a medium. It propagates in the same direction as the direction of vibration of molecules, i.e., a compressional wave. The speed of sound in air is about 343 m/s, and that in water is about 1500 m/s. Two quantities are associated with sound. One is frequency and the other is intensity (pressure). Frequency is the number of crests that pass a point in a second, measured in Hz. The audible frequency ranges different from species to species. For human beings, the lower limit is about 20 Hz, and the higher limit is about 20 kHz, decreasing as people ages. Sound frequencies below 20 kHz are called ‘infrasounds’, and above 20 kHz are called ‘ultrasounds’. Sound intensity is the sound power per unit area, which can be described in decibel (dB). The threshold of hearing varies with frequency. The quietest sound that a normal adult can hear is 20 μ Pa, corresponding to 0 dB, at about 1500 Hz. The noise of a jet engine is about 20 Pa, corresponding to 120 dB. Long-time exposure to sound higher than 120 dB is harmful to ear.

1.2.2 The hearing process

Sound waves are partially collected by the pinna before they enter into the ear canal. The ear canal functions as a tube that is open at one end and close at the other. This configuration allows sound to be enhanced over a certain frequency range [27]. For human, the length of the ear canal results in sound being enhanced around 3 - 4 kHz, as calculated from half-wavelength resonance. When sound reaches the eardrum, the configuration of the eardrum helps with the energy absorption of the sound. Airborne sound waves are converted to acoustic waves in fluid in the cochlea via the eardrum and the three-bone chain in the middle ear. This chain of sound transducer acts as levers that transmits sound efficiently from the ear canal to the inner ear. The motion of the stapes (or the oval window) initiates sound propagation in the cochlea.

The cochlea is a closed hydrodynamic system. The in- and out-ward motions of the stapes generate compression waves which travels at the speed of sound in the fluid. For the small size of the cochlea, the compression wave almost fills the entire cochlea immediately. In addition to bearing a compression wave, the fluid is also coupled to the BM (or the OoC in general) in the form of a traveling wave. The stiffness variation of the BM in the longitudinal direction results in the BM tuning to higher frequencies at the base and lower frequencies at the apex (Fig. 1.3). For each frequency, the longitudinal location on the BM that has the maximum tuning amplitude is called the best place (to the frequency). Correspondingly, for each longitudinal location on the BM there is a frequency that makes

the BM tune maximally; this frequency is called the characteristic frequency or the best frequency (at that location).

The motion of the BM is coupled to the motion of the TM and the OoC as a whole. The relative motion between the TM and the RL squishes the sub-TM fluid, and also rotates the tallest stereocilia on OHCs that are embedded into the lower-surface of the TM. The motion of the sub-TM fluid drives the stereocilia that have free ends in the fluid. The rotation of stereocilia opens the mechano-electrical transducer (MET) channel of the OHCs that allows ionic flow in and out of the OHCs. As sensory cells, OHCs can compress or elongate according to their membrane potentials. The dynamic motion of the OHCs is termed the somatic motility. The motion of the OHCs generates forces on the BM, and thus enhances the response of the BM. The enhanced BM motion will again stimulate the voltage-dependent motion of OHCs and so on. The process of the enhancement of the BM motion that involves the potential change of the surrounding structures is referred to as the active process. The activity of a cochlea is closely related to the health condition of the cochlea and the intensity of sound. The BM tuning in a dead cochlea is much less remarkable than that of a healthy cochlea. At the cochlear base, the BM has higher sensitivity at low sound intensity levels, and has lower sensitivity at high sound intensity levels. The BM sensitivity is a nonlinear function of sound intensities.

Both OHCs and IHCs contain afferent and efferent nerve fibers. The OHCs have more efferent nerve fibers while the IHCs have more afferent nerve fibers. Neural signals are sent to the brain via afferent nerve fiber. Signals are also sent back from the brain to hair cells via efferent nerve fibers. The sub-TM fluid flow rotates the stereocilia of IHCs. The deflection of the stereocilia of the IHCs opens the ionic channels on it. Ion flows through channels results in the change of the electronic environments of IHCs, which innervates the auditory nerve fibers.

1.2.3 Otoacoustic emissions (OAEs)

Probably one of the most remarkable features of the cochlea is that it not only receives sound, but produces sound as well. The ability of the cochlea to produce sound was first discovered and demonstrated by Kemp in 1978 [54]. The phenomenon that acoustic energy generated inside the cochlea and can be detected in the outer ear canal is called the otoacoustic emissions (OAEs). OAEs are low level response and are usually measured via an acoustic probe with a sensitive microphone.

OAEs can be classified into several types according to the acoustic stimuli that evoke

them [79], as shown in the following chart.

$$\text{OAEs} \left\{ \begin{array}{l} \text{spontaneous OAEs (SOAEs)} \\ \text{evoked OAEs (EOAEs)} \left\{ \begin{array}{l} \text{transiently evoked OAEs (TEOAEs)} \\ \text{stimulus-frequency evoked OAEs (SFOAEs)} \\ \text{distortion-product OAEs (DPOAEs)} \end{array} \right. \end{array} \right.$$

Unlike all the other classes of OAEs that require acoustic stimulations, the spontaneous OAE presents without external stimulation. The emitted signals of SOAEs are narrow-banded and can be recored over a long period of time. One of the special form of SOAEs is the “objective tinnitus”. Transiently evoked OAEs are responses elicited by toneburst (pure tone stimulations with short durations) or clicks (broad frequency range). These responses have delays with eliciting stimuli. The OAE that Kemp [54] initially discovered belongs to this type. Stimulus-frequency evoked OAEs are additional energy generated inside the cochlea at the frequency of a low-level constant tone stimulation. The emission has steady-state response, and its amplitude increase nonlinearly with the amplitude of the stimulation. Distortion product OAEs come from the nonlinearity of the cochlea; the emitted frequencies are algebraic combinations of primary tones.

Although OAEs can be classified in terms of the acoustic stimuli, these emissions are not totally different. Rather, they are closely related in the sense that they all rely on the active signal-transduction of the cochlea. To be specific, the active mechanical-electronic coupling process through hair cells makes the intracochlear sound generation possible. As a result, OAEs strongly depend on the physiological state of the cochlea. Situations such as damaged cochlea, hearing loss, toxic drugs, or hypoxia will all lead to the diminishing of OAEs. Hence, OAEs serve as non-invasive diagnostic tools for the hearing.

1.3 Motivation

This work is motivated by some findings from experiments and also the fact that cochlear amplification mechanism is not yet completely understood. The aim of this work is to answer, or to provide computational tools to answer, some fundamental problems in the mechanics of hearing, which involve both macro and micro fluidic effects in the cochlea.

1.3.1 Modeling the macro-fluid shear viscosity in a pressure-field model

In our current FEM cochlear model [82, 63], the fluid in the SV and ST has the pressure as the primary variable and is modeled as an inviscid flow. Given the small dimension of the cochlea, the fluid viscosity might potentially play a role in the cochlear mechanics. However, in order to incorporate fluid viscosity, the Navier-Stokes equation should be used, which involves at least four degrees of freedom per node in a FEM model. The computational cost associated with using the Navier-Stokes equation makes the method hard to be implemented in a cochlear model if rapid calculation is desired. Then it raises the question whether we can successfully model the fluid shear viscosity with a minor modification on the existing pressure-field fluid model? Is it possible to handle the viscosity for both thin and thick boundary layer thicknesses in a uniform way?

In addition to being able to model the fluid viscosity in the cochlear duct in a fast fashion, we would also like to know whether the macroscopic fluid viscosity indeed plays an important role in the cochlear mechanics, and under what conditions can the viscosity be neglected.

1.3.2 How is the stereocilia of the IHCs stimulated?

The response of the IHC hair bundle (HB) is essential to hearing since it innervates the auditory nerve fibers. One end of the IHC HB stands freely in the fluid in the TM-RL gap. For this configuration, the motion of the IHC HB can either be dominated by the fluid shearing, or by the pulsatile fluid mode in the TM-RL gap. The roles of these two modes are not completely understood yet. To analyze the fluid modes in the TM-RL gap, a complete model for the OoC micro-fluid environment is needed.

In addition to the two excitation modes of the IHC HB, the Hensen's stripe (HS) is also hypothesized to play an important role in the hearing. The distance between the HS and the IHC HB is exceptionally small (micro or sub-micro). Thermal fluctuation or noise may potentially contribute a large portion of the dynamic behaviors of the IHC HB. Understanding the role of the HS may help to unveil the 'optimized' hearing process.

1.3.3 The difference between the cochlear base and the apex

Experimental data measured at the cochlear base [11, 70, 91, 10] and the apex [12, 13, 14, 116] show that the BM tuning has different characteristics at these two longitudinal locations [89]. At the base, the BM gain is nonlinearly increased by the active process [70, 82], in which lower intensity stimulations give rise to higher gains [70, 91, 10]. However, at the apex, the BM shows a lower amplitude under active process than in a passive cochlea,

the so-called ‘negative feedback’ [116]. In addition, the BM gain at the apex with respect to various stimuli intensities are also different from the base. These experimental results suggest that there might be some fundamental difference of the cochlear amplification mechanism between the base and the apex. For example, the OHC somatic motility and the OHC HB electric motility may play different roles at the two spatial locations.

The finite element cochlear model used in this work is a linear model. Different intensities are modeled by various activity levels – higher activity levels produce higher gains, corresponding to low intensity stimulations. The model is especially developed to match experimental data at the base [10, 21]. There is no fundamental difference between the base and the apex in the model except for the tapered structure parameters in the longitudinal direction. If we use the current model to match experimental data at both the base [21] and the apex [30], the gradients of structure parameters turn out to be much larger than what are actually measured [2, 67]. The problem of having to use larger property gradients also exists in other cochlear models, and thus have lead to a number of discussions on the cochlear frequency mapping [34, 26]. It is possible that the active BM tuning and mechanical-electronic transduction are not correctly modeled in the existing cochlear models.

1.3.4 The emitted wave type for energy generated inside the cochlear

Compared to the acoustic stimulation, the intracochlear waves associated with OAEs are less understood. Both compression and traveling waves are considered as the possible emitted wave that is generated inside the cochlea [110]. In order to analyze the two types of waves, we must first understand how and where is the energy generated. Various hypotheses have been made in terms of the energy generation mechanism, and most experimental studies on emitted waves were based on the hypotheses of energy generation [87, 47, 24, 31, 32, 65]. Here we would like to find a way to analyze the emitted wave type without invoking hypotheses on the mechanism of energy generation.

1.3.5 Identifying multiple sources for BM responses

In a sensitive preparation, the BM shows multiple peaks in the spectrum responses and extended ringings in the temporal responses [77, 71, 22, 115]. These observations disappear if the sensitivity of the cochlea is slightly reduced, even if the cochlea is still healthy. It then comes as a question that where do these extra responses come from, and how would these help us to better understand cochlear mechanics.

One of the questions goes back to von Bekesy [2] as whether the cochlea supports

backward traveling waves. If yes, how does it relate to the measured BM temporal responses in a sensitive cochlea under intracochlear excitation. We would also like to know the role of cochlear activity in backward/forward traveling waves.

1.3.6 Evaluating the cochlear activity

Our understanding of the cochlear activity rely much on the gain function of the BM tuning. The amplified BM responses suggest the existence of cochlear amplification in a healthy cochlea. A more careful study of the cochlear amplification would require intracochlear energy calculation. However, due to the limited available experimental data, i.e., the intracochlear BM and pressure profiles are not available simultaneously, the cochlear energy cannot be calculated directly. It is thus of interest to estimate the cochlear activity by using limited experimental data. This estimation would involve solving inverse problems from available data. We can ask the question in a more interesting way: can we analyze the activity of the cochlea given that the BM response is only known over a small longitudinal segment (around 2 millimeters [84, 86]).

1.4 Organization of the thesis

The thesis is organized as follows:

Chapter II summarizes the FEM cochlear model that has been previously developed [82, 63]. The entire thesis is based on, or developed from, that model.

Chapter III provides a way to model fluid shear viscosity in a fluid-structure interaction problem for both thin and thick viscous boundary layers with minor modification on the existing pressure-field fluid model. The method can address the modeling of shear viscosity in the macro (in millimeters) intracochlear fluid. The method can also be used in MEMS device where fluid viscosity plays an important role in structural acoustic problems.

Chapter IV develops a method to study the viscous fluid-structure interaction problem in the micro (in micro or sub-micro scales) fluidic environments in the cochlea.

Chapter V studies the direction of macro wave propagation inside the cochlea for known intracochlear excitations.

Chapter VI analyzes multiply sources that may potentially contribute to the coda of the BM measured in experiments.

Chapter VII assesses the cochlear activity and studies the challenges associated with solving an inverse problem.

Chapter VIII concludes the thesis.

CHAPTER II

The mechano-electro-acoustical finite element cochlear model description

This chapter summarizes a physiologically based three dimensional mechano-electro-acoustical finite element cochlear model that has been developed by Ramamoorthy *et al.* [82], and Meaud and Grosh [63]. These models serve as the basis for the predictions and extensions to their theory presented in this document.

2.1 Fluid and the BM

The spiral cochlea is simplified as a box (Fig. 2.1) with rigid walls, except at the stapes and the round window. This is a standard simplification in cochlear modeling. The x , y , and z coordinates are in the longitudinal, radial, and vertical (normal to the BM) directions, respectively. The cochlear partition (including the TM and the OoC) locates on the $x - y$ plane, and each cochlear cross section is parallel to the $y - z$ plane. The SV and the ST are two equal sizes duct divided by the cochlear partition. The helicotrema locates at the end of the cochlea where the BM terminates, connecting the SV and the SV. The RM is acoustically transparent [2, 98] and hence is ignored in modeling the macroscopic fluid model.

The macroscopic fluid is modeled by the wave equation. The viscosity of the fluid is incorporated into the structural damping of the BM and in TM-RL shear interaction. Only harmonic motions of the system were considered. A time dependence of $\exp(i\omega t)$ is assumed. The governing equation for the bulk fluid domain is

$$\nabla^2 p + \left(\frac{\omega}{c}\right)^2 p = 0, \quad (2.1)$$

where p is the pressure of the fluid, c is the speed of sound in the fluid. The three-

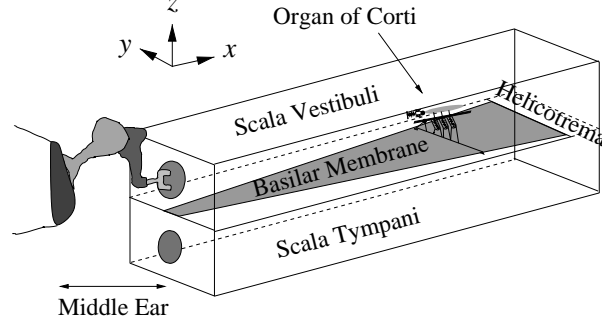


Figure 2.1: Illustration of the model used for simulating the cochlea. Organ of Corti is only pictured at one cross-section. In the mathematical model it is included over the entire length of the basilar membrane. Figure taken from Ramamoorthy *et al.* [82] (Fig. 1).

dimensional fluid is decomposed in the radial (y) direction [76] as,

$$p(x, y, z) = \sum_{m=1}^{M-1} p_m(x, z) \cos\left(\frac{2m\pi}{w}y\right), \quad -\frac{w}{2} \leq y \leq \frac{w}{2} \quad (2.2)$$

where w is the width of the duct, m is the mode number, and M is the total number of modes. The relationship between the fluid velocity and the fluid pressure is given by the linearized Euler relation

$$\nabla p = -i\rho\omega\mathbf{v}_f, \quad (2.3)$$

where ρ is the density of the fluid, and \mathbf{v}_f is the fluid velocity vector.

The BM is modeled as a set of simply supported beams in the current work. *In vivo* experiments showed that the BM can be modeled by the first symmetric mode [50] in the radial direction. Hence,

$$u_{bm}(x, y) = u_{bm}(x)\Psi(y), \quad (2.4)$$

where

$$\Psi(y) = \cos\left(\frac{\pi}{b}y\right) \quad -b/2 \leq y \leq b/2,$$

and b is the width of the membrane.

Using the model decomposition in Eq. 2.2 plus the orthogonality of the modes with respect to the rigid y -normal surfaces, Eq. 2.1 can be reduced to a series of 2-dimensional problems as,

$$\frac{\partial^2 p_m}{\partial x^2} + \frac{\partial^2 p_m}{\partial z^2} + \left[\left(\frac{\omega}{c}\right)^2 - \left(\frac{m\pi}{w}\right)^2 \right] p_m(x, z) = 0. \quad (2.5)$$

Assuming a locally reacting structure for the BM, the structural equation is

$$\frac{b}{2} \left(-M_{bm}(x)\omega^2 + iC_{bm}(x)\omega + K_{bm}(x) \right) u_{bm}(x) = \sum_{m=0}^{M-1} (p_m^{SV} - p_m^{ST})\mu_m + Q_{\mu\text{mech}}, \quad (2.6)$$

where M_{bm} , C_{bm} , and K_{bm} are the resultant mass, damping, and stiffness, respectively, p_m^{SV} and p_m^{ST} are the pressure loading on the BM from the fluid corresponding to mode m in the SV and the ST respectively, μ_m is the fluid-BM coupling coefficient [76],

$$\mu_m = \int_{-b/2}^{b/2} \cos\left(\frac{2m\pi}{w}y\right) \cos\left(\frac{\pi}{b}y\right) dy, \quad (2.7)$$

and $Q_{\mu\text{mech}}$ is the force from the micro-electro-mechanical model. The factor $b/2$ in Eq. 2.6 comes from the integration of the BM mode in the radial direction.

2.2 Electrical environment

The current flow in the longitudinal direction at each scala is modeled by one dimensional cables [81]. The circuit at each cochlear cross section is given by Fig. 2.2, which includes longitudinal cables in the SV, the ST, and the SM. The ST cable represents the potential in the ST close to the BM. The physical meanings and units of the symbols appearing in the figure is listed in Tab. 2.1

The dynamic equations of the electrical field is governed by Kirchoff's law, including the cables in the longitudinal direction and the cross-sectional circuits. The governing equations are [82],

$$\frac{1}{r_{sv}} \frac{\partial^2 \phi_{sv}}{\partial x^2} - \left(\frac{1}{R_{vl}} + \frac{1}{R_{vm}} \right) \phi_{sv} + \frac{1}{R_{vm}} \phi_{sm} = 0, \quad (2.8)$$

$$\frac{1}{R_{vm}} \phi_{sv} + \frac{1}{r_{sm}} \frac{\partial^2 \phi_{sm}}{\partial x^2} - \left(\frac{1}{R_{vm}} + 3Y_a \right) \phi_{sm} + 3Y_a \phi_{ohc} - I_{s1} = 0, \quad (2.9)$$

$$3Y_a \phi_{sm} - 3(Y_a + Y_m) \phi_{ohc} + 3Y_m \phi_{st} + I_{s1} - I_{s2} = 0, \quad (2.10)$$

$$3Y_m \phi_{ohc} + \frac{1}{r_{st}} \frac{\partial^2 \phi_{st}}{\partial x^2} - \left(\frac{1}{R_{tl}} + 3Y_m \right) \phi_{st} + I_{s2} = 0. \quad (2.11)$$

where $Y_a = 1/R_a^0 + i\omega C_a = G_a^0 + i\omega C_a$ and $Y_m = 1/R_m + i\omega C_m$ are the admittances at the apical and basolateral locations of the OHCs, respectively.

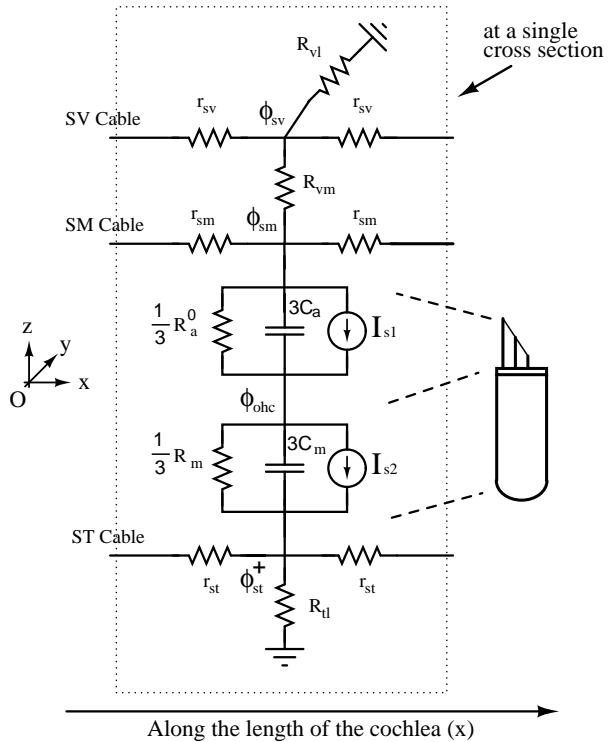


Figure 2.2: Electrical network at a given cross-section of the cochlea. The SV, SM, and ST cables run longitudinally along the cochlea. The factor of three multiplying the apical and the basolateral membrane capacitance, and dividing the apical and the basolateral membrane resistance of the OHC is to account for the three OHCs in a cross-section. Figure taken from Ramamoorthy *et al.* [82] (Fig. 2).

Table 2.1: Symbols and units in Fig. 2.2

Symbols	Physical meanings	Units
r_{sv}	resistance per unit length long the SV cable	Ω/m
r_{sm}	resistance per unit length long the SM cable	Ω/m
r_{st}	resistance per unit length long the ST cable	Ω/m
R_{vm}	resistance to the current flow from the SV to the SM	$\Omega \cdot \text{m}$
R_{vl}	resistance to the current flow from the SV to the ground	$\Omega \cdot \text{m}$
R_{tl}	resistance to the current flow from the ST to the ground	$\Omega \cdot \text{m}$
R_a^0	resting state of the apical resistance of the OHCs	$\Omega \cdot \text{m}$
C_a	apical capacitance of the OHCs	F/m
R_m	basolateral resistance of the OHCs	$\Omega \cdot \text{m}$
C_m	basolateral capacitance of the OHCs	F/m
$I_{s1,2}$	current sources due to the stereocilias and the OHCs	A/m
ϕ_{sv}	fluctuating part of the voltage in the SV	V
ϕ_{sm}	fluctuating part of the voltage in the SM	V
ϕ_{ohc}	fluctuating part of the voltage in the OHCs	V
ϕ_{st}	fluctuating part of the voltage in the ST	V

2.3 Kinematic model of microstructures

Fig. 2.3 shows the kinematic model of the OoC based on Ref. [16]. The BM is simply supported and has one degree of freedom. The TM has two degrees of freedom, one in the radical direction (shear) and the other in the transverse direction (bending). The DCs, which are in series with the OHCs, are modeled as rigid bodies since their impedance is several orders of magnitude higher than that of OHCs [67]. The stiff RL [48, 38] is modeled as a rigid plate. The HBs are regarded as rigid links rotating around pivots. Since the pillar cells have very high elastic modulus [104, 107], the arch of Corti is treated as a rigid body that can rotate around the bottom of the inner pillar cells.

There are three degrees of freedom in the OoC, one from the BM and the other two from the TM. The motions of the OHCs, HBs, and the RL are expressed in terms of the motions of the BM and the TM. To derive the equations of motion, some assumptions are imposed on the kinematic relations. The motions are small and thus can be linearized. The OHC (α) and HB (β) angles only refer to the middle row OHCs and HBs. The kinematic relations for the other two rows of cells are derived from their relations with the middle row cells. It is further assumed that $\alpha = \beta$, $\theta_1 = \theta_2 = \theta$ [68], and $L_0 = b/2$ [68].

Based on these assumption, the displacement of the apical end of the arch of Corti

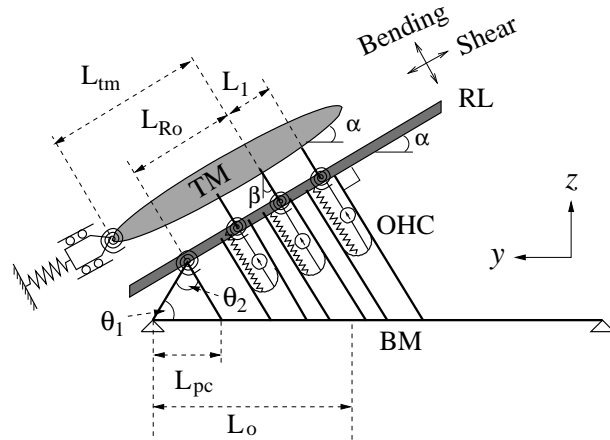


Figure 2.3: Micromechanical model for the organ of Corti structures. The sketch is drawn for $\alpha = \beta$. BM – Basilar Membrane, TM – Tectorial Membrane, OHC – Outer Hair Cell, RL – Reticular Lamina. L_{Ro} is the distance between RL pivot point on the arch of Corti and the middle OHC, L_1 is the radial distance between OHCs along the RL, θ_1 is the acute angle between the inner pillar cell and the BM, θ_2 is the acute angle between the inner and outer pillar cell, L_{pc} is the distance along the BM between the left edge of the BM and the contact point of the outer pillar cell with the BM, L_o is the distance along the BM between the left edge of the BM and the contact point of the middle OHC with the BM, and L_{tm} is the length of the TM from its pivot to the attachment point of the middle row HCs with the TM. Figure taken from Ramamoorthy *et al.* [82] (Fig. 3).

(top of the pillar cells) is approximated as

$$u_{ap}(x) = u_{bm}(x) \Psi_1(b/2 - L_{pc}) 2 \cos \theta, \quad (2.12)$$

where $u_{bm}(x)$ is the amplitude of the BM and $\Psi_1(b/2 - L_{pc})$ is the mode shape of the BM evaluated at $y = b/2 - L_{pc}$.

The OHCs compression, u_{ohc}^{comp} , is determined by the sum of the deflections of the OHC apex and OHC base. The displacement of the middle row OHC apex toward the BM along the OHC is,

$$u_{ohc2}^a(x) = u_{bm}(x) \Psi_1(b/2 - L_{pc}) 2 \cos \theta [-\cos(\theta - \alpha) + \cos(\theta - \beta)] - u_{tmb}(x). \quad (2.13)$$

The displacement of the middle row OHC base toward the RL along the OHC is,

$$u_{ohc2}^b(x) = u_{bm}(x) \cos(\alpha). \quad (2.14)$$

The sum of the rotations of the HBs and the RL relative to their resting positions gives the relative rotation between the HBs and the RL. The relative shear motion (outer normal to the HBs) between the top and the ends of the of the middle row HBs is,

$$u_{hb2}(x) = u_{bm}(x) \Psi_1(b/2 - L_{pc}) 2 \cos \theta \sin(\theta - \alpha) + u_{tms}(x). \quad (2.15)$$

The rotation of the HBs relative to their resting position is given by u_{hb2}/L_{hb} , where L_{hb} is the length of HBs. The RL displacement at the middle OHCs relative to the attachment of the pillar cells (positive normal to the RL) is,

$$u_{rl2}(x) = -u_{bm}(x) \Psi_1(b/2 - L_{pc}) 2 \cos \theta \cos(\theta - \beta) + u_{tmb}(x). \quad (2.16)$$

The rotation of the RL relative to its resting position is given by u_{rl2}/L_{ro} .

The motion of the first and the third rows OHCs and HBs can be derived from those of the middle row via the geometrical relations (see Fig. 2.3). For instance, the displacement of the apical end of the first row OHCs is,

$$u_{ohc1}^a(x) = u_{bm}(x) \Psi_1(b/2 - L_{pc}) 2 \cos \theta \left[-\cos(\theta - \alpha) + \left(1 - \frac{L_1}{L_{Ro}}\right) \cos(\theta - \beta) \right] - \left(1 - \frac{L_1}{L_{Ro}}\right) u_{tmb}(x). \quad (2.17)$$

2.4 TM longitudinal coupling

While the BM is modeled as locally reacting beams, the longitudinal viscoelastic coupling of the shear motion of the TM is included. However, the TM bending rigidity is neglected. The governing equation for the TM shear motion is,

$$F_{hb/tms}(x) = K_{tms}u_{tms} + C_{sub}^f \dot{u}_s + M_{tms} \ddot{u}_{tms} - \frac{\partial}{\partial x} \left(A_{tm}^{eff} G_{xy} \frac{\partial u_{tms}}{\partial x} + A_{tm}^{eff} \eta_{xy} \frac{\partial \dot{u}_{tms}}{\partial x} \right), \quad (2.18)$$

where G_{xy} and η_{xy} are the shear modulus and viscosity of the TM. $F_{hb/tms}$ is the force per unit length applied by the HBs in the shear direction[82]. C_{sub}^f is the damping coefficient from the sub-TM fluid. u_s is the relative shear displacement between the TM and the RL. A_{tm}^{eff} , K_{tms} , and M_{tms} are the effective cross-section area, the shear stiffness, and the shear mass per unit length of the TM, respectively.

2.5 Hair bundle conductance and OHC electromotility

The mechanical and the electrical domain of the cochlear model are coupled via the HB conductance and the OHC electromotility as responses to mechanical motions. The HB conductance is assumed to change linearly with the rotation of the HBs relative to the RL,

$$G_{a_j} = G_a^0 + G_a^1 L_{hb} \theta_{hb_j/rl_j}, \quad (2.19)$$

where $G_a^0 = 1/R_a^0$ is the HB conductance at the resting state, and G_a^1 is the mechano-electrical transducer (MET) sensitivity indicating the slope of the change of conductance with respect to the HB deflection. Subscript $j = 1, 2, 3$ is the radial counting index for the OHCs. G_a^0 and G_a^1 are constant at each cross section.

The current flowing through the j^{th} HB (I_{hb_j}) is the product of the apical admittance and the potential drop from the SM to the OHC interior. It is linearized as,

$$I_{hb_j} = (G_a^0 + i\omega C_a)(\phi_{sm} - \phi_{ohc}) + (V_{sm} - V_{ohc})G_a^1 L_{hb} \theta_{hb_j/rl_j}, \quad (2.20)$$

where V_{sm} and V_{ohc} are the resting state voltages in the SM and the OHCs, respectively. The current source I_{s1} in the model is defined as the contribution of the variable HB conductance,

$$I_{s1} = (V_{sm} - V_{ohc})G_a^1 L_{hb} \sum_{j=1}^3 \theta_{hb_j/rl_j}. \quad (2.21)$$

The OHC electro-motility relating the OHC strain and transmembrane voltage to the

OHC force and current [33, 29]. The linearized expression is

$$F_{ohc_j} = K_{ohc} u_{ohc_j}^{comp} + \epsilon_3 (\phi_{ohc} - \phi_{st}^+), \quad (2.22)$$

$$I_{ohc_j} = (\phi_{ohc} - \phi_{st}^+)/Z_m - i\omega\epsilon_3 u_{ohc_j}^{comp}. \quad (2.23)$$

In the above question, subscript j refer to the j^{th} row OHCs. F_{ohc} is the force exerted by the OHCs on the BM and the RL. I_{ohc} is the current flowing through the OHCs. ϵ_3 is the electromechanical coupling coefficient. Z_m is the net basolateral impedance of the OHC given by $1/Z_m = 1/R_m + i\omega C_m$ (see Fig. 2.2). And K_{ohc} is the stiffness of the OHCs. The current source I_{s2} in the model is defined as the contribution of the piezoelectric-like behavior of the OHCs,

$$I_{s2} = -i\omega\epsilon_3 \sum_{j=1}^3 u_{ohc_j}^{comp}. \quad (2.24)$$

Eqs. 2.20 and 2.23 relate the motion of the OoC to the additional current flow through the HBs and the OHCs, and Eq. 2.22 relates the change of the OHC transmembrane potential to the equivalent force generation by the OHCs.

2.6 Local governing equation

The motion of the TM and the OoC components forms a mechanical system. By converting the rotational stiffness of the coil springs for the HBs, the TM, and the RL to equivalent linear stiffness, the kinetic and potential energy at each longitudinal location for this system is

$$\mathcal{T} = \frac{1}{2}M_{tms}\dot{u}_{tms}^2 + \frac{1}{2}M_{tmb}\dot{u}_{tmb}^2 + \frac{1}{2}M_{bm}\dot{u}_{bm}^2, \quad (2.25)$$

$$\begin{aligned} \mathcal{V} = & \frac{1}{2}K_{bm}u_{bm}^2 + \frac{1}{2}K_{tms}u_{tms}^2 + \frac{1}{2}K_{tmb}u_{tmb}^2 + \frac{1}{2}K_{hb} \left[\left(u_{hb_1} + u_{rl_1} \frac{L_{hb}}{L_{Ro} - L_1} \right)^2 \right. \\ & + \left(u_{hb_2} + u_{rl_2} \frac{L_{hb}}{L_{Ro}} \right)^2 + \left. \left(u_{hb_3} + u_{rl_3} \frac{L_{hb}}{L_{Ro} + L_1} \right)^2 \right] \\ & + \frac{1}{2}K_{rl} \left(u_{rl_2} + \frac{u_{ap}}{L_{pc}} L_{Ro} \right)^2, \end{aligned} \quad (2.26)$$

where u is displacement, K is stiffness, and M is mass. Subscripts bm , tmb , and tms refer to the quantities of the BM, the TM bending, and the TM shearing, respectively.

The generalized work done by external forces to the TM and the OoC mechanical

system is,

$$\begin{aligned} \delta W = & - \sum_{j=1}^3 F_{ohc_j} \delta u_{ohc_j}^{comp} - \sum_m (p_m^{SV} - p_m^{ST}) \delta u_{bm} \mu_m \\ & - (C_{bm} \dot{u}_{bm}) \delta u_{bm} - (C_{tms} \dot{u}_{tms}) \delta u_{tms} - (C_{tmb} \dot{u}_{tmb}) \delta u_{tmb}, \end{aligned} \quad (2.27)$$

where C_{bm} , C_{tms} , and C_{tmb} are the viscous damping coefficients for the BM, the TM bending, and the TM shear modes, respectively. $u_{ohc_j}^{comp} = u_{ohc_j}^{comp}(u_{bm}, u_{tms}, u_{tmb})$ is a function depends on u_{bm} , u_{tms} , and u_{tmb} .

The variation of the Lagrangian ($L = \mathcal{T} - \mathcal{V}$) with respect to the three mechanical variables (u_{bm} , u_{tms} , and u_{tmb}) corresponding to the three degrees of freedom gives the governing equation of motion,

$$\frac{\partial}{\partial t} \frac{\partial L}{\partial \dot{u}_i} - \frac{\partial L}{\partial u_i} = Q_i, \quad (2.28)$$

where i varies over bm , tms , and tmb . Q_i is defined by

$$\delta W = - \sum_{i=\{bm,tms,tmb\}} Q_i \delta u_i. \quad (2.29)$$

2.7 Finite elements

The finite element weak form is obtained by multiplying the governing equations of the strong form by the weighting functions and integrating over the domain [76, 51]. The final finite element stiffness matrix takes the form,

$$\begin{bmatrix} \mathbf{K}_f & \mathbf{Q}_{fs} & \mathbf{0} \\ \mathbf{Q}_{sf} & \mathbf{K}_s & \mathbf{Q}_{se} \\ \mathbf{0} & \mathbf{Q}_{es} & \mathbf{K}_e \end{bmatrix} \begin{pmatrix} \mathbf{p} \\ \mathbf{u} \\ \phi \end{pmatrix} = \begin{pmatrix} \mathbf{f}_f \\ \mathbf{0} \\ \mathbf{0} \end{pmatrix}. \quad (2.30)$$

The non-reciprocal MET functions (see Sec. 2.5) makes the matrix non-symmetric. In the equation, \mathbf{K}_f , \mathbf{K}_s , and \mathbf{K}_e are the dynamic stiffness matrix of the fluid, the micro-mechanical structures, and the electronic environment, respectively. \mathbf{Q}_{es} and \mathbf{Q}_{se} are electrical-structural coupling matrix, and \mathbf{Q}_{fs} and \mathbf{Q}_{sf} are fluid-structure coupling matrix. \mathbf{f}_f is forcing on the fluid. In most cases it comes from the acoustic input from the stapes. The linear matrix is solved for fluid pressure (\mathbf{p}), structural displacements (\mathbf{u} , including u_{bm} , u_{tms} , and u_{tmb}), and electrical potentials (ϕ , including ϕ_{sv} , ϕ_{sm} , ϕ_{ohc} , and ϕ_{st}) at each node of the finite element formulation (mesh).

CHAPTER III

Including fluid shear viscosity in a structural acoustic finite element model using a scalar fluid representation

An approximate boundary condition is developed in this work to model fluid shear viscosity at boundaries of coupled fluid-structure system. The effect of shear viscosity is approximated by a correction term to the inviscid boundary condition, written in terms of second order in-plane derivatives of pressure. Both thin and thick viscous boundary layer approximations are formulated; the latter subsumes the former. These approximations are used to develop a variational formulation, upon which a viscous finite element method (FEM) model is based, requiring only minor modifications to the boundary integral contributions of an existing inviscid FEM model. Since this FEM formulation has only one degree of freedom for pressure, it holds a great computational advantage over the conventional viscous FEM formulation which requires discretization of the full set of linearized Navier-Stokes equations. The results from thick viscous boundary layer approximation are found to be in good agreement with the prediction from a Navier-Stokes model. When applicable, thin viscous boundary layer approximation also gives accurate results with computational simplicity compared to the thick boundary layer formulation. Direct comparison of simulation results using the boundary layer approximations and a full, linearized Navier-Stokes model are made and used to evaluate the accuracy of the approximate technique. Guidelines are given for the parameter ranges over which the accurate application of the thick and thin boundary approximations can be used for a fluid-structure interaction problem.

3.1 Introduction

There are many problems in acoustics and structural acoustics where fluid viscosity

plays an important role. For example, in micro-electro-mechanical systems and micro-scale biological structures, an inviscid approximation to the flow results in large errors in the predicted response. Using a linearized Navier–Stokes (N-S) solution, however, increases the number of unknowns by at least a factor of three compared to an inviscid approximation. Hence, there is a large computational burden associated with incorporating the correct physics. Significant effort has been devoted to develop accurate numerical methods to model fluid-structure interaction including viscosity [36, 43, 9, 105]. It is possible to discretize and solve the three dimensional (3-D) linearized N-S equations with fluid viscosity using a personal computer or small cluster of parallel nodes [9, 36]. Models with appropriate choice of fluid, structure, and coupling elements are able to predict accurate results, but the computational cost is high as a typical 3-D viscous fluid model utilizes fluid velocity and pressure as independent variables. In this paper, we show how to seamlessly include a boundary perturbation term into an inviscid finite element formulation (with one scalar nodal unknown) to accurately approximate the effects of viscosity for a wide range of boundary layer (BL) thicknesses in a structural acoustic system.

In order to avoid the computational burden associated with solving the 3-D N-S equations, simplifications of the viscous fluid field equations have been used to develop different approximate schemes. For interior structural acoustics problems when the viscous BL is comparable to the smallest dimension of the interior fluid domain, Beltman [3] used the thin–film fluid approximations to develop an efficient and accurate finite element method. For the case where the viscous BL is thin compared to the dimensions of the problem (or the domain is unbounded), Holmes and Cole [49] derived a modified boundary condition including viscosity. The modified boundary condition was obtained by matching the inner (inside the BL) and outer (outside the BL) solutions of pressure and velocity. The resulting equation was written in terms of pressure and its normal derivatives only. The Holmes and Cole boundary condition is not readily applicable in a numerical scheme because it involved higher order derivatives in the out-of-plane direction. A hybrid numerical and analytical solution for thermo-viscous fluid was presented by Bossart *et al.* [5]. The viscous boundary condition was derived from the N-S equation with the assumption that the viscous and thermal BL thicknesses are much smaller than the dimension of the problem. Inside the BL, the assumptions are the same as in Beltman’s approach [3]. The viscous correction term is incorporated into a variational scheme and, like the Holmes and Cole condition, involves higher order out-of-plane derivatives. In Bossart *et al.* [5], the higher order derivative is eliminated by introducing the wavenumber in the normal direction. The wavenumber is unknown but bounded and an iterative scheme to find the wavenumber was proposed (however, results for only a single iteration were

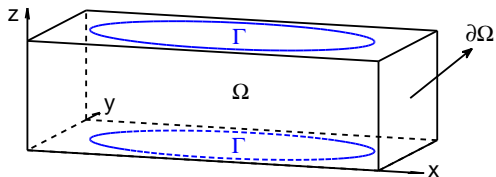


Figure 3.1: Schematic of a generic fluid-structure coupled system. Ω is the interior of fluid filled duct. The boundary of the duct is denoted by $\partial\Omega$, and $\Gamma \subset \partial\Omega$ is the flexible structure on the $z = 0$ and $z = L_z$ surfaces.

presented). Lim and Steele [58] used an alternate approach to model fluid viscosity in the cochlea duct through a semi-analytical WKB (Wentzel-Kramers-Brillouin) method (see also Steele and Taber [100]). The viscous BL at fluid-structure interface was included and a single mode of propagation included. The analytical approximation offers some advantages as no assumptions were necessary on the relative magnitude between in-plane and out-of-plane gradients since the in-plane gradients can be explicitly represented by in-plane wave numbers for each WKB-mode (or solution to the eikonal equation).

In this chapter, we develop a new viscous boundary correction to an inviscid formulation. We are primarily interested in liquid-structure interaction so that the thermal effect of the fluid is not considered. However, if the fluid is air, its thermal effect is coupled to the fluid pressure and density. In this case, the thermal effect becomes important and should be taken into account in the model (e.g., Beltman [3] and Bossart *et al.* [5]). We will show how to implement the modified boundary condition to an existing inviscid finite element scheme with minor changes to retain its low computational cost. As an example, this new formulation is used to analyze a fluid-structure interaction system comprised of a rectangular fluid-filled duct with a flexible structure occupying part of the boundary.

3.2 Method

Consider a viscous fluid contained within a rectangular enclosure shown in Fig. 3.1. The fluid geometry is given by $\Omega = \{0 \leq x \leq L_x, 0 \leq y \leq L_y, 0 \leq z \leq L_z\}$. We assume that the viscous BL thickness δ satisfies $\delta \ll L_x$ and L_y . The interior surface is $\partial\Omega$ and non-rigid boundaries are contained in Γ . For clarity of presentation, we restrict the flexible structures to the constant- z surfaces ($z = 0$ and $z = L_z$).

3.2.1 Viscous Boundary Layer Correction Theory

The mathematical model for viscous and compressible acoustic fluid is based on continuity equation, compressibility equation, and linearized N-S equations are given next:

$$\frac{\partial \rho_f}{\partial t} + \rho_f \nabla \cdot \mathbf{v} = 0, \quad (3.1)$$

$$\beta = \frac{1}{\rho_f} \frac{\partial \rho_f}{\partial P} \Big|_{\text{adiabatic conditions}}, \quad (3.2)$$

$$\rho_f \frac{\partial \mathbf{v}}{\partial t} = -\nabla P + \mu \nabla^2 \mathbf{v} + \frac{1}{3} \mu \nabla (\nabla \cdot \mathbf{v}), \quad (3.3)$$

where ρ_f is the fluid density, $\beta (= 1/\rho_f c^2)$ is the compressibility of the fluid, and \mathbf{v} is the fluid velocity vector. Time harmonic solutions of the form $e^{j\omega t}$ are sought. The velocity field is decomposed into the gradient of a scalar field Φ and the curl of a vector field $\tilde{\Psi}$ as

$$\mathbf{v} = \nabla \Phi + \nabla \times \tilde{\Psi}, \quad (3.4)$$

where Φ is related to pressure P by $\Phi = -(\alpha/j\omega\rho_f)P$, and $\alpha = 1 + (j\omega 4\mu/3\rho_f c^2)$. Eliminating Φ and \mathbf{v} in Eqs. 3.1-3.3 gives the following equations,

$$\nabla^2 P + \frac{\omega^2}{\alpha c^2} P = 0, \quad \text{in } \Omega, \quad (3.5)$$

$$\tilde{\Psi} = \frac{\mu}{j\omega\rho_f} \nabla^2 \tilde{\Psi}, \quad \text{in } \Omega. \quad (3.6)$$

For clarity of illustration, in the following we show the derivation of BL correction to the constant- z surfaces (the BL correction to the other surfaces follows directly, as will see later). Within the BL, one can scale the normal direction of the z variable by the BL thickness δ [49], and expand the viscosity vector field $\tilde{\Psi}$ in terms of δ as well. From the asymptotic analysis, the normal derivative, $\partial/\partial z$, dominates the other derivatives in the governing equation for $\tilde{\Psi}$ (Eq. 3.6), and the leading order approximation term of $\tilde{\Psi}$ (denoted as Ψ) in Eq. 3.6 is

$$\frac{\partial^2 \Psi}{\partial z^2} - \frac{j\omega\rho_f}{\mu} \Psi = 0, \quad \text{in } \Omega. \quad (3.7)$$

Following Steele and Taber [100], a solution for the vector potential Ψ in Eq. 3.7 is,

$$\Psi = \begin{pmatrix} \Psi_1 \\ \Psi_2 \\ \Psi_3 \end{pmatrix} = \begin{pmatrix} A_1(x, y)e^{\gamma z} + B_1(x, y)e^{\gamma(L_z - z)} \\ A_2(x, y)e^{\gamma z} + B_2(x, y)e^{\gamma(L_z - z)} \\ 0 \end{pmatrix}, \quad (3.8)$$

where $\gamma = \sqrt{j\omega\rho_f/\mu}$. The real part of γ is chosen to be negative so that $e^{\gamma z}$ decays with increasing z . The BL thickness δ is defined as $|1/\Re(\gamma)|$, given by $\delta = \sqrt{2\mu/\rho_f\omega}$. Ψ plays a significant role inside the BLs. Assuming negligible in-plane structural motion on Γ , one has the no-slip boundary condition at $z = 0$ and $z = L_z$,

$$v_x = \frac{\partial\Phi}{\partial x} - \frac{\partial\Psi_2}{\partial z} = 0, \quad v_y = \frac{\partial\Phi}{\partial y} + \frac{\partial\Psi_1}{\partial z} = 0, \quad \text{on } z = 0, L_z. \quad (3.9)$$

Extensions to non-zero in-plane motions are possible, but they are not included here. Except when explicitly mentioned, $\mathbf{v} = 0$ is prescribed on the other surfaces at $x = 0$, $x = L_x$, $y = 0$, and $y = L_y$.

The z -dependence of Ψ is now determined. Next we will use the boundary conditions in Eq. 3.9 to obtain the coefficients A_1 , A_2 , B_1 , and B_2 (in Eq. 3.8) for two cases.

3.2.1.1 Case 1: thin boundary layer approximation ($\delta \ll L_z$)

If $\delta \ll L_z$, then we assume that BL perturbation at one surface is not coupled to the other surface. For instance, the solution at $z = 0$ is taken to be

$$\Psi_1 = A_1(x, y)e^{\gamma z}, \quad \Psi_2 = A_2(x, y)e^{\gamma z}, \quad \Psi_3 = 0. \quad (3.10)$$

The unknown coefficients A_1 and A_2 are solved from the no-slip boundary condition at $z = 0$ (Eq. 3.9),

$$A_1(x, y) = -\frac{1}{\gamma} \frac{\partial\Phi}{\partial y} \Big|_{z=0}, \quad A_2(x, y) = \frac{1}{\gamma} \frac{\partial\Phi}{\partial x} \Big|_{z=0}. \quad (3.11)$$

The continuity of the normal velocity at $z = 0$ gives,

$$v_z = \frac{\partial\Phi}{\partial z} + \frac{\partial\Psi_2}{\partial x} - \frac{\partial\Psi_1}{\partial y} = j\omega W(x, y), \quad \text{on } z = 0, \quad (3.12)$$

where $W(x, y)$ is the normal displacement of the structure, defined to be positive in the positive z -direction. Substitution of Ψ_1 and Ψ_2 with Φ (by using Eqs. 3.10 and 3.11) into

Eq. 3.12, and replacement of Φ by P to have

$$\frac{\partial P}{\partial z} + \frac{1}{\gamma} \nabla_{xy}^2 P = \frac{1}{\alpha} \rho_f \omega^2 W(x, y), \quad \text{on } z = 0, \quad (3.13)$$

where ∇_{xy}^2 is the Laplace operator in the xy -plane. The second term on the left-hand-side of Eq. 3.13 is the correction term at $z = 0$ due to the viscosity.

Similarly, if we consider the viscous BL at $z = L_z$ alone, the solution of Ψ has the form,

$$\Psi_1 = B_1(x, y)e^{\gamma(L_z - z)}, \quad \Psi_2 = B_2(x, y)e^{\gamma(L_z - z)}, \quad \Psi_3 = 0. \quad (3.14)$$

Applying the no-slip boundary condition at $z = L_z$ yields,

$$B_1(x, y) = \frac{1}{\gamma} \frac{\partial \Phi}{\partial y} \Big|_{z=L_z}, \quad B_2(x, y) = -\frac{1}{\gamma} \frac{\partial \Phi}{\partial x} \Big|_{z=L_z}. \quad (3.15)$$

The corresponding pressure boundary condition at $z = L_z$ is

$$\frac{\partial P}{\partial z} - \frac{1}{\gamma} \nabla_{xy}^2 P = -\frac{1}{\alpha} \rho_f \omega^2 W(x, y), \quad \text{on } z = L_z. \quad (3.16)$$

Equations 3.13 and 3.16 are the viscous corrections for thin BLs on $z = 0$ and $z = L_z$, respectively. These equations can be used either individually (on either $z = 0$ or $z = L_z$) or simultaneously (on both $z = 0$ and $z = L_z$) to account viscosity on the constant- z surfaces.

Equations 3.13, 3.16 are then generalized to any portion of $\partial\Omega$

$$-\frac{\partial P}{\partial n} + \frac{1}{\gamma} \nabla_s^2 P = \frac{1}{\alpha} \rho_f \omega^2 W, \quad \text{on } \partial\Omega, \quad (3.17)$$

where W is the normal velocity on the structure, n is the outward normal of a surface, and ∇_s^2 is the in-plane (tangent) Laplace operator on the surface where n is defined. Equation 3.17 is a higher order approximation for the normal pressure derivative on the boundary (see also Appendix B). It is applicable on any surface $\partial\Omega$ (including the surfaces normal to the x and y directions) in this system because $\delta \ll L_x, L_y, L_z$ is assumed in this derivation.

3.2.1.2 Case 2: thick boundary layer approximation ($\delta \sim L_z$)

Next we consider the case where $\delta \ll L_z, L_y$ (the thin BL case handled in Sec. 3.2.1.1), but $\delta \sim L_z$ so that the viscous BL at $z = 0$ *couples* to the BL at $z = L_z$. Assuming the $z = 0$ and $z = L_z$ surfaces are parallel (this method of thick boundary layer approximation

is not valid if the two surfaces are not parallel) and following the same procedure as before, one solves the coefficients A_1 , A_2 , B_1 and B_2 (in Eq. 3.8) from the no-slip boundary condition,

$$\begin{aligned} A_1 &= -\frac{\frac{\partial\Phi}{\partial y}\big|_{z=0} - \frac{\partial\Phi}{\partial y}\big|_{z=L_z} e^{\gamma L_z}}{\gamma(1 - e^{2\gamma L_z})}, & B_1 &= -\frac{\frac{\partial\Phi}{\partial y}\big|_{z=0} e^{\gamma L_z} - \frac{\partial\Phi}{\partial y}\big|_{z=L_z}}{\gamma(1 - e^{2\gamma L_z})}, \\ A_2 &= \frac{\frac{\partial\Phi}{\partial x}\big|_{z=0} - \frac{\partial\Phi}{\partial x}\big|_{z=L_z} e^{\gamma L_z}}{\gamma(1 - e^{2\gamma L_z})}, & B_2 &= \frac{\frac{\partial\Phi}{\partial x}\big|_{z=0} e^{\gamma L_z} - \frac{\partial\Phi}{\partial x}\big|_{z=L_z}}{\gamma(1 - e^{2\gamma L_z})}. \end{aligned} \quad (3.18)$$

The terms with the coefficient $e^{\gamma L_z}$ are not negligible in this case. The components of Ψ are written as,

$$\begin{aligned} \Psi_1 &= \frac{2e^{\gamma L_z}}{\gamma(1 - e^{2\gamma L_z})} \left[-\frac{\partial\Phi}{\partial y}\bigg|_{z=0} \cosh \gamma(L_z - z) + \frac{\partial\Phi}{\partial y}\bigg|_{z=L_z} \cosh \gamma z \right], \\ \Psi_2 &= \frac{2e^{\gamma L_z}}{\gamma(1 - e^{2\gamma L_z})} \left[\frac{\partial\Phi}{\partial x}\bigg|_{z=0} \cosh \gamma(L_z - z) - \frac{\partial\Phi}{\partial x}\bigg|_{z=L_z} \cosh \gamma z \right]. \end{aligned} \quad (3.19)$$

Substitution Ψ into the normal velocity at $z = 0$ and $z = L_2$ gives the viscous boundary conditions for thick BLs,

$$\frac{\partial P}{\partial z}\bigg|_{z=0} + \frac{\beta_1}{\gamma} \left(\frac{\partial^2 P}{\partial x^2} + \frac{\partial^2 P}{\partial y^2} \right)\bigg|_{z=0} - \frac{\beta_2}{\gamma} \left(\frac{\partial^2 P}{\partial x^2} + \frac{\partial^2 P}{\partial y^2} \right)\bigg|_{z=L_z} = \frac{1}{\alpha} \rho_f \omega^2 W\bigg|_{z=0}, \quad (3.20)$$

$$\frac{\partial P}{\partial z}\bigg|_{z=L_z} - \frac{\beta_1}{\gamma} \left(\frac{\partial^2 P}{\partial x^2} + \frac{\partial^2 P}{\partial y^2} \right)\bigg|_{z=L_z} + \frac{\beta_2}{\gamma} \left(\frac{\partial^2 P}{\partial x^2} + \frac{\partial^2 P}{\partial y^2} \right)\bigg|_{z=0} = -\frac{1}{\alpha} \rho_f \omega^2 W\bigg|_{z=L_z}, \quad (3.21)$$

where

$$\beta_1 = \frac{1 + e^{2\gamma L_z}}{1 - e^{2\gamma L_z}}, \quad \beta_2 = \frac{2e^{\gamma L_z}}{1 - e^{2\gamma L_z}}. \quad (3.22)$$

Equations 3.20 and 3.21 differ from Eqs. 3.13 and 3.16 by having an additional term that couples the local pressure to the pressure on the opposite boundary. When the BL thickness is much smaller than the duct height, the real part of γL_z is a large negative number. In this case, $|\beta_1|$ is close to 1 and $|\beta_2|$ is approximately 0; Eqs. 3.20 and 3.21 reduce to Eqs. 3.13 and 3.16 for the thin (non-coupling) viscous BL correction. Hence, the thick BL case subsumes the thin BL approximation, but takes extra connectivity in the finite element method (FEM) scheme as will be seen.

3.2.2 Strong form

Here we state the strong form of the coupled fluid-structure problem.

In the fluid domain Ω , the governing equation is (Eq. 3.5)

$$\nabla^2 P + \frac{\omega^2}{\alpha c^2} P = 0, \quad \text{in } \Omega,$$

subjected to (Eq. 3.17)

$$-\frac{\partial P}{\partial n} + \frac{1}{\gamma} \nabla_s^2 P = \frac{1}{\alpha} \rho_f \omega^2 W, \quad \text{on } \partial\Omega$$

for the thin viscous BL case. If the viscous BL is thick on the z surfaces, $\partial P/\partial z$ is replaced by (Eqs. 3.20 and 3.21)

$$\frac{\partial P}{\partial z} \Big|_{z=0} + \frac{\beta_1}{\gamma} \left(\frac{\partial^2 P}{\partial x^2} + \frac{\partial^2 P}{\partial y^2} \right) \Big|_{z=0} - \frac{\beta_2}{\gamma} \left(\frac{\partial^2 P}{\partial x^2} + \frac{\partial^2 P}{\partial y^2} \right) \Big|_{z=L_z} = \frac{1}{\alpha} \rho_f \omega^2 W \Big|_{z=0},$$

$$\frac{\partial P}{\partial z} \Big|_{z=L_z} - \frac{\beta_1}{\gamma} \left(\frac{\partial^2 P}{\partial x^2} + \frac{\partial^2 P}{\partial y^2} \right) \Big|_{z=L_z} + \frac{\beta_2}{\gamma} \left(\frac{\partial^2 P}{\partial x^2} + \frac{\partial^2 P}{\partial y^2} \right) \Big|_{z=0} = -\frac{1}{\alpha} \rho_f \omega^2 W \Big|_{z=L_z}.$$

The structures on the $z = 0$ and $z = L_z$ surfaces interact with the fluid in the duct. The governing equation of the structure can be expressed as

$$\mathfrak{L}(W) = -P, \quad \text{on } \Gamma, \quad (3.23)$$

where \mathfrak{L} is a linear operator represents the structural dynamics. In this paper, examples are given for a membrane as the structural model with simply supported boundary condition,

$$\tilde{T}_x \frac{\partial^2 W}{\partial x^2} + \tilde{T}_y \frac{\partial^2 W}{\partial y^2} + \rho_p \omega^2 W = \alpha P, \quad \text{on } \Gamma, \quad (3.24)$$

subjected to

$$W = 0, \quad \text{on } \partial\Gamma, \quad (3.25)$$

where $\tilde{T}_x = T_x(1 + j\eta)$ and $\tilde{T}_y = T_y(1 + j\eta)$ are the membrane tensions in the x and y directions, respectively, with a damping coefficient η . ρ_p is the membrane density per unit area.

3.2.3 Variational formulation

The variational formula for the governing equation of the fluid (Eq. 3.5) is

$$\int_{\Omega} \left(\nabla \bar{P} \cdot \nabla P - \frac{\omega^2}{\alpha c^2} \bar{P} P \right) d\Omega - \int_{\partial\Omega} \bar{P} \nabla P \cdot \mathbf{n} dS = 0, \quad (3.26)$$

where \bar{P} is a weighting function and P is a trial solution [52], \mathbf{n} is the outward normal on the boundary, and S is the surface of Ω .

3.2.3.1 3-D formulation for thin boundary layer (case 1)

The surface integral in Eq. 3.26 (third term) can be rewritten using the thin BL correction (Eq. 3.17),

$$\int_{\partial\Omega} \bar{P} \nabla P \cdot \mathbf{n} dS = \frac{1}{\gamma} \int_{\partial\Omega} \bar{P} \nabla_s^2 P dS - \frac{1}{\alpha} \rho_f \omega^2 \int_{\Gamma} W \bar{P} dx dy. \quad (3.27)$$

The first integral on the RHS of Eq. 3.27 is a sum of six surface integrations on $\partial\Omega$. Taking the $z = 0$ surface as an example, by using the relation $\bar{P} \nabla^2 P = \nabla \cdot (\bar{P} \nabla P) - \nabla \bar{P} \cdot \nabla P$, the surface integral can be rewritten as

$$\underbrace{\frac{1}{\gamma} \int_{z=0} \bar{P} \nabla_{xy}^2 P dx dy}_{O(\delta)} = \frac{1}{\gamma} \int_{z=0} \nabla_{xy} \cdot (\bar{P} \nabla_{xy} P) dx dy - \frac{1}{\gamma} \int_{z=0} \nabla_{xy} \bar{P} \cdot \nabla_{xy} P dx dy, \quad (3.28)$$

where ∇_{xy} is a in-plane gradient operator in the x and y directions. Equation 3.28 is of order $O(\delta)$ since $1/\gamma$ has the same order as δ . By using the divergence theorem in 2-D, the first integral on the RHS of Eq. 3.28 becomes

$$\frac{1}{\gamma} \int_{z=0} \nabla_{xy} \cdot (\bar{P} \nabla_{xy} P) dx dy = \frac{1}{\gamma} \int_0^{L_x} \left(\bar{P} \frac{\partial P}{\partial y} \Big|_{z=0} \right) \Big|_{y=0}^{y=L_y} dx + \frac{1}{\gamma} \int_0^{L_y} \left(\bar{P} \frac{\partial P}{\partial x} \Big|_{z=0} \right) \Big|_{x=0}^{x=L_x} dy. \quad (3.29)$$

Applying the thin BL correction (Eq. 3.17) again to $\partial P/\partial y$ and $\partial P/\partial x$ on the RHS of Eq. 3.28 gives

$$\begin{aligned} \frac{1}{\gamma} \int_{z=0} \nabla_{xy} \cdot (\bar{P} \nabla_{xy} P) dx dy &= \frac{1}{\gamma^2} \underbrace{\int_0^{L_x} \left(\bar{P} \nabla_{xz}^2 P \Big|_{z=0, y=0} + \bar{P} \nabla_{xz}^2 P \Big|_{z=0, y=L_y} \right) dx}_{O(\delta^2)} \\ &+ \frac{1}{\gamma^2} \underbrace{\int_0^{L_y} \left(\bar{P} \nabla_{yz}^2 P \Big|_{z=0, x=0} + \bar{P} \nabla_{yz}^2 P \Big|_{z=0, x=L_x} \right) dy}_{O(\delta^2)}. \end{aligned} \quad (3.30)$$

Equation 3.30 (the first integral on the RHS of Eq. 3.28) is of order $O(\delta^2)$, which is negligible compared to the order of Eq. 3.28 [$O(\delta)$]. Hence, Eq. 3.28 is simplified as

$$\frac{1}{\gamma} \int_{z=0} \bar{P} \nabla_{xy}^2 P dx dy \approx -\frac{1}{\gamma} \int_{z=0} \nabla_{xy} \bar{P} \cdot \nabla_{xy} P dx dy. \quad (3.31)$$

By a similar derivation (Eqs. 3.28-3.30) to the other five surfaces ($z = L_z$, $x = 0, L_x$, $y = 0, L_y$), Therefore, the surface integral in Eq. 3.26 can be written as

$$\int_{\partial\Omega} \bar{P} \nabla P \cdot \mathbf{n} dS \approx -\frac{1}{\gamma} \int_{\partial\Omega} \nabla_s \bar{P} \cdot \nabla_s P dS - \frac{1}{\alpha} \rho_f \omega^2 \int_{\Gamma} W \bar{P} dx dy, \quad (3.32)$$

where ∇_s is the in-plane gradient operator on the surfaces. The first term on the RHS of Eq. 3.32 is a sum of six surface integrals on $\partial\Omega$. Substitution Eq. 3.32 into Eq. 3.26 yields,

$$\int_{\Omega} \nabla \bar{P} \cdot \nabla P d\Omega - \int_{\Omega} \frac{\omega^2}{\alpha c^2} \bar{P} P d\Omega + \frac{1}{\gamma} \int_{\partial\Omega} \nabla_s \bar{P} \cdot \nabla_s P dS + \frac{1}{\alpha} \rho_f \omega^2 \int_{\Gamma} W \bar{P} dx dy = 0, \quad (3.33)$$

which is the 3-D variational equation with thin viscous BL corrections. Both α and γ are functions of the viscosity μ . When $\mu = 0$, then $\alpha = 1$ and $1/\gamma = 0$, the inviscid form is recovered.

Remark: Equation 3.13 is consistent with Holmes and Cole's viscous boundary condition [49] although a different approach is used here. Using our sign convention for γ and including compressibility, the dimensional form of Holmes and Cole's equation at $z = 0$ is,

$$\frac{\partial P}{\partial z} - \frac{1}{\gamma} \left(\frac{\partial^2 P}{\partial z^2} + \frac{\omega^2}{\alpha c^2} P \right) = \frac{1}{\alpha} \rho_f \omega^2 W. \quad (3.34)$$

The difference between the above equation in Ref. [49] and Eq. 3.13 is that we keep the correction written in terms of the in-plane derivative as $\partial^2 P / \partial x^2 + \partial^2 P / \partial y^2$. This is the key step enabling the development of a variational formulation that can be used with an existing inviscid structural acoustic code with only minor modification. Otherwise, if we used Eq. 3.34, the boundary term at $z = 0$ becomes,

$$\int_{z=0} \bar{P} \frac{\partial P}{\partial z} dx dy = -\frac{1}{\gamma} \int_{z=0} \left[\bar{P} \frac{\partial^2 P}{\partial z^2} + \frac{\omega^2}{\alpha c^2} \bar{P} P \right] dx dy - \frac{1}{\alpha} \rho_f \omega^2 \int_{\Gamma} \bar{P} W dx dy. \quad (3.35)$$

The first term on the RHS of the equation cannot be evaluated by integration by parts because the higher-order boundary derivatives are not in the in-plane direction.

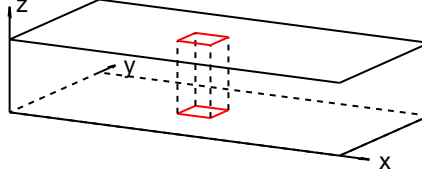


Figure 3.2: Schematic of the 3-D coupling boundary layer correction. The elements on $z = 0$ are coupled to the elements on $z = L_z$ through a 2-D configuration.

3.2.3.2 3-D formulation for thick boundary layer (case 2)

Using the thick BL correction (Eqs. 3.20, 3.21) on the $z = 0$ and $z = L_z$ surfaces and thin BL correction (Eq. 3.17) on the other surfaces, and following the derivation in Eqs. 3.27-3.33 (dropping order $1/\gamma^2$ terms), one obtains the final variational equation as

$$\begin{aligned}
& \int_{\Omega} \nabla \bar{P} \cdot \nabla P d\Omega - \int_{\Omega} \frac{\omega^2}{\alpha c^2} \bar{P} P d\Omega + \frac{1}{\alpha} \rho_f \omega^2 \int_{\Gamma} W \bar{P} dxdy + \frac{\beta_1}{\gamma} \int_{z=0, L_z} \nabla_s \bar{P} \cdot \nabla_s P dxdy \\
& + \frac{1}{\gamma} \int_{x=0, L_x} \nabla_s \bar{P} \cdot \nabla_s P dydz + \frac{1}{\gamma} \int_{y=0, L_y} \nabla_s \bar{P} \cdot \nabla_s P dx dz \\
& - \frac{\beta_2}{\gamma} \int (\nabla_s \bar{P}|_{z=L_z} \cdot \nabla_s P|_{z=0} + \nabla_s \bar{P}|_{z=0} \cdot \nabla_s P|_{z=L_z}) dxdy = 0. \tag{3.36}
\end{aligned}$$

In this case, the viscous BL is sufficiently thick that the two BLs interact in the z direction. The last integral in Eq. 3.36 requires an extra connectivity that couples the elements on $z = 0$ to those on $z = L_z$ (Fig. 3.2).

3.2.3.3 Formulation for the structure

The variational form of Eq. 3.24 follows in a standard way as in Eq. 3.26. Since simply supported boundary conditions are used, the weighting function \bar{W} vanishes on the boundary of the structure. Therefore, the variational form of Eq. 3.24 is

$$\int_{\Gamma} \left(\tilde{T}_x \frac{\partial \bar{W}}{\partial x} \frac{\partial W}{\partial x} + \tilde{T}_y \frac{\partial \bar{W}}{\partial y} \frac{\partial W}{\partial y} \right) dxdy - \int_{\Gamma} \rho_p \omega^2 \bar{W} W dxdy + \int_{\Gamma} \alpha \bar{W} P dxdy = 0, \tag{3.37}$$

which is applicable on both $z = 0$ and $z = L_z$.

Equations 3.33 (or 3.36) and 3.37 close the set of equations for the fluid-structure

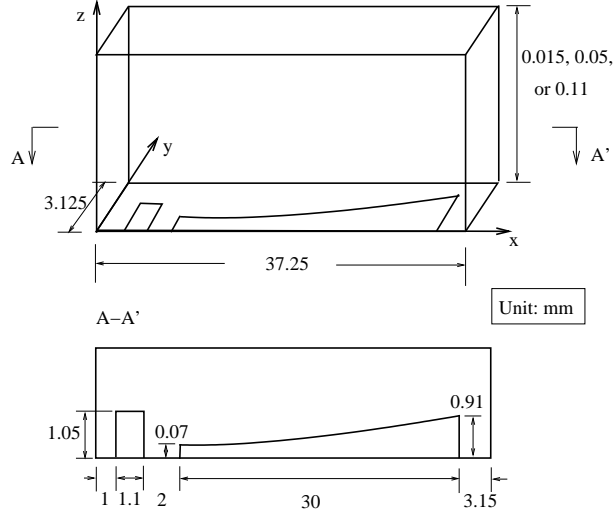


Figure 3.3: The dimension of the duct and the structure (not to scale).

coupled viscous BL correction problem.

3.3 Results

In this section, we present simulation results using the viscous BL approximation methods developed in this paper and compared to predictions obtained from a 3-D FEM model based on linearized N-S equations [9]. The geometry and the dimensions of the example problem were given in Ref. [9] (where experimental results are also presented) and are reproduced here in Fig. 3.3. In the present study, the duct height is varied among $15 \mu\text{m}$, $50 \mu\text{m}$, or $110 \mu\text{m}$. Symmetry boundary conditions are used at the $y = 0$ plane so that only half the geometry is modeled. The rectangular input membrane on $z = 0$ is driven by a constant external pressure field. The tapered structure on $z = 0$ is an orthogonally tensioned membrane. The input and tapered membranes are the only flexible surfaces on $\partial\Omega$, and thus Eq. 3.37 is only applied on $z = 0$. The material properties of the system are given in Table 3.1. In the results presented here, the simulation frequency is 12 kHz, which gives a BL thickness of $12.07 \mu\text{m}$ for the fluid properties listed in Table 3.1. The fluid in the model was silicone oil. The thickness of the tapered membrane was $1.7 \mu\text{m}$, upon which the areal density was calculated (also see Ref. [9] for more information). The BL correction is only used on the $z = 0$ and $z = L_z$ surfaces as δ/L_x , $\delta/L_y < 1/500$ (as will be discussed in the next section). The mesh sizes for the problem are 602 elements in x -direction, 20 elements in z -direction, and 24 elements in y -direction for 3-D models.

Symbols	Values	Units	Physical Meaning
ρ_f	911	kg/m ³	[fluid density]
c	1000	m/s	[fluid wave speed]
μ	5×10^{-3}	kg/(s·m)	[fluid viscosity]
ρ_p	3.6×10^{-3}	kg/m ²	[plate area density]
T_x	30	N/m	[tension in x]
T_y	240	N/m	[tension in y]
η	0.01		[structural damping factor]

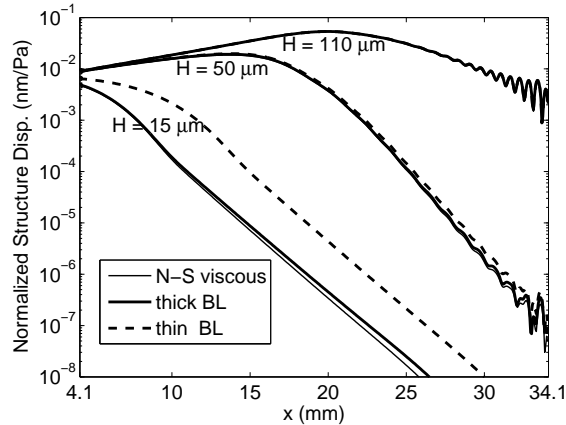


Figure 3.4: Comparison of the normalized structure displacements at the central line with respect to the input pressure among the N-S model (thin solid lines), the thin BL model (dashed lines), and the thick BL model (thick solid lines) on the $z = 0$ and $z = L_z$ surfaces with different duct heights ($L_z = 110\mu\text{m}$, $50\mu\text{m}$, and $15\mu\text{m}$). The three curves overlap in the $L_z = 110\mu\text{m}$ case.

3.3.1 Prediction from a 3-D model

In Fig. 3.4, the central-line structural displacement normalized to the input pressure is shown with different duct heights ($L_z = 110\mu\text{m}$, $50\mu\text{m}$, and $15\mu\text{m}$). Predictions are made from the N-S model, the thick BL model (Eq. 3.36), and the thin BL model (Eq. 3.33) applied to both the $z = 0$ and $z = L_z$ surfaces. As expected, when $L_z \gg \delta$, the thin BL and thick BL approximations closely match the N-S model. However, when $L_z \sim \delta$, the thin BL model over predicts the structural displacement (see the dashed line for the $15\mu\text{m}$ case). The thick BL model matches the N-S solution for all duct heights. Although the BL correction on the x and y surfaces is neglected, we still get good results because L_x/δ , $L_y/\delta > 500$ in the model. In this case, including the viscous BL correction on the x and y surfaces does not improve the accuracy of the results (results not shown). In Fig. 3.5, the normalized (with respect to the input pressure) longitudinal fluid displacement u_x on

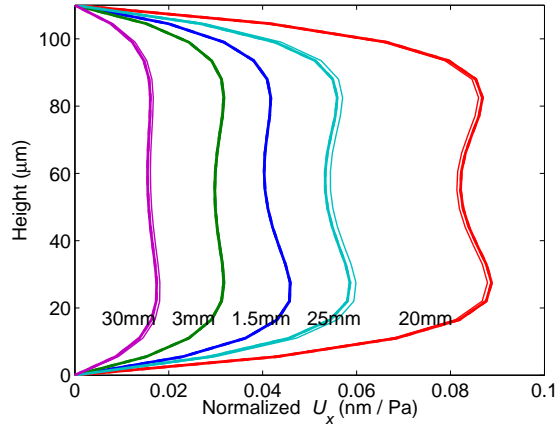


Figure 3.5: Comparison of normalized (with respect to the input pressure) fluid longitudinal displacement u_x on the central-plane ($y = 0$) among the N-S model (thin solid lines), the thin BL model (dashed lines), and the thick BL model (thick solid lines, overlapped with dashed lines) on the $z = 0$ and $z = L_z$ surfaces. The numbers on each group of curves indicate the selected longitudinal locations in the duct. The duct height is $110\mu\text{m}$.

the central-plane ($y = 0$) is shown for $L_z = 110\mu\text{m}$. Predictions are made from the N-S model, the thick BL model, and the thin BL model on the $z = 0$ and $z = L_z$ surfaces. The fluid displacement is not directly computed in the structural acoustic models (pressure is the only variable). The method used for estimating u_x in the fluid and producing the results in Fig. 3.5 is given in Appendix C. Good agreement is achieved among three models for this $110\mu\text{m}$ duct height. When the duct height is $50\mu\text{m}$, the thick BL model prediction of u_x still matches the N-S model, but the prediction from the thin BL model has noticeable differences compared to the thick BL model (results not shown) because small differences in pressure are magnified in post-processing.

Next (in Figs. 3.6 and 3.7), we explore the effect of including the thin BL correction on only one surface at $z = 0$ (Eq. 3.13), and compare the results to predictions from (1) a fully inviscid model and (2) to the thick BL model applied to both the $z = 0$ and $z = L_z$ surfaces (Eqs. 3.20 and 3.21). In Fig. 3.6, the central-line structural displacement from the inviscid model is strongly oscillatory and shows large errors compared to the thick BL solution, which is nearly identical to the N-S solution (the same simulations are given in Fig. 3.4). The model with one thin BL approximation at $z = 0$ clearly improves the prediction compared to the inviscid model. However, the BL approximation at $z = L_z$ is required in order to obtain accurate structural response at $z = 0$ even when $\delta/L_z \sim 1/10$ for the $L_z = 110\mu\text{m}$ case [see Fig. 3.6(a)]. When $L_z = 15\mu\text{m}$ [Fig. 3.6(b)], the difference between inviscid and BL correction (either one or both layers) models are more dramatic.

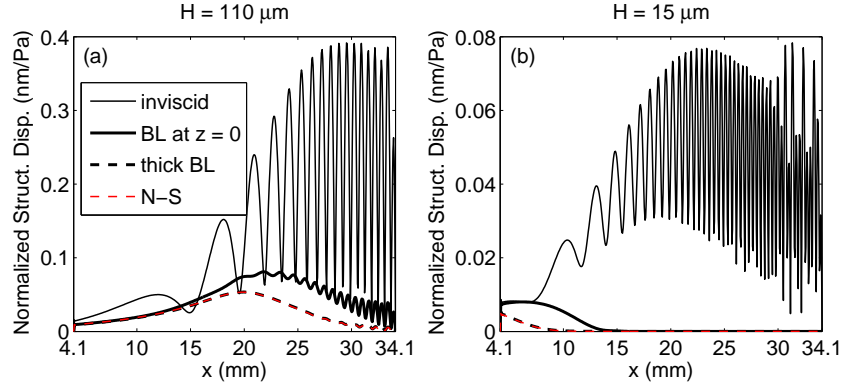


Figure 3.6: Central-line structural displacement normalized to the input pressure from the 3-D acoustic model. Thin solid lines: inviscid model. Thick solid lines: one thin BL correction on $z = 0$. Thick dashed lines: thick BL correction. Thin dashed lines: N-S solution. (a). $L_z = 110 \mu\text{m}$. $L_z/\delta = 9.12$. (b). $L_z = 15 \mu\text{m}$. $L_z/\delta = 1.24$.

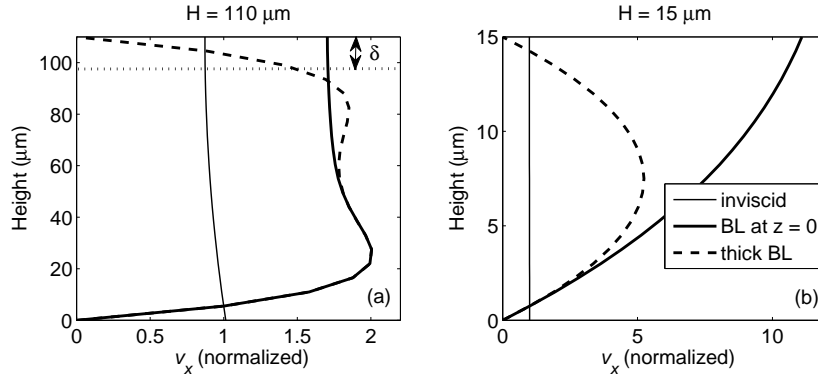


Figure 3.7: Variation of normalized longitudinal fluid velocity v_x (at $x = 30 \text{ mm}$) in the vertical direction in 3-D acoustic models. Thin solid lines: an inviscid model. Thick solid lines: one BL correction at $z = 0$. Thick dashed lines: thick BL correction. (a) $L_z = 110 \mu\text{m}$ ($L_z/\delta = 9.12$). The velocity is normalized to the velocity at $z = 5.5 \mu\text{m}$. (b) $L_z = 15 \mu\text{m}$ ($L_z/\delta = 1.24$). The velocity is normalized to the velocity at $z = 0.75 \mu\text{m}$.

Table 3.2: Root mean square errors of structural displacement for different L_z/δ ratios and models.

Model \ L_z/δ	1	5	10	50	100	500
inviscid	8788.27%	568.31%	520.25%	64.04%	48.53%	19.21%
thin BL on $z = L_z$	301.08%	103.96%	83.28%	49.17%	45.78%	19.21%
thin BL on $z = 0$	300.80%	99.25%	68.72%	6.15%	1.40%	$6.56 \times 10^{-3}\%$
two thin BLs	203.68%	0.15%	$1.09 \times 10^{-2}\%$	~ 0	~ 0	~ 0

In Fig. 3.7, the normalized longitudinal fluid velocity v_x on the central-plane ($y = 0$) is plotted. The inviscid model (thin solid lines) does not vanish at two surfaces because the model is not subjected to the non-slip boundary condition. Using one thin BL approximation at $z = 0$ (thick solid lines) enforces zero velocity at $z = 0$ while thick BL approximation (dashed lines) affects the velocity at both $z = 0$ and $z = L_z$ surfaces. The normalized thick BL solution seamlessly transits from the thin BL case to the Poiseuille-like case [as can be seen in Fig. 3.7(b)].

From Fig. 3.4 we can see that the structural prediction from the thick BL approximation model matches well with the N-S model for various duct heights. Thus, we use the prediction from the thick BL model as a reference solution (denoted as \hat{W}). Then we quantify the structural displacement error for four cases: (i) the thin BL model on both $z = 0$ and $z = L_z$, one BL correction either (ii) on $z = 0$ or (iii) on $z = L_z$, and (iv) the inviscid model (all denoted as W) using root mean square error (RMSE) by

$$\text{RMSE} = \left[\frac{\sum_{i=1}^N (W_i - \hat{W}_i)^2}{\sum_{i=1}^N \hat{W}_i^2} \right]^{\frac{1}{2}} \times 100\%, \quad (3.38)$$

where N is the total number of points on the center line of the structure from the FEM discretization. Table 3.2 lists the RMSEs from different models with various L_z/δ ratios. The geometry is the same the model shown in Fig. 3.3. The simulation frequency is still 12 kHz. Predictions with $\text{RMSE} < 3\%$ are considered to have sufficient accuracy and are highlighted in the table.

3.3.2 Computational cost

With 603 nodes in the x direction, 25 nodes in the y direction, and 21 nodes in the z direction, the N-S model can be simulated on two 25-GB Intel cores, and takes 3.05

hours to run. However, for the same mesh size, the viscous BL approximation model developed here can be simulated on a 4-GB Intel CoreTM2 machine (which cannot run the N-S model) with only 3.12 minutes. If accurate structural displacement is the only output quantity of interest, using 15 nodes in the y direction yields sufficient accuracy (results not shown). In this case, the N-S model can be simulated on two 4-GB Intel cores with 21.71 minutes, while the acoustic model takes 42.7 s to be simulated on the same 4-GB Intel CoreTM2 machine. The coupled elements for the thick BL model increase the bandwidth of the stiffness matrix in FEM, and thus may potentially increase the computational cost. In this example, however, the node numbering allows the pressure nodes at the top of the channel to be near the nodes on the bottom; hence the bandwidth is not significantly increased, and the difference in computational cost between the thin and thick BL approximations is negligible.

3.4 Discussion and conclusion

In the example problem used here, the structure is located on the $z = 0$ surface. Sufficiently accurate solutions (RMSE < 3%) require the use of thick BL approximation (with increased complicity in the FEM formulation) if $L_z \sim \delta$ (see Fig. 3.4, for the $15\mu\text{m}$ case only the thick BL approximation yields high accuracy). When δ/L_z is much less than 1, constant pressure approximation (lubrication theory) in Beltman’s model [3] becomes simpler and accurate. Using thin BL approximation on both the $z = 0$ and $z = L_z$ surfaces is sufficient if L_z is larger than $\sim 5\delta$ (see Table 3.2 and the $50\mu\text{m}$ case in Fig. 3.4). Using one BL on the $z = 0$ surface also provides sufficient accuracy if L_z is larger than $\sim 100\delta$ (Table 3.2). Here we can see that the influence of the viscous BL extends beyond the region of the normally-defined BL thickness [$\delta = |1/\Re(\gamma)|$, see Figs. 3.6(a) and 3.7(a)]. Although the BL correction on $z = L_z$ is important when L_z is less than $\sim 100\delta$, including the BL correction on the flexible surface (in this case $z = 0$) is more important than including the correction on the rigid surfaces (see Table 3.2). In the example, the distance from the x and y surfaces to the structure is much larger than 500δ ; hence, the error for not including BLs on these two surfaces is less than $6.56 \times 10^{-3}\%$ (see Table 3.2). For this reason, the BL correction on the x and y surfaces are negligible in the example. The effect of different viscous BL correction (thin or thick) on the accuracy of the prediction of fluid pressure is similar to that on the structure (results not shown).

In 3.2.1.1, the thin viscous BL condition is derived for the $z = 0$ and $z = L_z$ surfaces (Eqs. 3.13 and 3.16), and the result is generalized to all the boundaries on $\partial\Omega$ (Eq. 3.17). The generalization is based on the assumption that the BL on one surface does not couple

to the BLs on the other surfaces. This assumption holds well away from the corners or the intersection of two surfaces. In general, the thin viscous BL condition is applicable to any geometry (not necessarily a rectangular box used in this example) as long as the position of interest is away from surfaces of small radius of curvature or sharp boundaries, where one BL is coupled to another. We conjecture that the extension of this approach to curved surface using the thin BL (case 1) approach is straight forward. Thus, whenever applicable, the overall approximation for the whole system is a linear superposition of the BL approximations on each surface. In this case, viscosity can be flexibly implemented either on a single surface (e.g., $z = 0$ in Eq. 3.13) or on multiple surfaces. Sufficient accuracy can be achieved by using thin BL approximation if the minimum dimension of a system is larger than $\sim 5\delta$ (Table 3.2). For the thick BL condition, the linear superposition of the BL contributions no longer holds because the BLs from 6 surfaces are coupled. This work illustrates the implementation of thick BL approximation on one pair of parallel surfaces ($z = 0$ and $z = L_z$ in this paper). If BLs are thick in all dimensions, the current method does not apply, and an alternative approximation method (e.g., Stinson [101] or Beltman [3]) should be used.

As mentioned in 3.2.1, in this work we only consider the out-of-plane motion of the structure. Including in-plane motion is also possible. Appendix A illustrates (by taking the thin BL case on the $z = 0$ surface as an example) the derivation and implementation of the shear viscous BL correction for in-plane structure motion. This correction is found to be one order (δ) less than the out-of-plane correction. Although in-plane structure displacement will introduce shear stress on the fluid due to the non-slip boundary condition, the contribution of the viscous effect on the system is typically of a lower order, as derived in Appendix A.

To summarize, a viscous BL approximation is formulated in this work to include fluid viscosity in fluid-structure coupling problems. The method can be easily implemented in FEM to convert an inviscid acoustic model solved for pressure to a viscous one without changing the primary variable. Thus, the total degrees of freedom is unchanged and the size of the problem is well-controlled. The modified boundary condition has additional terms written in second order in-plane derivatives of the pressure evaluated at the boundaries. In the FEM model, the additional terms act as added damping in the stiffness matrix. Although in this work examples are for interior flows, the thin BL approximation is applicable to exterior flows as well.

The innovation of this work is that the FEM implementation of shear viscous BL correction is extended to the thick BL case where a coupling element between two parallel surfaces is required (the FEM implementation of thin viscous BL correction is in Cheng

[8]). The method is also implemented to a 3-D structural acoustic model. The prediction from the developed BL correction method matches well with the prediction from the 3-D N-S model. The computational efficiency is retained in the scalar field model. This work closes the problem of modeling shear viscosity in a scalar representation for a pair of parallel surfaces for both thin and thick viscous BL thicknesses.

CHAPTER IV

Micro fluid model in the reticular lamina-tectorial membrane gap with complex boundary conditions

Two different kinds of flow: (1) shearing of fluid between the reticular lamina (RL) and tectorial membrane (TM) and (2) so-called pulsating flow in the RL-TM gap have been implicated as the dominant source of fluidic stimulation of the inner hair cell (IHC) hair bundle (HB). However, the frequency and spatial dependence of these flows for IHC stimulation is unresolved *in vivo* and estimates of the effect of the cochlear amplifier on these flows has not been quantified. Indeed, the relative importance these flow modalities and active processes likely varies with tonotopic location. In this paper, a microfluidic model is developed which features the interaction of the subtectorial fluid with the TM, IHC HBs and the outer hair cell HBs. The framework of the model allows for incorporation into active macroscopic models as well as for comparison of experiments performed on excised sections of the cochlea.

4.1 Introduction

The ultimate fluidic stimulation in the cochlea is the excitation of the HBs of IHCs, which, after a cascade of events, leads to stimulation of the auditory nerve and the sensation of sound. Nowotny and Gummer [69] observed a transition from pulsatile subtectorial fluid flow at low frequencies to shear dominated flow at higher frequencies in electromechanical experiments on a temporal bone preparation of the guinea pig cochlea. In this study, we develop a model that includes the microfluidic flow in the RL-TM gap along with interface conditions at the IHC and the outer hair cell (OHC) HBs in order to analyze pulsatile and shear flows in the cochlea. The framework of this microfluidic model is suitable for inclusion in global electro-mechanical models of the cochlea, thereby enabling an analysis of the relative importance of these microfluidic effects on IHC stimulation as

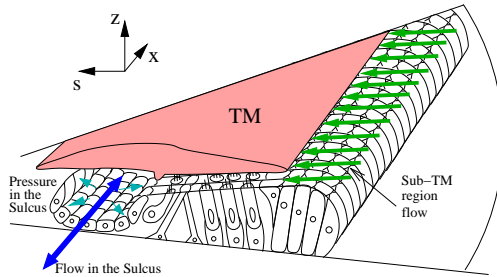


Figure 4.1: Schematic of an OoC cross section in the cochlea. x , s , and z are the longitudinal, radial, and vertical coordinates, respectively. The sub-TM microfluid between the TM and RL gap interacts with the OHC/IHC HBs, the HS, and the sulcus.

well as the coupling of OHC HB and somatic motility with these two flow modalities.

Theoretical models have been built to study the subtectorial fluid forcing on HBs (e.g., [4, 113]). Steele and Frommer performed theoretical and experimental work using a physical model of the situation to study the permeability of flow through HBs [39]. de Boer developed a model for fluid flow in the sulcus [18]. Recently, Baumgart and co-workers developed a numerical model to study fluid–structure interaction in the RL–TM gap and the organ of Corti (OoC) [1] delivering the most detailed estimates yet of flow in the subtectorial space. Our work here is most similar to Puria and Steele’s modeling of the microfluidic forcing of low frequency excitation on the IHC HBs [99]. We look to extend and modify that approach to model the interactions at high and low frequency regions of the cochlea as well as the fluidic coupling with electro-mechanical forces in the cochlea. In addition to theoretical work, our work is motivated by some well controlled *in vitro* experiments on segments of the cochlea by Chan and Hudspeth [6, 7] and by Gummer’s group [69, 93]. These studies provide the opportunity to compare predictions of the electromechanical behavior of the cochlea to experiments in a simpler setting than in the *in vivo* cochlea. Even though these simplified experimental settings do not admit traveling waves or normal acoustic excitation, the inherent electromotile machinery is at least in part intact and the greater access to the spatial dependence of the structural displacement makes a more detailed comparison possible than for *in vivo* preparations.

4.2 Modeling method

In this work, we focus on the elastodynamics of the TM, the subtectorial flow and its interactions with the IHC HBs, OHC HBs, and the flow in the sulcus. The fundamental kinematic and kinetic relation, as well as the electronic network (without longitudinal

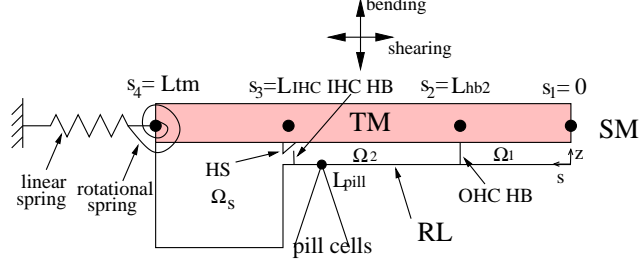


Figure 4.2: Schematic of the TM and the OoC model showing the microfluidic domains: Ω_1 between the OHC and the scala media (SM); Ω_2 between the IHC and OHC bundles; Ω_s the inner sulcus region. The TM is attached to a linear and a rotational spring at the spiral lamina. s and z are the radial and vertical coordinates, respectively. The positive direction of s points from OHC to IHC. The coordinates of the four nodes at $s_1 = 0$, $s_2 = L_{hb2}$, $s_3 = L_{IHC}$, and $s_4 = L_{tm}$, represents respectively the free end of the TM, the location of the second-row OHC, the location of the IHC/Hessen stripe, and the spiral lamina. L_{pill} is the distance from $s = 0$ to the tip of the pill cells. Both OHC HB and IHC HB are denoted by arrows.

coupling), for the OoC can be found in Ramamoorthy *et al.* [82], where the TM is modeled as a rigid body, and the sub-TM microfluid was not included.

A 3-D view of an OoC cross section is shown in Fig. 4.1 along with a cartoon of an OoC cross section in Fig. 4.2. In the current model, without loss of generality, only the middle row OHC and its HB are considered as the other two OHC rows and their HBs can be included in the same way as described in this paper. Since we consider a cross section model, most physical quantities have units of per unit length in the longitudinal direction. Time harmonic solutions with $e^{-j\omega t}$ is assumed in this work, where ω is the radian frequency of the system.

4.2.1 The TM model

The fluid force couples to the elastodynamics of the TM. We consider a TM model that both includes bending and shearing deformation, as well as with a micromechanical model of the OoC (such as in [82, 63]). The entire TM shearing motion is modeled by an elastic rod with an additional linear spring attached to the spiral lamina. Let $U^s(s)$ be the total TM shearing displacement, u_{tms} (a constant) be the displacement due to the linear spring (rigid shearing), and $u^s(s)$ be the displacement of the elastic rod (elastic shearing), then

$$U^s(s) = u_{tms} + u^s(s). \quad (4.1)$$

The entire TM bending is modeled by an Euler-Bernoulli beam with an additional rotational spring attached to the end (Fig. 4.2). Let $W^b(s)$ be the total TM bending displacement, $u_{tm b}(s)$ be the displacement due to the rotational spring (rigid bending), and $w^b(s)$ be the displacement of the Euler-Bernoulli beam (elastic bending), then

$$W^b(s) = u_{tm b}(s) + w^b(s). \quad (4.2)$$

Let $u_{tm b}^0$ be the rigid bending displacement at $s = L_{hb2}$. Denote ℓ_{tm} as the distance from the second row OHC HB to the rotational spring, i.e., $\ell_{tm} = L_{tm} - L_{hb2}$. Then the rigid bending $u_{tm b}(s)$ is

$$u_{tm b}(s) = -\frac{u_{tm b}^0}{\ell_{tm}}(s - L_{tm}). \quad (4.3)$$

Hence, there is only one degree of freedom, $u_{tm b}^0$, in the rigid bending motion of the TM.

The middle row OHC HB contributes to the TM shearing and bending. The structural models of the TM and OoC are coupled via kinematic constraints and kinetic (force) relations amongst the components.

For the elastodynamic part, The TM is discretized into three 1-D elements. The coordinates of the four nodes of the three elements are taken at $s_1 = 0$, $s_2 = L_{hb2}$, $s_3 = L_{IHC}$, and $s_4 = L_{tm}$, representing respectively the free end of the TM, the location of the second-row OHC, the location of the IHC/Hessen stripe, and the spiral lamina (Fig. 4.2). L_{tm} also represents the length of the TM. To include the dynamics of the TM, the entire OoC is modeled. The total degree of freedom in the OoC along with the BM is

$$[u_{bm}, u_1^s, u_2^s, u_3^s, u_4^s, u_{tm b s}, w_1^b, \phi_1, w_2^b, \phi_2, w_3^b, \phi_3, w_4^b, u_{tm b}^0, \phi_4]^T, \quad (4.4)$$

where u_{bm} is the displacement of the BM. u_i^s , w_i^b , and ϕ_i are the elastic shearing displacement, elastic bending displacement, and the elastic bending rotation of the TM at node i ($i = 1, 2, 3, 4$), respectively (the shape functions and related integrals for 1-D elements can be found in Appendix D). The displacement of the HB of the second-row OHC (u_{hb2}), the displacement of the RL at s_2 location (u_{rl2}), the apex and base displacements of the second-row OHC (u_{ohc2}^a and u_{ohc2}^b), and the displacement of the apical end of the arch of Corti (u_{ap}) are included in the model. The kinematic relation between u_{hb2} , u_{rl2} , u_{ohc2}^a ,

u_{ohc2}^b , and u_{ap} to u_{bm} , u_2^s , and w_2^b are given by [82]

$$u_{hb_2} = A_{21}u_{bm} + A_{23}U^s \Big|_{s=L_{hb_2}} + A_{24}W^b \Big|_{s=L_{hb_2}}, \quad (4.5)$$

$$u_{rl_2} = B_{21}u_{bm} + B_{23}U^s \Big|_{s=L_{hb_2}} + B_{24}W^b \Big|_{s=L_{hb_2}}, \quad (4.6)$$

$$u_{ohc_2}^a = C_{21}u_{bm} + C_{23}U^s \Big|_{s=L_{hb_2}} + C_{24}W^b \Big|_{s=L_{hb_2}}, \quad (4.7)$$

$$u_{ap} = D_1u_{bm}, \quad (4.8)$$

$$u_{ohc_2}^b = E_{21}u_{bm}, \quad (4.9)$$

where the coefficients A_{ij} , B_{ij} , C_{ij} , D_i , and E_{ij} represent the transformation from the displacements of the BM and TM to the other structures in the OoC.

The governing equation for the TM and the BM are obtained through the energy method. The total kinetic energy (per unit length) in an OoC cross section is

$$\begin{aligned} T = & -\frac{b}{4}\omega^2 M_{bm}u_{bm}^2 - \frac{1}{2}\omega^2 M_{tms}u_{tms}^2 - \frac{1}{6}\omega^2 M_{tmb} \left(\frac{L_{tm}}{\ell_{tm}} \right)^2 (u_{tmb}^0)^2 \\ & - \frac{1}{2}\omega^2 \rho_{tm} a_{tms} \int_0^{L_{tm}} (u^s)^2 ds - \frac{1}{2}\omega^2 \rho_{tm} a_{tmb} \int_0^{L_{tm}} (w^b)^2 ds, \end{aligned} \quad (4.10)$$

where b (depends on the longitudinal position) is the width of the BM. M_{bm} (kg/m²), M_{tms} (kg/m), and M_{tmb} (kg/m) are the effective mass per unit length of the BM, TM shearing, and TM bending, respectively, at a cross section. The effective mass of the TM may differ for the shearing and the bending modes due to the different manners of fluid loading on the TM. ρ_{tm} (kg/m³) is the density of the TM. a_{tms} (m) and a_{tmb} (m) are the section areas per unit length of the TM shearing and bending in the xz -plane for a given OoC cross section segment, given by

$$a_{tms} = \frac{M_{tms}}{L_{tm}\rho_{tm}}, \quad a_{tmb} = \frac{M_{tmb}}{L_{tm}\rho_{tm}}. \quad (4.11)$$

Both a_{tms} and a_{tmb} have units of length; these two quantities are essentially the effective heights of the TM shearing and bending. The additional factor $b/2$ associated with the BM kinetic energy term comes from the cross mode shape of the BM. The total potential

energy (per unit length) in an OoC cross section is

$$\begin{aligned}
V = & \frac{b}{4}K_{bm}u_{bm}^2 + \frac{1}{2}K_{tms}u_{tms}^2 + \frac{1}{2}E_{tm}^s a_{tms} \int_0^{L_{tm}} \left(\frac{\partial u^s}{\partial s} \right)^2 ds \\
& + \frac{1}{2}K_{tmb} \left(\frac{\partial u_{tmb}}{\partial s} \right)^2 + \frac{1}{2}E_{tm}^b I_{tm} \int_0^{L_{tm}} \left(\frac{\partial^2 w^b}{\partial s^2} \right)^2 ds \\
& + \frac{1}{2}K_{hb} \left(u_{hb2} + u_{rl2} \frac{h_{hb}}{L_{Ro}} \right)^2 + \frac{1}{2}K_{rl} \left(u_{rl2} + u_{ap} \frac{L_{Ro}}{L_{pc}} \right)^2 + \frac{1}{2}K_{ohc} (u_{ohc2}^a + u_{ohc2}^b)^2, \tag{4.12}
\end{aligned}$$

where K_{bm} (kg/m²s²) is the BM stiffness; K_{tms} (kg/ms²) and K_{tmb} (kg/ms²) are the stiffnesses of the linear and rotational springs attached to the TM, respectively; E_{tm}^s (kg/ms²) and E_{tm}^b (kg/ms²) are the elastic moduli for the TM shearing and bending, respectively; I_{tm} (m³) is the second moment of area of the TM per unit length in the xz -plane for a given OoC cross section segment, given by $I_{tm} = a_{tmb}^2/12$; K_{hb} (kg/ms²), K_{rl} (kg/ms²), and K_{ohc} (kg/ms²) are the stiffness of the OHC HB, RL, and OHC, respectively; h_{hb} is the height of the OHC HB; L_{Ro} and L_{pc} are defined in Fig. 3 in Ref. [82]. The generalized work done by external forces (non-conservative) (per unit length) is given by

$$\begin{aligned}
Q = & \sum_m (p_m^{SV} - p_m^{ST}) u_{bm} \mu_m + \epsilon_3 (\phi_{ohc} - \phi_{st}) (u_{ohc2}^a + u_{ohc2}^b) - \frac{b}{4} j \omega C_{bm} u_{bm}^2 \\
& - \frac{1}{2} j \omega C_{tms} u_{tms}^2 - \frac{1}{2} j \omega \zeta_{tm}^s \int_0^{L_{tm}} (u^s)^2 ds \\
& - \frac{1}{2} j \omega C_{tmb} \left(\frac{\partial u_{tmb}}{\partial s} \right)^2 - \frac{1}{2} j \omega \zeta_{tm}^b \int_0^{L_{tm}} (w^b)^2 ds \\
& + \int_{LIHC}^{L_{tm}} p_s W^b ds + \int_0^{LIHC} p_{gap} (W^b - u_{rl}^b) ds + \int_0^{LIHC} f_f (u_{tms} + u^s) ds + \frac{1}{2} f_{pbh} u_{hb2}, \tag{4.13}
\end{aligned}$$

where p_m^{SV} and p_m^{ST} are the pressure in the SV and ST, respectively, for the fluid mode m ; μ_m is the coupling coefficient between the fluid in SV/ST and the BM (see Ref. [82]); the term $\epsilon_3 (\phi_{ohc} - \phi_{st}) (u_{ohc2}^a + u_{ohc2}^b)$ represents the force contributed from the OHC active process [82]; C_{bm} (kg/m²s) is the viscous damping coefficient of the BM; C_{tms} (kg/ms) and C_{tmb} (kg/ms) are the damping coefficients of the linear and rotational springs attached to the TM, respectively; ζ_{tm}^s (kg/m²s) and ζ_{tm}^b (kg/m²s) are the viscosity for the TM shearing

and bending, respectively; p_s and p_{gap} are the fluid pressure in the sulcus and the TM-RL gap, respectively. p_{gap} may be replaced with p_{Ω_1} or p_{Ω_2} in some places to specify the fluid region under consideration. The u_{rl}^b in Eq. 4.13 is the displacement of the rigid RL in the direction normal to the RL. It can be obtained by the geometric relation in Ref. [82] as

$$\begin{aligned} u_{rl}^b(s) &= q(s)B_{21}u_{bm} + u_{ap} \cos(\theta_1 - \alpha) + q(s)B_{23}U^s|_{s=L_{hb_2}} + q(s)B_{24}W^b|_{s=L_{hb_2}} \\ &= q(s)B_{21}u_{bm} + D_1 \cos(\theta_1 - \alpha)u_{bm} + q(s)B_{23}(u_{tms} + u_2^s) + q(s)B_{24}(u_{tmb}^0 + w_2^b), \end{aligned} \quad (4.14)$$

where

$$q(s) = 1 + \frac{L_{hb_2} - s}{L_{Ro}}, \quad (4.15)$$

where L_{Ro} is the distance between the tip of the pillar cell and the second row OHC (defined the same as in Ref. [82]), i.e., $L_{Ro} = L_{pill} - L_{hb_2}$. The f_f in Eq. 4.13 is the shearing force (N/m²) exerted by the fluid in the TM-RL gap to the TM (see Sec. 4.2.2 for a derivation), given by

$$f_f = \mu \frac{\partial v_s}{\partial z} \Big|_{z=g_0}, \quad (4.16)$$

where μ is the fluid viscosity in the TM-RL gap; g_0 is the initial height of the gap (the distance between the lower surface of the TM and the upper surface of the RL). The f_{pbh} in Eq. 4.13 is the force per unit length applied on the HB by the fluid pressure difference across it,

$$f_{pbh} = [p_{\Omega_1}(s_2) - p_{\Omega_2}(s_2)] h_{hb}, \quad (4.17)$$

where p_{Ω_1} and p_{Ω_2} are the fluid pressure in regions Ω_1 and Ω_2 (see Fig. 4.2). Define the total energy of the OoC to be

$$\Pi = T + V + Q. \quad (4.18)$$

In Eqs. 4.12 and 4.13, the factor $(\partial u_{tmb}/\partial s)^2$ has the value $(u_{tmb}^0)^2/\ell_{tm}^2$. Variations of Π with respect to u_{bm} , u_{tms} , u^s , u_{tmb}^0 , and u^b give the governing equations for the BM, TM shearing, and TM bending, respectively. Due to the long expression, these governing equations are not listed here (see Appendix E for additional formulas).

4.2.2 The TM-RL fluid gap model

As shown in Fig. 4.2, the TM-RL fluid gap refers to the fluid regions Ω_1 and Ω_2 . The governing equations of the coupled fluid-structure interaction are handled by an extension of work in lubrication theory (e.g., Beltman [3]) to include shear deformation of the interface along with out-of-plane deformation. The pressure is assumed to be constant

in z and non-slip boundary conditions are applied at the RL and the TM interface. For small motions of the OoC, the shearing component of the RL is negligible if θ_1 is close to α in Fig. 3 in the Ref. [82]. In the following we neglect the shearing displacement of the RL; this displacement can be incorporated into the current model if necessary.

Conservation of momentum (linearized) in the radial direction gives the governing equation of the flow velocity v_s in the TM-RL gap,

$$-\rho_f j\omega v_s = -\alpha_f \frac{\partial p_{gap}}{\partial s} + \mu \frac{\partial^2 v_s}{\partial z^2}, \quad (4.19)$$

where $\alpha_f = 1 - j\omega\mu/3\rho_f c^2$. $\alpha_f = 1$ if the fluid is incompressible. From Eq. 4.19 we can see that the fluid velocity in the TM-RL gap is contributed by two factors: the pressure gradient in the gap and the shear motion of the TM. v_s is defined positive (real part) in the negative s direction. Equation 4.19 also provides the pressure gradient in the radial direction

$$\frac{\partial p_{gap}}{\partial s} = \frac{1}{\alpha_f} \rho_f j\omega v_s + \frac{\mu}{\alpha_f} \frac{\partial^2 v_s}{\partial z^2}. \quad (4.20)$$

By using the non-slip boundary conditions that $v_s|_{z=0} = 0$ and $v_s|_{z=g_0} = -j\omega U^s$, the velocity v_s is solved to be

$$v_s(s, z) = \frac{\alpha_f}{j\omega\rho_f} \frac{\partial p_{gap}}{\partial s} A(z) - j\omega(u_{tms} + u^s)B(z), \quad (4.21)$$

where

$$A(z) = 1 - \frac{\sinh(\gamma z) - \sinh[\gamma(z - g_0)]}{\sinh(\gamma g_0)}, \quad B(z) = \frac{\sinh(\gamma z)}{\sinh(\gamma g_0)}, \quad (4.22)$$

where $\gamma^2 = -j\omega\rho_f/\mu$. Integrating Eq. 4.21 from $z = 0$ to $z = g_0$ yields the volume flow rate per unit length (in the x direction) at the TM-RL gap

$$\dot{Q} = \frac{\alpha_f}{j\omega\rho_f} \frac{\partial p_{gap}}{\partial s} \tilde{A} - j\omega(u_{tms} + u^s)\tilde{B}, \quad (4.23)$$

where

$$\tilde{A} = \int_0^{g_0} A(z) dz = g_0 - 2 \frac{\cosh(\gamma g_0) - 1}{\gamma \sinh(\gamma g_0)}, \quad (4.24)$$

$$\tilde{B} = \int_0^{g_0} B(z) dz = \frac{\cosh(\gamma g_0) - 1}{\gamma \sinh(\gamma g_0)}. \quad (4.25)$$

After v_s being solved, the fluid viscous shearing force f_f in Eq. 4.16 can now be evaluated

as

$$f_f = -\alpha_f \tilde{B} \frac{\partial p_{gap}}{\partial s} - j\omega\mu \frac{\gamma \cosh(\gamma g_0)}{\sinh(\gamma g_0)} (u_{tms} + u^s). \quad (4.26)$$

Again, we can see that f_f depends on both the pressure gradient and the TM shearing motion.

Although we are primary consider a cross section model for the OoC, to avoid the fluid being ‘locked’ in a cross section, the fluid dynamics in the longitudinal (x) direction is considered as well. The conservation of momentum (linearized) in the longitudinal direction gives the governing equation of the flow velocity v_x in the TM-RL gap,

$$-\rho_f j\omega v_x = -\alpha_f \frac{\partial p_{gap}}{\partial x} + \mu \frac{\partial^2 v_x}{\partial z^2}, \quad (4.27)$$

where we also allow the longitudinal fluid velocity v_x varies in the gap height. Equation 4.27 provides the pressure gradient in the longitudinal direction

$$\frac{\partial p_{gap}}{\partial x} = \frac{1}{\alpha_f} \rho_f j\omega v_x + \frac{\mu}{\alpha_f} \frac{\partial^2 v_x}{\partial z^2}. \quad (4.28)$$

For a cross section, the motion of the OoC in the x direction is assumed to be zero. By using the non-slip boundary conditions $v_x|_{z=0} = 0$ and $v_x|_{z=g_0} = 0$, the velocity v_x is solved to be

$$v_x(x, z) = \frac{\alpha_f}{j\omega\rho_f} \frac{\partial p_{gap}}{\partial x} A(z), \quad (4.29)$$

which only depends on the longitudinal fluid pressure gradient.

Conservation of mass of the fluid in the TM-RL gap is

$$\frac{\partial v_s}{\partial s} + \frac{\partial v_x}{\partial x} + \frac{\partial v_z}{\partial z} + \frac{1}{\rho_f c^2} \frac{\partial p_{gap}}{\partial t} = 0, \quad (4.30)$$

where the fluid compressibility is considered for completeness. Substituting Eqs. 4.21 and 4.29 into Eq. 4.30 yields

$$\frac{\alpha_f}{j\omega\rho_f} \left(\frac{\partial^2 p_{gap}}{\partial s^2} + \frac{\partial^2 p_{gap}}{\partial x^2} \right) A(z) - j\omega \frac{\partial u^s}{\partial s} B(z) + \frac{\partial v_z}{\partial z} - \frac{j\omega}{\rho_f c^2} p_{gap} = 0. \quad (4.31)$$

Integrating Eq. 4.31 over z from $z = 0$ to $z = g_0$ yields the governing equation of the fluid in the TM-RL gap:

$$\frac{\partial^2 p_{gap}}{\partial s^2} + \frac{\partial^2 p_{gap}}{\partial x^2} + \frac{\omega^2 g_0}{c^2 \alpha_f \tilde{A}} p_{gap} = -\frac{\rho_f \omega^2}{\alpha_f \tilde{A}} \left[(W^b - u_{rl}^b) + \tilde{B} \frac{\partial u^s}{\partial s} \right]. \quad (4.32)$$

The right hand side of Eq. 4.32 is the forcing term for the fluid, which includes the contribution from the TM bending and shearing. To evaluate $\partial^2 p_{gap}/\partial x^2$ in a 2-D model that does not have x as a variable, we approximate this term by assuming that the cross section is a part of a 3-D model which allows traveling waves to go through. In this way, $\partial^2 p_{gap}/\partial x^2$ is related to the longitudinal wave number k_x in the cochlea, i.e., $\partial^2 p_{gap}/\partial x^2 \sim k_x^2 p_{gap}$. The k_x can be approximated by a long-wave cochlea model as [75]

$$k_x^2 = \frac{16j\omega\rho\epsilon}{\pi^2 H Z_{bm}(x)}, \quad (4.33)$$

where ϵ is the fraction of the width of the BM of the cochlear duct width, H is the height of the cochlear duct (SV or ST), and $Z_{bm}(x)$ is the effect impedance of the BM given by

$$Z_{bm}(x) = -j\omega m_{bm}(x) + \frac{k_{bm}(x)}{-j\omega} + r_{bm}(x). \quad (4.34)$$

where $m_{bm}(x)$, $k_{bm}(x)$, and $r_{bm}(x)$ are the effective mass, stiffness, and damping of the BM, respectively. By using this relation, Eq. 4.32 is can be simplified as

$$\frac{\partial^2 p_{gap}}{\partial s^2} + \left(k_x^2 + \frac{\omega^2 g_0}{c^2 \alpha_f \tilde{A}} \right) p_{gap} = -\frac{\rho_f \omega^2}{\alpha_f \tilde{A}} \left[(W^b - u_{rl}^b) + \tilde{B} \frac{\partial u^s}{\partial s} \right]. \quad (4.35)$$

Now we have a final 1-D governing equation for the fluid in the TM-RL gap.

Boundary conditions at the OHC and IHC HBs as well as at the inner sulcus and scala media are needed to close the problem. From conservation of mass, the fluid flux across the HBs is conserved. In addition, the fluid flux is the quantity that couples to the macrofluidic flow in the scala media and inner sulcus.

The variational form of Eq. 4.35 is

$$\begin{aligned} & \int_0^L \delta \frac{\partial p_{gap}}{\partial s} \frac{\partial p_{gap}}{\partial s} ds - \left(k_x^2 + \frac{\omega^2 g_0}{c^2 \alpha_f \tilde{A}} \right) \int_0^L \delta p_{gap} p_{gap} ds = \delta p_{gap} \frac{\partial p_{gap}}{\partial s} \Big|_0^L \\ & + \frac{\rho_f \omega^2}{\alpha_f \tilde{A}} \int_0^L \delta p_{gap} (W^b - u_{rl}^b) ds + \frac{\rho_f \omega^2 \tilde{B}}{\alpha_f \tilde{A}} \int_0^L \delta p_{gap} \frac{\partial u^s}{\partial s} ds. \end{aligned} \quad (4.36)$$

Here we have used a generic domain of integration with length L to represent either the fluid domain Ω_1 or Ω_2 . Since the two fluid domains have different boundary conditions (boundary conditions are written in terms of the pressure gradient), Eq. 4.36 applies to each domain separately. To match the dimension of symmetric fluid-structure coupling

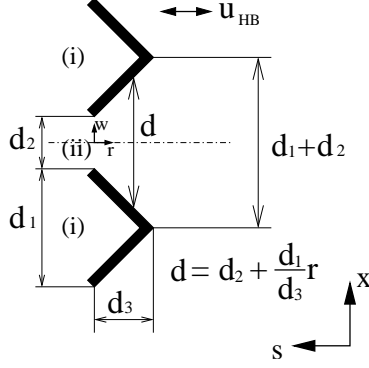


Figure 4.3: Schematic of the OHC HB configuration, viewed from the top of the RL plane (the $x - s$ plane as denoted in the bottom right corner of the figure). s and x are the global coordinates consistent with the coordinates indicated in Fig. 4.1. r and w are the local coordinates that describe the geometry relation between two adjacent OHC HBs in the longitudinal direction. The double arrow shows the direction of the displacement of the OHC HB (u_{HB}).

matrix, we re-scale Eq. 4.36 as

$$\begin{aligned} \frac{\alpha_f \tilde{A}}{\rho_f \omega^2} \int_0^L \delta \frac{\partial p_{gap}}{\partial s} \frac{\partial p_{gap}}{\partial s} ds - \left(\frac{\alpha_f \tilde{A}}{\rho_f \omega^2} k_x^2 + \frac{g_0}{\rho_f c^2} \right) \int_0^L \delta p_{gap} p_{gap} ds = \frac{\alpha_f \tilde{A}}{\rho_f \omega^2} \delta p_{gap} \frac{\partial p_{gap}}{\partial s} \Big|_0^L \\ + \int_0^L \delta p_{gap} (W^b - u_{rl}^b) ds + \tilde{B} \int_0^L \delta p_{gap} \frac{\partial u^s}{\partial s} ds. \end{aligned} \quad (4.37)$$

In the sequel, we consider the microfluidics around the HBs in order to determine the interface conditions accounting for the flow disturbance due to the HBs. To fix geometry, we refer to the location just before the OHC HB in Ω_1 as $s = L_{hb_2}^-$ and just beyond the HB in Ω_2 as $s = L_{hb_2}^+$. The IHC HBs are located in $L_{IHC}^- < s < L_{IHC}^+$.

4.2.2.1 Boundary condition at the OHC HBs

Although we are interested (at first) in a 2-D ($s-z$ plane) representation of the flow, in order to determine the fluid boundary condition at the OHC HB ($s = L_{hb_2}$), we must consider the longitudinal (x -direction) dependence of the flow, as shown in Fig. 4.3. There are two contributions to the flow. The first contribution is from flow associated with rotation of HBs [$0 < x < d_1$, denoted as region (i)]. Permeability *through* the stereocilia of the HB within a single OHC is assumed to be zero. The second contribution is due to flow in the gaps between the OHC HBs [$d_1 < x < d_1 + d_2$, denoted as region (ii)] (Fig. 4.3) from adjacent OHCs. Using Reynolds lubrication theory [73], the pressure

difference across the OHC HBs can be obtained by integration of the pressure gradient over the HBs (d_3) in the radial direction.

On the HB $s = L_{hb_2}$, a non-slip boundary condition is applied to the HB implying that the fluid velocity equals to the velocity of the HBs ($v_s = v_{hb_2}$), which is assumed to be linear in z (the HB is assumed to be rigid). Since the OHC HB is attached to the RL and also penetrates into the lower surface of the TM, it has the same displacement as the RL at $z = 0$ and as the TM at $z = g_0$. Hence,

$$u_{hb}(z) = \frac{z}{h_{hb}} u_{hb_2}, \quad (4.38)$$

where $h_{hb} = g_0$ is the height of the second row OHC HB. Here we assume that the HB height change due to the displacement of the HB is negligible. The height change may be important in the case that the HB does not form a rectangle angle with the RL [44], but this effect is not considered in this work. Then the linear velocity of the HB is

$$v_{hb_2}(z) = -j\omega \left[\frac{z}{h_{hb}} u_{hb_2} \right]. \quad (4.39)$$

Integration of the fluid velocity on the HB over the length (d_1) and height (h_{hb}) of the HB gives the volume flow rate due to the OHC HB motion,

$$\dot{Q}_{(i)} = d_1 \int_0^{h_{hb}} v_{hb_2} dz = -j\omega h_{hb} d_1 \left[\frac{1}{2} u_{hb_2} \right]. \quad (4.40)$$

According to the conservation of mass, the volume flow rate though the fluid gap (ii) is

$$\dot{Q}_{(ii)} = \dot{Q}|_{s=L_{hb_2}} (d_1 + d_2) - \dot{Q}_{(i)}, \quad (4.41)$$

where

$$\dot{Q}|_{s=L_{hb_2}} = \frac{\alpha_f}{j\omega\rho_f} \frac{\partial p_{gap}}{\partial s} \Big|_{s=L_{hb_2}} \tilde{A} - j\omega(u_{tms} + u_2^s) \tilde{B}, \quad (4.42)$$

is the volume flow rate (per unit length) in the TM-RL gap evaluated at $s = L_{hb_2}$. This type of notation will be used throughout this work.

For the OHC HB velocity given in Eq. 4.39, we can obtain the fluid velocity in the gap (ii) in the r direction, $v_{(ii)}$, in a similar way as the derivation of Eq. 4.21. The velocity

can be expressed as

$$v_{(ii)}(r, w, z) = \frac{\alpha_f}{j\omega\rho_f} \frac{\partial p_{(ii)}}{\partial r} \left[1 - \frac{\sinh \gamma(d/2 - w) + \sinh \gamma(w + d/2)}{\sinh(\gamma d)} \right] - j\omega \left[\frac{\sinh \gamma(d/2 - w) + \sinh \gamma(w + d/2)}{\sinh(\gamma d)} \right] \frac{z}{h_{hb}} u_{hb_2}, \quad (4.43)$$

where $d = d_2 + d_1 r/d_3$ is the width of the gap between the walls of HBs of two adjacent OHCs, as indicated by the geometry of the gap (see Fig. 4.3). Then $\dot{Q}_{(ii)}$ can be valued from $v_{(ii)}$ by

$$\dot{Q}_{(ii)} = \int_{-d/2}^{d/2} \int_0^{g_0} v_{(ii)} dz dw = \frac{\alpha_f}{j\omega\rho_f} \frac{\partial p_{(ii)}}{\partial r} \tilde{A}_{(ii)} g_0 - \frac{1}{2} j\omega \tilde{B}_{(ii)} g_0 u_{hb_2}, \quad (4.44)$$

where

$$\tilde{A}_{(ii)} = d - \tilde{B}_{(ii)}, \quad \tilde{B}_{(ii)} = 2 \frac{\cosh(\gamma d) - 1}{\gamma \sinh(\gamma d)}. \quad (4.45)$$

We will assume that $\gamma d \ll 1$. By the Taylor expansion of $\tilde{A}_{(ii)}$ and $\tilde{B}_{(ii)}$, these two quantities can be approximated as

$$\tilde{A}_{(ii)} \sim \frac{1}{12} \gamma^2 d^3, \quad \tilde{B}_{(ii)} \sim d. \quad (4.46)$$

This approximation is the same as assuming that the profile of $v_{(ii)}$ in w is a quadratic function. Hence, the pressure gradient in the gap (ii) can be solved from Eq. 4.44 as

$$\frac{\partial p_{(ii)}}{\partial r} = -\frac{12\mu}{\alpha_f g_0 d^3} \dot{Q}_{(ii)} - \frac{6j\omega\mu}{\alpha_f d^2} u_{hb_2}. \quad (4.47)$$

Denote

$$\Delta p_{ohc} = p_{\Omega_1} |_{s=L_{hb_2}^-} - p_{\Omega_2} |_{s=L_{hb_2}^+} \quad (4.48)$$

as the pressure difference across the OHC HB. By assuming that $\dot{Q}_{(ii)}$ is constant through the small radial domain d_3 , Δp_{ohc} can be calculated by integrating Eq. 4.47 over r ,

$$\Delta p_{ohc} = -\frac{12\mu}{\alpha_f g_0} \dot{Q}_{(ii)} \int_0^{d_3} \frac{1}{d^3} dr - \frac{6j\omega\mu}{\alpha_f} u_{hb_2} \int_0^{d_3} \frac{1}{d^2} dr \dots \quad (4.49)$$

The combination of Eqs. 4.40, 4.41, 4.42, 4.44, and 4.49 gives

$$\Delta p_{ohc} = -\frac{6j\omega\mu d_3}{\alpha_f d_2(d_1 + d_2)} u_{hb_2} - \frac{6\mu(d_1 + 2d_2)d_3}{\alpha_f g_0 d_2^2(d_1 + d_2)^2} \times \left[\left(\frac{\alpha_f}{j\omega\rho_f} \frac{\partial p_{gap}}{\partial s} \Big|_{s=L_{hb_2}} \tilde{A} - j\omega(u_{tms} + u_2^s) \tilde{B} \right) (d_1 + d_2) + \frac{1}{2} j\omega h_{hb} d_1 u_{hb_2} \right]. \quad (4.50)$$

Equation 4.49 shows that the pressure difference across the OHC HB depends on the pressure gradient at the OHC HB, the TM shearing motion, the displacement of the OHC HB, and the surrounding geometry. Here we have shown that the problem of different scales are incorporated: in the local coordinate r and w in Fig. 4.3, we consider the geometrical effect of the OHC HB with non-zero dimension. In the global coordinate s the entire OHC HB is a single point without dimension so that the $(\partial p_{gap}/\partial s)|_{s=L_{hb_2}}$ term in Eq. 4.50 is a part of the boundary conditions in Eq. 4.37. The concept of incorporating different scales will be used throughout this work.

The pressure gradient at the OHC HB can then be obtained from Eq. 4.49 as

$$\frac{\partial p_{gap}}{\partial s} \Big|_{s=L_{hb_2}} = \beta_{bm} u_{bm} + \beta_s u_{tms} + \beta_s u_2^s + \beta_b u_{tmb}^0 + \beta_b w_2^b + \beta_p \Delta p_{ohc}, \quad (4.51)$$

where

$$\beta_{bm} = \frac{\omega^2 \rho_f g_0 d_1}{2\alpha_f \tilde{A}(d_1 + d_2)} A_{21} = \frac{\rho_f \omega^2}{\alpha_f \tilde{A}} A_{21} \beta_{ds}, \quad (4.52)$$

$$\beta_s = -\frac{\omega^2 \rho_f \tilde{B}}{\alpha_f \tilde{A}} + \frac{\rho_f \omega^2 g_0}{\alpha_f \tilde{A}} \frac{1}{2} \left(\frac{d_1}{d_1 + d_2} + \frac{2d_2}{d_1 + 2d_2} \right) A_{23} = -\frac{\omega^2 \rho_f \tilde{B}}{\alpha_f \tilde{A}} + \frac{\rho_f \omega^2}{\alpha_f \tilde{A}} A_{23} \beta_{ds}, \quad (4.53)$$

$$\beta_b = \frac{\omega^2 \rho_f g_0 d_1}{2\alpha_f \tilde{A}(d_1 + d_2)} A_{24} = \frac{\rho_f \omega^2}{\alpha_f \tilde{A}} A_{24} \beta_{ds}, \quad (4.54)$$

$$\beta_p = -\frac{j\omega\rho_f g_0 d_2^2(d_1 + d_2)}{6\mu(d_1 + 2d_2)d_3 \tilde{A}} = -\frac{j\omega\rho_f}{6\mu \tilde{A}} \beta_{dp}. \quad (4.55)$$

where

$$\beta_{ds} = \frac{g_0}{2} \left(\frac{d_1}{d_1 + d_2} + \frac{2d_2}{d_1 + 2d_2} \right), \quad \beta_{dp} = \frac{g_0 d_2^2(d_1 + d_2)}{d_3(d_1 + 2d_2)}. \quad (4.56)$$

4.2.2.2 Boundary condition at the IHC HB

A similar strategy is used at the IHC HB, except that the geometry is different, with the HBs forming a nearly continuous “wall” in the x -direction, with a gap in the height (i.e., z -direction) between the apical end of the IHC HB and the TM/Hensen’s stripe

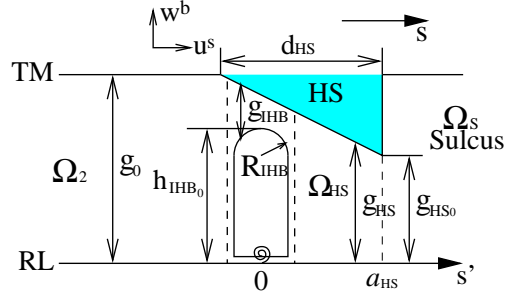


Figure 4.4: Schematic of the configuration in the surrounding region of the HS and IHC HB. s' is the local coordinate with the origin located at the middle line of the IHC HB. Loosely speaking, $s = s' + L_{IHC}$. The three vertical dashed lines have coordinates from left to right: $s' = -R_{IHB}$, $s' = R_{IHB}$, and $s' = a_{HS}$. The notations of the geometry are listed in Tab. 4.1. RL: reticular lamina. TM: tectorial membrane. HS: Hessen's stripe. IHC: inner hair cells. HB: hair bundles. IHB: a short cut for IHC HB.

Table 4.1: A list of geometry in Fig. 4.4.

g_0	resting height of the TM-RL fluid gap
g_{HS_0}	resting distance between the lowest point of the HS and the upper surface of the RL
$g_0 - g_{HS_0}$	height of the HS
d_{HS}	width of the HS
g_{HS}	distance between the lower surface of the HS and the upper surface of the RL
g_{IHB}	gap distance between the lower surface of the HS and the IHC HB tip
h_{IHB_0}	highest position of the IHC HB tip
R_{IHB}	radius of the tip of the IHC HB
a_{HS}	local coordinate of the end of the HS at the resting position
Ω_2	fluid domain in the TM-RL gap between the IHC and the second-row OHC
Ω_{HS}	fluid domain beneath the HS for $R_{IHB} \leq s' \leq a_{HS}$
Ω_s	fluid domain in the sulcus

(HS). The configuration around the IHC HBs is illustrated in Fig. 4.4. Once again the fluid flux comes from two contributions. The first is the flux around the apical tips of the HB. This flow will depend on the pressure difference between Ω_2 and in the HS micro-domain, Ω_{HS} . For larger deflections of the TM, this flow will be nonlinear, as the gap (on the order of a few hundred nanometers) may become commensurate with the deflections. However, for displacements closer to threshold (sub-nanometer up to a few nanometers), the problem can be considered linear. The second contribution will come from the motion of the IHC HB relative to the TM and RL. The IHC HB has its own dynamic equation of motion. This relative motion of the HB rotation will give rise to a net flux, in the same way as the OHC HBs.

To derive the boundary condition around the IHC HB, the following assumptions on the geometry and scaling are made:

- u^s is uniform over the HS region;
- the whole IHC HB is underneath the triangular HS region;
- the effects of the HS regions before the IHC HB (negative s direction) can be neglected. Hence, $a_{HS}/d_{HS} \sim 1$;
- with the deflection of the IHC HB and the shearing of the TM, the tip region of the IHC HB does not move outside the triangular region underneath the HS;
- the deflection of the IHC HB does not change the height of the HB h_{IHB_0} ;
- the radius of the IHC HB tip is much smaller than the height of the IHC HB, i.e., $R_{IHB} \ll g_0, h_{IHB_0}$;
- the curvature of the IHC HB tip plays an important role on the thin fluid gap over it. Hence the gap distance between the bottom of the HS and the tip of the IHC HB has the same order as R_{IHB} , i.e., $g_{IHB} = O(R_{IHB})$.

Let h_{IHB} be the height of the tip of the IHC HB. Denote s' as the local coordinate and set the $s' = 0$ position at the middle line of IHC HB (as shown in Fig. 4.4). Then h_{IHB} can be approximated as

$$h_{IHB} = h_{IHB_0} - \frac{(s')^2}{R_{IHB}}, \quad -R_{IHB} \leq s' \leq R_{IHB}. \quad (4.57)$$

The vertical distance from the lower surface of the HS to the upper surface of the RL at $s = L_{IHC}$ is

$$g_{HS} = -\frac{g_0 - g_{HS_0}}{d_{HS}}(s' - U^s|_{s=L_{IHC}} - a_{HS}) + g_{HS_0} + W^b|_{s=L_{IHC}} - u_{rl}^b|_{s=L_{IHC}}, \quad (4.58)$$

Note that in Eq. 4.58 we have notations of both the global coordinate s and the local coordinate s' . Similar to the idea mentioned in Sec. 4.2.2.1, the mixture of global and local coordinates reflects the connection between different scales in this work. In general, quantities specified by the coordinate s and s' refer to the global and local properties, respectively.

Denote u_{IHB} as the absolute displacement at the tip of the IHC HB in the direction parallel to the shearing of the TM. Similar to the calculation of the volume flow rate through the OHC HB (see Eq. 4.40), the volume flow rate through the IHC HB, denoted as \dot{Q}_{IHB} , is

$$\dot{Q}_{IHB} = -j\omega h_{IHB_0} \left(\frac{1}{2} u_{IHB} \right). \quad (4.59)$$

From the conservation of mass, the volume flow rate through the IHC HB tip gap (the gap between the upper surface of the IHC HB and the lower surface of the HS) is

$$\begin{aligned} \dot{Q}_2 &= \dot{Q}|_{s=L_{IHC}} - \dot{Q}_{IHB} \\ &= \frac{\alpha_f}{j\omega\rho_f} \frac{\partial p_{gap}}{\partial s} \Big|_{s=L_{IHC}} \tilde{A} - j\omega \tilde{B} U^s|_{s=L_{IHC}} + j\omega h_{IHB_0} \left(\frac{1}{2} u_{IHB} \right). \end{aligned} \quad (4.60)$$

Similar to the fluid in the TM-RL gap, the fluid velocity in the s' -direction within the IHC HB tip gap, v_{itip} , is governed by

$$\frac{\partial p_{IHB}}{\partial s'} = \frac{1}{\alpha_f} \rho_f j\omega v_{itip} + \frac{\mu}{\alpha_f} \frac{\partial^2 v_{itip}}{\partial z^2}, \quad (4.61)$$

where p_{IHB} is the fluid pressure in the IHC HB tip gap. By using the non-slip boundary conditions that

$$v_{itip}|_{z=g_{HS}} = -j\omega U^s|_{s=L_{IHC}}, \quad v_{itip}|_{z=h_{IHB}} = -j\omega u_{IHB}, \quad (4.62)$$

the fluid velocity in the tip gap is solved as

$$v_{itip} = \frac{\alpha_f}{j\omega\rho_f} \frac{\partial p_{IHB}}{\partial s'} \left[1 - \frac{\sinh \gamma(g_{HS} - z) + \sinh \gamma(z - h_{IHB})}{\sinh \gamma(g_{HS} - h_{IHB})} \right] - j\omega \frac{\sinh \gamma(g_{HS} - z)}{\sinh \gamma(g_{HS} - h_{IHB})} u_{IHB} - j\omega \frac{\sinh \gamma(z - h_{IHB})}{\sinh \gamma(g_{HS} - h_{IHB})} U^s|_{s=L_{IHC}}. \quad (4.63)$$

We can see that three components contribute to the v_{itip} : the pressure gradient in the tip gap, the shear motion of the TM, and the displacement of the IHC HB. By integrating Eq. 4.63 from $z = h_{IHB}$ to $z = g_{HS}$, we have the volume flow rate \dot{Q}_2 in the IHC HB tip gap

$$\dot{Q}_2 = \frac{\alpha_f}{j\omega\rho_f} \frac{\partial p_{IHB}}{\partial s'} \tilde{A}_{IHB} - j\omega (U^s|_{s=L_{IHC}} + u_{IHB}) \tilde{B}_{IHB}, \quad (4.64)$$

where

$$\tilde{A}_{IHB} = (g_{HS} - h_{IHB}) - 2 \frac{\cosh \gamma(g_{HS} - h_{IHB}) - 1}{\gamma \sinh \gamma(g_{HS} - h_{IHB})}, \quad (4.65)$$

$$\tilde{B}_{IHB} = \frac{\cosh \gamma(g_{HS} - h_{IHB}) - 1}{\gamma \sinh \gamma(g_{HS} - h_{IHB})}. \quad (4.66)$$

Since the height of the IHC HB tip gap ($g_{HS} - h_{IHB}$, could be in the scale of sub-micron) is much less than the viscous boundary layer thickness (typically close to 10 microns depending on the simulation frequency), then $\gamma(g_{HS} - h_{IHB}) \ll 1$. Hence, by using Taylor expansion, \tilde{A}_{IHB} and \tilde{B}_{IHB} can be approximated as

$$\tilde{A}_{IHB} = \frac{1}{12} \gamma^2 (g_{HS} - h_{IHB})^3, \quad (4.67)$$

$$\tilde{B}_{IHB} = \frac{1}{2} (g_{HS} - h_{IHB}). \quad (4.68)$$

Substituting Eqs. 4.67 and 4.68 into Eq. 4.64 yields the pressure gradient in the IHC HB tip gap as function of the local coordinate s' :

$$\frac{\partial p_{IHB}}{\partial s'} = - \frac{12\mu}{\alpha_f (g_{HS} - h_{IHB})^3} \dot{Q}_2 - \frac{6j\omega\mu}{\alpha_f (g_{HS} - h_{IHB})^2} (U^s|_{s=L_{IHC}} + u_{IHB}). \quad (4.69)$$

Denote p_{HS} as the fluid pressure beneath the HS in the range $s' \in [R_{IHB}, a_{HS}]$. Define

$$\Delta p_{IHB} = p_{HS}|_{s'=R_{IHB}} - p_{\Omega_2}|_{s'=-R_{IHB}} \quad (4.70)$$

as the pressure difference across the IHC HB tip gap. By assuming that \dot{Q}_2 is constant over the IHC HB tip gap, we can obtain the pressure difference across the IHC HB by

integrating the pressure gradient in Eq. 4.69 over s' , i.e.,

$$\begin{aligned} \Delta p_{IHB} = & -\frac{12\mu\dot{Q}_2}{\alpha_f} \int_{-R_{IHB}}^{R_{IHB}} \frac{ds'}{(g_{HS} - h_{IHB})^3} \\ & - \frac{6j\omega\mu}{\alpha_f} (U^s|_{s=L_{IHC}} + u_{IHB}) \int_{-R_{IHB}}^{R_{IHB}} \frac{ds'}{(g_{HS} - h_{IHB})^2}. \end{aligned} \quad (4.71)$$

The integration can be approximated as (see Appendix F Eqs. F.1 to F.14 for a derivation)

$$\Delta p_{IHB} = -\frac{12\mu\dot{Q}_2}{\alpha_f} I_3 - \frac{6j\omega\mu}{\alpha_f} (U^s|_{s=L_{IHC}} + u_{IHB}) I_2, \quad (4.72)$$

where

$$I_3 = 12\pi R_{IHB}^{\frac{1}{2}} \sigma^{-\frac{5}{2}}, \quad I_2 = 4\pi R_{IHB}^{\frac{1}{2}} \sigma^{-\frac{3}{2}}, \quad (4.73)$$

for a linear approximation, where

$$\sigma = 4 \frac{g_0 - g_{HS_0}}{d_{HS}} a_{HS} + 4(g_{HS_0} - h_{IHB_0}) - R_{IHB} \left(\frac{g_0 - g_{HS_0}}{d_{HS}} \right)^2. \quad (4.74)$$

In the above linear approximation, we have used the assumption of infinitesimal motion such that all the geometries used in the calculated are the same as the resting state. Considering nonlinear effect is possible, but it is not included in this work.

The fluid velocity in the IHC HB tip gap, v_{itip} , varies in space as a function of s' , so is the fluid shear viscosity. The resultant shear viscous force exerted over the tip of the IHC HB can be obtained by integration as

$$f_{\mu IHB} = \int_{-R_{IHB}}^{R_{IHB}} \mu \frac{\partial v_{itip}}{\partial z} \Big|_{z=h_{IHB}} ds'. \quad (4.75)$$

From Eq. 4.63, the fluid gradient in z evaluated at $z = h_{IHB}$ is

$$\begin{aligned} \frac{\partial v_{itip}}{\partial z} \Big|_{z=h_{IHB}} = & \frac{\alpha_f}{j\omega\rho_f} \frac{\partial p_{IHB}}{\partial s'} \left[\gamma \frac{\cosh \gamma(g_{HS} - h_{IHB}) - 1}{\sinh \gamma(g_{HS} - h_{IHB})} \right] \\ & - j\omega U^s|_{s=L_{IHC}} \frac{\gamma}{\sinh \gamma(g_{HS} - h_{IHB})} + j\omega u_{IHB} \frac{\gamma \cosh \gamma(g_{HS} - h_{IHB})}{\sinh \gamma(g_{HS} - h_{IHB})}. \end{aligned} \quad (4.76)$$

By using $\gamma(g_{HS} - h_{IHB}) \ll 1$, Eq. 4.76 is approximated as

$$\frac{\partial v_{itip}}{\partial z} \Big|_{z=h_{IHB}} = -\frac{\alpha_f}{2\mu} \frac{\partial p_{IHB}}{\partial s'} (g_{HS} - h_{IHB}) - j\omega(U^s|_{s=L_{IHC}} - u_{IHB}) \frac{1}{(g_{HS} - h_{IHB})}. \quad (4.77)$$

Substituting Eq. 4.69 into Eq. 4.77, and then into Eq. 4.75 yields

$$f_{\mu IHB} = 6\mu\dot{Q}_2 \int_{-R_{IHB}}^{R_{IHB}} \frac{ds'}{(g_{HS} - h_{IHB})^2} + 2j\omega\mu(U^s|_{s=L_{IHC}} + 2u_{IHB}) \int_{-R_{IHB}}^{R_{IHB}} \frac{ds'}{(g_{HS} - h_{IHB})}, \quad (4.78)$$

which is approximated as (see Appendix F Eqs. F.1 to F.14 for a derivation)

$$f_{\mu IHB} = 6\mu\dot{Q}_2 I_2 + 2j\omega\mu(U^s|_{s=L_{IHC}} + 2u_{IHB}) I_1, \quad (4.79)$$

where

$$I_1 = 2\pi R_{IHB}^{\frac{1}{2}} \sigma^{-\frac{1}{2}}. \quad (4.80)$$

The shear viscous force applied on the IHC HB depends on the local pressure gradient, the shear motion of the TM, and the displacement of the IHC HB.

For the pressure difference defined in Eq. 4.70, the force applied on the IHC HB due to the pressure difference ($\Delta p_{IHB} h_{IHB_0}$) is in the negative s direction for positive Δp_{IHB} . Hence, the total force acting on the IHC HB, as a combined effect of the pressure difference across the HB and the resultant fluid shear viscous force, is $f_{\mu IHB} - \Delta p_{IHB} h_{IHB_0}$. Denote

$$\theta_3^b = \frac{u_{rl}^b|_{s=L_{IHC}} - u_{rl}^b|_{s=L_{pill}}}{L_{pill} - L_{IHC}}, \quad (4.81)$$

as the relative rotational angle between the RL and the IHC HB due to the bending motion of the RL. θ_3^b is defined as positive if the relative angle change opens the ion channel of the IHC HB. By Eq. 4.14, θ_3^b has the expression

$$\theta_3^b = \frac{1}{L_{Ro}} [B_{21}u_{bm} + B_{24}(u_{tms} + u_2^s) + B_{24}(u_{tmb}^0 + w_2^b)]. \quad (4.82)$$

Hence, for the massless IHC HB, the balance of the IHC HB is given by

$$f_{\mu IHB} - \Delta p_{IHB} h_{IHB_0} = (u_{IHB} - \theta_3^b h_{IHB_0}) K_{IHB}, \quad (4.83)$$

where K_{IHB} is the stiffness of the IHC HB. Substituting Eqs. 4.72 and 4.79 into Eq. 4.83 yields

$$6\mu\tau_1\dot{Q}_2 + 2j\omega\mu\tau_2U^s|_{s=L_{IHC}} + 2j\omega\mu\tau_3u_{IHB} = u_{IHB}K_{IHB} - \theta_3^b h_{IHB_0} K_{IHB}, \quad (4.84)$$

where

$$\tau_1 = I_2 + \frac{2}{\alpha_f} I_3 h_{IHB_0}, \quad \tau_2 = I_1 + \frac{3}{\alpha_f} I_2 h_{IHB_0}, \quad \tau_3 = 2I_1 + \frac{3}{\alpha_f} I_2 h_{IHB_0}. \quad (4.85)$$

Substituting Eq. 4.60 into Eq. 4.84 yields

$$u_{IHB} = \frac{1}{\sigma_5} \left[\sigma_1 \frac{\partial p_{gap}}{\partial s} \Big|_{s=L_{IHC}} + \sigma_2 u_{tms} + \sigma_3 u_2^s + \sigma_4 u_3^s + \sigma_6 u_{bm} + \sigma_7 (u_{tmb}^0 + w_2^b) \right], \quad (4.86)$$

where

$$\sigma_1 = 6\mu\tau_1 \frac{\alpha_f}{j\omega\rho_f} \tilde{A}, \quad \sigma_2 = \sigma_3 + 2j\omega\mu(\tau_2 - 3\tau_1\tilde{B}), \quad (4.87)$$

$$\sigma_3 = B_{23} \frac{h_{IHB_0}}{L_{Ro}} K_{IHB_0}, \quad \sigma_4 = 2j\omega\mu(\tau_2 - 3\tau_1\tilde{B}), \quad (4.88)$$

$$\sigma_5 = K_{IHB} - j\omega\mu(2\tau_3 + 3\tau_1 h_{IHB_0}). \quad (4.89)$$

$$\sigma_6 = B_{21} \frac{h_{IHB_0}}{L_{Ro}} K_{IHB_0}, \quad \sigma_7 = B_{24} \frac{h_{IHB_0}}{L_{Ro}} K_{IHB_0} \quad (4.90)$$

Equation 4.86 shows that the motion of the IHC HB is a combined effect of the fluid dynamics in the TM-RL gap and the kinetics of the OoC.

In the region beyond the IHC HB under the HS, the fluid velocity, v_{HS} , is (similar to the derivation for Eq. 4.63)

$$v_{HS} = \frac{\alpha_f}{j\omega\rho_f} \frac{\partial p_{HS}}{\partial s'} \left[1 - \frac{\sinh \gamma(g_{HS} - z) + \sinh(\gamma z)}{\sinh(\gamma g_{HS})} \right] - j\omega \frac{\sinh(\gamma z)}{\sinh(\gamma g_{HS})} U^s \Big|_{s=L_{IHC}}. \quad (4.91)$$

Integrating Eq. 4.91 from $z = 0$ to $z = g_{HS}$ yields the total volume flow rate beneath the HS

$$\dot{Q}|_{s=L_{IHC}} = \frac{\alpha_f}{j\omega\rho_f} \frac{\partial p_{HS}}{\partial s'} \tilde{A}_{HS} - j\omega \tilde{B}_{HS} U^s \Big|_{s=L_{IHC}}, \quad (4.92)$$

where

$$\tilde{A}_{HS} = g_{HS} - 2 \frac{\cosh(\gamma g_{HS}) - 1}{\gamma \sinh(\gamma g_{HS})}, \quad (4.93)$$

$$\tilde{B}_{HS} = \frac{\cosh(\gamma g_{HS}) - 1}{\gamma \sinh(\gamma g_{HS})}. \quad (4.94)$$

In Eq. 4.92, we use the approximation that the volume flow rate beneath the HS is the

same as the volume flow rate in the TM-RL gap at $s = L_{IHC}$. Similarly, upon the assumption that $\gamma g_{HS} \ll 1$, \tilde{A}_{HS} and \tilde{B}_{HS} are approximated as

$$\tilde{A}_{HS} = \frac{1}{12} \gamma^2 g_{HS}^3, \quad \tilde{B}_{HS} = \frac{1}{2} g_{HS}. \quad (4.95)$$

Substituting Eq. 4.95 into Eq. 4.92 yields the pressure gradient beneath the HS

$$\frac{\partial p_{HS}}{\partial s'} = -\frac{12\mu}{\alpha_f g_{HS}^3} \dot{Q}|_{s=L_{IHC}} - \frac{6j\omega\mu}{\alpha_f g_{HS}^2} U^s|_{s=L_{IHC}}. \quad (4.96)$$

Define

$$\Delta p_{HS} = p_s - p_{HS}|_{s'=R_{IHB}} \quad (4.97)$$

as the pressure difference across the HS. Then

$$\begin{aligned} \Delta p_{HS} &= -\frac{12\mu}{\alpha_f} \dot{Q}|_{s=L_{IHC}} \int_{R_{IHB}}^{a_{HS}} \frac{ds'}{g_{HS}^3} - \frac{6j\omega\mu}{\alpha_f} U^s|_{s=L_{IHC}} \int_{R_{IHB}}^{a_{HS}} \frac{ds'}{g_{HS}^2} \\ &= -\frac{12\mu}{\alpha_f} \dot{Q}|_{s=L_{IHC}} I'_3 - \frac{6j\omega\mu}{\alpha_f} I'_2 U^s|_{s=L_{IHC}}. \end{aligned} \quad (4.98)$$

where

$$I'_3 = \frac{d_{HS}}{2(g_0 - g_{HS_0})} \left[(g_{HS_0})^{-2} - \left(\frac{g_0 - g_{HS_0}}{d_{HS}} (a_{HS} - R_{IHB}) + g_{HS_0} \right)^{-2} \right], \quad (4.99)$$

$$I'_2 = \frac{d_{HS}}{(g_0 - g_{HS_0})} \left[(g_{HS_0})^{-1} - \left(\frac{g_0 - g_{HS_0}}{d_{HS}} (a_{HS} - R_{IHB}) + g_{HS_0} \right)^{-1} \right], \quad (4.100)$$

for a linear approximation (see Appendix F Eqs. F.14 to F.17 for a derivation).

The total pressure difference between the sulcus and the TM-RL gap is

$$p_s - p_{\Omega_2}|_{s=L_{IHC}^-} = \Delta p_{IHB} + \Delta p_{HS}. \quad (4.101)$$

By applying Eqs. 4.72 and 4.98, we can write Eq. 4.101 as

$$\begin{aligned} p_s - p_{\Omega_2}|_{s=L_{IHC}^-} &= -\frac{12\mu}{\alpha_f} \left[\dot{Q}_2 I_3 + \dot{Q}|_{s=L_{IHC}} I'_3 \right] \\ &\quad - \frac{6j\omega\mu}{\alpha_f} \left[U^s|_{s=L_{IHC}} (I_2 + I'_2) + u_{IHB} I_2 \right]. \end{aligned} \quad (4.102)$$

Substituting Eqs. 4.23 (evaluated at $s = L_{IHC}$), 4.60, and 4.86 into Eq. 4.102 yields

$$p_s - p_{\Omega_2}|_{s=L_{IHC}^-} = \left(\gamma_1 + \gamma_4 \frac{\sigma_1}{\sigma_5} \right) \frac{\partial p_{gap}}{\partial s} \Big|_{s=L_{IHC}} + \left(\gamma_2 + \gamma_4 \frac{\sigma_2}{\sigma_5} \right) u_{tms} + \gamma_4 \frac{\sigma_3}{\sigma_5} u_2^s + \left(\gamma_2 + \gamma_4 \frac{\sigma_4}{\sigma_5} \right) u_3^s + \gamma_4 \frac{\sigma_6}{\sigma_5} u_{bm} + \gamma_4 \frac{\sigma_y}{\sigma_5} (u_{tmb}^0 + w_2^b), \quad (4.103)$$

where

$$\gamma_1 = -\frac{12\mu}{j\omega\rho_f} \tilde{A}(I_3 + I_3'), \quad (4.104)$$

$$\gamma_2 = \frac{12j\omega\mu}{\alpha_f} \left[\tilde{B}(I_3 + I_3') - \frac{1}{2}(I_2 + I_2') \right], \quad (4.105)$$

$$\gamma_4 = -\frac{6j\omega\mu}{\alpha_f} (I_2 + I_3 h_{IHB_0}). \quad (4.106)$$

The pressure gradient at IHC HB can be solved from Eq. 4.103 as

$$\begin{aligned} \frac{\partial p_{gap}}{\partial s} \Big|_{s=L_{IHC}^-} &= \frac{\sigma_5}{\gamma_1\sigma_5 + \gamma_4\sigma_1} \left(p_s - p_{\Omega_2}|_{s=L_{IHC}^-} \right) - \frac{\gamma_2\sigma_5 + \gamma_4\sigma_2}{\gamma_1\sigma_5 + \gamma_4\sigma_1} u_{tms} \\ &- \frac{\gamma_4\sigma_3}{\gamma_1\sigma_5 + \gamma_4\sigma_1} u_2^s - \frac{\gamma_2\sigma_5 + \gamma_4\sigma_4}{\gamma_1\sigma_5 + \gamma_4\sigma_1} u_3^s - \frac{\gamma_4\sigma_6}{\gamma_1\sigma_5 + \gamma_4\sigma_1} u_{bm} - \frac{\gamma_4\sigma_7}{\gamma_1\sigma_5 + \gamma_4\sigma_1} (u_{tmb}^0 + w_2^b). \end{aligned} \quad (4.107)$$

Similarly, this pressure gradient is a combined effect of the fluid dynamics in the TM-RL gap and the kinetics of the OoC.

4.2.2.3 Boundary conditions at the scala media

An impedance boundary condition is used to relate the flux of the fluid at the TM-RL fluid gap and the macroscopic flow pressure in the scala media (SM). This boundary condition utilizes Eq.4.23 evaluated at $s = 0$ to determine the TM-RL flux and couples that to the macrofluidic pressure boundary conditions in the SM. Denote p_{sm} as the pressure (in the SM) on the OoC, which will be the same as the pressure node in the SV evaluated at $z = 0$. The boundary condition for the TM-RL fluid gap at $s = 0$ is,

$$Z_{sm} \bar{v}_s|_{s=0} = (p_{gap}|_{s=0} - p_{sm}) g_0, \quad (4.108)$$

where Z_{sm} is the end-impedance at $s = 0$,

$$Z_{sm} = -j\omega m_{sm} - \frac{k_{sm}}{j\omega} + c_{sm}, \quad (4.109)$$

where m_{sm} , k_{sm} , and c_{sm} are the effective mass, stiffness, and damping per unit length at the outer edge of the TM-RL gap. $\bar{v}_s|_{s=0}$ is the average TM-RL fluid velocity at $s = 0$, given by

$$\bar{v}|_{s=0} = \frac{1}{g_0} \left(\frac{\alpha_f}{j\omega\rho_f} \frac{\partial p_{gap}}{\partial s} \Big|_{s=0} \tilde{A} - j\omega\tilde{B}U^s|_{s=0} \right). \quad (4.110)$$

Therefore, the pressure gradient at the boundary is

$$\frac{\partial p_{gap}}{\partial s} \Big|_{s=0} = \frac{j\omega\rho_f g_0^2}{\alpha_f Z_{sm} \tilde{A}} (p_{gap}|_{s=0} - p_{sm}) - \frac{\omega^2 \rho_f \tilde{B}}{\alpha_f \tilde{A}} U^s|_{s=0}, \quad (4.111)$$

where $U^s|_{s=0} = u_{tms} + u_1^s$.

4.2.2.4 A summary on the boundary conditions

As shown in Eq. 4.37, for each fluid element in Ω_1 and Ω_2 , two boundary conditions at the two ends of each elements is needed. The entire TM-RL gap is discretized into two element and four pressure nodes. For short notation, let

$$p_1 = p_{\Omega_1}|_{s=0}, \quad p_2 = p_{\Omega_1}|_{s=L_{hb_2}^-}, \quad p_3 = p_{\Omega_2}|_{s=L_{hb_2}^+}, \quad p_4 = p_{\Omega_2}|_{s=L_{IHC}^-}. \quad (4.112)$$

We have derived the fluid boundary conditions at each boundary written in terms of the pressure gradient (see Eqs. 4.51, 4.107, and 4.111). The following is a summary of all the boundary conditions for the TM-RL fluid gap. For the fluid region Ω_1 , the boundary conditions are

$$\frac{\partial p_{gap}}{\partial s} \Big|_{s=0} = \frac{j\omega\rho_f g_0^2}{\alpha_f Z_{sm} \tilde{A}} (p_1 - p_{sm}) - \frac{\omega^2 \rho_f \tilde{B}}{\alpha_f \tilde{A}} (u_{tms} + u_1^s), \quad (4.113)$$

$$\frac{\partial p_{gap}}{\partial s} \Big|_{s=L_{hb_2}^-} = \beta_{bm} u_{bm} + \beta_s (u_{tms} + u_2^s) + \beta_b (u_{tmb}^0 + w_2^b) + \beta_p (p_2 - p_3). \quad (4.114)$$

For the fluid region Ω_2 , the boundary conditions are

$$\frac{\partial p_{gap}}{\partial s} \Big|_{s=L_{hb_2}^+} = \beta_{bm} u_{bm} + \beta_s (u_{tms} + u_2^s) + \beta_b (u_{tmb}^0 + w_2^b) + \beta_p (p_2 - p_3), \quad (4.115)$$

$$\begin{aligned} \frac{\partial p_{gap}}{\partial s} \Big|_{s=L_{IHC}^-} &= \frac{\sigma_5}{\gamma_1 \sigma_5 + \gamma_4 \sigma_1} \left(p_s - p_{\Omega_2}|_{s=L_{IHC}^-} \right) - \frac{\gamma_2 \sigma_5 + \gamma_4 \sigma_2}{\gamma_1 \sigma_5 + \gamma_4 \sigma_1} u_{tms} \\ &- \frac{\gamma_4 \sigma_3}{\gamma_1 \sigma_5 + \gamma_4 \sigma_1} u_2^s - \frac{\gamma_2 \sigma_5 + \gamma_4 \sigma_4}{\gamma_1 \sigma_5 + \gamma_4 \sigma_1} u_3^s - \frac{\gamma_4 \sigma_6}{\gamma_1 \sigma_5 + \gamma_4 \sigma_1} u_{bm} - \frac{\gamma_4 \sigma_7}{\gamma_1 \sigma_5 + \gamma_4 \sigma_1} (u_{tmb}^0 + w_2^b). \end{aligned} \quad (4.116)$$

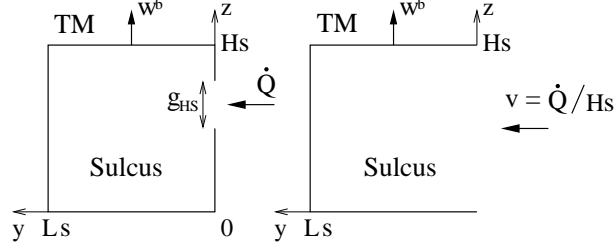


Figure 4.5: Schematic of the configuration of the sulcus (see Ω_s in Fig. 4.2). The local coordinate y is in the same direction as s . The effective fluid velocity at the inlet of the sulcus is assumed to be \dot{Q}/H_s that uniformly extends over the entire height of the sulcus. The width of the sulcus L_s is defined as $L_s = L_{tm} - L_{IHC}$.

These four boundary conditions are ready to be used directly in the boundary term in Eq. 4.37.

4.2.3 The sulcus fluid model

The sulcus is represented by a fluid duct with area A_s , width L_s (defined as $L_s = L_{tm} - L_{IHC}$), and height $H_s = A_s/L_s$ (Fig. 4.5). Let y be the local coordinate in the radial direction. The sulcus fluid is modeled as a 1-D domain running in the longitudinal direction (x), where the pressure is constant in the $y - z$ plane.

At the inlet of the sulcus the fluid volume rate is \dot{Q} (Fig. 4.5), the same as the \dot{Q} in the TM-RL fluid gap. Changes in the cross sectional area of the sulcus are contributed by the TM normal displacement over the inner sulcus, $W^b L_s$ (as in [18]). For simplicity, the effective fluid velocity at the inlet of the sulcus is assumed to be \dot{Q}/H_s that uniformly extends over the entire height of the sulcus (Fig. 4.5). The coordinates dependence of the velocity and pressure in the sulcus are assumed as

$$v_x = v_x(x), \quad v_y = v_y(x, y), \quad v_z = v_z(x, z), \quad p_s = p_s(x). \quad (4.117)$$

The linearized NS equation in the x direction and its boundary conditions are

$$-\rho_f j\omega v_x = -\alpha_f \frac{\partial p_s}{\partial x} + \mu \frac{\partial^2 v_x}{\partial x^2}, \quad v_x(0) = 0, \quad v_x(L_{bm}) = 0, \quad (4.118)$$

where L_{bm} is the length of the BM. Then v_x is solved as

$$v_x = \frac{\alpha_f}{j\omega\rho_f} \frac{\partial p_s}{\partial x}. \quad (4.119)$$

The linearized NS equation in the y direction and its boundary conditions are

$$-\rho_f j\omega v_y = \mu \frac{\partial^2 v_y}{\partial y^2}, \quad v_y(0) = \frac{\dot{Q}|_{s=L_{IHC}}}{H_s}, \quad v_y(L_s) = 0. \quad (4.120)$$

Then v_y is solved as

$$v_y = \frac{\dot{Q}|_{s=L_{IHC}}}{H_s} \frac{\sinh \gamma(L_s - y)}{\sinh \gamma L_s}. \quad (4.121)$$

The linearized NS equation in the z direction and its boundary conditions are

$$-\rho_f j\omega v_z = \mu \frac{\partial^2 v_z}{\partial z^2}, \quad v_z(0) = 0, \quad v_z(H_s) = -j\omega \bar{W}^b. \quad (4.122)$$

where $\bar{W}^b = W^b|_{s=L_{IHC}}/2$ is the average TM bending displacement over the sulcus. Then v_z is solved as

$$v_z = -j\omega \bar{W}^b \frac{\sinh \gamma z}{\sinh \gamma H_s}. \quad (4.123)$$

The conservation of mass of the fluid requires

$$\frac{\partial v_x}{\partial x} + \frac{\partial v_y}{\partial y} + \frac{\partial v_z}{\partial z} + \frac{1}{\rho_f c^2} \frac{\partial p_s}{\partial t} = 0. \quad (4.124)$$

Substituting the expressions of v_x , v_y , and v_z into Eq. 4.124 yields

$$\frac{\alpha_f}{j\omega \rho_f} \frac{\partial^2 p_s}{\partial x^2} - \frac{\dot{Q}|_{s=L_{IHC}}}{H_s} \frac{\gamma \cosh \gamma(L_s - y)}{\sinh \gamma L_s} - j\omega \bar{W}^b \frac{\gamma \cosh \gamma z}{\sinh \gamma H_s} - \frac{j\omega}{\rho_f c^2} p_s = 0. \quad (4.125)$$

Integrating Eq. 4.125 over the y and z domains yields

$$\frac{\partial^2 p_s}{\partial x^2} + \frac{\omega^2}{c^2 \alpha_f} p_s = -\frac{j\omega \rho_f}{\alpha_f} \left(\frac{-j\omega \bar{W}^b}{H_s} - \frac{\dot{Q}|_{s=L_{IHC}}}{H_s L_s} \right). \quad (4.126)$$

Similar to the flow in the TM-RL gap, for a single cross section, $\partial^s p_s / \partial x^2 \sim k_x^2 p_s$ is assumed. We also rescale Eq. 4.126 by multiplying it with $\alpha_f H_s / \omega^2 \rho_f$. Then Eq. 4.126 becomes

$$\left(\frac{\alpha_f H_s}{\omega^2 \rho_f} k_x^2 + \frac{H_s}{\rho_f c^2} \right) p_s + \frac{1}{2} W^b|_{s=L_{IHC}} - \frac{j}{\omega L_s} \dot{Q}|_{s=L_{IHC}} = 0. \quad (4.127)$$

Substituting Eq. 4.107 into Eq. 4.23 (evaluated at $s = L_{IHC}$) yields

$$\begin{aligned} \dot{Q}|_{s=L_{IHC}} = & -j\omega \lambda_1 (p_s - p_{\Omega_2}|_{s=L_{IHC}^-}) + j\omega \lambda_2 u_{tms} + j\omega \lambda_3 u_2^s + j\omega \lambda_4 u_3^s \\ & + j\omega \lambda_5 u_{bm} + j\omega \lambda_6 (u_{tmb}^0 + w_2^b), \end{aligned} \quad (4.128)$$

where

$$\lambda_1 = \frac{\alpha_f \tilde{A}}{\omega^2 \rho_f} \cdot \frac{\sigma_5}{\gamma_1 \sigma_5 + \gamma_4 \sigma_1}, \quad \lambda_2 = \frac{\alpha_f \tilde{A}}{\omega^2 \rho_f} \cdot \frac{\gamma_2 \sigma_5 + \gamma_4 \sigma_2}{\gamma_1 \sigma_5 + \gamma_4 \sigma_1} - \tilde{B}, \quad (4.129)$$

$$\lambda_3 = \frac{\alpha_f \tilde{A}}{\omega^2 \rho_f} \cdot \frac{\gamma_4 \sigma_3}{\gamma_1 \sigma_5 + \gamma_4 \sigma_1}, \quad \lambda_4 = \frac{\alpha_f \tilde{A}}{\omega^2 \rho_f} \cdot \frac{\gamma_2 \sigma_5 + \gamma_4 \sigma_4}{\gamma_1 \sigma_5 + \gamma_4 \sigma_1} - \tilde{B}, \quad (4.130)$$

$$\lambda_5 = \frac{\alpha_f \tilde{A}}{\omega^2 \rho_f} \cdot \frac{\gamma_4 \sigma_6}{\gamma_1 \sigma_5 + \gamma_4 \sigma_1}, \quad \lambda_6 = \frac{\alpha_f \tilde{A}}{\omega^2 \rho_f} \cdot \frac{\gamma_4 \sigma_7}{\gamma_1 \sigma_5 + \gamma_4 \sigma_1}. \quad (4.131)$$

Substituting Eq. 4.128 into Eq. 4.127 yields

$$\begin{aligned} & \left(\frac{\alpha_f H_s}{\omega^2 \rho_f} k_x^2 + \frac{H_s}{\rho_f c^2} - \frac{\lambda_1}{L_s} \right) p_s + \frac{\lambda_1}{L_s} p_{\Omega_2} \Big|_{s=L_{IHC}^-} + \frac{\lambda_2}{L_s} u_{tms} + \frac{\lambda_3}{L_s} u_2^s + \frac{\lambda_4}{L_s} u_3^s \\ & + \frac{\lambda_5}{L_s} u_{bm} + \frac{\lambda_6}{L_s} (u_{tmb}^0 + w_2^b) + \frac{1}{2} \left(\frac{L_{tm} - L_{IHC}}{\ell_{tm}} u_{tmb}^0 + w_3^b \right) = 0, \end{aligned} \quad (4.132)$$

which is the governing equation for the fluid pressure p_s in the sulcus region.

4.2.4 SV/ST fluid model

The fluid in SV and ST is modeled by a 3-D rectangular box with height $2H$ (both the SV and ST have height H) and width B . Since only a cross section is considered, the cochlear length does not play a role here. Let $z \in [-H, H]$ be the domain in the vertical direction, and $y \in [-B/2, B/2]$ be the domain in the radial direction. x runs longitudinally. The governing equation for the fluid is

$$\frac{\partial^2 p}{\partial x^2} + \frac{\partial^2 p}{\partial y^2} + \frac{\partial^2 p}{\partial z^2} + \frac{\omega^2}{\alpha_f c^2} p = 0. \quad (4.133)$$

By using the linearized Euler relation, the boundary condition at the BM ($z = 0$) is

$$\frac{\partial p}{\partial z} \Big|_{z=0} = \frac{\rho_f \omega^2}{\alpha_f} u_{BM}. \quad (4.134)$$

In the x direction, the approximation $\partial^s p / \partial x^2 \sim k_x^2 p$ is used. In the y direction, by assuming that the cochlear lateral wall is rigid, the pressure has mode shape

$$\phi_m = \cos \left[\frac{m\pi}{B} \left(y + \frac{B}{2} \right) \right], \quad m = 0, 2, 4, \dots \quad (4.135)$$

Denote p_m as the SV/ST fluid pressure at each cross section associated with mode m , then the governing equation for p_m is

$$\frac{\partial^2 p_m}{\partial z^2} + \left[k_x^2 + \frac{\omega^2}{\alpha_f c^2} - \left(\frac{m\pi}{B} \right)^2 \right] p_m = 0. \quad (4.136)$$

The BM is approximated by the first mode, i.e.,

$$u_{BM}(y) = u_{bm} \sin \left[\frac{\pi}{b} \left(y + \frac{b}{2} \right) \right]. \quad (4.137)$$

where b is the width of the BM. Substituting Eqs. 4.135 and 4.137 into Eq. 4.134 yields

$$\sum \frac{\partial p_m}{\partial z} \cos \left[\frac{m\pi}{B} \left(y + \frac{B}{2} \right) \right] = \frac{\rho_f \omega^2}{\alpha_f} u_{bm} \sin \left[\frac{\pi}{b} \left(y + \frac{b}{2} \right) \right], \quad \text{on } z = 0. \quad (4.138)$$

By using the orthogonality of the fluid mode shape, integrating Eq. 4.138 over y yields

$$\frac{\partial p_m}{\partial z} \Big|_{z=0} = \frac{\rho_f \omega^2}{\alpha_f W_m} u_{bm} \mu_m, \quad (4.139)$$

where

$$W_m = \int_{-B/2}^{B/2} \phi_m^2 dy = \begin{cases} B & \text{if } m = 0 \\ B/2 & \text{if } m \neq 0 \end{cases}. \quad (4.140)$$

and

$$\mu_m = \int_{-b/2}^{b/2} \phi_m \sin \left[\frac{\pi}{b} \left(y + \frac{b}{2} \right) \right] dy. \quad (4.141)$$

The variational form of Eq. 4.136 for the fluid in the SV is

$$\int_0^H \delta \frac{\partial p_m}{\partial z} \frac{\partial p_m}{\partial z} dz + \left[\left(\frac{m\pi}{B} \right)^2 - k_x^2 - \frac{\omega^2}{\alpha_f c^2} \right] \int_0^H \delta p_m p_m dz + \delta p_m \Big|_{z=0} \frac{\rho_f \omega^2}{\alpha_f W_m} u_{bm} \mu_m = 0, \quad (4.142)$$

and for the fluid in the ST is,

$$\int_{-H}^0 \delta \frac{\partial p_m}{\partial z} \frac{\partial p_m}{\partial z} dz + \left[\left(\frac{m\pi}{B} \right)^2 - k_x^2 - \frac{\omega^2}{\alpha_f c^2} \right] \int_{-H}^0 \delta p_m p_m dz - \delta p_m \Big|_{z=0} \frac{\rho_f \omega^2}{\alpha_f W_m} u_{bm} \mu_m = 0. \quad (4.143)$$

Rescale the two variational equations

$$\begin{aligned} \frac{\alpha_f W_m}{\rho_f \omega^2} \int_0^H \delta \frac{\partial p_m}{\partial z} \frac{\partial p_m}{\partial z} dz + \frac{\alpha_f W_m}{\rho_f \omega^2} \left[\left(\frac{m\pi}{B} \right)^2 - k_x^2 - \frac{\omega^2}{\alpha_f c^2} \right] \int_0^H \delta p_m p_m dz \\ + \delta p_m|_{z=0} u_{bm} \mu_m = 0, \end{aligned} \quad (4.144)$$

$$\begin{aligned} \frac{\alpha_f W_m}{\rho_f \omega^2} \int_{-H}^0 \delta \frac{\partial p_m}{\partial z} \frac{\partial p_m}{\partial z} dz + \frac{\alpha_f W_m}{\rho_f \omega^2} \left[\left(\frac{m\pi}{B} \right)^2 - k_x^2 - \frac{\omega^2}{\alpha_f c^2} \right] \int_{-H}^0 \delta p_m p_m dz \\ - \delta p_m|_{z=0} u_{bm} \mu_m = 0. \end{aligned} \quad (4.145)$$

4.2.5 The overall FEM matrix and post-processing

The entire linearized cross section model can be represented by a matrix

$$\begin{bmatrix} \mathbf{K}_p & \mathbf{Q}_{ps} & \mathbf{0} \\ \mathbf{Q}_{sp} & \mathbf{K}_s & \mathbf{Q}_{se} \\ \mathbf{0} & \mathbf{Q}_{es} & \mathbf{K}_e \end{bmatrix} \begin{bmatrix} \mathbf{p} \\ \mathbf{u} \\ \phi \end{bmatrix} = \begin{bmatrix} \mathbf{f}_p \\ \mathbf{f}_s \\ \mathbf{f}_\phi \end{bmatrix}, \quad (4.146)$$

where \mathbf{p} is a vector with all the pressure nodes (including the nodes in the TM-RL gap, in the SV/ST, and the sulcus) in a cross section; \mathbf{u} is a displacement vector given by Eq. 4.4; ϕ is the vector for the electric fields in the SV, SM, OHC, and ST (see [82] for more detail),

$$\phi = [\phi_{sv}, \phi_{sm}, \phi_{ohc}, \phi_{st}]^T. \quad (4.147)$$

\mathbf{K}_p , \mathbf{K}_s , and \mathbf{K}_e are the stiffness matrices for the pressure, structure, and electron field, respectively. The \mathbf{Q} 's matrices are the coupling matrices among different fields. \mathbf{f}_p , \mathbf{f}_s , and \mathbf{f}_ϕ are the forcing terms in each fields. To speed the matrix solving, we can condense the variables and solve \mathbf{p} , \mathbf{u} , and ϕ individually. For instance, if \mathbf{u} is the vector of primary interest, we can transform the matrix solving into

$$\mathbf{u} = (\mathbf{K}_s - \mathbf{Q}_{sp} \mathbf{K}_p^{-1} \mathbf{Q}_{ps} - \mathbf{Q}_{se} \mathbf{K}_e^{-1} \mathbf{Q}_{pe})^{-1} (\mathbf{f}_s - \mathbf{Q}_{sp} \mathbf{K}_p^{-1} \mathbf{f}_p - \mathbf{Q}_{se} \mathbf{K}_e^{-1} \mathbf{f}_e). \quad (4.148)$$

Then \mathbf{f}_p and \mathbf{f}_ϕ can be solved as,

$$\mathbf{p} = -\mathbf{K}_p^{-1} \mathbf{Q}_{ps} \mathbf{u} + \mathbf{K}_p^{-1} \mathbf{f}_p, \quad (4.149)$$

$$\phi = -\mathbf{K}_e^{-1} \mathbf{Q}_{es} \mathbf{u} + \mathbf{K}_e^{-1} \mathbf{f}_e. \quad (4.150)$$

Table 4.2: Geometric parameters for the cross sectional model.

Parameters	values
d_1	7 μm
d_2	3 μm
d_3	5 μm
g_0	1 μm (base) to 6 μm (apex)
g_{HS_0}	1.3 μm
d_{HS}	1 μm
a_{HS}	1 μm
h_{IHB_0}	1.8 μm
R_{IHB}	0.15 μm
L_{hb_2}	26 μm
L_{IHC}	66 μm
L_{tm}	86 μm (base) to 206 μm (apex)
H_s	same as L_s

After \mathbf{u} , \mathbf{p} , and ϕ being solved, all the other quantities can be obtained by post-processing. For example, we can obtain the pressure gradient at $s = L_{IHC}^-$, $(\partial p_{gap}/\partial s)|_{s=L_{IHC}^-}$, directly from Eq. 4.107. Then the IHC HB displacement, u_{IHB} , is obtained from Eq. 4.86. Now \dot{Q}_2 in Eq. 4.60 can be evaluated. Based on what we have obtained, the pressure difference across the IHC HB, Δp_{IHB} , and the viscous force on the IHC HB tip, $f_{\mu IHB}$, follow immediately from Eqs. 4.72 and 4.79, respectively. In this way, we can obtain any quantity that we have introduced in this work.

4.3 Results

In this part, we show some preliminary results of the model prediction at a cross section at $x = 4$ mm, where the best frequency is about 17 kHz. Tables 4.2 and 4.3 give lists of estimated geometric parameters (most are estimated for the $x = 4$ mm in particular) and material properties used in the model. For the parameters not listed in the tables (especially for the parameters in the electronic field), they are the same as those used in the 3-D cochlear model [82, 63, 56]. The fluid mesh in the SV/ST is 50 μm per element. The cross section is excited by a unit force on the BM (the first entry in \mathbf{f}_s in Eq. 4.146 is 1, and the rest is zero). No other force is present (both \mathbf{f}_p and \mathbf{f}_ϕ are identically zero in Eq. 4.146).

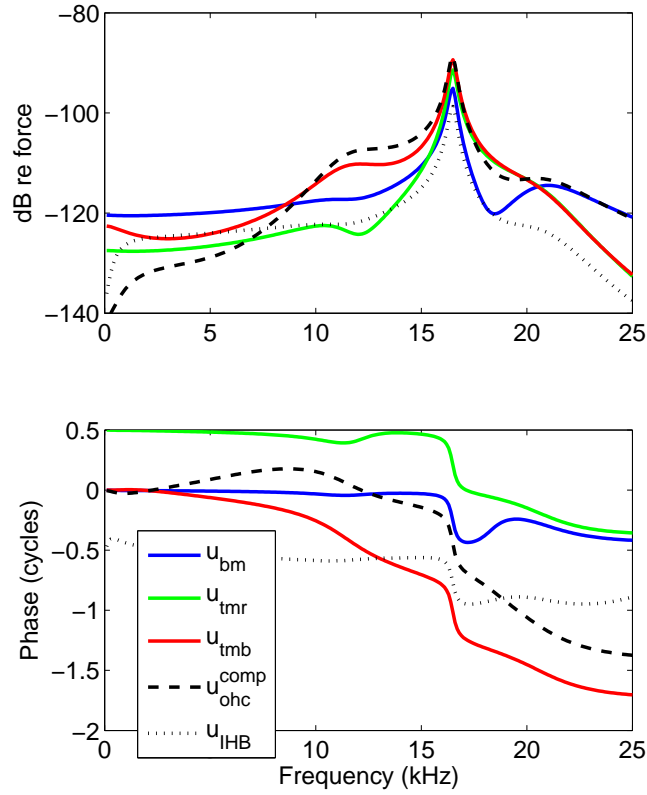


Figure 4.6: Model prediction of the spectrum amplitudes (a) and phases (b) of the BM, TM shearing ($U^s|_{s=L_{hb_2}}$), TM bending ($W^b|_{s=L_{hb_2}}$), OHC compression, and the IHC HB displacement at $x = 4$ mm with respect to a unit force on the BM.

Table 4.3: Material properties for the cross sectional model (x is in meters).

Parameters	values
K_{bm}	$4.5 \times 10^9 (h/h_0)^3 (b_0/b)^4 \text{ kg/m}^2\text{s}^2$
K_{hb}	$5.5 \times 10^4 e^{-330x} \text{ kg/ms}^2$
K_{IHB}	$5.5 \times 10^3 e^{-325x} \text{ kg/ms}^2$
K_{rl}	$5.5 \times 10^3 e^{-325x} \text{ kg/ms}^2$
K_{ohc}	$5.5 \times 10^3 e^{-325x} \text{ kg/ms}^2$
K_{tms}	$2.4 \times 10^2 e^{-300x} \text{ kg/ms}^2$
K_{tmb}	$2.4 \times 10^4 e^{-300x} \text{ kg/ms}^2$
E_{tm}^s	$1.3 \times 10^6 e^{-156.2x} \text{ kg/ms}^2$
E_{tm}^b	$1.53 \times 10^4 e^{-156.2x} \text{ kg/ms}^2$
ρ_{rm}	$1 \times 10^3 \text{ kg/m}^3$
M_{tms}	$2.08 \times 10^{-6} e^{50x} \text{ kg/m}$
M_{tmb}	$2.08 \times 10^{-6} e^{50x} \text{ kg/m}$
ζ_{tm}^s	0
ζ_{tm}^b	$0.1 \text{ kg/m}^2\text{s}$
μ	0.01 kg/ms
C_{bm}	$(1.7039/b) \text{ kg/m}^2\text{s}$
C_{tms}	0.01 kg/ms
C_{tmb}	0.5 kg/ms

4.3.1 The motion of the OoC

Figure 4.6 shows the model prediction of the spectrum responses of the BM, TM shearing ($U^s|_{s=L_{hb_2}}$), TM bending ($W^b|_{s=L_{hb_2}}$), OHC compression, and the IHC HB displacement. All the structures have similar amplitude-frequency responses, especially around the best frequency (about 17 kHz). Since our model is a cross sectional model, the characteristic of the traveling wave in the cochlea cannot be seen here. Hence, the responses are similar to a resonance system, with half-cycle phase change across the best frequency.

4.3.2 Forces on the IHC HB

Figure 4.7 shows the model prediction of the two components of the force acting on the IHC HB. The force due to the pressure difference across the IHC HB (solid line), calculated from $\Delta p_{IHB} h_{IHB_0}$ by Eq. 4.72, is predicted as positive below the best frequency and is negative above the best frequency. The phase change of the pressure difference shows that below and above the best frequency, the modes of the pressure load on the IHC HB are different. Up to the best frequency, the pressure drives the IHC HB towards the negative s direction (excitatory direction of the nerve excitation). The force due to the shear viscosity on the IHC HB tip, calculated by Eq. 4.79, is predicted to be positive,

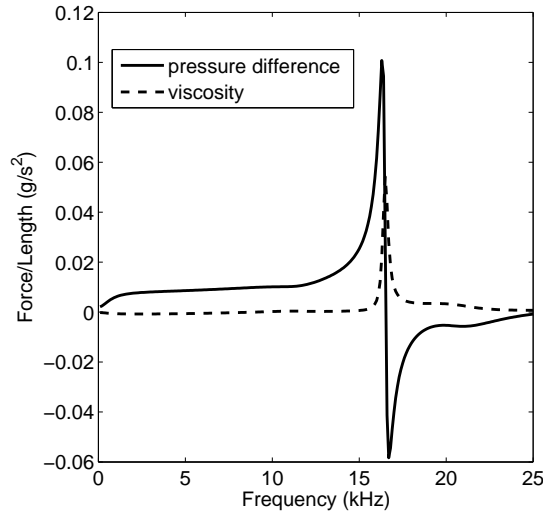


Figure 4.7: Model prediction of the spectrum forces (real part) per unit length on the IHC HB with respect to a unit force on the BM. Solid line: force on the IHC HB due to the pressure different across the IHC HB. Dashed line: force on the IHC HB due to the shear viscosity on the IHC HB tip. Both forces are small below and above the best frequency, and have larger values around the best place. The pressure difference has a phase change across the best frequency.

indicating that the fluid viscosity drags the IHC HB in the positive s direction (inhibition direction of the nerve excitation). Since the amplitude of the force coming from the pressure difference is higher than the force due to viscosity, the motion of the IHC HB is mainly dominated by the pressure difference across it. For both forces, the amplitudes are small below and above the best frequency, and have larger values around the best place.

Figure 4.8 shows the model prediction of the vertically averaged fluid velocity (real part) in the TM-RL gap at $s = L_{IBC}$. Below and above the best frequency, the fluid velocity is negligible compared to the velocity at the best frequency, indicating a sudden fluid flux when the excitation frequency crosses the best frequency of the system. The sign of the averaged fluid velocity is negative (in the excitatory direction of the nerve excitation). The predicted non-trivial fluid velocity implies that fluid motion in the thin gap is possible.

4.4 Discussion and conclusion

In this work, the viscous flow in the sub-TM region is modeled. The flow is coupled to the motion of the TM, the RL, the HBs of IHCs and OHCs, the HS, the fluid in the sulcus, and the fluid in the SV. The micro fluid is modeled in a 1-D domain running

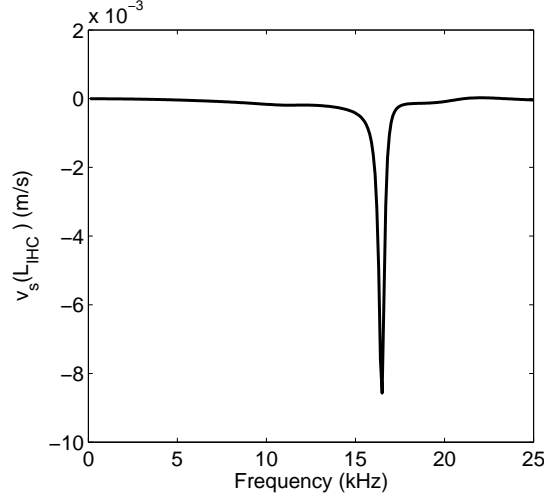


Figure 4.8: Model prediction of the spectrum vertically averaged fluid velocity (real part) in the TM-RL gap at $x = 4$ mm, $s = L_{IBC}$ with respect to a unit force on the BM. The averaged fluid velocity is small below and above the best frequency, and have a Dirac Delta function type response at the best frequency.

in the radial direction with pressure as the primary variable. The essential part of the fluid model is the derivative at the boundary of each 1-D element written in terms of the gradient of the pressure. The analytical boundary conditions are derived from the conservation of mass, which takes into account the viscous effect of the fluid, the fluid-structure interaction, the dynamics of the structures, and the complex geometry of the surrounding structures. Primary results show that although the height of the TM-RL gap is less than the viscous boundary layer thickness, fluid flow in the radial direction is still possible so as to stimulate the IHC HB. The IHC HB is mainly driven by the pressure difference across the HB. The displacement of the IHC HB has a similar profile as the displacement of the rest structures in the OoC.

The method developed here can be implemented into a 3-D cochlear model so as to provide a tool to determine the spatial dependence of flow modality in the sub-TM region; determine the relative importance of motility (either OHC somatic or HB motility) on IHC HB stimulation; analyze the role of the HS and the noise to signal ratio in the hearing, and evaluate the importance of the shearing and bending effects on the TM. In addition, the cross sectional model can be used to simulate the electromechanical experiments utilizing a cochlear segment (e.g., [6, 7, 69]).

The innovation of this work is that the model overcomes the challenge of modeling multiscale problems by combining both analytical and numerical methods. The viscous structure-fluid coupling effect on complex geometries in the IHC HB, HS, and OHC HB

is solved analytically. The analytical expressions serve as boundary conditions to the FEM model. This chapter provides a method for bridging the gaps between scales and can further be used to the global cochlear model to understand the various working mechanisms of the cochlea.

CHAPTER V

Direction of wave propagation in the cochlea for internally excited basilar membrane

Otoacoustic emissions are an indicator of a normally functioning cochlea and as such are a useful tool for non-invasive diagnosis as well as for understanding cochlear function. While these emitted waves are hypothesized to arise from active processes and exit through the cochlear fluids, neither the precise mechanism by which these emissions are generated nor the transmission pathway is completely known. With regard to the acoustic pathway, two competing hypotheses exist to explain the dominant mode of emission. One hypothesis, the backward-traveling wave hypothesis, posits that the emitted wave propagates as a coupled fluid-structure wave while the alternate hypothesis implicates a fast, compressional wave in the fluid as the main mechanism of energy transfer. In this chapter, we study the acoustic pathway for transmission of energy from the *inside* of the cochlea to the outside through a physiologically-based theoretical model. Using a well-defined, compact source of internal excitation, we predict that the emission is dominated by a backward traveling fluid-structure wave. However, in an active model of the cochlea, a forward traveling wave basal to the location of the force is possible in a limited region around the best place. Finally, the model does predict the dominance of compressional waves under a different excitation, such as an apical excitation. The model predicts von Békésy's so-called paradoxical forward traveling waves in such a case.

5.1 Introduction

Decades of theoretical and experimental studies (e.g., [78, 112, 116, 72]) have shown that external acoustic stimuli give rise to two types of intracochlear pressure waves, the compression wave (fluid-borne) and the so-called traveling wave (a coupled fluid-structure wave). The compression wave, or fast wave, travels at the speed of sound, propagating

the length of the cochlea in tens of microseconds. The traveling wave couples the fluid to the basilar membrane (BM). This wave is also called the slow wave because of its low group velocity near the location of the peak response (the best place) for a pure tone stimulation. Its group velocity is usually several hundred times slower than that of the compressional wave. Presently, there is a debate as which type of pressure wave dominates otoacoustic emissions (OAEs) from the cochlea [110]. OAEs (e.g., [54, 88, 14]) are generated by an excitation within the cochlea and emitted towards the outer ear canal [97]. As a physiological phenomenon, the distortion product OAE (DPOAE) is associated with healthy ears and has clinical applications for noninvasive diagnosis of hearing pathologies [41]. In order to use the DPOAE as an effective tool for understanding maladies and the mechanics of the cochlea, the dominant intracochlear wave type [87, 31] and the direction of wave propagation along the BM [47] of the emission must be characterized. In this chapter, we use a theoretical model of the cochlea to study how an intracochlear force acting on the BM generates an emitted disturbance at the stapes as a means to understand the acoustic pathways for emissions from the cochlea.

Experiments have been performed to determine the dominant wave type of the DPOAE [85, 87, 47, 24, 31, 32, 65], but no agreement has been reached [110]. Two contradictory hypotheses exist to explain the DP emission pattern: (1) the slow (traveling) [106, 31, 32, 65] and (2) the fast (compression) [85, 87, 47, 24] wave hypotheses. The slow-wave hypothesis states that the emission is dominated by the slow traveling wave, which travels along the BM in the backward direction, as opposed to the forward wave generated by acoustic stimuli. This hypothesis is supported by measurements of emission delays [31, 65], intracochlear pressure patterns [31, 32], and fine structures in the emission spectrum [106, 31]. The fast-wave hypothesis posits that the emission is dominated by the fast compressive wave, which rapidly propagates to the stapes after DPs are generated. This hypothesis has also been supported by multiple experiments, including the study of the BM response patterns [24, 47] and DP round-trip calculations [87]. These different experimental results and the lack of agreement reveal that the DPOAE mechanism is not completely understood. In order to analyze an experiment, assumptions regarding the DP nonlinear generation mechanism(s) and the emission process are inevitable. Of the DP generation process, the distortion product is generally hypothesized to arise from the interaction of two primary tones in a region near the best place of the higher tone [87]. However, other spatial regions may also contribute to the DP emission, and the spatial extent of the nonlinearity is unknown. Of the emission process, multiple reflection sources, such as the wave-fixed component, the place-fixed component [31], or distributed roughness of structures [117], are hypothesized to affect the emission. While the generation and emission

processes are difficult to experimentally separate, mathematical models can analyze them individually.

There is a long history of mathematical modeling of waves in the cochlea generated by external acoustic stimuli (e.g., [19]), but the intracochlear wave pattern generated by internal force excitation has not been extensively studied. In a study closely aligned to the present chapter, de Boer *et al.* [23] used a “classical” three-dimensional model [23] to predict the BM response to a localized input and to an approximation of the spatial extent of the forcing from harmonic distortions. The “classical” model found backward traveling waves dominate the emission. Sisto *et al.* [96] used a one dimensional model of the cochlear fluid coupled to a nonlinear model of the basilar membrane to study distortion product emissions. They found a negative phase slope under some choices of stapes reflectivity and of the parameters of their active model. However, these models are one duct fluid models, which do not admit all modes of fast wave propagation. Matthews and Molnar [62] built a two dimensional nonlinear BM damping model for the cochlea that coupled to the middle and external ears, and predicted the emission of a distortion component. Vetesnik *et al.* [108] used a two dimensional model of the cochlear fluids along with a nonlinear model of the outer hair cells to predict the generation of nonlinearities and their propagation from the cochlea. Each model represents the nonlinearity using differing degrees of complexity and physiological realism. In the present study, we seek to answer a somewhat simpler question, namely “how does sound leave the cochlea if the BM is excited by an internal force or pressure source?”. In this way, we avoid the complexity (and uncertainty) of the generation of the nonlinearity, allowing a greater focus on the structural acoustics of the wave propagation.

This work uses a physiologically-based cochlear model. This linear finite element model couples mechanical, electronic, and acoustical elements [82] to capture the physiological and physical characteristics of the cochlea. Fluid compressibility is included in the present model. Embedded in the model is the ability to switch activity on or off, enabling the model to represent both healthy and unhealthy cochleae, corresponding to *in vivo* and *in vitro* experimental preparations, respectively. Previous results [82, 63] show that the model’s predicted BM responses to acoustic stimuli match experimental measurements quite well. This model allows for both forward and backward directions of wave propagation and, since the model has two acoustic ducts, symmetric and antisymmetric waves are likewise admitted. Internal forces are prescribed on the BM at a selected longitudinal location. Because the forcing location is completely prescribed, the model can be used to unambiguously predict delays from the excitation region to the stapes or anywhere else in the cochlea. Hence, this model is not associated with any assumption regarding DP gen-

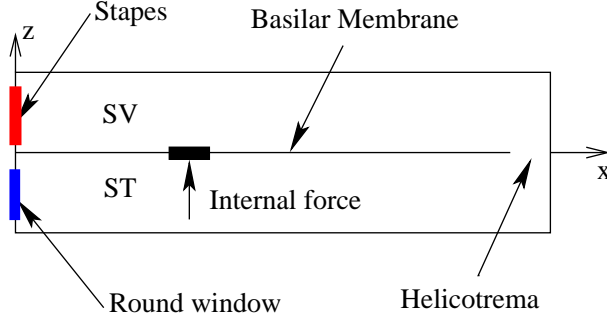


Figure 5.1: Schematic of the cochlear rectangular box model and an internal force excitation on the BM.

eration locations or wave propagation patterns; it focuses on the fundamental responses of the cochlea under a given internal disturbance.

5.2 Model description

The present mathematical cochlear model is based on a mechano-electro-acoustical three-dimensional finite element model [82] and includes a tectorial membrane (TM) model with longitudinal viscoelastic coupling [63]. Chapter II summarizes the model.

In this chapter, a known intracochlear force is used to excite the BM (Fig. 5.1). In this way, the origin of the energy is completely prescribed. This prescription contrasts the DPOAE experiments, in which the origin of the DP is uncertain. The forcing location is chosen at a central location along the cochlea in order to ease visualization. Unless otherwise specified, the center of the internal force locates on the BM at 6.5 mm from the base ($x = 6.5$ mm), where the best frequency is about 10 kHz. The uniform amplitude force has a $300 \mu\text{m}$ spatial span. Results (not illustrated) show that for such a small spatial span of the internal force, no notable difference of the normalized BM spatial responses (away from the forcing location) exists among uniform force, bell-shaped force, and even single point force excitations.

This study's finite element mesh size is the same as that in earlier work [82]: $25 \mu\text{m}$ per element in the longitudinal direction (x) and $50 \mu\text{m}$ per element in the vertical direction (z). Parameters in the model come from available guinea-pig data. Most of the parameters used in this work can be found in Ramamoorthy *et al.* [82] and Meaud and Grosh [63]. Table 5.1 gives the parameters either adjusted from or not included in the earlier work [82, 63]. The steady-state cochlear response of a fixed frequency is obtained from each single-frequency simulation. In order to compute impulse responses, frequencies are swept from 200 Hz to 500 kHz or 800 kHz (depending on the temporal resolution required) with

200 Hz increments, and then the inverse Fourier transform is applied to these frequency domain data to obtain time domain results.

5.3 Results

This section presents the results from numerical simulations of the cochlear model. Cochlear responses under the internal force excitation are compared to those under external acoustic stimuli because the latter is well established. Responses in temporal and spatial domains are emphasized because they can either identify wave arrival times or help to visualize the direction of wave propagation and the BM amplification. As an alternative method to determine the direction of wave propagation, the relative BM responses at two longitudinal locations in the frequency domain are calculated because these quantities can be measured under very similar experimental conditions [47]. In addition, the temporal stapes displacement under an excitation from the apex will be presented to study the fast wave generation in the model.

5.3.1 Impulse responses

The impulse responses of the stapes due to internal force excitation on the BM are compared to the impulse responses of the BM due to acoustic stimuli at the stapes. The onset motion of the stapes or the BM determines wave arrival times.

Fig. 5.2 compares the impulse responses of the BM at 6.5 mm under the acoustic input (thick solid lines) and the impulse responses of the stapes under the internal force on the BM at 6.5 mm (thin solid lines). Each response is normalized to its own maximum value. In Fig. 5.2 (a, c), the BM and the stapes responses overlap, and only the BM response (thick curves) is visible. Passive responses decay after ~ 0.6 msec (Fig. 5.2(a)) while active responses last for ~ 1.6 msec (Fig. 5.2(b)). Hence, the impulse responses of both the stapes (under internal excitations) and the BM (under acoustic stimuli) damp quickly in the passive cochlea and persist longer in the active cochlea. One substantive result is that the two normalized passive responses in Fig. 5.2(a) are exactly the same, and this is a consequence of structural acoustic *reciprocity* for a passive system (see Appendix G and Ref. [59]). In the active cochlea (Fig. 5.2(b)) the two wave forms do not overlap, but the arrival times of their first few peaks, valleys, and zeros are aligned. At the time scale used for Figs. 5.2(a, b), the wave form appears smooth.

As a way of determining the existence of the fast wave, the impulse response arrival times are compared to the compression wave traveling time. For the speed of sound in water, it takes about $4.3 \mu\text{s}$ for sound to travel from the stapes to the BM at 6.5 mm

Table 5.1: Material properties for the cochlear model (x is in meters).

Property	Value	Source
Speed of sound in the fluid	1500 m/s	From water
BM width (b)	80 μm (base) to 180 μm (apex)	based on [35]
BM thickness (h)	7 μm (base) to 1.7 μm (apex)	based on [35]
L_1	13 μm	Ref. [83]
L_{Ro}	40 μm	Ref. [83]
Duct length (L)	1.85 cm	Ref. [35]
Helicotrema length	0.1 cm	assumed
Stapes stiffness	$1.8 \times 10^7 \text{ N/m}^3$	assumed
Stapes damping	$5.8 \times 10^2 \text{ N}\cdot\text{s/m}^3$	assumed
Round window stiffness	$1.8 \times 10^3 \text{ N/m}^3$	assumed
Round window damping	$5.8 \times 10^2 \text{ N}\cdot\text{s/m}^3$	assumed
BM stiffness per unit area (K_{bm})	$4.498 \times 10^9 (h/h_0)^3 (b_0/b)^4 \text{ N/m}^3$	based on [45]
TM bending stiffness (K_{tmb})	$1.233 \times 10^4 e^{(-400x)} \text{ N/m}^2$	based on [118]
TM shear stiffness (K_{tms})	$1.233 \times 10^4 e^{(-400x)} \text{ N/m}^2$	assumed
RL stiffness (K_{rl})	$4.008 \times 10^3 e^{(-420x)} \text{ N/m}^2$	based on [16]
HB stiffness (K_{hb})	$1.879 \times 10^4 e^{(-420x)} \text{ N/m}^2$	estimated from [103]
OHC stiffness (K_{ohc})	$4.008 \times 10^3 e^{(-420x)} \text{ N/m}^2$	based on [46]
BM viscous damping per unit area (C_{bm})	$(0.1/b) \text{ N}\cdot\text{s/m}^3$	assumed
TM bending damping per unit length (C_{tmb})	$0.05 \text{ N}\cdot\text{s/m}^2$	assumed
TM shear damping per unit length (C_{tms})	$0.03 \text{ N}\cdot\text{s/m}^2$	assumed
Effective TM shear mass M_{tms}	$\rho_{\text{tm}} h_{\text{tm}}^0 b_{\text{tm}}^0 e^{50x} \text{ kg/m}$ $\rho_{\text{tm}} = 1000 \text{ kg/m}^3,$ $h_{\text{tm}}^0 = 18 \mu\text{m}, b_{\text{tm}}^0 = 60 \mu\text{m}$	From [82]
ψ (angle of forward inclination of the OHC)	0	assumed
δx (feed-forward distance)	0	assumed
ϵ_3	$(-1.22 \times 10^{-5} - 1.6 \times 10^{-4}x) \text{ N/m/mV}$	based on Ref. [53]
$g_a(0)$	4.0018 S/rad/m for full activity	free parameter
α (spatial decay rate of the maximum conductance)	150 m^{-1}	based on [114]
r_{st}	150 M Ω /m	based on R_{OC} in [102]

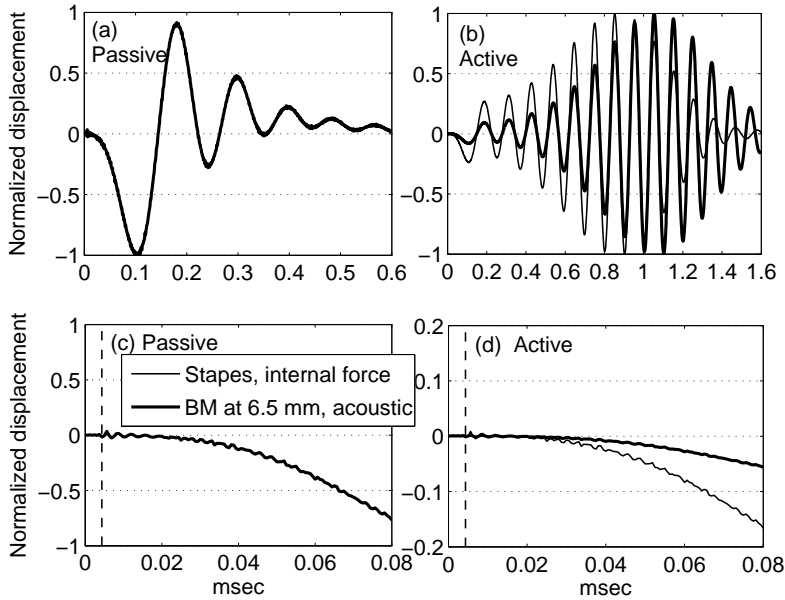


Figure 5.2: Impulse responses of the BM at 6.5 mm from the base under acoustic stimuli (thick solid lines) and the impulse responses of the stapes under internal force excitation (thin solid lines). Temporal resolution: $0.625 \mu\text{s}$. Each response is normalized to its own maximum value (normalization factors: passive acoustic, $4.887 \times 10^{-4} \mu\text{m}$; passive internal force, $6.332 \times 10^{-3} \mu\text{m}$; active acoustic, $6.455 \times 10^{-3} \mu\text{m}$; active internal force, $2.833 \times 10^{-2} \mu\text{m}$). (a) Long time scale responses of the passive model. (b) Long time scale responses of the fully active model. (c) Early temporal responses of the passive model. (d) Early temporal responses of the fully active model. The thin vertical dashed lines in (c) and (d) indicate the time for sound in water to travel from the stapes to the BM at 6.5 mm, or from the BM at 6.5 mm to the stapes. The result predicts the identical normalized passive responses under two excitation methods, and same traveling-wave arrival time for active response.

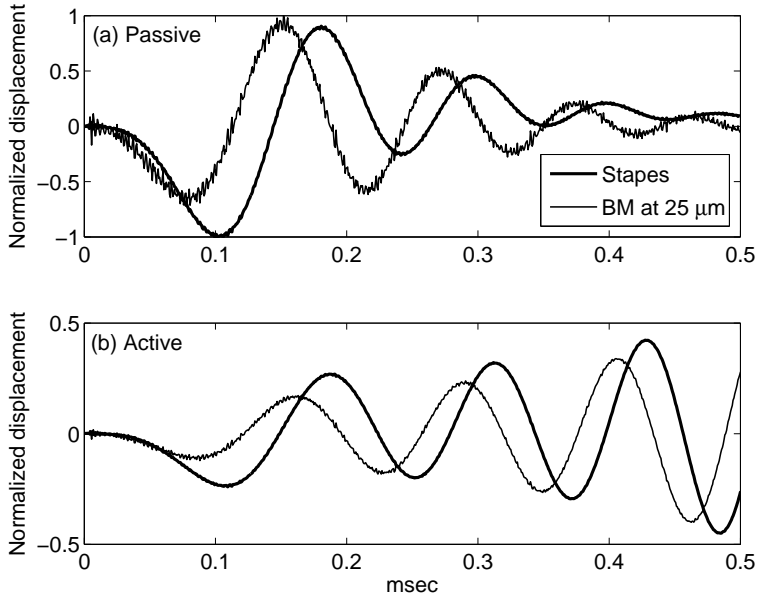


Figure 5.3: Difference between the stapes and the BM responses at $25 \mu\text{m}$ under internal force excitation. Thick solid lines: responses of the stapes. Thin solid lines: responses of the BM at $25 \mu\text{m}$ away from the stapes. Temporal resolution: $0.625 \mu\text{s}$. Each displacement is normalized to its own maximum value (normalization factors: passive stapes, $6.332 \times 10^{-3} \mu\text{m}$; passive BM at $25 \mu\text{m}$, $1.661 \mu\text{m}$; active stapes, $2.833 \times 10^{-2} \mu\text{m}$; active BM at $25 \mu\text{m}$, $12.02 \mu\text{m}$). (a) Prediction from the passive model. (b) Prediction from the fully active model. In both cases, the BM wave form leads the stapes response, indicating that the traveling wave propagates towards the base.

(or equivalently from the BM at 6.5 mm to the stapes). Fig. 5.2(c, d) indicates this time scale with vertical dashed thin lines. Both the passive and the active cases show that the stapes and the BM at 6.5 mm show small oscillations when the compression wave arrives. As can be seen in the finer time scale, the small perturbation due to the compression wave superimposes on the otherwise smooth wave form that represents the traveling-wave response. The amplitude of the perturbation is very small compared to the amplitude of the traveling-wave response.

In order to analyze the cochlear basal responses as the disturbance travels on the BM, Fig. 5.3 compares normalized impulse responses of the stapes (thick solid lines) and the BM at $25 \mu\text{m}$ away from the stapes (thin solid lines) under internal force excitation. In Fig. 5.3(a), similar to Fig. 5.2, the fast wave disturbance is a perturbation on the wave form of the traveling wave. The responses from the BM and the stapes show a similar trend, but the arrival time of the first peak of the BM at $25 \mu\text{m}$ is earlier than that of the

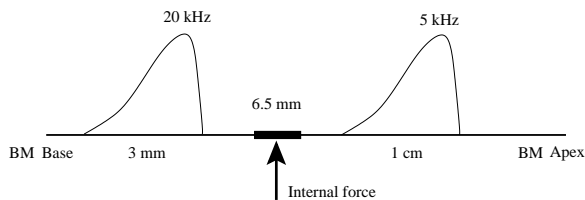


Figure 5.4: Schematic of the spatial mappings of 5 kHz and 20 kHz along with an idealization of the BM responses. The unit internal forcing is applied on the BM at 6.5 mm from the base. The best place for 5 kHz is ~ 10 mm, apical to the forcing location. The best place for 20 kHz is ~ 3 mm, basal to the forcing location.

stapes. The temporal gap between the two initial peaks of the wave forms represents the time needed for the emitted slow wave to travel from the BM at $25 \mu\text{m}$ to the stapes, which is much longer than the compression wave requires. The phenomenon is also evident in an active cochlea that the first peak/valley of the wave form of the BM at $25 \mu\text{m}$ leads the stapes (Fig. 5.3(b)).

5.3.2 Spatial response

This section presents steady-state spatial responses of the BM under internal force excitation at 6.5 mm. In the spatial (longitudinal) domain, the direction of wave propagation can be visualized from the spatial dependence of phases. Two frequencies, 5 kHz and 20 kHz, are simulated for two reasons. First, the distances between their corresponding best places (~ 10 mm and 3 mm, respectively) and the forcing place (6.5 mm) are sufficient such that there is no interaction between the forcing and the active response near the best place. Second, the response patterns for these two frequencies are representative of the generic cases when the best place is basal (20 kHz) and apical (5 kHz) of the excitation location (Fig. 5.4).

Fig. 5.5 shows the BM responses referenced to the stapes under 5 kHz internal force excitation (solid lines). For comparison, the dashed lines show the same frequency acoustic responses, and the short dashed lines indicate mirror reflections of the phases (0-6 mm) under acoustic stimuli. In the passive cochlea (Fig. 5.5 (a) and (b)), basal to the forcing place, the BM amplitude decreases as it approaches the stapes. The phase slope and value under the internal force excitation have opposite signs to those under the acoustic stimulation, but do not overlap upon mirror reflection. Apical to the forcing place, the BM amplitude peaks at the best place, just as with the acoustically induced response. The phase from the internal force excitation replicates the phase from the acoustic stimulation except that there is a one cycle offset. In the active cochlea (Fig. 5.5 (c) and (d)), basal

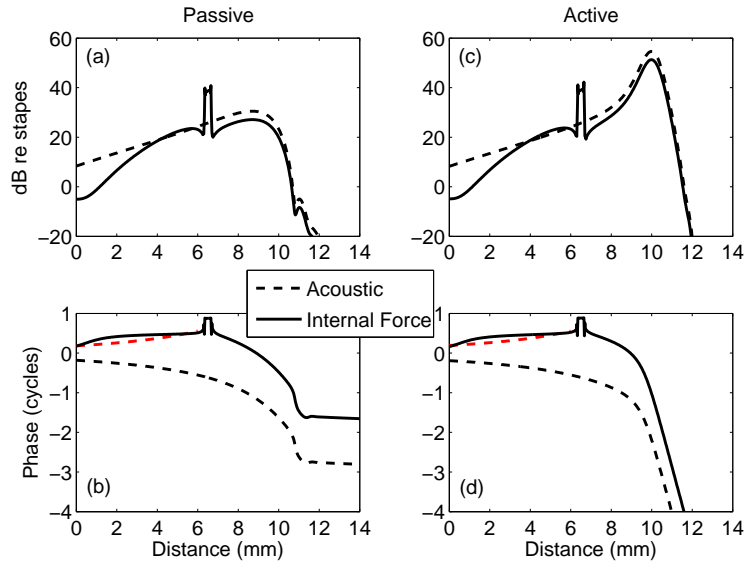


Figure 5.5: BM responses at 5 kHz under acoustic and internal force inputs. The best place is around 10 mm. Both amplitudes and phases are normalized with respect to the stapes. Solid lines: responses under the BM excitation at 6.5 mm from the base. Dashed lines: responses under acoustic stimuli. For reference, mirror reflection of the phase under acoustic stimuli for locations basal to the force (< 6 mm) is shown with short dashed lines. (a) and (b): predictions from a passive model. (c) and (d): predictions from an active model. (a) and (c): BM amplitudes referenced to the stapes. (b) and (d): BM phases in cycles. A backward-traveling wave is predicted from the response under the internal BM excitation, while a forward-traveling wave dominates the response to acoustic stimulation.

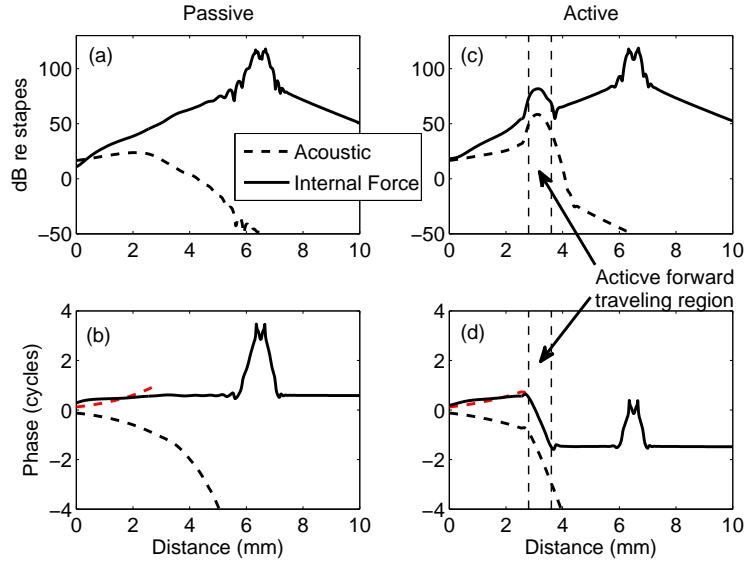


Figure 5.6: BM responses at 20 kHz under acoustic and internal force inputs. The best place is around 3 mm. Both amplitudes and phases are normalized with respect to the stapes. Solid lines: responses under the BM excitation at 6.5 mm from the base. Dashed lines: response under acoustic stimuli. For reference, mirror reflection of the phase under acoustic stimuli for locations basal to the best place (< 2.8 mm) is shown with short dashed lines. (a) and (b): predictions from a passive model. (c) and (d): predictions from an active model. (a) and (c): BM amplitudes referenced to the stapes. (b) and (d): BM phases in cycles. A backward-traveling wave, along with an active forward-traveling region (enclosed by two vertical dashed lines), is predicted from the response under the internal BM excitation.

to the forcing place, both the BM amplitude and the phase are identical to the passive cochlea (the responses in Fig. 5.5 (c) and (d) will overlap with those in Fig. 5.5 (a) and (b) if plotted together because of the small influence of activity in this region). Apical to the forcing place, the BM magnitude is amplified at the best place as is acoustic response, which is very similar to the passive cochlea. The active phase under the internal force excitation has more forward-traveling-wave phase accumulation compared to the passive phase, and is parallel to the phase under acoustic stimulation, with a one cycle offset as in the passive case.

The results predicted in Fig. 5.6 come from the same simulation parameters in Fig. 5.5 except that the excitation frequency is changed to 20 kHz. Since the response apical to the excitation region is evanescent, only locations basal to the 10 mm place are plotted. In the passive cochlea (Fig. 5.6 (a) and (b)), there is a monotonic decrease in the BM amplitude as the BM spatially approaches the stapes. The BM phase, shows a small

backward-wave slope, is, however, almost flat. Hence, the response is dominated by the evanescent decay from the excitation region and is very different in amplitude and phase from the acoustic response (shown in dashed lines). In the active cochlea (Fig. 5.6 (c) and (d)), the best place becomes visible within a restricted region (from 2.8 mm to 3.6 mm as enclosed by two vertical dashed lines), with the BM magnitude amplified and the phase accumulated as a forward traveling wave. Basal to the best place region, like Fig. 5.5, the phase and the slope of the phase elicited by internal force excitation have opposite signs to those under acoustic stimulation. Apical to the best place region, the phase is a constant and thus does not continue to accumulate. Hence, under the internal force excitation the forward wave pattern is limited to the best place region, and thus is a local phenomenon as opposed to the global forward wave under the acoustic stimulation. Since this best place region only appears in the active cochlea, hereafter it is defined as the “active forward-traveling-wave region”.

5.3.3 Variation of stimulus frequencies

In Figs. 5.5 and 5.6, since the best places of stimulus frequencies are far away from 6.5 mm, no strong interaction is observed between the force and the BM amplification near the best place. However, interaction between the BM tuning and the internal force may occur when these two locations are overlapping or close. Fig. 5.7 shows the active BM spatial responses referenced to the stapes under internal force excitation at 6.5 mm with different stimulus frequencies that are close to 10 kHz, the best frequency at 6.5 mm. In the amplitude panel, irregularities such as multiple peaks and notches appear basal and close to the forcing place. Notches beyond the best place, where the amplitude of the BM vibration decays quickly, are a manifestation of the interaction of the first wavenumber locus (corresponding to the traveling wave) as it cuts off with the second root locus as it cuts in [75, 109]. Localized evanescent fields can be seen around the forcing location, especially for the 13 kHz case. Notches designated by arrows in Fig. 5.7 (a) indicate the interaction between forward and backward waves basal to the forcing location. In the phase panel, at the very base, waves of all frequencies propagate backwards in a similar manner; at the best place of each excitation frequency, a forward traveling wave is identified; basal and close to the forcing place, irregularities in phase happen as well. Comparison between the amplitudes and the phases shows that whenever a ‘notch’ (coming from the interaction of waves from two directions) appears in the amplitude, a corresponding half cycle jump appears in the phase. These characteristics of irregularity in the amplitude and in the phase suggest the existence of evanescent waves and the interaction of waves from two directions.

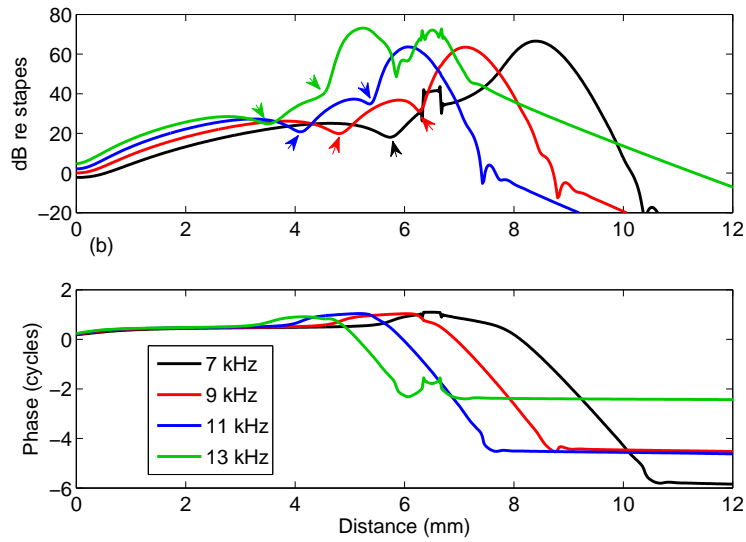


Figure 5.7: Active BM spatial responses under unit force excitation on the BM at 6.5 mm with different stimulus frequencies. The best places of 7 kHz, 9 kHz, 11 kHz, and 13 kHz excitations are, respectively, around 8.5 mm, 7.1 mm, 6.0 mm, and 5.3 mm (from our active model prediction). Both BM amplitudes (a) and phases (b) are normalized to the motion of the stapes. BM amplitude ‘notches’ from wave interaction in two directions are denoted by arrows; these ‘notches’ correspond to half-cycle phase jumps. Waves basal to the forcing place are dominated by backward-traveling waves, with the appearance of a forward-traveling region if the excitation frequency is higher than the best frequencies of the forcing place (e.g., for 11 kHz and 13 kHz).

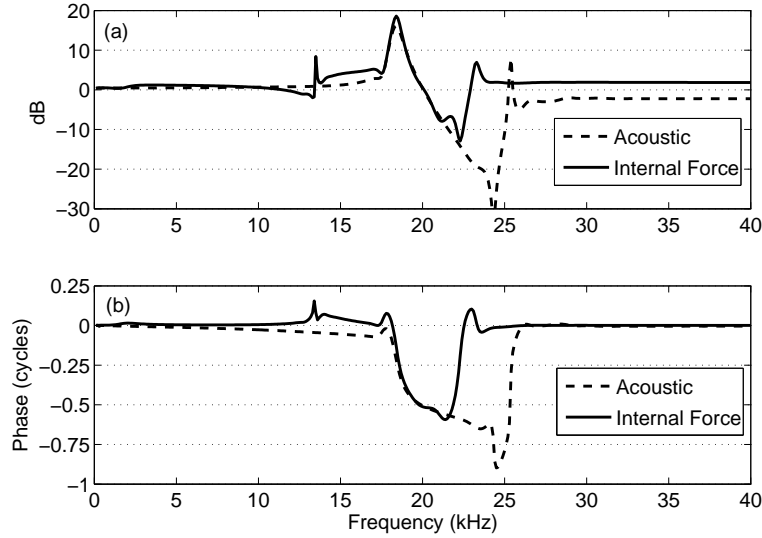


Figure 5.8: The relative active BM amplitudes (a) and phases (b) at the 3.2 mm place relative to the 3.0 mm place under a unit internal force excitation on the BM at 6.5 mm (solid lines). The same relative response under an acoustic stimulation is plotted for comparison (dashed lines). The best frequencies at 3.0 mm and 3.2 mm are 20.3 kHz and 19.5 kHz (from our active model prediction), respectively. Negative phase values indicate that the wave travels forward, and conversely for positive phase.

5.3.4 Relative response at two locations

Although temporal and steady-state spatial responses have provided much information on the emitted wave direction, it is always helpful to directly compare the steady-state motions of two nearby longitudinal locations on the BM to investigate their relative responses, as this comparison can be experimentally achieved as well [47]. Fig. 5.8 shows the relative active BM response between 3.2 mm and 3.0 mm (3.2 mm referenced to 3.0 mm, the best frequencies at 3.0 mm and 3.2 mm are 20.3 kHz and 19.5 kHz, respectively) under the internal force excitation on the BM at 6.5 mm (solid lines). The same relative response under the acoustic stimulation is included for comparison (dashed lines). Since the relative amplitude is in a dB scale, a positive value indicates that the amplitude of the BM at 3.2 mm is higher than that at 3.0 mm; for the relative phase, a negative value indicates that the BM at 3.2 mm lags the BM at 3.0 mm and the wave propagates forwards. For almost all frequencies less than 22 kHz, the relative amplitudes of the two locations due to the two excitation methods are identical (the main exception is at 13.5 kHz). Above 25 kHz, as is expected from Fig. 5.6 (c), the relative amplitude under internal force excitation is always positive. In the phase panel, below 18 kHz under internal

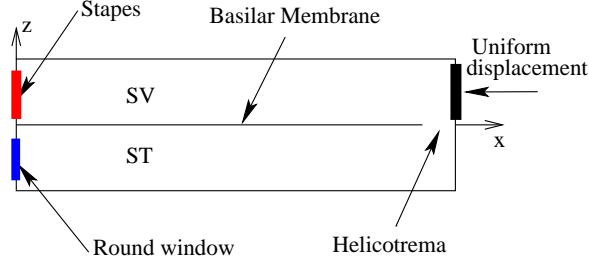


Figure 5.9: Schematic of the cochlear apex excitation model.

force excitation, the wave propagates backwards from 3.2 mm to 3.0 mm as indicated by the negative relative phase, which is opposite to that under acoustic stimulation. Between 18-22 kHz, the relative phases under two excitation methods are almost identical, showing that the locally generated active response at the best place under the internal force excitation is the same as the global forward traveling wave under the acoustic stimulation. Hence, a forward traveling wave is observed when stimulus frequencies are close to the best frequencies of 3.0 mm and 3.2 mm. Above 23 kHz, under the internal force excitation, the BM at 3.2 mm moves in phase with the BM at 3.0 mm, which is consistent with the flat phase apical to the “active forward-traveling wave region” in Fig. 5.6 (d).

5.3.5 Apex excitation

In an effort to generate non-negligible compression waves in the model, an apical displacement excitation (as shown in Fig. 5.9) is modeled. Here the “non-negligible” refers to a large compression wave that is able to generate a forward traveling wave from the reflection at the stapes. The entire cochlear length is 19.5 mm, and sound takes $13 \mu\text{s}$ to travel from the apex to the stapes.

Since the cochlear model is linear, the maximum displacement of the stapes is proportional to the apex displacement input. In Fig. 5.10 (a), the time scale is chosen to show the decay of a periodic train of impulses. In Fig. 5.10 (b), a magnified view shows that the first impulse arrives at $13 \mu\text{s}$ (as indicated by the dashed line) and the successive impulses are at $26 \mu\text{s}$ intervals, the round trip time for a compressional wave.

Fig. 5.10 (c, d) shows the prediction of the active steady-state spatial response of the BM referenced to the stapes under a 20 kHz apex input. Both the amplitude in Fig. 5.10 (c) and the phase in Fig. 5.10 (d) show a forward-traveling wave that peaks at the 3 mm best place. The BM response in Fig. 5.10 (c, d) is different from the active internal force response in Fig. 5.6 where only a small region of forward-traveling wave is found at the best place. Indeed, the spatial BM response under the apex input is almost identical to that under acoustic stimuli. The high BM amplitude in Fig. 5.10 (d) near the apical

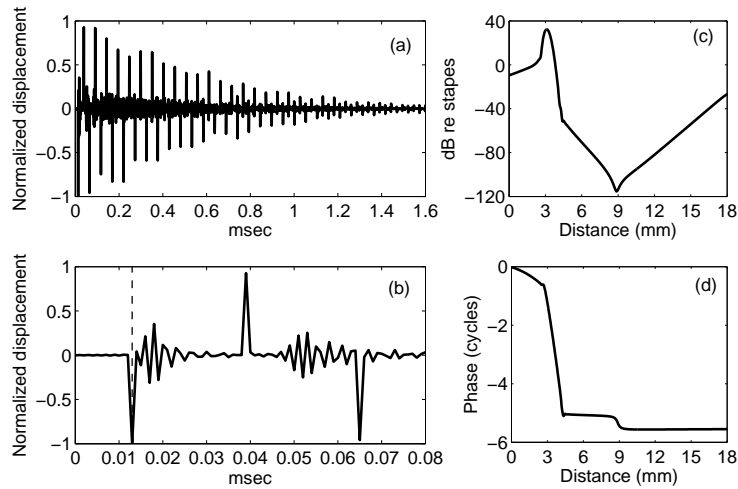


Figure 5.10: Cochlear responses under the apex input. (a, b). Normalized impulse responses of the stapes under the apex excitation. Temporal resolution: $1 \mu\text{s}$. (a). Long time scale response of the active model. (b). A copy of (a) that emphasizes short time scale response of the active model. The thin vertical dashed line in (b) indicates the time ($13 \mu\text{s}$) for sound in water to travel from the cochlear apex to the stapes. (c, d). The active steady-state spatial response of the BM referenced to the stapes under 20 kHz apex input. The best place is around 3 mm. (c). Amplitude in dB. (d) Phase in cycles. The motion of the stapes is induced by the compression wave, and the forward-traveling wave exists in the entire cochlea.

region is due to the input source at the apex.

5.4 Discussion

5.4.1 Reciprocity and traveling times

The passive impulse response at the 6.5 mm location arising from stapes excitation is identical to the impulse response of the stapes due to a localized force at the 6.5 mm location, as shown in Fig. 5.2 (a). This is a manifestation of structural acoustic reciprocity [59] (see the Appendix G for a derivation). The impulse response represents energy from all frequencies, and the reciprocity relation holds for time-harmonic forcing as well. Puria *et al.* [80] performed the reciprocity experiment in human cadaver cochleae in the frequency domain and found that the forward and backward group delays were nearly identical, in accordance with the structural acoustic reciprocity relation.

Unlike the passive cochlea, the response of an active cochlea does not exhibit reciprocity under the two excitations, as seen in Fig. 5.2 (b). The deflection of the OHC stereocilia contributes to the stereocilia current but not to the force, thereby breaking the symmetric coupling between the structural and electronic elements in the model [82]. However, the first few peaks, valleys, and zeros of their wave-form responses are aligned, as seen in Fig. 5.2, which shows that it takes very nearly the same amount of time for the BM at 6.5 mm to respond to the traveling wave under acoustic stimuli and the stapes to respond under internal BM force excitation at 6.5 mm. Therefore, the linear active cochlear model bears a symmetric traveling-wave-responding time scale with respect to two excitation methods. Note that even when hair-bundle forcing is included in the model, the coupling is still not symmetric [64].

The group delay from the internal force to the stapes at the ~ 10 kHz best frequency of an active cochlea (100 Hz frequency resolution) is 0.895 ms (computed from derivative of the phase of the transfer function in the frequency domain [not shown]). This is less than the 1.12 ms forward group delay from the acoustic stimulation to the BM at 6.5 mm (figure not shown). The group delay represents the amount of time required for the peak of the energy in a frequency band to propagate in a given distance. This energy travel time is nicely shown in Fig. 5.2(b) where the peak of the stapes-induced vibration on the BM occurs at ~ 1.12 ms (just as predicted by the group delay calculation). Similarly, the peak of the vibration of the stapes due to the internal force is predicted by the group delay. Similar to common usage in signal analysis [74], Siegel *et al.* [95] also analyzed the time scale of group delays at best frequencies and referred to it as the “center of gravity” of impulse responses. If the BM at 6.5 mm is excited by a single point force instead of

a 300 μm uniform force, the backward group delay increases to 1.08 ms. This increase shows that a smaller spatial span of the internal force increases the backward group delays because the spatial locations with shorter time delays are no longer encompassed by the force. The (small) 40 μs difference between the forward 1.12 ms and the backward 1.08 ms is due to the non-reciprocal relation in the active cochlea by the MET function. Nevertheless, both the predicted backward group delay under internal force excitation and the predicted forward group delay under the acoustic stimulation, which are 200-300 times slower than the 4.3 μs compression wave traveling time, are comparable with the group-delay trend lines from experiments on guinea-pigs [92]. Therefore, the emitted wave under an internal force excitation is dominated by a traveling wave.

For the passive cochlea, the predicted group delay is 0.15 ms as directly read from the peak in Fig. 5.2. This delay is consistent with the analytical transient time given by Peterson and Bogert (from Eq. 17 in Ref. [78]) for only the antisymmetric (slow) wave, which predicts 0.156 ms based on the 10 kHz best frequency at 6.5 mm. The similarity of these two solutions indicates that the largest contribution to the response in Fig. 5.2 comes from the slow wave.

5.4.2 The response to internal force excitation is dominated by backward traveling waves

One of the most straightforward ways to visualize the direction of wave propagation inside the cochlea is to obtain the spatial phase accumulation along the BM, as presented in Figs. 5.5 and 5.6. The slope of the phase indicates the dominant direction of wave propagation. As can be seen in Fig. 5.5, when the forcing region is basal to the best place of the stimulus frequency, a forward-traveling wave occurs with the same phase slope as an acoustically excited traveling wave. Basal to the forcing location, the solution is dominated by a backward wave even for the active case, but this wave is not a purely negative going wave as the phase is not simply the reflection of the spatial phase of the acoustically excited wave (compare the short dashed lines to the solid lines in Figs. 5.5 (b) and (d)). de Boer *et al.* [23] used a different mathematical model and obtained the same result as our's (Fig. 2 in Ref. [23]). In that model, the BM impedance was locally determined by the inverse-solution method based on experimental data. An active DP generated pressure amplitude was constructed to represent the DP force origin. Their predicted “left-going wave” and the “right-going wave” are exactly the backward (basal to the forcing place) and the forward (apical to the forcing place) waves predicted in Fig. 5.5, respectively. This forward or “right-going” wave is different from the forward wave found by Ren's group [47], who attributed the forward wave that traveled from the

stapes to the DP generation place to the dominant emitted fast wave.

In Fig. 5.6, the best place of the stimulus frequency is basal to the forcing place. In the passive cochlea, the almost flat phase indicates an evanescent wave emanating from the force. In the active cochlea, an evanescent disturbance reached the best place from the forcing location. This disturbance gives rise to an “active forward traveling region”. In this region, electromotility locally generates a *forward* traveling wave. Our model predicts that basal to the best place, this locally generated wave travels back to the stapes with a spatial phase that is almost a perfect mirror replica of the acoustically-induced forward wave.

The direction of wave propagation apical to the forcing place is not controversial; the main uncertainty lies in the region basal to the forcing place. The impulse response of the stapes and at a location $25\ \mu\text{m}$ away from the stapes due to a force at 6.5 mm show that the BM wave-form response leads the stapes response (Fig. 5.3). This implies that a backward traveling wave propagates along the BM. Hence, the wave motion of the BM is not induced by the stapes; otherwise, the BM would respond later than the stapes. Backward wave propagation in the region basal to the “active forward-traveling region” can also be seen for frequencies less than 18 kHz in Fig. 5.8. In this figure, the phase of the nearby locations is used to infer the direction of wave propagation, as used experimentally by Ren’s group [47]. The irregularities in the phase and amplitudes below 18 kHz in Fig. 5.8 arise from the interaction of the reverse-going evanescent wave and the locally generated forward going wave (see the notch in the spatial pattern beyond the “active forward traveling region” designated by the dashed vertical lines in Fig. 5.6 (c) as well as the notches in Fig. 5.7). These waves are not really standing waves as the reverse-going “wave” is evanescent in this case (as the excitation frequency is greater than the best frequency of the excitation location).

5.4.3 Forward traveling waves basal to the excitation location are possible

As discussed, the model shows that under the internal BM force excitation, the dominant emitted wave is the backward traveling wave. However, this dominant backward traveling wave does not exclude the existence of a forward traveling wave in the cochlea. One main finding in this chapter is that, as predicted in Fig. 5.6, an “active forward traveling region” is locally (at the best place) possible. Fig. 5.6 is a typical representation of the case when the forcing region does not overlap with the best place of the stimulus frequency. As shown in Fig. 5.7, a region of forward propagation is a robust prediction for the active model when the excitation frequency is greater than the best frequency of the forcing location. We also varied the location of the forces and found the same

phenomenon. For the internally excited cochlea, changing the impedance of the stapes modifies the reflectivity of the model at the boundary. But in our model, even when the impedance of the stapes is increased or reduced by three orders, the predicted BM phase is almost identical to Fig. 5.6 (result not shown). Thus, the local active generation and the backward wave basal to the best place are intrinsic phenomena in our model. In Sisto *et al.*'s [96] model, however, the reflection of the stapes plays an important role on the direction of wave propagation because the reflexivity of the stapes directly couples to the traveling wave in the 1-d model.

5.4.4 When does the non-negligible compression wave exist?

A non-negligible compressional wave will be generated in our model when some form of volumetric energy is injected into the cochlea. For instance, acoustically excited stapes motion generates a fast wave [72]; displacement excitation at the apex (as shown in Fig. 5.9) gives rise to both a pronounced fast wave (see Fig. 5.10 (a, b)) and a forward traveling wave (see Fig. 5.10 (c, d)). Our results show that localized forcing of the BM does not strongly couple to a compressional mode in the two cochlear channels. Indeed, forcing the BM in our model mainly couples to a pressure *difference* in the SV and ST (where there is a pressure jump across the boundary), generating a motion that is nearly orthogonal to the fast wave which has a constant pressure profile in the cochlear cross section. Spatial plots of intracochlear pressure show that, indeed, acoustic stimulation gives rise to symmetric pressure that is of the same order of magnitude of the traveling-wave pressure, and the symmetric pressure is negligible under internal force excitation (results not shown). We also investigated the influence of the relative impedance of the stapes and the round window on the compression wave by adjusting the two impedances. When the two impedances are the same, no compression wave exists in the cochlea under internal BM force excitation (results not shown), which further confirmed that localized forcing of the BM is not essentially associated with volumetric energy injection.

In order to explore alternative means for exciting pronounced fast waves in the cochlea, we used point acoustic sources at the 6.5 mm location. If a single pressure source is placed in the SV, this pressure input acts as a net fluid volume source that launches a compression wave in the cochlea (the compression wave was verified by calculating the temporal response of the intracochlear pressure, and a similar result to Fig. 5.10 is obtained), resulting in a forward-traveling wave on the BM. The direction of propagation of this wave is strongly influenced by the impedance of the stapes and the round window (result not shown), a result consistent with Sisto *et al.*'s [96] result. However, if a dipole pressure source is present (i.e., one positive pressure node in the SV and one negative

pressure node in the ST), the fluid volume change is canceled and no compression wave is generated. In the latter case, the dominant emitted wave is still the slow backward-traveling wave (result not shown).

5.4.5 Implications on the DPOAE

When two primary tones (f_1, f_2) are presented to the cochlea, DPOAEs are generated at frequencies corresponding to algebraic combinations of the two primaries, notably $2f_1 - f_2$, $2f_2 - f_1$ with $f_2 > f_1$. It is often hypothesized that the DP is generated near the f_2 best place [87] as the amplitudes of the two primaries maximally overlap in this region. In the experiments from Ren's group reported in Ref. [47], the BM vibration at two nearby locations on the BM (separated by $196 \mu\text{m}$) was measured at the $2f_1 - f_2$ DP frequency in response to acoustic stimulus at the two primaries. For $2f_1 - f_2$ frequencies below the best frequency of the most apical measurement location, we would expect a positive phase slope indicating a backward traveling wave. As indicated by the dashed lines in Fig. 2(B,D) in Ref. [47], the measured phase instead showed a negative phase slope for emissions at these frequencies, indicating the dominance of a forward traveling wave. If the DP generation site $2f_1 - f_2$ is near the f_2 best place, then the forcing location is basal to the best place for that frequency (as $2f_1 - f_2 < f_2$). This replicates the situation shown in Fig. 5.5, where for a localized force, backward traveling waves are predicted to dominate. The intention of this chapter is not to simulate the forcing from a DP. However, if the region of forcing was extended to the base (as a uniform force), then forward traveling waves are predicted by our model. The forcing at the DP frequency arising from the nonlinear interaction of the primaries is likely more complicated (with variable phases and amplitudes). Sisto *et al.* [96] were able to control the width of the region of the DP force generation in a nonlinear cochlear model by varying the model parameters. They found that forward propagation waves could be generated by the DP if the activity was sufficiently broad and the reflectivity of the stapes was realistic. Although the model of Sisto *et al.* [96] is incomplete as it does not admit fast waves in the same way as a more complete two-duct model does (either an elegant post-processing step, as in Yoon *et al.* [112] or our more straightforward approach would be needed to include this effect), it nicely points out that when activity is present an internal force can generate forward traveling waves. Our model predicts such a situation when the best place of the stimulus frequency is apical to the force (see Fig. 5.5).

In this work, the calculated group delays in an active cochlear model show that the backward delay from the forcing place to the stapes is similar to that from the stapes to the forcing place under acoustic stimuli. Therefore, the predicted intracochlear round trip

delay is approximately twice the forward group delay. However, Ren *et al.*'s [87] measurement showed that the intracochlear round trip delay was even less than the forward delay at the f_2 best place. The interpretation was: the DP generation place was slightly basal to the f_2 best place (the hypothesized DP generation place) so that the actual forward delays was less than what was expected, and the emitted wave was the compression wave. Our model shows that without volumetric energy, no remarkable compression wave will be generated. But our model does show that if the forcing place spreads a wide range, the backward delay is reduced. Hence, Ren *et al.*'s round trip measurement may indicate a more complicated DP source than it is hypothesized, e.g., it may spreads wide basal to the f_2 best place (as consistent with what has discussed above as hypothesized by Sisto *et al.* [96]). Indeed, the notion of a more basal DP generation region has now been widely hypothesized [87, 65, 61]. Alternatively, some, as yet unidentified, source of volumetric change in the cochlear structures could also give rise to a fast wave.

5.5 Conclusion

In this work, the emitted wave type is studied under a prescribed internal force excitation on the BM. In this way, the location of the generated energy is known. The temporal response of the stapes and the spatial response of the BM indicate that the emitted wave is a traveling wave. Little compression wave is present under an internal force on the BM. However, under an apical excitation, a compression wave is launched, and thus the emitted wave is a compression wave. In this case, as initiated by the motion of the stapes, the traveling wave in the cochlea still propagates from the base to the apex. The condition of generating fast waves in the cochlea is also identified, i.e., must have sources that contribute to volumetric changes of the intracochlear fluid. In a passive cochlea, the principle of reciprocity holds because the final linear FEM matrix is symmetric. A structural acoustic formulation is also derived to prove the reciprocity (see Appendix G).

The innovation of this work is using numerical experiments to study the emitted wave types for prescribed excitations, as well as the proof of structural acoustic reciprocity in a passive cochlea. In addition, we showed that intracochlear volumetric change is required in order to generate a compression wave.

CHAPTER VI

The coda of the transient response in a sensitive cochlea

In a sensitive cochlea, the basilar membrane (BM) velocity response due to transient external acoustic excitation or to localized transient internal bipolar electrical excitation gives rise not only to a primary impulse response, but also to a coda of delayed secondary responses (sometimes called echoes or ringing) with varying amplitudes but similar spectral content around the best frequency of the measurement location. The coda is physiologically vulnerable, disappearing when the cochlea is compromised even slightly. The multicomponent sensitive response is not yet completely understood. We use a mathematical model to describe how the response at the point of excitation can be traced back to three sources. Surprisingly, the first BM response is due to a fast wave emergent from the point of excitation, reflected by the stapes and then repropagated (in amplified fashion) as a traveling wave back to the point of excitation; the second is due to a reverse, slow, traveling wave which is likewise reflected at the stapes back to the measurement location by the stapes. The coda is also due to systematic (not random) perturbations of the organ of Corti properties. Implications for normal hearing and for the interpretation of otoacoustic emissions are discussed.

6.1 Introduction

In a sensitive cochlea, the basilar membrane (BM) velocity response due to transient external acoustic excitation or to localized transient internal bipolar electrical excitation gives rise not only to a primary impulse response, but also to a coda of delayed secondary responses (sometimes called echoes or ringing) with varying amplitudes but similar spectral content around the best frequency of the measurement location [77, 71, 22, 115]. The coda is physiologically vulnerable, disappearing when the cochlea is compromised even

slightly. The multicomponent sensitive response is not yet completely understood. In this work, we use a mathematical model to describe how the response at the point of excitation can be traced back to three sources.

6.2 Method

The mathematical model is a linear, physiologically-based mechano-electro-acoustical finite element model [82, 63]. The model includes the following components: compressible fluid, kinematics and kinetics of the organ of Corti (OoC), dynamics of the tectorial membrane (TM) and the BM, a longitudinally coupled viscoelastic model of the TM, longitudinal coupling of the electric cables in the scala vestibuli (SV) and scala tympani (ST), electromotility of the outer hair cells, and conductance of the stereocilia.

This study’s finite element mesh is the same as that used before [56]. Parameters in the model is from guinea-pig. Most of the parameters used in this work can be found in Li and Grosh [56], with the stiffness of the oval window adjusted to 1.8×10^7 N/m³ [90], and the stiffness of the round window adjusted to 1.8×10^6 N/m³ [111]. The impulse response is obtained in the same way as described in [56]. In this work, frequencies are swept from 200 Hz to 80 kHz with 200 Hz increments.

Both acoustic and internal force/pressure [56] simulations are used. We use two means of local intracochlear stimulation. The first is to apply a point force directly to the BM and the second means consists of two localized point fluid pressure sources, one in the ST and the other in the SV (see Fig. 6.1). Both pressure nodes are attached to the BM (with the same vertical coordinate). Denote the amplitudes of the pressure sources in the ST and SV as p^- and p^+ , respectively. The amplitudes of the two pressure sources may be varied to control the amount of symmetric ($p^- : p^+ = 1 : 1$) and asymmetric ($p^- : p^+ \neq 1 : 1$) excitation present. Unless otherwise specified, the location of the internal force or pressure is at $x = 4$ mm, where the best frequency is about 17 kHz in the guinea-pig. The BM responses we are interested in is also at 4 mm.

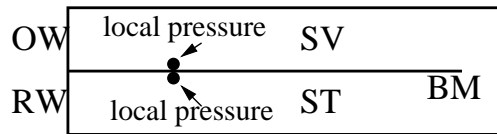


Figure 6.1: Schematic of the rectangular cochlear model. The internal pressure sources are denoted by solid dots pointed by arrows. OW: oval window. RW: round window. SV: Scala Vestibuli. ST: Scala Tympani. BM: basilar membrane.

To perturb the impedance of the cochlear partition, a filtered roughness [94, 22] is

superimposed onto the otherwise smooth mechano-electrical transducer (MET) sensitivity. To create filtered roughness, the raw roughness is randomly generated by MATLAB, and then Fourier transformed into the wavenumber domain. All the information corresponding to $\lambda < \lambda_0$ (here λ_0 is a fixed value, we use $\lambda_0 = 200\mu\text{m}$) is truncated (replaced by 0). The truncated series is then inverse Fourier transformed to the spatial domain as a filtered roughness.

For the purpose of clear illustration, we will also use a designed roughness with certain wavelength. A 1% level of such a designed roughness is defined as

$$r = \left(0.01\sqrt{2}\right) \sin\left(\frac{2\pi}{\lambda(x)/2}x\right), \quad (6.1)$$

where x is the longitudinal coordinate along the cochlea. $\lambda(x)$ is a function of the wavelengths at the best place for any given frequency. For example, the best frequency of 17 kHz in a guinea pig model is about 4 mm; then $\lambda(4\text{ mm})$ gives the wavelength of the BM at 4 mm under 17 kHz acoustic stimulation. Unless otherwise specified, we will use 0.05% roughness in this work.

6.3 Results

6.3.1 Unperturbed responses

In this part we will show the cochlear responses with smooth parameters.

Figure 6.2 shows the predicted normalized active BM temporal responses at 4 mm under acoustic [Fig. 6.2(a)] and a pair of symmetric internal pressure sources [Fig. 6.2(b)]. The gray curve in Fig. 6.2(b) is copied from Fig. 6.2(a) so that the two responses can be easily compared. The active BM responses at 4 mm has a group delay of ~ 0.7 msec under both acoustic and symmetric internal pressure simulations. The negligible delay difference between the pressure and the acoustic simulation [see Fig. 6.2(b)] comes from the compression wave travels from the location of the pressure sources to the stapes. We will use t_g , which is about 0.7 msec, to denote the forward group delay at $x = 4$ mm under acoustic simulation in a fully active model. In Fig. 6.2(b), the BM does not show an initial response at $t = 0$ because the net force on the BM is balanced by the pair of symmetric pressure sources.

Figure 6.3 shows the predicted normalized active BM temporal response at 4 mm under an internal point force on the BM at 4 mm. Since the internal force excitation does not typically generate a fast wave in the cochlea [56], the BM (at 4 mm) does not respond at t_g , as can be seen in the figure. Rather, the BM responds at $2t_g$, showing a round

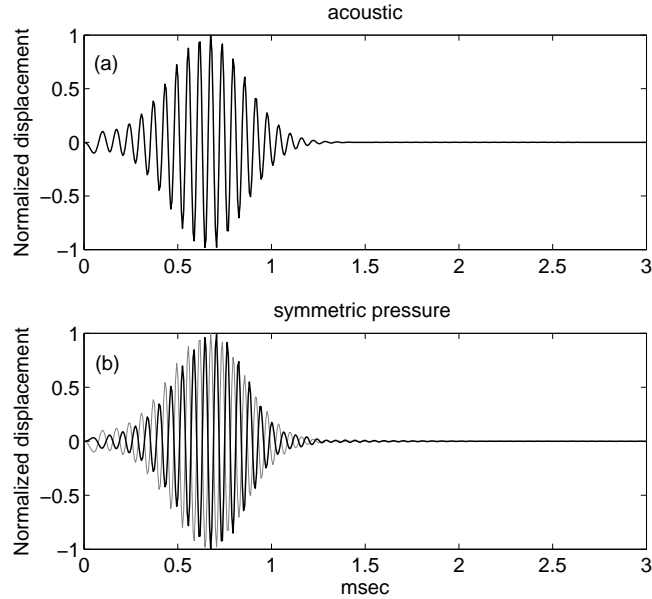


Figure 6.2: Normalized active BM temporal responses at 4 mm under acoustic (a) and a pair of symmetric internal pressure sources (b). The gray curve in (b) is the acoustic response copied from (a) for easy comparison. The two responses has the same group delay of ~ 0.7 msec.

trip of a traveling wave from the forcing place to the cochlear base, and then back to the forcing place. Unlike the symmetric pressure source stimulation shown in Fig. 6.2(b), the BM response under internal force stimulation has a large initial peak at $t = 0$ due to the forcing. However, there is no significant oscillation (or ringing) following directly from the initial response.

Figure 6.4 shows the predicted normalized BM temporal response at 4 mm under an internal pressure source beneath the BM at 4 mm ($p^- : p^+ = 1 : 0$) for different activity levels. Since a pressure source on one side of the BM applies a net force on it, the BM response is similar to the response under a point force [compare Fig. 6.4(a) and Fig. 6.3], having a wave at $2t_g$. An intracochlear pressure source also generates a compression wave in the cochlea [Fig. 6.2(b), see also Ref. [56]]; the BM responds to the compression wave at t_g . In Fig. 6.4(a), the wave form at $2t_g$ is not symmetric (unlike the wave form in Fig. 6.3, which is symmetric); the response at $t < 2t_g$ is slightly wider and higher, which is due to the small response at t_g . When the pressure source is vertically moving away from the BM, the peak at t_g will start to dominate and the peak at $2t_g$ will be relatively smaller then (results not shown). Although the activity levels are different, the amplitude of the initial peak at $t = 0$ is almost a constant (see the caption of Fig. 6.4), and no

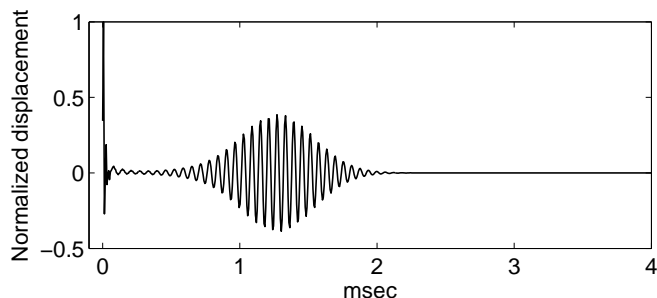


Figure 6.3: Normalized active BM temporal response at 4 mm under an internal point force on the BM at 4 mm.

significant oscillation follows the peaks, either. The relative amplitudes of the traveling waves decrease with decreasing activity levels. The group delays also decrease as the activities reduce.

6.3.2 Perturbed responses

The perturbed responses refer to the cochlear responses with perturbed parameters (adding roughness). We will first present results by using designed roughness (see Eq. 6.1). The results from a more general roughness (with filtering) will be presented later.

Figure 6.5 shows the normalized active BM temporal response at 4 mm with 0.05% designed perturbation (Eq. 6.1) on the MET channel. Figure 6.5(a) shows the prediction under acoustic simulation. Compared to the smooth acoustic response in Fig. 6.2 (a), in a perturbed cochlea, the BM exhibits extended ringings (or coda) following the first peak at t_g . Figure 6.5(b) shows the prediction under an internal force at 4 mm. Compared to the smooth internal force response in Fig. 6.3, in a perturbed cochlea, the BM has non-trivial oscillations before $2t_g$, as well as multiple ringings after $2t_g$. Figure 6.5(c) shows the prediction under internal pressure sources with amplitude ratio $p^- : p^+ = 1 : 0.98$. Since the pressure at the two sides of the BM is close in amplitude, the BM responses are mostly dominated by a fast wave. The non-symmetric pressure sources also results in a small net force on the BM, which sets the BM in motion at $t = 0$. The extended ringings in this case has a timing at $t_g, 3t_g, 5t_g, 7t_g, \dots$, which is also found in the experiments by Ren.

Figure 6.6 shows the BM spectrum corresponding to Fig. 6.5(c). The multiple peaks in the amplitude and the step-wise phase increasing around the best frequency are observed. Two thin solid vertical lines enclose the region of the middle peak; two thin solid horizontal lines enclose the region corresponding to the intersection of the two vertical lines and the phase. As shown in the figure, one peak in the BM amplitude corresponds to a half-cycle

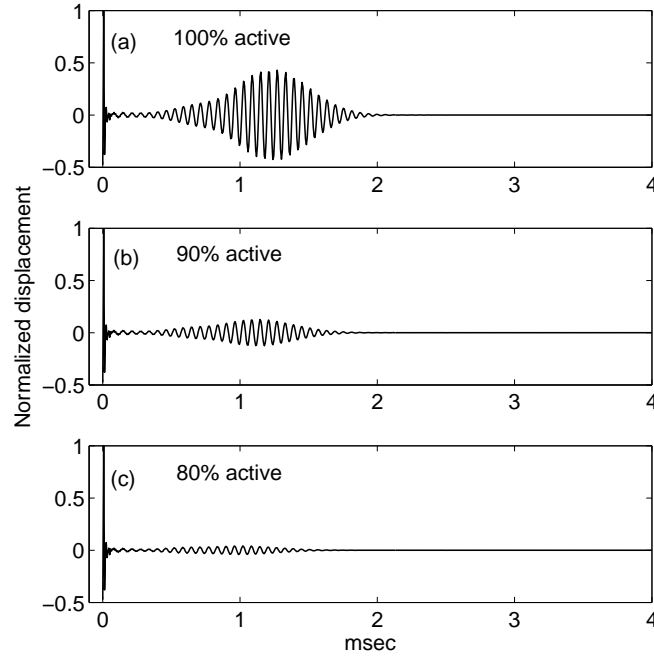


Figure 6.4: Normalized BM temporal response at 4 mm under an internal pressure source beneath the BM at 4 mm ($p^- : p^+ = 1 : 0$) for different activity levels. The normalization ratio among the 100%, 90%, and 80% activity levels is 279.1 : 280.2 : 281.4, which is close to 1 : 1 : 1. (a) A prediction from a 100% active model. (b) A prediction from a 90% active model. (c) A prediction from a 80% active model. The three responses show a similar initial amplitude, but the relative amplitudes of the traveling waves decrease with decreasing activity levels.

phase jump, consistent with the experimental finding from Ren. The multiple peaks and phase jump will disappear in a smooth cochlea.

In the following, we will show the model prediction by using filtered roughness, instead of designed roughness, on the MET channel. Two profiles of roughness (both filtered in the same way but the raw roughnesses are different) will be used to investigate the BM responses. For easy book-keeping, we denote the two filtered roughness profiles as R1 and R2.

Figure 6.7 shows the prediction of normalized active acoustic BM temporal responses at 4 mm with two sets of roughness profile. Both roughnesses give rise to additional ringings beside the first peak at t_g . However, the ringings generated by R1 is limited and small, while the ringings generated by R2 is non-trivial and persists over time. Figure 6.8 shows the corresponding BM spectrum response under roughness R1 [(a) and (b)] and R2 [(c) and (d)]. For both R1 and R2, multiple amplitude peaks around the best frequency

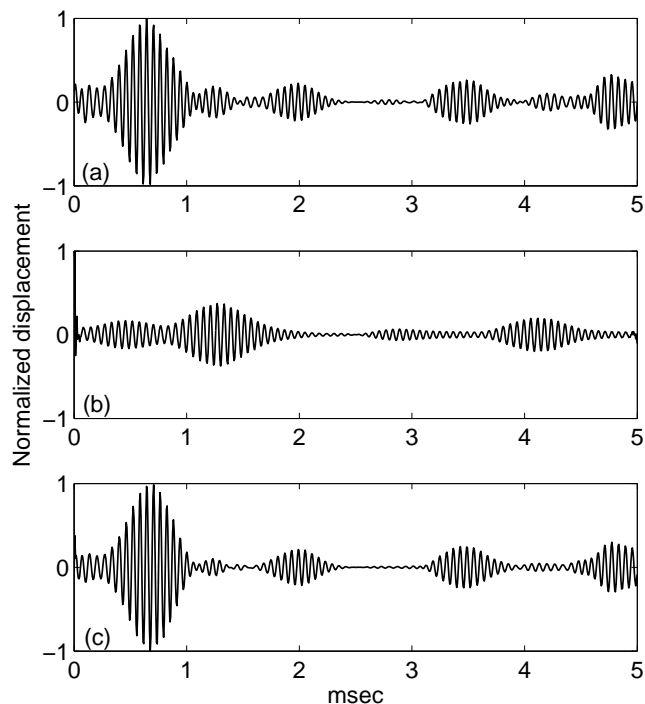


Figure 6.5: Normalized active BM temporal response at 4 mm with 0.05% designed perturbation (Eq. 6.1) on the MET channel. (a) Acoustic simulation. (b) Internal force excitation at 4 mm. (c) Internal pressure sources with $p^- : p^+ = 1 : 0.98$. Extended ringings are observed. In (c), the group delays of ringings are approximately at $t_g, 3t_g, 5t_g, 7t_g, \dots$.

are observed, but the peaks in Fig. 6.8 (c) are more pronounced.

6.4 Discussion

6.4.1 Compression wave in the cochlea

When pressure source is present inside the cochlea, the compression wave is launched. The compression wave travels from the location of the pressure source to the cochlea base within a few microsecond (calculated from the speed of sound in the fluid). When the compression wave reaches the stapes, it sets the stapes in motion, which is similar to the acoustic stimulation of the cochlea that energy is transmitted to the stapes. Following the motion of the stapes, the cochlea responds in the same way under acoustic stimulation. The tiny difference in the group delay between Fig. 6.2 (b) and (a) come from the compression wave traveling time from the pressure source to the cochlea. If the BM is always measured at $x = 4$ mm, but the location of the pressure source is varied in the

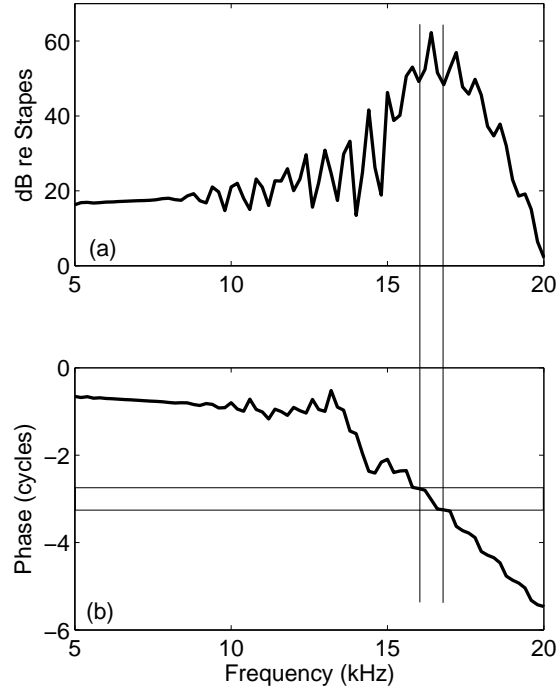


Figure 6.6: Active BM spectrum response at 4 mm with 0.05% designed perturbation (Eq. 6.1) on the MET channel for internal pressure sources ($p^- : p^+ = 1 : 0.98$) excitation. (a) BM amplitude in dB with respect to the stapes. (b) BM phase in cycles with respect to the stapes. Two thin solid vertical lines enclose the region of the middle peak around the best frequency; two thin solid horizontal lines enclose the region corresponding to the intersection of the two vertical lines and the phase.

longitudinal direction (as the experimental setup in Ren's lab), then the group delay of the BM is always close to t_g , with small difference due to the different compression wave traveling time.

When the pressure at the two sides of the BM is balance, the BM response is totally due to the excitation from the stapes, as seen in Fig. 6.2 (b). However, if the pressure is not balanced and a net force is generated on the BM, then the BM response is the combination from the effects of the force (see the discussion below) and the acoustic wave due to the stapes. The two effects may not have equal contribution. If the net force on the BM is comparably larger, then the BM response is dominated by the response from a net force, as shown in Fig. 6.4 (a).

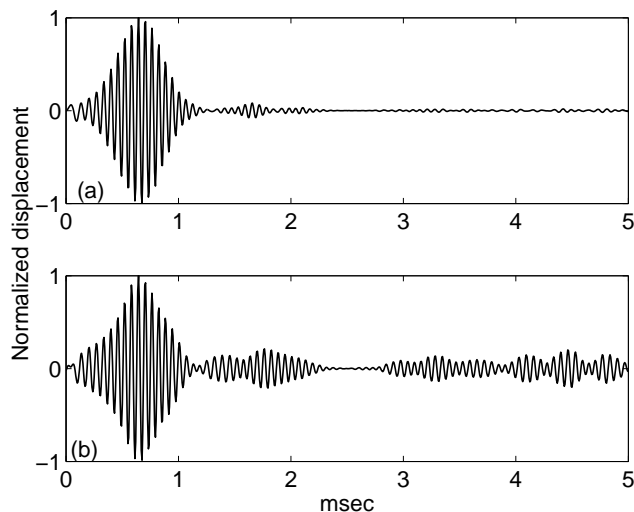


Figure 6.7: Normalized active BM temporal responses at 4 mm with 0.05% filtered perturbation on the MET channel under acoustic simulation. (a) Response under R1. (b) Response under R2.

6.4.2 Passive initial response and one directional amplification

As shown in Fig. 6.4 (see the figure caption), the initial BM peak at $t = 0$ is a manifestation of a passive response, since the amplitude of the peak keeps almost the same for different activity levels. The BM oscillation reduces quickly following the initial peak, due to the damping in the system and the longitudinal coupling both in the structure and in the fluid that spreads the energy very fast.

An internal force on the BM does not typically generate a compression wave in the cochlea, but initiates a traveling wave that propagates along the BM [56]. The traveling wave is carried by the BM and propagates in both directions (one in apical-wards and one basal-wards) from the location of forcing. When the basal-wards wave reaches the cochlear base, it is then reflected and propagates forwards. So the round-trip traveling wave delay is twice the forward group delay t_g , provided that the back- and forward- waves propagate at the same speed. From the $2t_g$ group delay under internal force excitation seen in Fig. 6.3, our model suggests that only the reflected traveling wave (in the forward direction) from the stapes is amplified. Although the backward traveling wave from the forcing place is always carried by the BM, it is not amplified. Comparing Fig. 6.4(a), (b), and (c), the ringing at t_g is largely decreased when the cochlea is less active. Hence, the wave amplification at $2t_g$ comes from the active cochlear mechanism built in our model.

From the acoustic response, we know that it takes time (i.e., t_g) for the cochlea to build amplification. Likewise, for the internal force excitation, it takes $2t_g$ for the wave

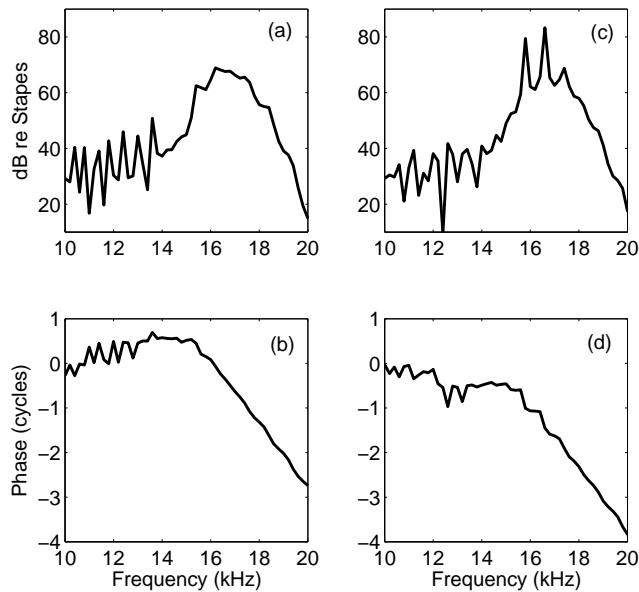


Figure 6.8: Active BM spectrum response at 4 mm with 0.05% filtered perturbation on the MET channel under acoustic simulation. (a) and (b) Response under R1. (c) and (d) Response under R2. (a) and (c) BM amplitude in dB with respect to the stapes. (b) and (d) BM phase in cycles with respect to the stapes.

to be amplified at the location of forcing. Therefore, it is no surprising that the initial BM peak at $t = 0$ is a passive response. The peak decays quickly without significant oscillation being followed because the wave amplified by the active process has not yet been built up at $t = 0$.

6.4.3 About roughness and scattering

Based on our model prediction, in a totally smooth cochlea, neither the extended ringings in the temporal domain nor the multiple peaks around the best frequency in the spectrum is observed. However, these two features are often seen in the experiments [77, 71, 22, 115]. With a filtered roughness, especially when the wavelength of the roughness is half the traveling wavelength [94], as one used in Eq. 6.1, our model predicts a series of ringings with the timing $t_g, 3t_g, 5t_g, 7t_g, \dots$ [see Fig. 6.5(c)] also seen in some sensitive *in vivo* measurements (Ren's experiment). Since a non-trivial compression wave is generated by using a pair of $p^- : p^+ = 1 : 0.98$ internal pressure source, then the group delay of the first ringing, i.e., t_g , is expected to be consistent with the acoustic simulation. The group delays of the successive ringings have the same gap of $2t_g$, which we attribute to the round trip traveling from the BM at 4 mm to the cochlear base and then back to

the BM at 4 mm. The special pattern of the roughness (Eq. 6.1) enhances the internal coherent reflections in the cochlea [94, 22] and generates a series of systematic ringings in the temporal domain as well as the multiple peaks and half-phase jumps in the spectrum.

We have used this ‘perfect’ roughness (Eq. 6.1) to show the enhancement of reflected waves with the right phases. However, in reality, the roughness in the cochlea is not expected to be that perfect. Also, in sensitive *in vivo* measurements, the $t_g, 3t_g, 5t_g, 7t_g, \dots$ ringing pattern is not always observed (according to Ren’s experiments), and the waveforms vary from cochlea to cochlea. Here we have considered a more general case by using filtered roughnesses, where the component of roughness with wavelength more than half the wavelength of the traveling wave (the traveling wave length is chosen for an active cochlea at 4 mm) is removed. Figure 6.7 (a) and (b) show that for the same filtering with different random seeds, the intracochlear reflection and scattering are different. Under the roughness profile R1, extended ringings are not remarkable in the BM temporal response, and the amplitude peaks around the best frequency in the associated spectrum are less sharp, but still exist. After a close look at R1 and R2, we found that around $x = 4$ mm, the profile of R1 is more far away from being regular like that in Eq. 6.1 than the profile of R2. For the roughness profile R2, always successive ringings are present in Fig. 6.7 (b), the specific waveform are different from that in Fig. 6.5(a). In a real cochlea, roughness may come in different ‘seeds’. Indeed, the ringing pattern in different experimental measurements are different (according to Ren’s data), but the initial peak always has the largest amplitude and has the group delay t_g , which is seen in our model prediction as well.

We have also found in our model that if a different filtering is used for a fixed random profile, the successive ringings in the temporal domain will also diminish (results not shown), which including a random profile without filtering at all. The restriction on the roughness to be well filtered in order to generate ringings may due to the mesh in our model. The longitudinal mesh size in our model is $25 \mu\text{m}$, which is much larger than the distance between two adjacent outer hair cells. Although a more dense roughness distribution does not imply well-filtering, a random system of larger size may possess a certain pattern (an analogy to the random matrix theory) that enhance the wave reflection and scattering.

In the model, we only use a 0.05% roughness. Although the amplitude of the roughness is quite small, when of appropriate profile (e.g., Eq. 6.1), the small roughness can generate significant extended ringings that persist [see Figs. 6.5 and 6.7 (b)]. If the roughness amplitude is increased without reducing the cochlear activity level, the system goes unstable (results not shown). Meanwhile, sufficient activity is required to have ringings,

since roughness is added onto the MET channel. A slighter lower activity level will also decrease the ringings.

6.4.4 Implication on the otoacoustic emissions

In otoacoustic emissions, sound is generated inside the cochlea and emitted from the ear canal. This phenomenon only presents in ears with normal hearing, i.e., in sensitive cochleae. Although the ringing patterns are different for different filtered roughness profiles [see Figs. 6.5(a) and 6.7], multiple peaks (large or small) in the BM spectrum always exist, and are related to the half-cycle difference in the phase. These features are typically observed in the otoacoustic emission. When the roughness happens to have the appropriate roughness, the coda in the BM temporal response is significantly enhanced. From the predicted coda in this model, the otoacoustic emission may be significantly effected by very small perturbations on the cochlear impedance with appropriate wavelength as predicted by [117].

6.5 Conclusion

In this work, we found that the BM velocity response of a sensitive cochlear model at the point of excitation can be decomposed into three components. The first is due to a fast wave emergent from the point of excitation, reflected by the stapes and then repropagated (in an amplified fashion) as a traveling wave back to the point of excitation. The group delay of this component is within a few microseconds of the delay for a forward traveling wave excited by external acoustic stimulation. By varying the amplitude of two point pressure sources in the cochlear fluid, we find that this component is due to symmetric pressure forcing (as in [56]). The second component consists of a reverse, slow, traveling wave which is likewise reflected at the stapes back to the measurement location by the stapes. Using a point force on the BM [56], we can stimulate such a slow wave (results shown in Fig. 6.3). The surprising result for the point forcing is that the group delay of the response *at* the location of excitation is nearly twice that from normal acoustic, distant stimulation. We now realize that the model predicts that the drive point response is dominated by a slow wave reflected at the stapes (hence the group delay is predicted to be twice that of a forward propagating wave) and that there is comparably little local, sustained response due to a localized force (see the short time behavior near $t = 0$ in Fig. 6.3). The coda, or longer time behavior, is due to random perturbations of the active component on the MET sensitivity (see Figs. 6.5 and 6.7), similar to the perturbations in the real part of the local impedance shown in [94] and [22]. This coda disappears when

activity is reduced or the perturbations are removed.

In addition, we found that the BM motion in an active cochlea is one-side amplified: the short-time motion is not directly amplified by an impulse internal force applied on the BM; rather, the BM is amplified at nearly twice the forward group delay from the reflected traveling wave (from the cochlear base) generated by the internal force. The amplitude of the reflected wave decreases dramatically with decreasing activity.

The innovation of this work is the discovery of one-side amplification in an active cochlear under an internal force excitation on the cochlear partition by performing numerical experiments in the FEM cochlear model, as well as the modeling of the extended ringings in the temporal response of the BM by adding designed perturbations on the active component of the cochlear partition.

CHAPTER VII

Assessing the activity of the cochlea

The existence and assessment of activity in a healthy cochlea is one of the central question in the cochlear mechanics. To analyze the activity of the cochlea, either by calculating the power flow, or estimate the basilar membrane impedance, the intracochlear pressure should be obtained first. In many cases, the WKB approximation is adopted to estimate the cochlear pressure. In this work, we will study the accuracy of using the WKB method to estimate the BM impedance. In this part, the BM response over a segment around the best place is known. We will also solve the intracochlear pressure by using the transformed BM spatial response from the spectrum response through a FEM scheme, as well as investigate the usability of the scaling symmetry-based transformation. In this part, the known BM spatial response over a segment will be used to facilitate the transformation. For both parts, we check the validity of respective methods by comparing the predicted result to the self-consistent FEM output. By taking the advantage of comparing results to the FEM data, we found that the assessment of activity is a hard problem. Application to the experimental data will be presented later.

7.1 Introduction

Then sensitivity and frequency selectivity in the mammalian cochlea is well beyond any common material. Due to the existence of damping and viscosity, energy is always dissipated during wave propagation in any passive structures. However, under physiological conditions, waves in the cochlea can propagation and amplified compared to a damaged cochlea. Hence, the existence and assessment of activity in a healthy cochlea is one of the central question in the cochlear mechanics.

To analyze the activity of the cochlea, either by calculating the power flow, or estimate the basilar membrane (BM) impedance, the intracochlear pressure should be obtained first. However, the measurement of the intracochlear pressure is difficult because of the

technical difficulty associated with the fabrication of pressure probes as well as the difficulty of preserving the physiology condition of the cochlea during measurements. Olson was able to measure the pressure in gerbils at a fixed basal place with different transverse locations [72], but the pressure measurement over an extended longitudinal region is not available, not to mention measuring the intracochlear pressure and the BM response simultaneously in a single set of experiment. Hence, the intracochlear pressure is usually estimated by known BM responses.

In most experiments, the BM response is measured at a fixed longitudinal location and the stimuli frequency is varied. In this way, the BM spectrum response at a given location is obtained. To analyze the longitudinal pattern of the cochlear activity, the spectrum response is usually transformed into the spatial domain by using the frequency-location mapping. Only minor modification is performed at the cochlear base [20] after data transformation, because the assumption of scaling symmetry is typically taken for granted. Recently, Ren *et al.* [86] and Fisher *et al.* [37] performed 3D measurements of the BM response over a longitudinal segment around the best place with multiple stimuli intensities, and the activity were analyzed as well.

Unlike experimental work, mathematical modeling provides a useful tool to perform numerical experiments and have a prediction of cochlears response which are available from physiological experiments. For a physiologically-based 3-D cochlear model (e.g., as those developed by Ramamoorthy *et al.* [82]), both the BM response and the intracochlear pressure can be obtained in the entire spatial domain, which would facilitate the analysis of the cochlear activity.

In this work, we will first use the prediction from our FEM model to calculate the power flow at each cross section in the scala vestibuli to understand the energy dissipation and amplification in the cochlea. The real part of the BM impedance is calculated as well as a second method of accessing the cochlear activity. In addition, we will study the accuracy of using the WKB method to estimate the BM impedance. In this part, the BM response over a segment around the best place is known. We will also solve the intracochlear pressure by using the transformed BM spatial response from the spectrum response through a FEM scheme, as well as investigate the usability of the scaling symmetry-based transformation. In this part, the known BM spatial response over a segment will be used to facilitate the transformation. For both parts, we check the validity of respective methods by comparing the predicted result to the self-consistent FEM output. Application to the experimental data will be presented later.

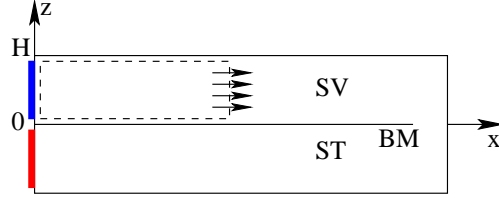


Figure 7.1: Illustration of the power flow through each cross section. The dashed rectangular box represents a control volume where the total power flow across all its boundaries is zero.

7.2 Assessment of cochlear activity via power flow

In this part, we assume that the intracochlear pressure is known everywhere. The activity of the cochlea can be estimated by the power flow through each fluid cross section at a location x .

7.2.1 Method

Let H be the duct height of the SV. We can draw a control volume in the SV with boundaries at $z = 0$, $z = H$, $x = 0$, and an arbitrary x location (see the dashed rectangular box in Fig. 7.1). Since no net energy is generated *inside* the fluid, the total power flow across all the boundaries of the control volume is zero. The wall at $z = H$ is rigid so that no power flow crosses this boundary. The activity of the cochlea injects power to the fluid through the boundary at $z = 0$. Hence, the power flow difference between an arbitrary x location and $x = 0$ implies the power flow injected by the active cochlear process. Without loss of generality, we analyze the power flow at each cross section at each longitudinal location as a function of x .

We consider a 2-D control volume where the fluid modes in the radial direction are neglected. Hence, the power flow through each cross section is essentially the power flow across a line in the SV (as shown in Fig. 7.1). Throughout this work, we assume that the cochlear response varies with time as $e^{i\omega t}$. For known intracochlear pressure, the fluid velocity in the longitudinal direction, v_f , is estimated by the linearized Euler relation,

$$v_f = -\frac{1}{i\omega\rho} \frac{\partial p_{\text{asym}}}{\partial x}, \quad (7.1)$$

where p_{asym} is the antisymmetric part of the intracochlear pressure (associated with the

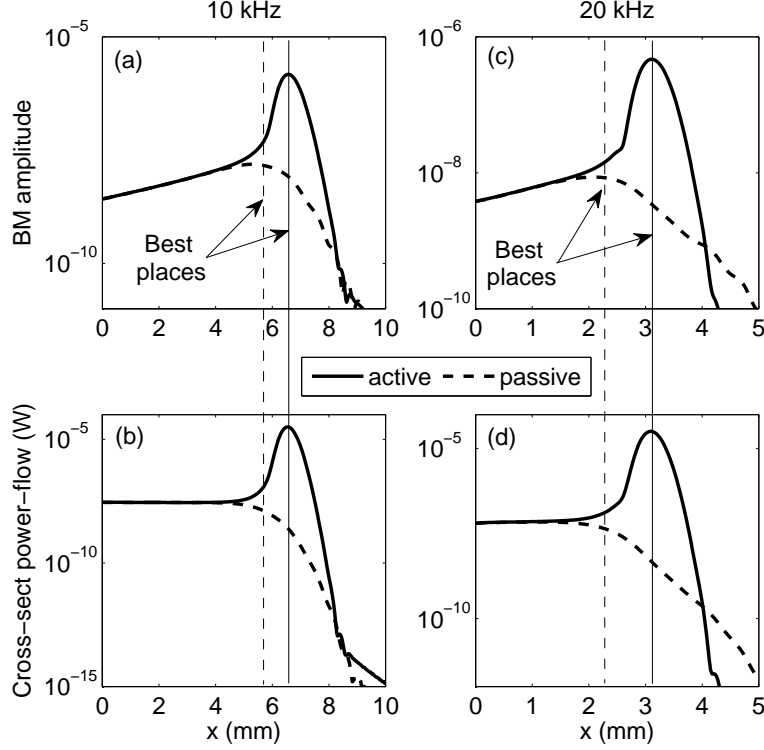


Figure 7.2: Predicted power flow at each cross section in the SV [in (b) and (d)] for both the active (thick solid lines) and passive (thick dashed lines) models. The BM amplitudes [in (a) and (c)] are plotted for reference. The vertical thin solid and dashed lines indicate the location of best places in an active and a passive model, respectively. (a) and (b), 10 kHz. (c) and (d), 20 kHz. The intracochlear pressure is predicted by the FEM model [82]. Decreasing and increasing power flow in x indicated power dissipation and injection, respectively, from the organ of Corti.

traveling wave). The time-averaged power flow through each cross section is

$$P(x) = \frac{1}{2} \int_0^H \Re \{ p_{\text{asym}}(x) v_f^*(x) \} dz, \quad (7.2)$$

where $*$ represents the complex conjugate.

7.2.2 Result

Here we show the result of power flow at each cross section based on the predicted intracochlear pressure from our FEM model [82]. Both active and passive models are used. The cochlea is stimulated from single-frequency acoustic inputs.

Figure 7.2 shows the predicted power flow at each cross section in the SV [in (b) and (d)] for both the active (thick solid lines) and passive (thick dashed lines) models. The BM amplitudes [in (a) and (c)] are plotted for reference. The vertical thin solid and dashed lines indicate the location of best places in an active and a passive model, respectively. In the very basal region, the cross sectional power flow in both the active and passive models is almost flat. This is due to that (1) the fluid is inviscid in the FEM model and (2) the motion of the organ of Corti (OoC) is very small basal to the best place so that the energy dissipation through the OoC is negligible. Beyond the flat region, the cross sectional power flow in the passive and the active model is different: In the passive model, the power flow decreases with increasing x . Power dissipation is evident when the location reaches the best places. In the active model, the power flow increases with increasing x until it reaches the best places, implying active power injection from the OoC to the fluid basal to the best place.

7.3 Assessment of cochlear activity via impedance

In a linear locally reacting cochlear model, the specific acoustic impedance of the BM (Z_{BM}) is defined as the pressure difference across the BM divided by the BM velocity. The BM impedance Z_{BM} , as a function of the longitudinal coordinate x and radial frequency ω , has the form

$$Z_{BM}(x, \omega) = i\omega m(x) + c(x) + \frac{k(x)}{i\omega}, \quad (7.3)$$

where $m(x)$, $c(x)$, and $k(x)$ are the effective BM mass, damping, and stiffness per unit area, respectively. We use the idea of ‘effective’ to consider the combined effect of any structure in the organ of Corti. The real part of the impedance, $\Re\{Z_{BM}\} = c(x)$, is a measurement of the effective BM damping. If $\Re\{Z_{BM}\} < 0$ over a segment of the BM, then the cochlea is thought to be active over that region.

In the following, the BM response is taken as a known data, either from direct measurement/model prediction or from the frequency-space mapping. The BM impedance is estimated either from WKB approximation via wavenumber estimation, or from pressure approximation via FEM, both based on the known BM responses.

7.3.1 Pressure estimation via WKB

In this part, we assume that the BM displacement is known over a spatial segment; the goal is to find the BM impedance over this segment. A 3-D single rectangular duct model will be used. The duct length is irrelevant for the purpose of wavenumber finding and

pressure estimation. Hence, we have a box model for scala vestibula (SV) with uniform height H and width B . Denote x , y , and z as the longitudinal, radial, and transverse coordinates, respectively. The origin of the y coordinate is defined at the centerline of the box model.

Using mode decomposition, we assume that the BM displacement $u(x, y)$ can be decomposed as

$$u(x, y) = u(x)\psi(y), \quad (7.4)$$

where $\psi(y)$ is the radial mode of the BM, given by

$$\psi(y) = \sin \left[\frac{\pi}{b} \left(y + \frac{b}{2} \right) \right], \quad (7.5)$$

where $b(x) < B$ is the width of the BM. Now we have reduced the BM to a 1-D structure in the longitudinal variable x . Suppose that the BM is a membrane-like structure, satisfying the governing equation

$$\frac{d^2 u}{dx^2}(x) + k_x^2(x)u(x) = 0, \quad (7.6)$$

where $k_x(x)$ is the local wave number, which is a complex function in x , and also depends on the frequency of the system. However, the dependence of ω will not be explicitly solved, but is automatically embedded in $k_x(x)$ since we only look at a segment around a best place. By neglecting the wave reflected from the cochlear apex, the WKB method approximates the BM displacement as

$$u(x) = U(x)e^{-i \int k_x(x) dx}. \quad (7.7)$$

Only the right-going (towards the cochlear apex) wave is considered. Similarly, the traveling wave pressure *on* the BM has the form

$$p_{\text{BM}}(x, y) = P(x)e^{-i \int k_x(x) dx} \psi(y), \quad (7.8)$$

where $P(x)$ is a complex function to be determined.

7.3.1.1 Approximation for the BM profile

Let λ be a large constant, which can be understood as $k_x(x)$ taken at a particular x position. Then $k_x(x)/\lambda$ is of order $O(1)$. The asymptotic expansion of $U(x)$ can be expressed as [57]

$$U(x) = a_0(x) + \frac{1}{\lambda} a_1(x) + \frac{1}{\lambda^2} a_2(x) + \dots, \quad (7.9)$$

where $a_i(x)$ ($i = 0, 1, 2, \dots$) are functions to be determined. The solution of a_i is solved from a_j for $j \in [i - 1]$. The first order solution is approximated by $U(x) \approx a_0(x)$; the second order by $U(x) \approx a_0(x) + a_1(x)/\lambda$; etc.

For the first order approximation, $U(x)$ is solved for the orders of $O(\lambda^2)$ and $O(\lambda)$ in the expansion, which has the form [57]

$$U(x) = U(x_0) \sqrt{\frac{k_x(x_0)}{k_x(x)}}, \quad (7.10)$$

where x_0 is a fixed point on the BM. Since $U(x)$ is a complex function in x , the phase and amplitude of the BM displacement are not solely determined by the exponential term $e^{-i \int k_x(x) dx}$; $U(x)$ adjusts the phase and amplitude as well. For the first-order WKB approximation (Eqs. 7.7 and 7.10) to be valid, we must have

$$\left| \frac{dk_x}{dx} \right| \ll |k_x^2| \quad (7.11)$$

to be satisfied. Let ϵ be the ratio of $|dk_x/dx|$ and $|k_x^2|$, i.e.,

$$\epsilon = \frac{1}{|k_x^2|} \left| \frac{dk_x}{dx} \right|. \quad (7.12)$$

When the condition $|dk_x/dx| \ll |k_x^2|$ is not satisfied, a second order WKB approximation is needed. A further solution in the order of $O(1)$ in the asymptotic expansion gives the second order approximation [57]

$$U(x) = U(x_0) \sqrt{\frac{k_x(x_0)}{k_x(x)}} \left\{ 1 - \frac{i}{4} \int \left[\frac{3(k'_x)^2}{2k_x^3} - \frac{k''_x}{k_x^2} \right] dx \right\}, \quad (7.13)$$

which can be written as

$$U(x) = U(x_0) \sqrt{\frac{k_x(x_0)}{k_x(x)}} \left\{ 1 + \frac{3i}{16} \left[\frac{k'_x(x_0)}{k_x^2(x_0)} - \frac{k'_x(x)}{k_x^2(x)} \right] + \frac{i}{16} \int \frac{k''_x}{k_x^2} dx \right\}. \quad (7.14)$$

Comparing Eq. 7.14 with Eq. 7.10, we can see that the additional terms in the second order approximation is in k'_x/k_x , which is exactly the same order of ϵ . Hence, when k'_x/k_x is negligible, using the first order approximation is acceptable.

7.3.1.2 Wave number estimation

Suppose that we have been given $u(x)$ over a segment on the BM around a best place; then we can estimate $k_x(x)$ based on Eqs. 7.7 and 7.10. We will use the Fourier expansion to approximate $k_x(x)$. The Levenberg-Marquardt algorithm [55, 60, 40] will be used to fit the coefficients of expansion. Before fitting, an initial estimation is needed as an initial guess for the algorithm. The wave number estimation is based on knowing

$$e^{-i \int k_x(x) dx} = e^{\int \Im k_x(x) dx} e^{-i \int \Re k_x(x) dx}, \quad (7.15)$$

where $e^{\int \Im k_x(x) dx}$ primarily determine the amplitude of the BM, and $e^{-i \int \Re k_x(x) dx}$ the phase.

- The real part:

Use the original phase from the given BM data, the integral of the real part of the wave number is initially approximated by

$$- \int \Re k_x(x) dx = \sum_{m=1} a_{rm} \sin(b_{rm}x + c_{rm}) = Phase(x). \quad (7.16)$$

The real part of the wave number is expressed as

$$\Re k_x(x) = - \left[\sum_{m=1} a_{rm} \sin(b_{rm}x + c_{rm}) \right]' = - \sum_{m=1} a_{rm} b_{rm} \cos(b_{rm}x + c_{rm}). \quad (7.17)$$

- The imaginary part:

Obtain the amplitude of the BM $U(x)$ from the given BM data. The integral of the imaginary part of the wave number is initially approximated by

$$\int \Im k_x(x) dx = \sum_{m=1} a_{im} \sin(b_{im}x + c_{im}) = \ln \frac{|u(x)|}{|u(x_0)|}. \quad (7.18)$$

The imaginary part of the wave number is expressed as

$$\Im k_x(x) = \left[\sum_{m=1} a_{im} \sin(b_{im}x + c_{im}) \right]' = \sum_{m=1} a_{im} b_{im} \cos(b_{im}x + c_{im}). \quad (7.19)$$

By knowing the real and imaginary parts of the wave number, the initial estimation of $k_x(x)$ is obtained. For the first order WKB approximation for the BM, we can write down the function to be fitted explicitly. We know that the WKB approximation for the

BM displacement $u(x)$ is

$$u(x) = U(x_0) \sqrt{\frac{k_x(x_0)}{k_x(x)}} e^{-i \int k_x(x) dx}, \quad (7.20)$$

where $U(x_0) = |U(x_0)|e^{i\theta_0}$ is a constant obtained from measurements. θ_0 is the phase at x_0 . Therefore, $u(x)$ is rewritten as

$$u(x) = |U(x_0)| \frac{(a^2 + b^2)^{1/4}}{c^{1/2}} e^{\int_{x_0} \Im k_x(x) dx} e^{i \left[\frac{1}{2} \arctan \frac{b}{a} - \int_{x_0} \Re k_x(x) dx + \theta_0 \right]}, \quad (7.21)$$

where

$$\begin{aligned} a &= \Re k_x(x_0) \Re k_x(x) + \Im k_x(x_0) \Im k_x(x), & b &= \Re k_x(x) \Im k_x(x_0) - \Re k_x(x_0) \Im k_x(x), \\ c &= (\Re k_x(x))^2 + (\Im k_x(x))^2. \end{aligned} \quad (7.22)$$

The real and imaginary parts of the BM displacement $u(x)$ is given by

$$\Re u(x) = |U(x_0)| \frac{(a^2 + b^2)^{1/4}}{c^{1/2}} e^{\int_{x_0} \Im k_x(x) dx} \cos \left[\frac{1}{2} \arctan \frac{b}{a} - \int_{x_0} \Re k_x(x) dx + \theta_0 \right], \quad (7.23)$$

$$\Im u(x) = |U(x_0)| \frac{(a^2 + b^2)^{1/4}}{c^{1/2}} e^{\int_{x_0} \Im k_x(x) dx} \sin \left[\frac{1}{2} \arctan \frac{b}{a} - \int_{x_0} \Re k_x(x) dx + \theta_0 \right]. \quad (7.24)$$

In order to obtain reliable fit for $k_x(x)$, both real and imaginary parts of the experimental data are used to minimized the squared sum of approximated $u(x)$ and given $u(x)$. In order to achieve the simultaneous fit for both real and imaginary parts, the following structure is used: let m be the number of given points of $u(x)$ in x , let

$$X : x_1, x_2, \dots, x_m, x_1, x_2, \dots, x_m \quad (7.25)$$

be the new variables ($2m$ in total), and let

$$Y : \Re u(x_1), \Re u(x_2), \dots, \Re u(x_m), \Im u(x_1), \Im u(x_2), \dots, \Im u(x_m) \quad (7.26)$$

be the data to be fitted ($2m$ in total). It turns out that as long as the data fitting is confined within a BM segment around the best place, the wavenumber finding process is satisfactory - the fitted BM response is almost identical to the given BM response.

Once $k_x(x)$ is obtained, dk_x/dx can be directly calculated by differentiate the Fourier expansion term by term. We will use $k_x(x)$ to estimate the intracochlear pressure, or the BM impedance, as follows.

7.3.1.3 Pressure approximation

The compressible wave function for the pressure in the cochlea is

$$\frac{\partial^2 p}{\partial x^2} + \frac{\partial^2 p}{\partial y^2} + \frac{\partial^2 p}{\partial z^2} + \left(\frac{\omega}{c}\right)^2 p = 0. \quad (7.27)$$

Apply the rigid wall boundary condition except on the BM, the traveling pressure has the form [100]

$$p(x, y, z) = \sum_m B_m \cosh \alpha_m(z - H) \phi_m(y) e^{-i \int k_x(x) dx}, \quad (7.28)$$

where

$$\phi_m(y) = \cos\left(\frac{2m\pi y}{B}\right), \quad (7.29)$$

is the pressure cross-sectional mode shape in the y direction, H and B are the height and width of the cochlea, respectively.

Due to the no-through boundary condition on the BM, the fluid displacement/velocity is the same as the BM. According to the linearized Euler relation, at $z = 0$ we have

$$\frac{\partial p}{\partial z} = \rho \omega^2 u(x, y). \quad (7.30)$$

Substituting Eq. 7.28 into Eq. 7.30 yields

$$-\sum_m B_m \alpha_m \sinh(\alpha_m H) \phi_m(y) = \rho \omega^2 U(x) \psi(y). \quad (7.31)$$

By using the orthogonality of ϕ_m , we have

$$B_m = -\rho \omega^2 U(x) \frac{A_m(x)}{\alpha_m \sinh(\alpha_m H) I_\phi}, \quad (7.32)$$

where $b(x)$ is the width of the BM, and

$$A_m(x) = \int_{-b/2}^{b/2} \phi_m(y) \psi(y) dy, \quad (7.33)$$

$$I_\phi = \int_{-B/2}^{B/2} \phi_m^2(y) dy = \begin{cases} B & \text{if } m = 0 \\ \frac{1}{2}B & \text{if } m = 1, 2, 3, \dots \end{cases}. \quad (7.34)$$

Assume that α_m varies slowly with x so that $d\alpha_m/dx$ is negligible. Substituting Eq. 7.28 into Eq. 7.27 yields

$$\begin{aligned} & \sum_m \left[\frac{d^2 B_m}{dx^2} - ik_x(x) \frac{dB_m}{dx} - i \frac{d(k_x B_m)}{dx} \right] e^{-i \int k_x(x) dx} \cosh \alpha_m(z - H) \phi_m(y) \\ & + \sum_m \left[-k_x^2(x) + \alpha_m^2 - \left(\frac{2m\pi}{B} \right)^2 + \left(\frac{\omega}{c} \right)^2 \right] B_m e^{-i \int k_x(x) dx} \cosh \alpha_m(z - H) \phi_m(y) = 0. \end{aligned} \quad (7.35)$$

By using the orthogonality of $\phi_m(y)$, we have

$$\frac{d^2 B_m}{dx^2} - ik_x \frac{dB_m}{dx} - i \frac{d}{dx} (k_x B_m) + \left[-k_x^2 + \alpha_m^2 - \left(\frac{2m\pi}{B} \right)^2 + \left(\frac{\omega}{c} \right)^2 \right] B_m = 0. \quad (7.36)$$

Assume that all quantities vary slowly with x so that d/dx is negligible. Then α_m is approximated as

$$\alpha_m^2 = k_x^2(x) + \left(\frac{2m\pi}{B} \right)^2 - \left(\frac{\omega}{c} \right)^2. \quad (7.37)$$

At $z = 0$, equate Eq. 7.28 with Eq. 7.8 to have

$$P(x)\psi(y) = \sum_m B_m \cosh(\alpha_m H) \phi_m(y). \quad (7.38)$$

Substituting the expression of B_m , we obtain a relation between $U(x)$ and $P(x)$,

$$P(x)\psi(y) = -\rho\omega^2 U(x) \sum_m \frac{A_m(x) \phi_m(y)}{\alpha_m \tanh(\alpha_m H) I_\phi}. \quad (7.39)$$

Multiplying both sides of the above equation with $\psi(y)$ and integrating over y to have

$$P(x) = -\rho\omega^2 U(x) \sum_m \frac{A_m^2(x)}{\alpha_m \tanh(\alpha_m H) I_\phi I_\psi}, \quad (7.40)$$

where

$$I_\psi = \int_{-b/2}^{b/2} \psi^2(y) dy = \frac{1}{2}b(x). \quad (7.41)$$

Let

$$h_{eq} = \sum_m \frac{A_m^2(x)}{\alpha_m \tanh(\alpha_m H) I_\phi I_\psi}, \quad (7.42)$$

be the effective fluid height in the z direction; it can be determined if $k_x(x)$ is known. The expression on the effective height in Eq. 7.42 is consistent with those derived in the literature (e.g., Steele and Taber [100]). The pressure can then be expressed as

$$P(x) = -\rho\omega^2 U(x) h_{eq}. \quad (7.43)$$

The BM impedance is solved as

$$Z_{BM} = \frac{p_{BM}}{v_{BM}} = \frac{p_{BM}}{i\omega u} = i\rho\omega h_{eq}. \quad (7.44)$$

Note that to obtain Eq. 7.42, we have used the approximation twice that d/dx is negligible: one is to reach Eq. 7.35, and the other is to reach Eq. 7.37. From Eq. 7.37 we can see that α_m is strongly related to $k(x)$. Neglecting $d\alpha_m/dx$ is equivalent to neglecting $dk(x)/dx$, which may not be valid. Including the d/dx terms would require solving the differential equation (substituting Eq. 7.28 into Eq. 7.27) numerically with known boundary conditions [58].

7.3.1.4 Results

In this section, we will check the validation of data fitting by using the Levenberg-Marquardt algorithm. The activity of the cochlea is discussed by looking at the real part of the BM impedance. The suitability of the WKB approximation for the BM impedance is analyzed, by comparing to the reference data from the FEM output.

In the following, the known BM responses come from the FEM model [82, 63] prediction under single-frequency acoustic stimulations. The parameters in the FEM model comes from a guinea pig (see [56] for a list). Figure 7.3 shows the result of the wavenumber fitting by comparing the fitted BM response to the known BM responses [see (b) and (d)]. A first-order WKB approximation is used here. The original data is the BM responses under 20 kHz acoustic excitation. Three terms of Fourier expansion are used for each of the real and imaginary part in Fig. 7.3. Using too few terms will cause insufficient data representation, and too many terms will cause instability. The appropriate number of terms to use depends on the specific profile of the BM response. Figure 7.3 shows that the BM result obtained from Eq. 7.20 (denoted as ‘fit’ in the figure legend) is in good agreement with the given BM responses (denoted as ‘ref’ in the figure legend), for

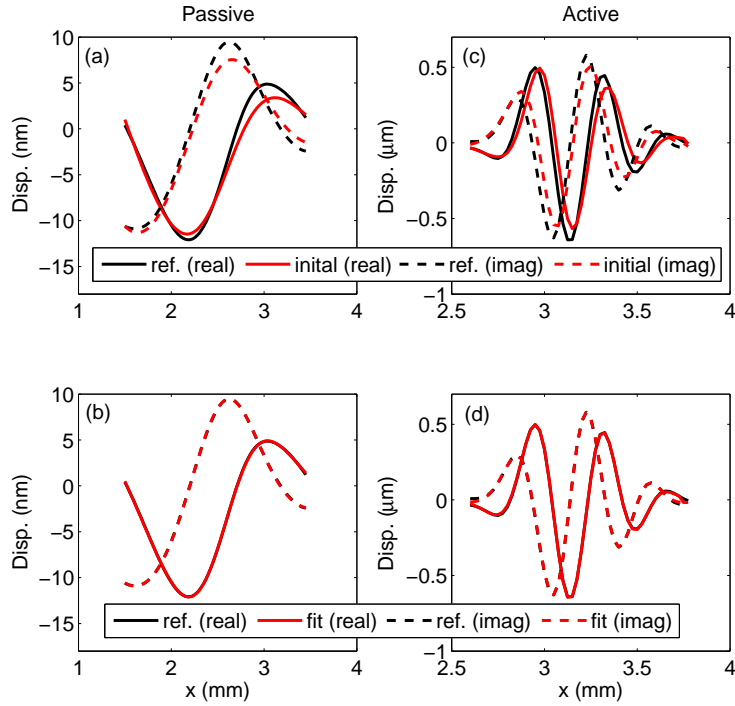


Figure 7.3: Results of wavenumber fitting on both the real and imaginary parts of the BM displacements by using the first order WKB BM approximation. The reference (ref.) displacements (considered as the given data) are the original BM displacements from the FEM model under 20 kHz acoustic simulation. (a) and (b), BM responses from a passive model. (c) and (d), BM responses from an active model. The initial displacements refer to the displacements given by the initial guess before the Levenberg-Marquardt algorithm is implemented [see (a) and (c)]. The fitted displacements refer to the BM displacements after the Levenberg-Marquardt algorithm is implemented [see (b) and (d)]. The data fitting gives accurate results in terms of the reproduction of the given displacements.

both the passive and active data, showing that the data fitting part is reliable. A fitting based on the second-order WKB approximation gives the same good result. Hence, the data-fitting process can recover the original BM profile by approximating the wave number of the cochlea. Note that the first- and the second- order WKB approximation may give different approximated $k_x(x)$ based on whether the higher order terms need to be retained.

In addition to the BM displacement, the anti-symmetric intracochlear pressure from the FEM prediction is also exported. We will use the BM impedance calculated from the FEM prediction, which represent a set of self-consistent data, as the reference value. Figure 7.4 shows $\Re\{Z_{BM}\}$ from an active cochlear model, with stimuli frequencies 20 kHz (best place is around 3.1 mm) [(a) and (b)] and 10 kHz (best place is around 6.5 mm) [(c) and (d)]. The spatial span is such chosen that the best place is in the center of the data. The reference $\Re\{Z_{BM}\}$ is shown in solid lines in Fig. 7.4 (b) and (d). A segment of negative $\Re\{Z_{BM}\}$ is seen basal to the best place, indicating the activity of the cochlea in that region. The zero position of $\Re\{Z_{BM}\}$ aligns with the peak of the BM turning (results not shown), as also found by others [94, 22]. The $\Re\{Z_{BM}\}$ approximated by the WKB has the same sign as that calculated from the the FEM, although the absolute values are different. The first- and second- order WKB approximation give similar results. $\epsilon \ll 1$ is mostly satisfied [see Fig. 7.4 (a) and (c)] for the active model.

In experiments, the spatial span under measurement is fixed for various simulation levels and cochlear conditions [86, 37]. Figure 7.5 shows the computed $\Re\{Z_{BM}\}$ from the WKB approximation with the same spatial range as that in Fig. 7.4, but a pass model is used. Since the model is passive, activity is not expected. The sign of $\Re\{Z_{BM}\}$ from the WKB approximation agrees with that of the reference value from the FEM output [Fig. 7.5(b) and (d)], all being positive showing the passive nature of the model. The WKB approximation implemented on the 20 kHz data is better than the implementation on the 10 kHz data, as we can see from Fig. 7.5(b) and (d) that the $\Re\{Z_{BM}\}$ predicted by the WKB has the same spatial trend compared to the FEM output for the 20 kHz case. For the 10 kHz case, however, the $\Re\{Z_{BM}\}$ predicted by the WKB has a different spatial pattern as $\Re\{Z_{BM}\}$ in the FEM model. Note that for both ϵ and $\Re\{Z_{BM}\}$, the second order WKB BM approximation gives a different result compared to the first order WKB BM approximation. In Fig. 7.5(b), a second-order WKB approximation gives a more smooth BM impedance, which is also close to the reference value.

If we fix the spatial segment (a window) of the BM for both the active and the passive model (as what can be done in experiments), the best place of BM response in the passive model is out of the window. Hence, we would like to see how the WKB method works if

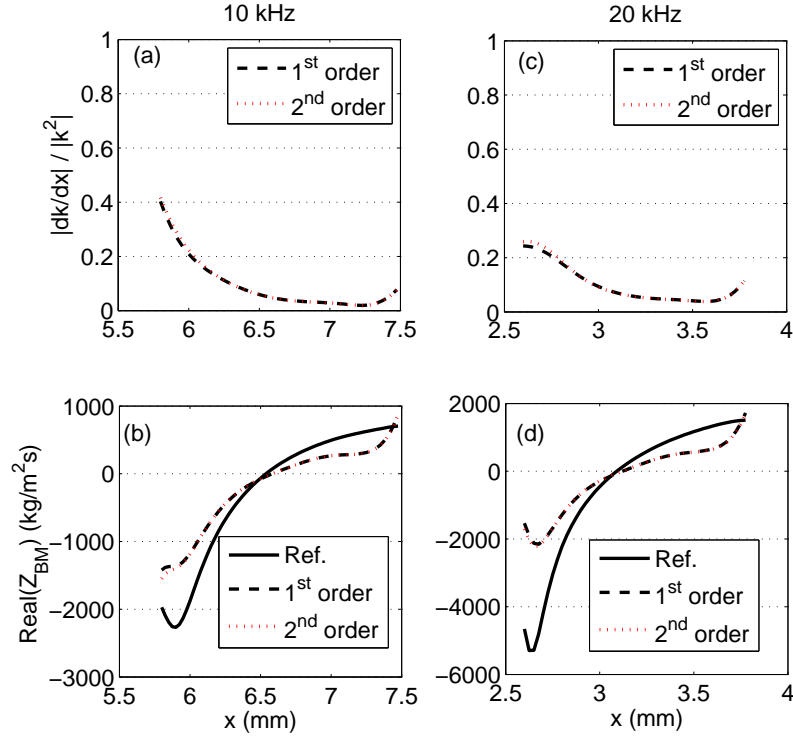


Figure 7.4: The value of ϵ [(a) and (c)] and the real part of the BM impedance [(b) and (d)] for an active model under acoustic simulations. Two orders of WKB BM approximation are compared. Dashed lines: first-order approximation. Dotted lines: second-order approximation. Solid lines: reference value from the FEM output. (a) and (b), 10 kHz. (c) and (d), 20 kHz. In (a) and (c), ϵ is obtained from the result of data fitting. In (b) and (d), the reference BM impedance (solid lines) comes from the direct output of the FEM model prediction. The BM impedances approximated by the WKB method are given by dashed (first-order) and dotted (second order) lines. $\epsilon \ll 1$ is mostly satisfied, and the tow orders of approximation almost give the same $k_x(x)$. The sign of $\Re\{Z_{BM}\}$ from the WKB BM approximation is consistent with the reference value from the FEM output.

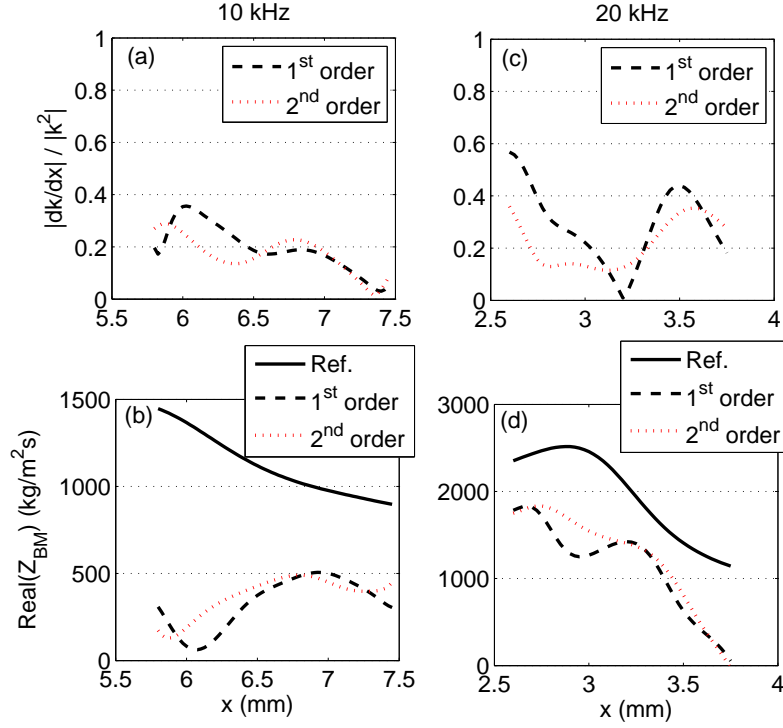


Figure 7.5: The value of ϵ [(a) and (c)] and the real part of the BM impedance [(b) and (d)] for a passive model under acoustic simulations. The spatial span is the same as that in Fig. 7.4, which does not include the entire peak for the passive model. Two orders of WKB approximation are compared. Dashed lines: first-order approximation. Dotted lines: second-order approximation. Solid lines: reference value from the FEM output. (a) and (b), 10 kHz. (c) and (d), 20 kHz. In (a) and (c), ϵ is obtained from the result of data fitting. In (b) and (d), the reference BM impedance (solid lines) comes from the direct output of the FEM prediction. The BM impedances approximated by the WKB method are given by dashed and dotted lines. The sign of $\Re\{Z_{BM}\}$ from WKB approximation agrees with that of the reference value from the FEM output, but the amplitudes are different. For both ϵ and $\Re\{Z_{BM}\}$, the second order WKB BM approximation gives a different result compared to the first order WKB BM approximation.

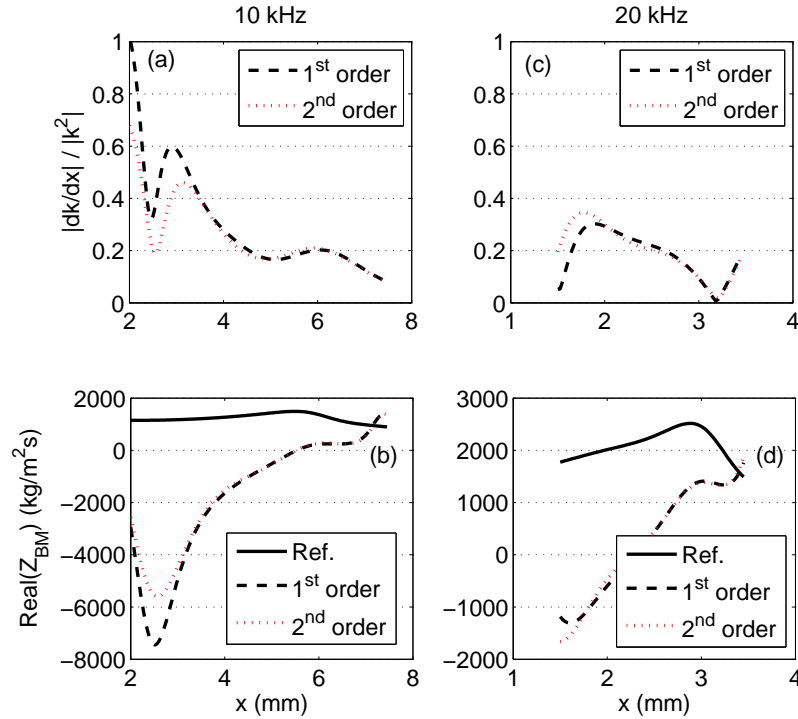


Figure 7.6: The value of ϵ [(a) and (c)] and the real part of the BM impedance [(b) and (d)] for a passive model under acoustic simulations. The spatial span is such chosen that the best place is included. Two orders of WKB approximation are compared. Dashed lines: first-order approximation. Dotted lines: second-order approximation. Solid lines: reference value from the FEM output. (a) and (b), 10 kHz. (c) and (d), 20 kHz. In (a) and (c), ϵ is obtained from the result of data fitting. In (b) and (d), the reference BM impedance (solid lines) comes from the direct output of the FEM prediction. The BM impedances approximated by the WKB method are given by dashed and dotted lines. The sign of $\Re\{Z_{BM}\}$ from WKB approximation is inconsistent with the reference value from the FEM output.

the entire peak of the BM is included in the model. Figure 7.6 shows the similar content as in Fig 7.5, but the BM segment is such chosen that the best place is included in the model, i.e., an spatial extension to the base. The reference $\Re\{Z_{BM}\}$ [solid lines in Fig. 7.6 (b) and (d)] is all positive around the best places for both frequencies, which is consistent with the model being passive. However, the $\Re\{Z_{BM}\}$ approximated by the WKB has the opposite sign in the majority region over the segment [see dashed and dotted lines in Fig. 7.6 (b) and (d)], which is inconsistent with the FEM output and the model being passive. The value of ϵ in Fig. 7.6 (a) and (c) are higher than those in Fig. 7.4 (a) and (c), especially in Fig. 7.6 (c). The first- and second- order WKB approximation give overall similar results (all have the wrong sign). However, the difference at the basal region is larger, where the sign of $\Re\{Z_{BM}\}$ is wrong in the WKB approximation.

7.3.2 Pressure estimation via FEM

To estimate the intracochlear pressure via FEM, the BM spatial response should be available from the very base and go beyond the best place (the evanescent region). The motion of the stapes should also be provided.

In experiments, the measured BM responses are available in two format. One is the BM responses measured at a fixed longitudinal location under varying stimuli frequency, i.e., the BM spectrum at a given location. The other is the BM responses measured over a small segment on the BM (usually around a best place) for a given simulation frequency. Hence, we need to use the available data in both format to approximate the BM response starting from the base to the evanescent region.

7.3.2.1 Frequency-space transformation

The basis of constructing a spatial BM response from a frequency response comes from the ‘scaling symmetric’ approximation [20]. For a given BM spectrum response measured at x_0 with best frequency f_0 , we can use the frequency-space mapping [42] to get an approximated BM spatial response simulated at frequency f_0 . The transformation is given as follows,

$$x_{\text{tran}} = -\tilde{x} + \frac{1}{a} \log_{10} \left(\frac{f}{A} + k \right), \quad (7.45)$$

where x_{tran} is the desired spatial coordinate, \tilde{x} , a , A , and k are constants. x_{tran} and \tilde{x} are in mm, and f is in kHz. Let A and ϕ be the amplitude and phase, respectively, of the measured BM spectrum response. Based on long-wave approximation, the transformed

BM response (with amplitude A' and phase ϕ') is adjusted by [20]

$$A' = A\sqrt{f/f_0}, \quad (7.46)$$

$$\phi' = \left(\phi + \frac{\pi}{2}\right) \frac{f_0 e^{\frac{1}{2}\alpha x_{\text{tran}}} - 1}{f e^{\frac{1}{2}\alpha x_0} - 1} - \frac{\pi}{2}, \quad (7.47)$$

where $\alpha = a/\log e$ [20].

7.3.2.2 Pressure solution

Suppose now that the stapes and the transformed BM responses are given. The pressure is solved as an acoustic boundary value problem through a FEM model. The predicted pressure depends on the geometry of the problem, as well as the given essential boundary conditions. In the model, we eliminate all the physiology properties of the cochlea, and only treat it as a pure acoustic boundary problem for a given geometry. Hence, the entire BM response is pre-scribed. In the above section, we obtain the approximated BM response from the base to the place beyond the best place (the evanescent region). In the apical region (beyond the evanescent region that are not approximated by the frequency-space transformation), the BM responses are assumed to be 0. The entire cochlea is consist of two rectangular ducts, connected at the apex via the helicotrema. The stapes displacement is another essential boundary condition. Since the exact material property of the round window is unknown, to reduce uncertainty of the model, the cochlear fluid is modeled as incompressible so that the displacement of the round window is identical (up to a sign difference) to that of the stapes (as given) in the FEM output.

7.3.2.3 Results

In this section, we will also use the prediction from the FEM model, both for the spectrum and spatial BM responses. The predicted intracochlear pressure and BM impedance are compared to the self-consistent FEM output to check the validity of the method of transformation and pressure prediction. All the BM responses come from the active incompressible cochlear model under acoustic simulations. For the spectrum response, the BM is taken at $x_0 = 3.1$ mm; for the spatial response, the simulation frequency is $f_0 = 20$ kHz (the best place for a 20 kHz simulation is at $x = 3.1$ mm, as predicted by our active cochlear model).

In the frequency-space transformation, we let $\tilde{x} = 15$, $a = 1.8/18.5$, $A = 0.35$, and $k = 0.85$ in Eq. 7.45, as similar to the values for the guinea pig used by Greenwood [42]. The value of α used in Eq. 7.47 is adjusted from the one proposed by de Boer

[20]. Figure 7.7 shows the result of comparison between the transformed data from the BM spectrum (dashed lines) and the original BM spatial response (solid lines). The transformed amplitude has higher values at the base compared to the original spatial response [see Fig. 7.7 (a)], although the adjustment in Eq. 7.46 has already reduced the amplitude at base. Two different values of α are used for the phase transformation [see Fig. 7.7 (b) and (c)]. In Fig. 7.7 (b), the phase at most regions basal to the best place is matched with the original phase. In Fig. 7.7 (c), the phase at $x = 0$ is matched to the supposed-to-be value (based on the FEM model). These two transformations, along with the amplitude in Fig. 7.7 (a), will be used as a part of the essential boundary conditions to solve for intracochlear pressure. Also, as we can see from the figure, the transformation does not match the width of the BM peak and the slope of the phase simultaneously. The constants \tilde{x} and a are chosen to match the slope of the phase around the best place, which determines the position of zeros in the real part of the BM spatial response.

Before estimating the intracochlear pressure from transformed BM responses, the validity of the acoustic boundary value FEM model is first checked by the self-consistent FEM output, i.e., we use the original BM spatial response and the corresponding stapes motion as the essential boundary conditions to calculate the intracochlear pressure and the BM impedance, and compare them to the original intracochlear pressure and the BM impedance. In the testing, the simulation frequency is 20 kHz, the BM profile from $x = 0$ to $x = 4.6$ mm (the best place is 3.1 mm) comes from the original BM displacement; the BM data apical to $x = 4.6$ mm is set to be zero. The recovered intracochlear pressure solved from the boundary value problem matches the original pressure without noticeable difference; the calculated $\Re\{Z_{BM}\}$ also matches well with the reference impedance (results not show). Hence, the boundary value problem itself is valid, and can be used to approximate the intracochlear pressure from transformed BM response, as long as the given BM profile is reliable.

Figure 7.8 shows the recovered anti-symmetric intracochlear pressure and $\Re\{Z_{BM}\}$ from the transformed BM profile shown in Fig. 7.7. For $\alpha = 0.3796$ (calculate from $3.05/18.5 \log_{10}(e)$) in Fig. 7.8 (a) and (b) [the corresponding transformed BM profile is given in Fig. 7.7 (a) and (b)], the recovered anti-symmetric pressure is close to the original anti-symmetric pressure except at the very basal region [see the insertion in Fig. 7.8 (a)] where the transformed BM phase differs from the original phase [see the insertion in Fig. 7.7 (b)]. The difference in $\Re\{Z_{BM}\}$ between the recovered and the original is much larger than that in pressure [Fig. 7.8 (b)]. Despite the large difference in values, the estimated $\Re\{Z_{BM}\}$ from the transformed BM profile also has a negative region, basal to the best place ($x_0 = 3.1$ mm), showing the activity of the cochlea in that region.

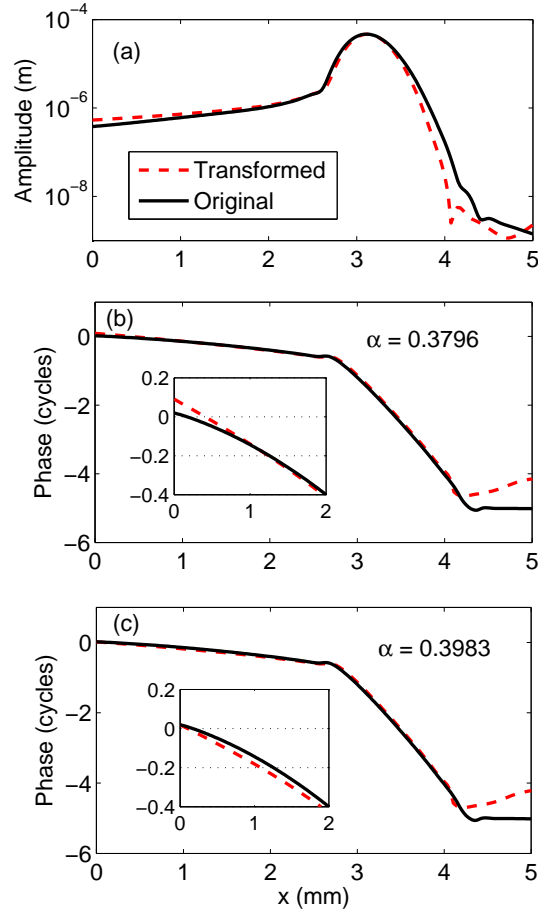


Figure 7.7: Comparison between transformed data from the BM spectrum (dashed lines) and the original BM spatial response (solid lines). All the spectrum and spatial responses are obtained from an active incompressible cochlear model under acoustic simulation. For the spectrum response, the BM is taken at $x_0 = 3.1$ mm; for the spatial response, the simulation frequency is $f_0 = 20$ kHz. (a) BM amplitude. (b) and (c), BM phase in cycles. The insertions in (b) and (c) are the zoomed-in BM phases at the base. (b), $\alpha = 0.3796$. (c), $\alpha = 0.3983$. The transformation matches the width of the BM peaks and the slope of the phase slightly differently, but the overall transformed response is similar to the original BM spatial response.

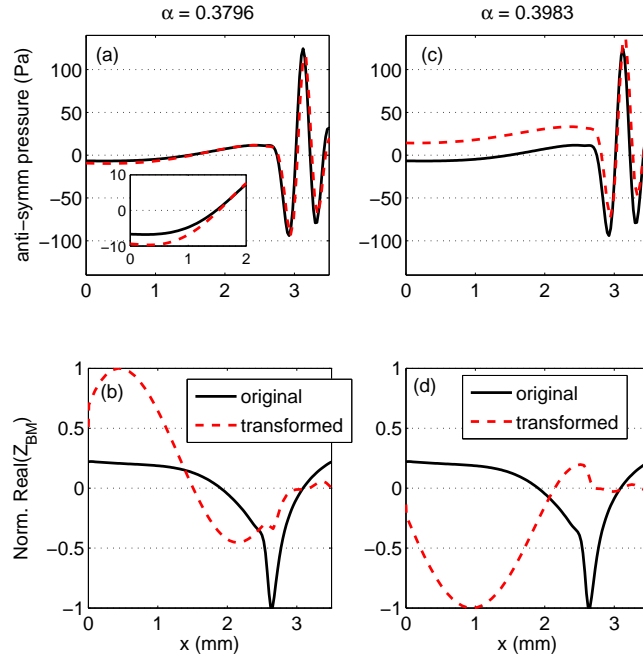


Figure 7.8: Compression between the prediction from the transformed BM response (dashed lines) and the original values (solid lines) on the anti-symmetric intracochlear pressure and $\Re\{Z_{BM}\}$. The profiles of transformed BM response and the original response are shown in Fig. 7.7. (a) and (b), the anti-symmetric pressure is calculated from transformed BM response in Fig. 7.7 (a) and (b). The insertion in (a) shows the zoomed in response at $x = 0$. (c) and (d), the anti-symmetric pressure is calculated from transformed BM response in Fig. 7.7 (a) and (c). (a) and (c) show the real part of the anti-symmetric intracochlear pressure at the basal region. (b) and (d) show the normalized real part of the BM impedance. Normalization factors: 5.2943×10^3 for the original FEM output; 2.9201×10^4 for the transformation given by $\alpha = 0.3796$; 4.7503×10^4 for the transformation given by $\alpha = 0.3983$.

The negative region of $\Re\{Z_{BM}\}$ in recovered response is wider than that of the original response, but also cross the zero at the best place (the BM peak). For $\alpha = 0.3983$ (calculated from $3.2/18.5 \log_{10}(e)$) in Fig. 7.8 (c) and (d) [the corresponding transformed BM profile is given in Fig. 7.7 (a) and (c)], the recovered pressure is shifted above at the basal region. The error in pressure results in larger error in $\Re\{Z_{BM}\}$ [see Fig. 7.8 (d)]. The recovered $\Re\{Z_{BM}\}$ from transformed BM profile has opposite sign to the original $\Re\{Z_{BM}\}$ everywhere basal to the best place. Although in Fig. 7.7 (c) the transformed BM phase is matched at $x = 0$, the prediction of activity still fails in this case.

The acoustic boundary value model is very sensitive to the given boundary conditions, both for the BM profile and the stapes motion (result not shown). Although the difference in the transformed phases in Fig. 7.7 (b) and (c) is small, the recovered pressure differs a lot, and thus the approximated $\Re\{Z_{BM}\}$.

7.4 Application to the experimental data

In this section, we will use the experimental data from gerbils measured by Ren *et al.* [86] as the given BM data to investigate the activity of the cochlea and the validity of the frequency-space mapping. In addition to the data obtained from the experiments, the methods of approximation require additional parameters that will be involved in the model. Table 7.1 gives a list of the estimated parameters.

Table 7.1: Geometrical parameters used for the gerbil model.

Property	Value	Sources
Speed of sound (c)	1500 m/s	From water
Fluid density (ρ)	1000 kg/m ³	From water
BM width (b)	200 μ m	estimated from experiment
Duct height (H)	1 mm	estimated
Duct width (B)	1 mm	estimated

7.4.1 WKB approximation

In this part, we will use the BM spatial response measured in experiments [86] as the known data to investigate the activity of the model. Among the data from 10 dB to 90 dB, the responses from 30 dB to 80 dB will be used to estimate the BM impedance. For the 10 dB and 20 dB responses, due to the high noise-response ratio in the data (see Fig. 4 in the original paper [86]), a reliable fitting is hard to obtain.

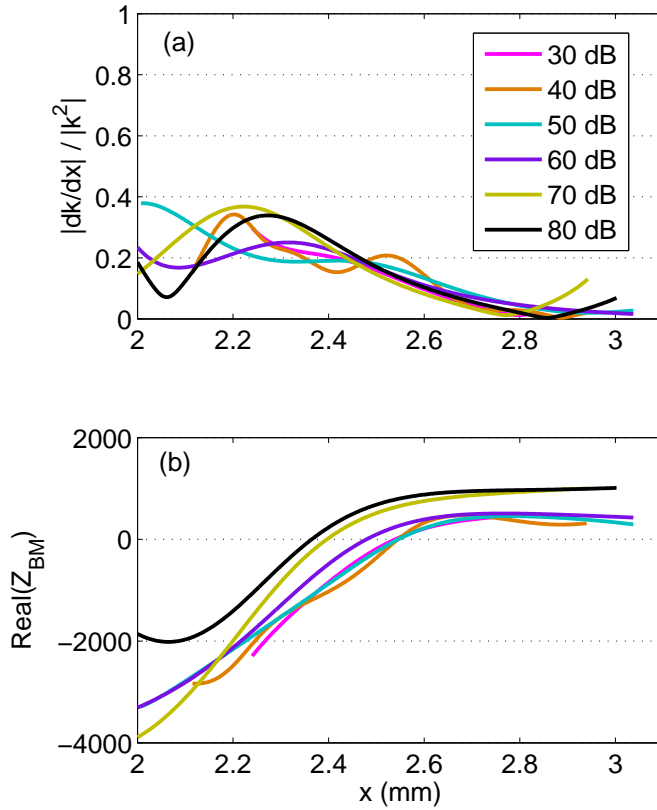


Figure 7.9: First order WKB approximation for the value of ϵ (a) and the real part of the BM impedance (b) from the measured gerbil cochlear responses under various acoustic simulation levels at 16 kHz. Two terms of Fourier expansion are used in the data fitting. (a) $\epsilon \ll 1$ is almost satisfied. (b) the negative region of $\Re\{Z_{BM}\}$ basal to the best place (around 2.5 mm) indicates that the cochlea has activity there. The zeros move to the basal as the sound pressure level increases.

Figure 7.9 shows the estimation of $\Re\{Z_{BM}\}$ from known BM displacements [86] ranging from 30 dB to 80 dB. The first order WKB approximation is used. $\epsilon \ll 1$ is almost satisfied [see Fig. 7.9 (a)]. A negative $\Re\{Z_{BM}\}$ region is predicted for each sound pressure level response [see Fig. 7.9 (b)]. Hence, activities are predicted to exist at least up to 80 dB under 16 kHz acoustic simulation in gerbils. As simulation level increases, the BM peak moves to the basal [86], which is reflected in the longitudinal location of zeros of $\Re\{Z_{BM}\}$ in Fig. 7.9 (b). The result is consistent with the activity analysis from the *in vivo* measurement in chinchilla [37].

7.4.2 Frequency-space transformation

In this section, we apply the frequency-space transformation to the spectrum response of the BM [86], and compare the transformed BM profile to the measured BM response over a longitudinal segment [84, 86]. The purpose of this section is to provide an idea on how accurate the transformation is, by taking the advantage that the BM spatial profile is available over a segment.

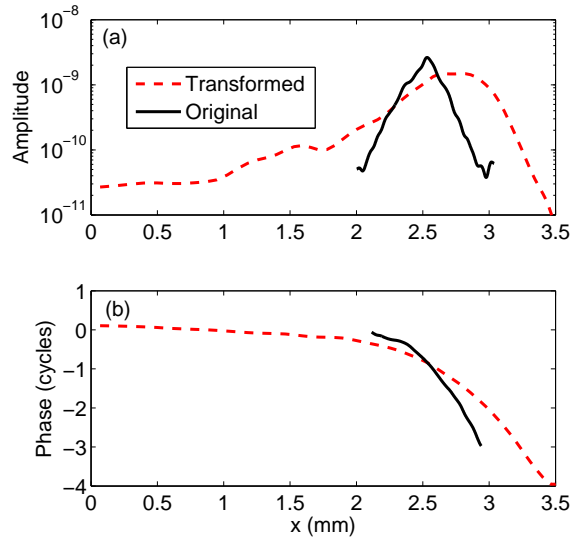


Figure 7.10: Frequency-spatial transformation based on the frequency-space mapping given in Eq. 7.48. The BM spectrum response (dashed lines) comes from Fig. 3 in [86]. The original spatial data (solid lines) comes from Fig. 4 in the same paper. SPL = 40 dB for both data. (a) The BM amplitude. Adjustment (see Eq. 7.46) is implemented. (b) The BM phase in cycles. No adjustment is implemented.

The frequency-location mapping changes in developing gerbils [66]. Muller [66] provided mappings for subadult (11-18 days) and adult (2-4 months) gerbils. The adult

gerbil's mapping from Muller is similar to Greenwood's mapping [42]. In Ren's 2011 experiments [86], the gerbils were about 6 weeks, which were close to adults. Using the mapping from Greenwood [42] (translated 6.4 mm)

$$x = -6.4 + \frac{1}{0.174} \log \left(\frac{f}{0.4} + 0.85 \right), \quad (7.48)$$

where x is in mm, and f is in kHz. The transformation from the frequency domain to the spatial domain is shown in Fig. 7.10, where the amplitude adjustment (see Eq. 7.46) is implemented but not the phase adjustment. The BM spectrum response (dashed lines) comes from Fig. 3 in [86]. The original spatial data (solid lines) comes from Fig. 4 in the same paper. SPL = 40 dB for both data. The 6.4 mm translation is such chosen that the best place in phase is matched between the transformed and the original responses. From Fig. 7.10(a) we can see that the spatial prediction from the frequency-location mapping (dashed lines) gives a broader spatial peak than the original BM spatial data (solid lines). A comparison between Fig. 7.10 (a) and (b) shows that the best places for amplitude and phase do not match in the two data sets. The frequency-location mapping for subadult gerbils from Muller would give a similar situation. Hence, transformation from the BM spectrum data under the frequency-location mapping does not match the original spatial BM profile. An adjustment of the mapping function is necessary if a precise transformation is needed. However, the adjustment is not pre-known without actually knowing the real BM spatial profile.

In the transformation, the best place frequency f_0 for the spectrum data should correspond to the best place x_0 in the spatial data from a single frequency simulation [20]. The best frequency in Fig. 3 in [86] is closer to 15 kHz. We will use an adjusted transformation mapping and compare the result to the 15 kHz spatial response in Fig. 4 in [84]. In this case, the 60 dB spectrum data in [86] will be used since the simulation level in [84] is 60 dB. The adjusted mapping is given by

$$x = -2.370 + \frac{1}{0.31} \log \left(\frac{f}{0.4} + 0.85 \right). \quad (7.49)$$

Figure 7.11 shows the frequency-spatial transformation based on the frequency-space mapping given in Eq. 7.49. The spectrum data come from Fig. 3 (60 dB) in [86] (dashed lines). The spatial data come from Fig. 4 (15 kHz, 60 dB) in [84] (thick solid lines) and Fig. 4 (60 dB) in [86] (thin solid lines). The transformation mapping is matched for the phase in [84]. The amplitude adjustment (see Eq. 7.46) is implemented but not the phase adjustment. After the mapping adjustment in Eq. 7.49, the transformed data

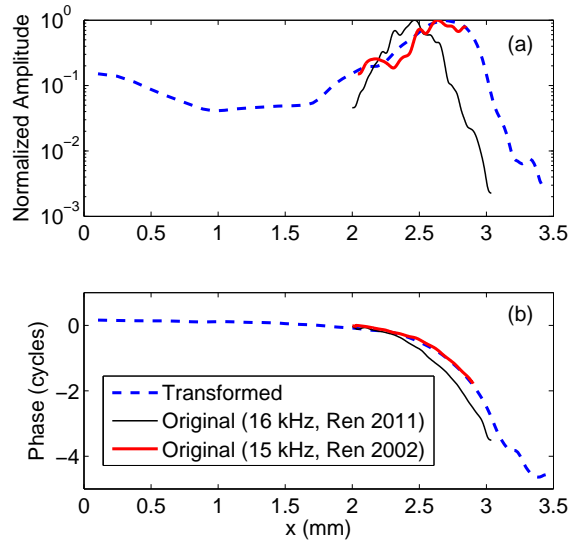


Figure 7.11: Frequency-spatial transformation based on the frequency-space mapping given in Eq. 7.49. Dashed lines: 60 dB BM spectrum response comes from Fig. 3 in [86]. Thin solid lines: BM spatial response under 60 dB 16 kHz acoustic stimulation [86]. Thick solid lines: BM spatial response under 60 dB 15 kHz acoustic stimulation [84]. The transformation mapping is matched for the phase in [84]. (a) The BM amplitude. Adjustment (see Eq. 7.46) is implemented. (b) The BM phase in cycles. No adjustment is implemented.

almost matches the 15 kHz spatial data within the longitudinal segment. However, the transformed response cannot match both the phase and amplitude for the data in [86]. The small peak before the best frequency in the spectrum data in [86] is also transformed into the spatial domain. However, there is not enough information to reconstruct the basal part of the transformed data.

7.5 Discussion

7.5.1 Cross sectional power flow and the real part of the BM impedance

The cross sectional power flow and real part of the BM impedance give consistent information on the activity of the cochlea because a negative damping of the BM suggests additional power injection into the fluid from the cochlear partition. In the passive model, energy dissipation is expected, as shown by the dashed lines in Fig. 7.2 (b) and (d). Consistently, the $\Re\{Z_{BM}\}$ in Fig. 7.6 (b) and (d) (see the solid lines) is positive throughout. In the active model, cross sectional energy increases basal to the best place, and decreases apical to the best place [Fig. 7.2 (b) and (d), see the solid lines]. The peaks of the BM

amplitude and the cross sectional power flow line up exactly. Consistently, the $\Re\{Z_{BM}\}$ in Fig. 7.4 (b) and (d) (see the solid lines) is negative basal to the best place (about 3.1 mm), and moves to positive when it crosses the best place. Hence, in an active model, the best place is the spatial location beyond which the active process stops adding energy to the cochlea. Also, the predicted active cross sectional power flow in Fig. 7.2 (d) shows that the power starts to increase when it closes to $x = 2$ mm. Indeed, the solid line in Fig. 7.8 (b) or (d) indicates that $\Re\{Z_{BM}\}$ turns to negative when it closes to $x = 2$ mm.

7.5.2 Wave number approximation

The wave number is an important quantity in describing the wave propagation in the cochlea. Due to the spatial variation of the property of the BM, as well as the cochlear turning at different frequencies and physiological conditions, the wavenumber in the cochlea varies with the longitudinal location x , the stimulation frequency ω , and the healthy condition of the cochlea. Hence, there is no a single constant k that can describe the motion of the cochlea. In the cochlear modeling, the wave number can either be represented by a function in x indicating the local property at each position x , i.e., the local wave number [25], or an integration over k from $-\infty$ to ∞ for each constant k [17].

Based on either long or short wave approximation, the BM motion can be approximated by being related to different powers of the local wavenumber [37]. For known BM motion, the wavenumber can then be approximated based on the relation between the BM motion and the local number [37]. In this work, we also approximate the local wavenumber from the known BM response over a segment. However, we do not assume any long or short wave in the model. The relation between the BM displacement and the wave number is solved from Eq. 7.6 by using asymptotic expansion [57]. The solution is given in Eqs. 7.7 and 7.8. By either using the first or the second order WKB approximation, we can estimate the local wavenumber $k_x(x)$ by fitting with the known BM spatial motion. If a first order approximation is of sufficient accuracy, meaning that the extra terms in Eq. 7.14 is negligible, then the first and second order approximations should have a similar estimation on $k_x(x)$. Such a condition would require $k'_x/k_x^2 \sim o(1)$ to hold, which is the condition for the entire WKB method to be valid in a cochlear problem [25].

Based on the data fitting in this work, the first order WKB BM approximation is good for the active model (see Fig. 7.4(a) and (c), where the value of ϵ overlap for the two orders of approximation). In the passive model, for both the short (Fig. 7.5) and long (Fig. 7.6) BM segments under use, the local wave number $k_x(x)$ approximated by the two orders are always different, especially in the basal portion of each segment. Hence, $k'_x/k_x^2 \sim o(1)$ does not hold in the passive cochlea, which can also be roughly read from ϵ

in Figs. 7.4-7.6 (a) and (c). The value of ϵ in the active model is in general smaller than that in the passive model. However, the exact value of ϵ for which $k'_x/k_x^2 \sim o(1)$ to hold is hard to be established, as there is no criteria for setting a boundary for ϵ .

7.5.3 Impedance estimation

The real part of the BM impedance is the effective damping of the BM, the sign of which suggests the local activity of the cochlea. In order to obtain the impedance, the pressure difference across the BM must be obtained, in addition to the known BM response. As mentioned in Sec. 7.3.1.3, the pressure approximation starts with the assumption that $d\alpha_m/dx$ is negligible, which is violated if $dk(x)/dx$ is not negligible compared to $k^2(x)$. Although it is relatively hard to determine the negligibility of $dk(x)/dx$ based on ϵ , we can, however, compare the difference between the first and second order of the WKB BM approximation. If the $k_x(x)$ fitted from the first order WKB (Eq. 7.10) is the same as that fitted from the second order WKB (Eq. 7.14), then $k'_x/k_x^2 \sim o(1)$ is thought to be valid, which leads to Eq. 7.35. One more similar assumption is needed to obtain the expression for α_m given in Eq. 7.37. Hence, the final effective height (Eq. 7.42, see also [100, 37]) is based on the first order WKB approximation. If the approximation on d/dx is not introduced, more intensive calculation is involved, which includes solving a nonlinear second order ordinary differential equation. However, the boundary condition for the differential equation is yet unknown in the inverse problem. Lim and Steele [58] solved a forward problem by using WKB in the short wave region and the Runge-Kutta method in the long wave region to handle the limitation of the WKB method.

Figure. 7.4-7.6 (b) and (c) show that the impedance approximated by the WKB is valid for the active model, but not accurate in the passive model, especially for the passive case where a longer BM segment is utilized (a long wave region is involved). There may have multiple reason for the model to fail in the passive case, for example, the wave reflection may be important, although previous investigation did not find the importance [25]. Here, we attribute the inaccuracy to the approximation that d/dx is neglected when calculating the effective height h_{eq} . Although the sign of $\Re\{Z_{BM}\}$ is right for the passive model where only a short segment (does not contain the best place) of the BM is used (Fig. 7.5), the amplitudes are still not satisfactory compared to the FEM data. It is hard to tell where the prediction of $\Re\{Z_{BM}\}$ in Fig. 7.5 is robust and shows the real mechanism of a passive cochlear behind, or just due to luck to have the right sign. Overall, using the WKB method to estimate the BM impedance has its limitation, as mentioned by de Boer [25] as well.

For far, the current WKB model predicts activity in an sensitive gerbil cochlea for

at least up to 80 kHz, as shown in Fig. 7.9. The zeros in $\Re\{Z_{BM}\}$ move to the base as the intensity increases. Fisher *et al.* performed experiments in chinchilla and reached a similar conclusion [37]. In their impedance calculation, the effective height is essentially the same as Eq. 7.42 used here, although a different scheme was used to estimate the local wavenumber.

7.5.4 Pressure recovery by using the FEM

Although the recovery method itself is checked to be valid, provided that the given BM profile (from the very base up to the evanescent region) and the stapes motion are exactly correct, the method is hard to implement in reality. As seen from Figs. 7.7 and 7.8, a tiny difference in the phase of the BM profile results in a huge error in the sign of $\Re\{Z_{BM}\}$. The recovered intracochlear pressure is very sensitive to the given essential boundary conditions.

In this example (Figs. 7.7 and 7.8), the ‘right’ phase is known since we have the exact spatial BM output from the FEM model. Therefore, we can tune the value of α to adjust the transformed BM response as much as possible, as seen in the difference in the recovered pressure based on different adjustments. However, in reality, the BM spatial response is only known in a small segment around the best place [84, 86], and no data is available at the very base of the cochlea. Hence, it is unlikely to finely tune the transformation parameter and make the prediction right. For this reason, we did not show the recovered pressure and an estimation for $\Re\{Z_{BM}\}$ based on the transformed experimental spatial data in Fig. 7.11.

7.5.5 Transformation by using scaling symmetry

By assuming scaling symmetry, we can potentially transform the spectrum BM responses measured at x_0 to a spatial response with underlined simulation frequency f_0 associated with x_0 , by using the frequency-location mapping. The exponent in the mapping (e.g., the value of a in Greenwood [42], could be different for different bases) determines the slope of the mapping relation. In the reverse problem that the spectrum data is transformed to the spatial data, the exponent determines the width of the peak of the BM amplitude and the slope of the phase. Figure 7.10 shows that by using a frequency-location mapping from gerbils (either young or adult), the transformed phase is flatter than the measured spatial phase, and the peak of the amplitude is wider than the measured spatial data. Hence, the scaling symmetric does not work directly without modification.

A better transformation can be obtained by tuning the exponent (with the help from the measured BM data over of spatial segment), as shown in Fig. 7.11 (see the dashed line and the thin solid line). Despite any difference in experimental conditions or individual difference in cochleae, Fig. 7.11 indicates that after some proper tuning of the mapping parameters, the transformed response is close to the original spatial responses if the underlined x_0 and f_0 are consistent. If x_0 and f_0 are not consistent, then based on the data shown in Figs. 7.10 and 7.11, the BM amplitude and phase cannot be well-transformed in a single mapping.

In the spectrum data, multiple peaks in amplitude can be seen below the best frequency (e.g., Fig. 3 in [86]). These peaks are also transformed into the spatial response as shown in Fig. 7.11(a). However, at this point, we do not have enough information to determine whether these peaks should exist in the spatial domain, or how should the basal response be re-constructed, in addition to the adjustment proposed by de Boer [20].

7.6 Conclusion

In this work, both the cross sectional fluid power flow in the SV and the real part of the BM impedance are calculated by using the predicted data from the FEM model described in Chapter II. The longitudinal variation of the cross sectional power flow implies the power dissipation or injection, respectively, from the organ of Corti due to the damping or the active cochlear process. The real part of the BM impedance is the resistance of the BM, the sign of which implies either dissipation or activity of the cochlea. Thus, the cross sectional fluid power flow and the real part of the BM impedance provide the same information on the cochlear activity. The FEM model prediction indicates that energy is dissipated in a passive cochlea and in an active cochlea, activity exists basal to the best place, and terminates at the best place.

In addition, this work studies an inverse problem: Find the BM impedance for a given BM response over a region. Two methods are used for the inverse problem: the WKB method and the pressure recovery through the boundary value FEM problem. The WKB methods requires two steps to find the BM impedance: wavenumber estimation and pressure solving. In the wavenumber estimation, an asymptotic expansion is used to fit the wavenumber. In this way, no assumption on long or short waves on the BM is needed. In the pressure solving step, the spatial variation of all the quantities are neglected as an approximation for solving differential equations. The WKB method fails in the long wave region, and thus solving a full differential equation is required in that region [58]. For the pressure recovery through the boundary value FEM problem, an estimation of

the BM profile is required from the base to the location beyond the best place. This pressure recovery method is found to be very sensitive to the given boundary conditions. Thus, the method can hardly be implemented in reality where the BM response is roughly estimated.

This work also implements the WKB method to the experimental data from Ren *et al.* [86]. Activity is predicted by the model for simulation levels at least up to 80 dB. The experimental data [84, 86] also suggests that adjustments should be made before the ‘scaling invariance’ is implemented. However, the guideline for adjustments is not clear at this moment because the exact spatial pattern of the BM is unknown. Direct measurement of the BM spatial profile over a longer region would be helpful to understand the difference between spectrum and spatial responses.

The innovation of this work is the approximation of the local wavenumber by using asymptotic expansion without evoking assumptions on long or short waves. In addition, the FEM model is used to check the accuracy of the WKB method and the boundary-value-problem for intracochlear pressure recovery, which provides a self-consistent criterion for model validation.

CHAPTER VIII

Conclusion

In this work, the micro and macro fluidic effects in cochlear mechanics are studied. Although the effects from two scales are not analyzed in a coupled way, the method of coupling is developed, which enables further studies on coupled waves of different scales in the cochlea. The following summarizes this work.

8.1 Viscous boundary layer correction

In Chapter III, a viscous boundary layer approximation is formulated to include fluid viscosity in fluid-structure coupling problems. The method can be easily implemented in FEM to convert an inviscid acoustic model solved for pressure to a viscous one without changing the primary variable. Thus, the total degrees of freedom is unchanged and the size of the problem is well-controlled. The modified boundary condition has additional terms written in second order in-plane derivatives of the pressure evaluated at the boundaries. In the FEM model, the additional terms act as added damping in the stiffness matrix. Although in this work examples are for interior flows, the thin BL approximation is applicable to exterior flows as well.

The innovation of this work is that the FEM implementation of shear viscous boundary layer correction is extended to the thick boundary layer case where a coupling element between two parallel surfaces is required (the FEM implementation of thin viscous boundary layer correction is in Cheng [8]). The method is also implemented to a 3-D structural acoustic model. The prediction from the developed boundary layer correction method matches well with the prediction from the 3-D Navier-Stokes model. The computational efficiency is retained in the scalar field model. This chapter closes the problem of modeling shear viscosity in a scalar representation for a pair of parallel surfaces for both thin and thick viscous boundary layer thickness.

8.2 Macro wave propagation in the cochlea

Chapters V and VI study the macro wave propagation in the cochlea. The cochlea is stimulated by different methods to analyze the direction of wave propagation and the existence of a compression or a traveling wave. Results show that if a volumetric change of the intracochlear fluid is associated with a simulation method (eg., apical excitation), then both a compression and a traveling wave are present. In this case, the cochlear response is similar to the response to an acoustic stimulation that the traveling wave propagates forward along the BM. The forward traveling wave generates a forward group delay, denoted as t_g , on the BM at each longitudinal location for a given frequency.

If no volumetric change of the intracochlear fluid is associated with a simulation method, for example, an internal force excitation on the BM, then no compression wave is generated. In this case, a traveling dominates in the cochlea, which propagates in both directions away from the location of the excitation. For the backward traveling wave, it will be reflected at the stapes and then re-propagates forwards to amplify the motion of the BM. The backward and reflected forward waves in total generate a round-trip group delay $2t_g$. In addition, we found that the BM motion in an active cochlea is one-side amplified: the short-time motion is not directly amplified by an impulse internal force applied on the BM; rather, the BM is amplified at nearly twice the forward group delay from the reflected traveling wave (from the cochlear base) generated by the internal force. The amplitude of the reflected wave decreases dramatically with decreasing activity. In a passive cochlea, the principle of reciprocity holds because the final linear FEM matrix is symmetric. A structural acoustic formulation is also derived to prove the reciprocity (see Appendix G). If an excitation method gives rise to both an intracochlear volumetric change and a net force on the BM, then we will see a combined effect from an acoustic response and a round-trip group delay.

In an active cochlear model, perturbation on the active component will change the cochlear response. It is interesting to note that instability occurs when the perturbation is too high. If a perturbation is deterministic based on a half-wavelength pattern, or properly filtered from a random data, then the spatial characteristic of the perturbation provides multiple sources of reflection such that the reflected waves are enhanced and echoes are present in the cochlear response. More work is needed to precisely understand the relation between echoes and the pattern of perturbations.

The innovation of this part of work is using numerical experiments to study the emitted wave types under different prescribed excitations. The structural acoustic reciprocity in a passive cochlea and the one-side amplification in an active cochlea are discovered. These

two relations are fundamental properties of wave propagation in the cochlea. In addition, we showed that intracochlear volumetric change will give rise to a compression wave in the cochlea. Echoes in the temporal responses may be contributed by both the compression and the traveling waves, as well as the perturbation on the active component of the cochlear partition.

8.3 Micro fluid-structure interaction

In Chapter IV, the viscous flow in the sub-TM region is modeled. The flow is coupled to the motion of the TM, the RL, the HBs of IHCs and OHCs, the HS, the fluid in the sulcus, and the fluid in the SV. The micro fluid is modeled in a 1-D domain running in the radial direction with pressure as the primary variable. The essential part of the fluid model is the derivative at the boundary of each 1-D element written in terms of the gradient of the pressure. The analytical boundary conditions are derived from the conservation of mass, which takes into account the viscous effect of the fluid, the fluid-structure interaction, the dynamics of the structures, and the complex geometry of the surrounding structures. Primary results show that although the height of the TM-RL gap is less than the viscous boundary layer thickness, fluid flow in the radial direction is still possible so as to stimulate the IHC HB. The IHC HB is mainly driven by the pressure difference across the HB. The displacement of the IHC HB has a similar profile as the displacement of the rest structures in the OoC.

The method developed here can be implemented into a 3-D cochlear model so as to provide a tool to determine the spatial dependence of flow modality in the sub-TM region; determine the relative importance of motility (either OHC somatic or HB motility) on IHC HB stimulation; analyze the role of the HS and the noise to signal ratio in the hearing, and evaluate the importance of the shearing and bending effects on the TM. In addition, the cross sectional model can be used to simulate the electromechanical experiments utilizing a cochlear segment (e.g., [6, 7, 69]).

The innovation of this work is that the model overcomes the challenge of modeling multiscale problems by combining both analytical and numerical methods. The viscous structure-fluid coupling effect on complex geometries in the IHC HB, HS, and OHC HB is solved analytically. The analytical expressions serve as boundary conditions to the FEM model. This chapter provides a method for bridging the gaps between scales and can further be used to the global cochlear model to understand the various working mechanisms of the cochlea.

8.4 Cochlear activity

In Chapter VII, both the cross sectional fluid power flow in the SV and the real part of the BM impedance are calculated by using the predicted data from the FEM model described in Chapter II. The longitudinal variation of the cross sectional power flow implies the power dissipation or injection, respectively, from the organ of Corti due to the damping or the active cochlear process. The real part of the BM impedance is the resistance of the BM, the sign of which implies either dissipation or activity of the cochlea. Thus, the cross sectional fluid power flow and the real part of the BM impedance provide the same information on the cochlear activity. The FEM model prediction indicates that energy is dissipated in a passive cochlea and in an active cochlea, activity exists basal to the best place, and terminates at the best place.

In addition, this work studies an inverse problem: Find the BM impedance for a given BM response over a region. Two methods are used for the inverse problem: the WKB method and the pressure recovery through the boundary value FEM problem. The WKB method requires two steps to find the BM impedance: wavenumber estimation and pressure solving. In the wavenumber estimation, an asymptotic expansion is used to fit the wavenumber. In this way, no assumption on long or short waves on the BM is needed. In the pressure solving step, the spatial variation of all the quantities are neglected as an approximation for solving differential equations. The WKB method fails in the long wave region, and thus solving a full differential equation is required in that region [58]. For the pressure recovery through the boundary value FEM problem, an estimation of the BM profile is required from the base to the location beyond the best place. This pressure recovery method is found to be very sensitive to the given boundary conditions. Thus, the method can hardly be implemented in reality where the BM response is roughly estimated.

This work also implements the WKB method to the experimental data from Ren *et al.* [86]. Activity is predicted by the model for simulation levels at least up to 80 dB. The experimental data [84, 86] also suggests that adjustments should be made before the ‘scaling invariance’ is implemented. However, the guideline for adjustments is not clear at this moment because the exact spatial pattern of the BM is unknown. Direct measurement of the BM spatial profile over a longer region would be helpful to understand the difference between spectrum and spatial responses.

The innovation of this work is the approximation of the local wavenumber by using asymptotic expansion without evoking assumptions on long or short waves. In addition, the FEM model is used to check the accuracy of the WKB method and the boundary-

value-problem for intracochlear pressure recovery, which provides a self-consistent criterion for model validation.

8.5 Future work

Many problems in the cochlea remain unsolved. One of the goals of the cochlear research is to understand the working mechanism of the cochlea. In the following, we give a brief discussion on what can be done based on the work in this dissertation:

(1) A problem that directly related to the TM-RL gap fluid modes: both the shearing and squirting fluid modes are hypothesized to be possible modes for the IHC HB activation, but it is unclear the role each plays. Here, based on the elastic model for the TM and the coupling between the fluid and the TM, we can predict the fluid mode in the gap.

(2) A long-debated question as for the OHC somatic motility and OHC HB electric motility which one player a more important role in the active hearing. This problem has been studied widely, but not under the full consideration of the coupled fluid-stereocilia interaction. Here, based on the fluid model for the TM-RL gap, we can take into account the contribution of the fluid viscosity and pressure on the dynamics of the OHC HB.

(3) Study the effect of the HS on hearing, including the noise-sound ratio and the hearing optimization (if exists). The distance between the HS and the IHC HB plays an important role. This distance changes with time as the OoC deforms. Hence, a nonlinear model of the fluid-structure interaction in the surrounding areas of the HS and IHC HB is required.

(4) Study the interaction between the macro and the micro fluidic effects in the cochlea. We have seen that in an active cochlea, the temporal BM response exhibits ringings that absent in a passive cochlea. Since the micro-fluid is coupled to the macro-waves in the cochlea, the OHC, OHC HB, and IHC HB must also respond to this periodic ringings. This may related to the hypothetical cycle-by-cycle amplification of the active hearing process. The model developed in this work would provide a tool to investigate the possible mechanism of the amplification in hearing.

(5) Develop a better model to assess the cochlear activity based on the BM profile over a small segment. In this work, we showed that the WKB method does not work if the BM segment contains a long-wave region. The problem can be handled if the relevant differential equation is solved numerically, instead of using the WKB method. However, boundary conditions are needed for solving the second order differential equation, which are unknown from experiments. Hence, either a reasonable approximation for the boundary condition is required, or an alternative method for activity evaluation is needed.

APPENDICES

APPENDIX A

Inclusion of in-plane structure motion in the shear viscous boundary layer correction

Here we illustrate how to include and implement in-plane structure motion in the model by using the thin BL case (derived in 3.2.1.1) applied on the $z = 0$ surface as an example.

Suppose the structure on the $z = 0$ surface has displacement $U(x, y)$, $V(x, y)$, and $W(x, y)$ in the x , y , and z directions, respectively. Then the non-slip boundary condition on $z = 0$ in Eq. 3.9 is replaced by

$$v_x = \frac{\partial \Phi}{\partial x} - \frac{\partial \Psi_2}{\partial z} = j\omega U(x, y), \quad v_y = \frac{\partial \Phi}{\partial y} + \frac{\partial \Psi_1}{\partial z} = j\omega V(x, y), \quad \text{on } z = 0. \quad (\text{A.1})$$

Taking the solution of Ψ_1 and Ψ_2 as given in Eq. 3.10, the two coefficients A_1 and A_2 are solved as

$$A_1(x, y) = -\frac{1}{\gamma} \frac{\partial \Phi}{\partial y} \Big|_{z=0} + \frac{j\omega}{\gamma} V, \quad A_2(x, y) = \frac{1}{\gamma} \frac{\partial \Phi}{\partial x} \Big|_{z=0} - \frac{j\omega}{\gamma} U. \quad (\text{A.2})$$

Following the same derivation in 3.2.1.1, Eq. 3.13 is now written as

$$\frac{\partial P}{\partial z} + \frac{1}{\gamma} \nabla_{xy}^2 P = \frac{1}{\alpha} \rho_f \omega^2 \left(W + \frac{1}{\gamma} \frac{\partial U}{\partial x} + \frac{1}{\gamma} \frac{\partial V}{\partial y} \right), \quad \text{on } z = 0, \quad (\text{A.3})$$

which is the thin BL correction on $z = 0$ with both out-plane and in-plane structure motion.

For the FEM implementation, substituting Eq. A.3 into the surface integral in Eq. 3.26

for $z = 0$, we have

$$- \int_{z=0} \bar{P} \frac{\partial P}{\partial z} dx dy = \frac{1}{\gamma} \int_{z=0} \bar{P} \nabla_{xy}^2 P dx dy - \frac{1}{\alpha} \rho_f \omega^2 \int_{z=0} \bar{P} \left(W + \frac{1}{\gamma} \frac{\partial U}{\partial x} + \frac{1}{\gamma} \frac{\partial V}{\partial y} \right) dx dy. \quad (\text{A.4})$$

Equation A.4 differs from Eq. 3.27 (for the $z = 0$ surface) by having the following two additional terms (forget about the factor $\rho_f \omega^2 / \alpha$ for now):

$$\frac{1}{\gamma} \int_{z=0} \bar{P} \frac{\partial U}{\partial x} dx dy \quad \text{and} \quad \frac{1}{\gamma} \int_{z=0} \bar{P} \frac{\partial V}{\partial y} dx dy. \quad (\text{A.5})$$

Taking the first term for an example (the second term follows in the same way), we can evaluate it by integration by part:

$$\frac{1}{\gamma} \int_{z=0} \bar{P} \frac{\partial U}{\partial x} dx dy = \frac{1}{\gamma} \int_0^{L_y} \left(\int_0^{L_x} \bar{P} \frac{\partial U}{\partial x} dx \right) dy = \frac{1}{\gamma} \int_0^{L_y} \left(\bar{P} U \Big|_{x=0}^{x=L_x} - \int_0^{L_x} U \frac{\partial \bar{P}}{\partial x} dx \right) dy. \quad (\text{A.6})$$

Both $U|_{x=0}$ and $U|_{x=L_x}$ vanish since they are either evaluated on the rigid boundary (if the structure does not occupy the whole x dimension) or due to the simply supported boundary condition for the structure. Hence

$$\frac{1}{\gamma} \int_{z=0} \bar{P} \frac{\partial U}{\partial x} dx dy = - \frac{1}{\gamma} \int_{z=0} U \frac{\partial \bar{P}}{\partial x} dx dy, \quad (\text{A.7})$$

which is ready to be incorporated into the FEM scheme.

Note that Eq. A.7 is of order δ (see 3.2.3.1 for more detail) compared to the W term in Eq. A.4. Hence, the contribution of the shear viscous effect from the in-plane displacement is a second order correction.

APPENDIX B

Asymptotic analysis

Consider a generic surface with normal coordinate n and in-plane (tangent) coordinates s_1 and s_2 . Inside the BL, we can scale the normal coordinate with the BL thickness δ [49] as n/δ . Let L be a characteristic scale of the surface. $\delta \ll L$ is satisfied. Then we can introduce the following non-dimensional variables,

$$s_1^* = \frac{s_1}{L}, \quad s_2^* = \frac{s_2}{L}, \quad n^* = \frac{n}{\delta}, \quad \epsilon = \frac{\delta}{L} \ll 1, \quad P^* = \rho_f \omega^2 L^2 P. \quad (\text{B.1})$$

On the rigid walls $\partial\Omega \setminus \Gamma$, Eq. 3.17 becomes

$$\frac{\partial P^*}{\partial n^*} + \frac{1}{\sqrt{2j}} \epsilon^2 \left(\frac{\partial^2 P^*}{\partial s_1^{*2}} + \frac{\partial^2 P^*}{\partial s_2^{*2}} \right) = 0. \quad (\text{B.2})$$

Expand P^* with the small parameter ϵ ,

$$P^* = P_0^* + \epsilon P_1^* + \epsilon^2 P_2^* + \dots. \quad (\text{B.3})$$

Substitution of Eq. B.3 into Eq. B.2 gives the following orders of equations,

$$\epsilon^0 : \quad \frac{\partial P_0^*}{\partial n^*} = 0, \quad (\text{B.4})$$

$$\epsilon^1 : \quad \frac{\partial P_1^*}{\partial n^*} = 0, \quad (\text{B.5})$$

$$\epsilon^2 : \quad \frac{\partial P_2^*}{\partial n^*} + \frac{1}{\sqrt{2j}} \left(\frac{\partial^2 P_0^*}{\partial s_1^{*2}} + \frac{\partial^2 P_0^*}{\partial s_2^{*2}} \right) = 0. \quad (\text{B.6})$$

Hence, for the first and second order approximation we have $\partial P/\partial n = 0$ on the boundary. Equation 3.17 represents a higher order viscous BL correction.

APPENDIX C

Derivation of longitudinal fluid velocity in the acoustic model

In the acoustic model, pressure is the only degree of freedom in the fluid domain, and thus the fluid velocity/ displacement is not explicitly solved. In this part, we derive the longitudinal fluid velocity/displacement in the acoustic model with viscous BL approximation on the z surfaces.

In case 1 (thin viscous BL), when BL correction is applied on $z = 0$ only (Eq. 3.13), Eq. 3.4 gives

$$v_x = \frac{\partial \Phi}{\partial x} - \frac{\partial \Phi}{\partial x} \Big|_{z=0} e^{\gamma z}. \quad (\text{C.1})$$

The correction term in Eq. C.1 (second term on the RHS) decays exponentially away from $z = 0$ since the real part of γ is chosen to be negative. When BL correction is applied on $z = L_z$ only (Eq. 3.16), the corresponding velocity v_x is,

$$v_x = \frac{\partial \Phi}{\partial x} - \frac{\partial \Phi}{\partial x} \Big|_{z=L_z} e^{\gamma(L_z-z)}, \quad (\text{C.2})$$

Again, the correction term in Eq. C.2 decays exponentially away from $z = L_z$.

If corrections at $z = 0$ and $z = L_z$ are applied simultaneously, the fluid velocity v_x can be approximated as,

$$v_x = \frac{\partial \Phi}{\partial x} - \frac{\partial \Phi}{\partial x} \Big|_{z=0} e^{\gamma z} - \frac{\partial \Phi}{\partial x} \Big|_{z=L_z} e^{\gamma(L_z-z)}. \quad (\text{C.3})$$

which is a linear superposition of the contribution of viscous correction at each surface. When the BL is thin, $e^{\gamma z}$ (or $e^{\gamma(L_z-z)}$) essentially vanishes at $z = L_z$ (or $z = 0$). Hence, Eq. C.3 satisfies the non-slip boundary condition in an approximated manner.

In case 2 (thick viscous BL), v_x is

$$v_x = \frac{\partial \Phi}{\partial x} + \beta_2 \left[\frac{\partial \Phi}{\partial x} \Big|_{z=0} \sinh \gamma(L_z - z) + \frac{\partial \Phi}{\partial x} \Big|_{z=L_z} \sinh \gamma z \right]. \quad (\text{C.4})$$

Once the velocity v_x is obtained, the displacement u_x is given by $u_x = v_x/j\omega$.

APPENDIX D

Shape functions for the 1-D elements

In this work, both the elastic TM model and the TM-RL fluid gap model are discretized into 2-nodes 1-D elements in the radial direction. For a standard notation, let x_1 and x_2 be the global coordinate of each element. $h = x_2 - x_1$ is the element size. Let $\xi \in [-1, 1]$ be the local coordinate for each element. The transformation between x and ξ is given by

$$\xi(x) = \frac{2x - x_1 - x_2}{h}, \quad x(\xi) = \frac{h\xi + x_1 + x_2}{2}. \quad (\text{D.1})$$

Thus we have the following scaling relation

$$dx = \frac{h}{2}d\xi, \quad \frac{d}{dx} = \frac{2}{h} \frac{d}{d\xi}. \quad (\text{D.2})$$

The element for the fluid gap is the same as the element for the elastic TM shearing model. Take the elastic TM shearing u^s for example. In each element,

$$u^s = N_1 u_1^s + N_2 u_2^s, \quad (\text{D.3})$$

where

$$N_1 = -\frac{1}{2}\xi + \frac{1}{2}, \quad N_2 = \frac{1}{2}\xi + \frac{1}{2}. \quad (\text{D.4})$$

Both N_1 and N_2 take on the value 1 locally and 0 at the other node. Some typical evaluations in the model related to the shape function at the element level are

$$\int_0^h N_{i,x} N_{j,x} dx = \begin{pmatrix} \frac{1}{h} & -\frac{1}{h} \\ -\frac{1}{h} & \frac{1}{h} \end{pmatrix}, \quad \int_0^h N_i N_{j,x} dx = \begin{pmatrix} -\frac{1}{2} & \frac{1}{2} \\ -\frac{1}{2} & \frac{1}{2} \end{pmatrix}, \quad (\text{D.5})$$

$$\int_0^h N_i N_j dx = \begin{pmatrix} \frac{h}{3} & \frac{h}{6} \\ \frac{h}{6} & \frac{h}{3} \end{pmatrix}, \quad \int_0^h N_i ds = \begin{pmatrix} \frac{h}{2} \\ \frac{h}{2} \end{pmatrix}, \quad \int_0^h N_{i,s} ds = \begin{pmatrix} -1 \\ 1 \end{pmatrix}. \quad (\text{D.6})$$

For the elastic TM bending w^b , in each element,

$$w^b = N_1^h w_1^b + N_2^h \phi_1 + N_3^h w_2^b + N_4^h \phi_2, \quad (\text{D.7})$$

$$\phi = N_{1,\xi}^h w_1^b + N_{2,\xi}^h \phi_1 + N_{3,\xi}^h w_2^b + N_{4,\xi}^h \phi_2, \quad (\text{D.8})$$

where

$$\begin{aligned} N_1^h &= \frac{1}{4} (\xi^3 - 3\xi + 2), & N_2^h &= \frac{h}{8} (\xi^3 - \xi^2 - \xi + 1), \\ N_3^h &= \frac{1}{4} (-\xi^3 + 3\xi + 2), & N_4^h &= \frac{h}{8} (\xi^3 + \xi^2 - \xi - 1). \end{aligned} \quad (\text{D.9})$$

Both N_1^h and N_3^h take on the value 1 locally and 0 at the other node; their first order derivatives vanish at both nodes. Both N_2^h and N_4^h vanish at both nodes; their first order derivatives take on the value 1 locally and 0 at the other node. The superscript ‘ h ’ indicates the Hermite cubic shape functions. Some typical evaluations in the model related to the shape function at the element level are

$$\int_0^h N_i^h N_j dx = \begin{pmatrix} \frac{7h}{20} & \frac{3h}{20} \\ \frac{h^2}{20} & \frac{h^2}{30} \\ \frac{3h}{20} & \frac{7h}{20} \\ -\frac{h^2}{30} & -\frac{h^2}{20} \end{pmatrix}, \quad \int_0^h N_i^h dx = \begin{pmatrix} \frac{h}{2} \\ \frac{h^2}{12} \\ \frac{h}{2} \\ -\frac{h^2}{12} \end{pmatrix}, \quad (\text{D.10})$$

$$\int_0^h N_i^h N_j^h dx = \begin{pmatrix} \frac{13h}{35} & \frac{11h^2}{210} & \frac{9h}{70} & -\frac{13h^2}{420} \\ \frac{11h^2}{210} & \frac{h^3}{105} & \frac{13h^2}{420} & -\frac{h^3}{140} \\ \frac{9h}{70} & \frac{13h^2}{420} & \frac{13h}{35} & -\frac{11h^2}{210} \\ -\frac{13h^2}{420} & -\frac{h^3}{140} & -\frac{11h^2}{210} & \frac{h^3}{105} \end{pmatrix}, \quad (\text{D.11})$$

$$\int_0^h N_{i,xx}^h N_{j,xx}^h dx = \begin{pmatrix} \frac{12}{h^3} & \frac{6}{h^2} & -\frac{12}{h^3} & \frac{6}{h^2} \\ \frac{6}{h^2} & \frac{4}{h} & -\frac{6}{h^2} & \frac{2}{h} \\ -\frac{12}{h^3} & -\frac{6}{h^2} & \frac{12}{h^3} & -\frac{6}{h^2} \\ \frac{6}{h^2} & \frac{2}{h} & -\frac{6}{h^2} & \frac{4}{h} \end{pmatrix}. \quad (\text{D.12})$$

Followings are integrals related to the above shapes functions; they are listed here for

records. For $q(s)$ defined in Eq. 4.15, we have

$$\int_0^{L_{hb_2}} q(s) \begin{pmatrix} N_1 \\ N_2 \end{pmatrix} ds = \begin{pmatrix} \frac{h_{hb_2}^2}{3L_{Ro}} + \frac{h_{hb_2}}{2} \\ \frac{h_{hb_2}^2}{6L_{Ro}} + \frac{h_{hb_2}}{2} \end{pmatrix}, \quad \int_{L_{hb_2}}^{L_{IHC}} q(s) \begin{pmatrix} N_1 \\ N_2 \end{pmatrix} ds = \begin{pmatrix} \frac{h_{IHC} - L_{hb_2}}{3} \\ \frac{h_{IHC} - L_{hb_2}}{6} \end{pmatrix}. \quad (D.13)$$

For the TM rigid bending related integrals:

$$\int_0^{L_{hb_2}} \frac{s - L_{tm}}{\ell_{tm}} \begin{pmatrix} N_1 \\ N_2 \end{pmatrix} ds = \frac{L_{hb_2}}{6\ell_{tm}} \begin{pmatrix} L_{hb_2} - 3L_{tm} \\ 2L_{hb_2} - 3L_{tm} \end{pmatrix}, \quad (D.14)$$

$$\int_{L_{hb_2}}^{L_{IHC}} \frac{s - L_{tm}}{\ell_{tm}} \begin{pmatrix} N_1 \\ N_2 \end{pmatrix} ds = \frac{L_{Ro}}{6\ell_{tm}} \begin{pmatrix} L_{IHC} + 2L_{hb_2} - 3L_{tm} \\ 2L_{IHC} + L_{hb_2} - 3L_{tm} \end{pmatrix}. \quad (D.15)$$

APPENDIX E

Extended derivations for a cross section

Here we provide some additional derivations for the cross section model that are too long to be included in the main text.

The expression $(W^b - u_{rl}^b)$ is expanded as

$$\begin{aligned} W^b(s) - u_{rl}^b(s) = & -D_1 \cos(\theta_1 - \alpha) u_{bm} - \frac{(s - L_{tm})}{\ell_{tm}} u_{tmb}^0 + w^b(s) \\ & - q(s) [B_{21} u_{bm} + B_{23} (u_{tms} + u_2^s) + (u_{tmb}^0 + w_2^b)] . \end{aligned} \quad (\text{E.1})$$

Variation of Π with respect to u_{bm} yields,

$$\begin{aligned} & \frac{b}{2} [-\omega^2 M_{bm} - j\omega C_{bm} + K_{bm}] u_{bm} + [K_{hb} \alpha_{21}^2 + K_{rl} \beta_{21}^2 + K_{ohc} (C_{21} + E_{21})^2] u_{bm} \\ & + [K_{hb} \alpha_{21} \alpha_{23} + K_{rl} B_{23} \beta_{21} + K_{ohc} C_{23} (C_{21} + E_{21})] (u_{tmb} + u_2^s) \\ & + [K_{hb} \alpha_{21} \alpha_{24} + K_{rl} B_{24} \beta_{21} + K_{ohc} C_{24} (C_{21} + E_{21})] (u_{tmb}^0 + w_2^b) \\ & + \epsilon_3 (\phi_{ohc} - \phi_{st}) (C_{21} + E_{21}) + \frac{1}{2} [p_{\Omega_1}|_{s=L_{hb_2}} - p_{\Omega_2}|_{s=L_{hb_2}}] h_{hb} A_{21} + \sum_m (p_m^{SV} - p_m^{ST}) \mu_m \\ & - B_{21} \int_0^{L_{IHC}} p_{gap} q(s) ds - D_1 \cos(\theta_1 - \alpha) \int_0^{L_{IHC}} p_{gap} ds = 0 , \end{aligned} \quad (\text{E.2})$$

where

$$\alpha_{2j} = A_{2j} + B_{2j} \frac{h_{hb}}{L_{Ro}}, \quad \beta_{21} = B_{21} + D_1 \frac{L_{Ro}}{L_{pc}} . \quad (\text{E.3})$$

Variation of Π with respect to u_{tms} yields,

$$\begin{aligned}
& (-\omega^2 M_{tms} - j\omega C_{tms} + K_{tms})u_{tms} - \left[2j\omega\mu \frac{\gamma \cosh(\gamma g_0)}{\sinh(\gamma g_0)} \int_0^{L_{IHC}} ds \right] u_{tms} \\
& - \alpha_f \tilde{B} \int_0^{L_{IHC}} \frac{\partial p_{gap}}{\partial s} ds - 2j\omega\mu \frac{\gamma \cosh(\gamma g_0)}{\sinh(\gamma g_0)} \int_0^{L_{IHC}} u^s ds - B_{23} \int_0^{L_{IHC}} q(s) p_{gap} ds \\
& + [K_{hb}\alpha_{21}\alpha_{23} + K_{rl}B_{23}\beta_{21} + K_{ohc}C_{23}(C_{21} + E_{21})] u_{bm} \\
& + [K_{hb}\alpha_{23}^2 + K_{rl}B_{23}^2 + K_{ohc}C_{23}^2] (u_{tms} + u_2^s) \\
& + [K_{hb}\alpha_{23}\alpha_{24} + K_{rl}B_{23}B_{24} + K_{ohc}C_{23}C_{24}] (u_{tmb}^0 + w_2^b) \\
& + \epsilon_3(\phi_{ohc} - \phi_{st})C_{23} + \frac{1}{2} [p_{\Omega_1}|_{s=L_{hb_2}} - p_{\Omega_2}|_{s=L_{hb_2}}] h_{hb}A_{23} = 0. \tag{E.4}
\end{aligned}$$

Variation of Π with respect to u^s yields,

$$\begin{aligned}
& - (\omega^2 \rho_{tm} a_{tms} + j\omega \zeta_{tm}^s) \int_0^{L_{tm}} u^s \delta u^s ds + E_{tm}^s a_{tms} \int_0^{L_{tm}} \left(\frac{\partial u^s}{\partial s} \right) \delta \left(\frac{\partial u^s}{\partial s} \right) ds \\
& - 2j\omega\mu \frac{\gamma \cosh(\gamma g_0)}{\sinh(\gamma g_0)} (u_{tms}) \int_0^{L_{IHC}} \delta u^s ds - 2j\omega\mu \frac{\gamma \cosh(\gamma g_0)}{\sinh(\gamma g_0)} \int_0^{L_{IHC}} u^s \delta u^s ds \\
& - \alpha_f \tilde{B} \int_0^{L_{IHC}} \frac{\partial p_{gap}}{\partial s} \delta u^s ds - B_{23} \delta u_2^s \int_0^{L_{IHC}} q(s) p_{gap} ds \\
& + [K_{hb}\alpha_{21}\alpha_{23} + K_{rl}B_{23}\beta_{21} + K_{ohc}C_{23}(C_{21} + E_{21})] u_{bm} \delta u_2^s \\
& + [K_{hb}\alpha_{23}^2 + K_{rl}B_{23}^2 + K_{ohc}C_{23}^2] (u_{tms} + u_2^s) \delta u_2^s \\
& + [K_{hb}\alpha_{23}\alpha_{24} + K_{rl}B_{23}B_{24} + K_{ohc}C_{23}C_{24}] (u_{tmb}^0 + w_2^b) \delta u_2^s \\
& + \epsilon_3(\phi_{ohc} - \phi_{st})C_{23} \delta u_2^s + \frac{1}{2} [p_{\Omega_1}|_{s=L_{hb_2}} - p_{\Omega_2}|_{s=L_{hb_2}}] h_{hb}A_{23} \delta u_2^s = 0. \tag{E.5}
\end{aligned}$$

Variation of Π with respect to u_{tmb}^0 yields,

$$\begin{aligned}
& \frac{1}{\ell_{tm}^2} \left(-\frac{1}{3} \omega^2 M_{tmb} L_{tm}^2 - j\omega C_{tmb} + K_{tmb} \right) u_{tmb}^0 \\
& - \frac{1}{\ell_{tm}} \int_{L_{IHB}}^{L_{tm}} p_s s ds + \frac{1}{2} \left[p_{\Omega_1}|_{s=L_{hb_2}} - p_{\Omega_2}|_{s=L_{hb_2}} \right] h_{hb} A_{24} \\
& - \int_0^{L_{IHB}} p_{gap} \left(\frac{s - L_{tm}}{\ell_{tm}} \right) ds - B_{24} \int_0^{L_{IHB}} q(s) p_{gap} ds \\
& + [K_{hb} \alpha_{21} \alpha_{24} + K_{rl} B_{24} \beta_{21} + K_{ohc} C_{24} (C_{21} + E_{21})] u_{bm} \\
& + [K_{hb} \alpha_{23} \alpha_{24} + K_{rl} B_{23} B_{24} + K_{ohc} C_{23} C_{24}] (u_{tms} + u_2^s) \\
& + [K_{hb} \alpha_{24}^2 + K_{rl} B_{24}^2 + K_{ohc} C_{24}^2] (u_{tmb}^0 + w_2^b) + \epsilon_3 (\phi_{ohc} - \phi_{st}) C_{24} = 0. \tag{E.6}
\end{aligned}$$

Variation of Π with respect to w^b yields,

$$\begin{aligned}
& - (\omega^2 \rho_{tm} a_{tmb} + j\omega \zeta_{tm}^b) \int_0^{L_{tm}} w^b \delta w^b ds + E_{tm}^b I \int_0^{L_{tm}} \left(\frac{\partial^2 w^b}{\partial s^2} \right) \delta \left(\frac{\partial^2 w^b}{\partial s^2} \right) ds \\
& + \int_{L_{IHB}}^{L_{tm}} p_s \delta w^b ds + \frac{1}{2} \left[p_{\Omega_1}|_{s=L_{hb_2}} - p_{\Omega_2}|_{s=L_{hb_2}} \right] h_{hb} A_{24} \delta w_2^b \\
& + \int_0^{L_{IHB}} p_{gap} \delta w^b ds - B_{24} \delta w_2^b \int_0^{L_{IHB}} q(s) p_{gap} ds \\
& + [K_{hb} \alpha_{21} \alpha_{24} + K_{rl} B_{24} \beta_{21} + K_{ohc} C_{24} (C_{21} + E_{21})] u_{bm} \delta w_2^b \\
& + [K_{hb} \alpha_{23} \alpha_{24} + K_{rl} B_{23} B_{24} + K_{ohc} C_{23} C_{24}] (u_{tms} + u_2^s) \delta w_2^b \\
& + [K_{hb} \alpha_{24}^2 + K_{rl} B_{24}^2 + K_{ohc} C_{24}^2] (u_{tmb}^0 + w_2^b) \delta w_2^b + \epsilon_3 (\phi_{ohc} - \phi_{st}) C_{24} \delta w_2^b = 0. \tag{E.7}
\end{aligned}$$

Based on the shape functions listed in App. D, the variational equations for δp_1 , δp_2 ,

δp_3 , and δp_4 can be obtained from Eq. 4.37. The variational equation for δp_1 is

$$\begin{aligned}
& \frac{\alpha_f \tilde{A}}{\rho_f \omega^2} \int_0^{L_{hb_2}} N_{1,s} \sum N_{i,s} p_i ds - \left(\frac{\alpha_f \tilde{A}}{\rho_f \omega^2} k_x^2 + \frac{g_0}{\rho_f c^2} \right) \int_0^{L_{hb_2}} N_1 \sum N_i p_i ds \\
& + \frac{\alpha_f \tilde{A}}{\rho_f \omega^2} \frac{\partial p_{gap}}{\partial s} \Big|_{s=0} + [B_{21} u_{bm} + B_{23}(u_{tms} + u_2^s) + B_{24}(u_{tmb}^0 + w_2^b)] \int_0^{L_{hb_2}} q(s) N_1 ds \\
& + D_1 \cos(\theta_1 - \alpha) u_{bm} \int_0^{L_{hb_2}} N_1 ds - \tilde{B} \int_0^{L_{hb_2}} N_1 \sum N_{i,s} u_i^s ds \\
& + u_{tmb}^0 \int_0^{L_{hb_2}} \frac{s - L_{tm}}{\ell_{tm}} N_1 ds - \int_0^{L_{hb_2}} N_1 \sum N_i^h \phi_i ds = 0. \tag{E.8}
\end{aligned}$$

By evaluating the shape functions and applying the boundary condition in Eq. 4.113, Eq. E.8 can be rewritten as

$$\begin{aligned}
& - \frac{j g_0^2}{\omega Z_{sm}} p_{sm} + \left[\frac{j g_0^2}{\omega Z_{sm}} + \frac{\alpha_f \tilde{A}}{\rho_f \omega^2 h_1} - \left(\frac{\alpha_f \tilde{A}}{\rho_f \omega^2} k_x^2 + \frac{g_0}{\rho_f c^2} \right) \frac{h_1}{3} \right] p_1 \\
& - \left[\frac{\alpha_f \tilde{A}}{\rho_f \omega^2 h_1} + \left(\frac{\alpha_f \tilde{A}}{\rho_f \omega^2} k_x^2 + \frac{g_0}{\rho_f c^2} \right) \frac{h_1}{6} \right] p_2 + D_1 \cos(\theta_1 - \alpha) \frac{h_1}{2} u_{bm} - \frac{\tilde{B}}{2} u_1^s - \frac{\tilde{B}}{2} u_2^s \\
& - \tilde{B} u_{tms} + \left(\frac{h_1^2}{3L_{ro}} + \frac{h_1}{2} \right) [B_{21} u_{bm} + B_{23}(u_{tms} + u_2^s) + B_{24}(u_{tmb}^0 + w_2^b)] \\
& + \frac{h_1(h_1 - 3L_{tm})}{6\ell_{tm}} u_{tmb}^0 - \frac{7h_1}{20} w_1^b - \frac{h_1^2}{20} \phi_1 - \frac{3h_1}{20} w_2^b + \frac{h_1^2}{30} \phi_2 = 0, \tag{E.9}
\end{aligned}$$

where $h_1 = L_{hb_2}$. The variational equation for δp_2 is

$$\begin{aligned}
& \frac{\alpha_f \tilde{A}}{\rho_f \omega^2} \int_0^{L_{hb_2}} N_{2,s} \sum N_{i,s} p_i ds - \left(\frac{\alpha_f \tilde{A}}{\rho_f \omega^2} k_x^2 + \frac{g_0}{\rho_f c^2} \right) \int_0^{L_{hb_2}} N_2 \sum N_i p_i ds \\
& - \frac{\alpha_f \tilde{A}}{\rho_f \omega^2} \frac{\partial p_{gap}}{\partial s} \Big|_{s=L_{hb_2}^-} + [B_{21} u_{bm} + B_{23}(u_{tms} + u_2^s) + B_{24}(u_{tmb}^0 + w_2^b)] \int_0^{L_{hb_2}} q(s) N_2 ds \\
& + D_1 \cos(\theta_1 - \alpha) u_{bm} \int_0^{L_{hb_2}} N_2 ds - \tilde{B} \int_0^{L_{hb_2}} N_2 \sum N_{i,s} u_i^s ds \\
& + u_{tmb}^0 \int_0^{L_{hb_2}} \frac{s - L_{tm}}{\ell_{tm}} N_2 ds - \int_0^{L_{hb_2}} N_2 \sum N_i^h \phi_i ds = 0. \tag{E.10}
\end{aligned}$$

By evaluating the shape functions and applying the boundary condition in Eq. 4.114, Eq. E.10 can be rewritten as

$$\begin{aligned}
& - \left[\frac{\alpha_f \tilde{A}}{\rho_f \omega^2 h_1} + \left(\frac{\alpha_f \tilde{A}}{\rho_f \omega^2} k_x^2 + \frac{g_0}{\rho_f c^2} \right) \frac{h_1}{6} \right] p_1 + \left[\frac{j \alpha_f \beta_{dp}}{6 \mu \omega} + \frac{\alpha_f \tilde{A}}{\rho_f \omega^2 h_1} - \left(\frac{\alpha_f \tilde{A}}{\rho_f \omega^2} k_x^2 + \frac{g_0}{\rho_f c^2} \right) \frac{h_1}{3} \right] p_2 \\
& - \frac{j \alpha_f \beta_{dp}}{6 \mu \omega} p_3 + \left[D_1 \cos(\theta_1 - \alpha) \frac{h_1}{2} - A_{21} \beta_{ds} \right] u_{bm} + \frac{h_1}{6 \ell_{tm}} (2h_1 - 3L_{tm}) u_{tmb}^0 \\
& + \left[\tilde{B} - A_{23} \beta_{ds} \right] (u_{tms} + u_2^s) + \frac{\tilde{B}}{2} (u_1^s - u_2^s) - A_{24} \beta_{ds} u_{tmb}^0 \\
& + \left(\frac{h_1^2}{6L_{ro}} + \frac{h_1}{2} \right) [B_{21} u_{bm} + B_{23}(u_{tms} + u_2^s) + B_{24}(u_{tmb}^0 + w_2^b)] \\
& - \frac{3h_1}{20} w_1^b - \frac{h_1^2}{30} \phi_1 - \left(\frac{7h_1}{20} + A_{24} \beta_{ds} \right) w_2^b + \frac{h_1^2}{20} \phi_2 = 0. \tag{E.11}
\end{aligned}$$

The variational equation for δp_3 is

$$\begin{aligned}
& \frac{\alpha_f \tilde{A}}{\rho_f \omega^2} \int_{L_{hb_2}}^{L_{IHC}} N_{1,s} \sum N_{i,s} p_i ds - \left(\frac{\alpha_f \tilde{A}}{\rho_f \omega^2} k_x^2 + \frac{g_0}{\rho_f c^2} \right) \int_{L_{hb_2}}^{L_{IHC}} N_1 \sum N_i p_i ds \\
& + \frac{\alpha_f \tilde{A}}{\rho_f \omega^2} \frac{\partial p_{gap}}{\partial s} \Big|_{s=L_{hb_2}^+} + [B_{21} u_{bm} + B_{23}(u_{tms} + u_2^s) + B_{24}(u_{tmb}^0 + w_2^b)] \int_{L_{hb_2}}^{L_{IHC}} q(s) N_1 ds \\
& + D_1 \cos(\theta_1 - \alpha) u_{bm} \int_{L_{hb_2}}^{L_{IHC}} N_1 ds - \tilde{B} \int_{L_{hb_2}}^{L_{IHC}} N_1 \sum N_{i,s} u_i^s ds \\
& + u_{tmb}^0 \int_{L_{hb_2}}^{L_{IHC}} \frac{s - L_{tm}}{\ell_{tm}} N_1 ds - \int_{L_{hb_2}}^{L_{IHC}} N_1 \sum N_i^h \phi_i ds = 0. \tag{E.12}
\end{aligned}$$

By evaluating the shape functions and applying the boundary condition in Eq. 4.115, Eq. E.12 can be rewritten as

$$\begin{aligned}
& - \frac{j \alpha_f \beta_{dp}}{6 \mu \omega} p_2 + \left[\frac{j \alpha_f \beta_{dp}}{6 \mu \omega} + \frac{\alpha_f \tilde{A}}{\rho_f \omega^2 h_2} - \left(\frac{\alpha_f \tilde{A}}{\rho_f \omega^2} k_x^2 + \frac{g_0}{\rho_f c^2} \right) \frac{h_2}{3} \right] p_3 + \frac{\tilde{B}}{2} (u_2^s - u_3^s) \\
& - \left[\frac{\alpha_f \tilde{A}}{\rho_f \omega^2 h_2} + \left(\frac{\alpha_f \tilde{A}}{\rho_f \omega^2} k_x^2 + \frac{g_0}{\rho_f c^2} \right) \frac{h_2}{6} \right] p_4 + \left[D_1 \cos(\theta_1 - \alpha) \frac{h_2}{2} + A_{21} \beta_{ds} \right] u_{bm} \\
& + \left[-\tilde{B} + A_{23} \beta_{ds} \right] (u_{tms} + u_2^s) + A_{24} \beta_{ds} (u_{tmb}^0 + w_2^b) \\
& + \frac{h_2}{3} [B_{21} u_{bm} + B_{23}(u_{tms} + u_2^s) + B_{24}(u_{tmb}^0 + w_2^b)] + \frac{L_{Ro}}{6 \ell_{tm}} (h_2 - 3 \ell_{tm}) u_{tmb}^0 \\
& - \frac{7 h_2}{20} w_2^b - \frac{h_2^2}{20} \phi_2 - \frac{3 h_2}{20} w_3^b + \frac{h_2^2}{30} \phi_3 = 0, \tag{E.13}
\end{aligned}$$

where $h_2 = L_{IHC} - L_{hb_2}$. The variational equation for δp_4 is

$$\begin{aligned}
& \frac{\alpha_f \tilde{A}}{\rho_f \omega^2} \int_{L_{hb_2}}^{L_{IHC}} N_{2,s} \sum N_{i,s} p_i ds - \left(\frac{\alpha_f \tilde{A}}{\rho_f \omega^2} k_x^2 + \frac{g_0}{\rho_f c^2} \right) \int_{L_{hb_2}}^{L_{IHC}} N_2 \sum N_i p_i ds \\
& - \frac{\alpha_f \tilde{A}}{\rho_f \omega^2} \frac{\partial p_{gap}}{\partial s} \Big|_{s=L_{IHC}^-} + [B_{21} u_{bm} + B_{23}(u_{tms} + u_2^s) + B_{24}(u_{tmb}^0 + w_2^b)] \int_{L_{hb_2}}^{L_{IHC}} q(s) N_2 ds \\
& + D_1 \cos(\theta_1 - \alpha) u_{bm} \int_{L_{hb_2}}^{L_{IHC}} N_2 ds - \tilde{B} \int_{L_{hb_2}}^{L_{IHC}} N_2 \sum N_{i,s} u_i^s ds \\
& + u_{tmb}^0 \int_{L_{hb_2}}^{L_{IHC}} \frac{s - L_{tm}}{\ell_{tm}} N_2 ds - \int_{L_{hb_2}}^{L_{IHC}} N_2 \sum N_i^h \phi_i ds = 0. \tag{E.14}
\end{aligned}$$

By evaluating the shape functions and applying the boundary condition in Eq. 4.116, Eq. E.14 can be rewritten as

$$\begin{aligned}
& - \left[\frac{\alpha_f \tilde{A}}{\rho_f \omega^2 h_2} + \left(\frac{\alpha_f \tilde{A}}{\rho_f \omega^2} k_x^2 + \frac{g_0}{\rho_f c^2} \right) \frac{h_2}{6} \right] p_3 + \left[\frac{\alpha_f \tilde{A}}{\rho_f \omega^2 h_2} - \left(\frac{\alpha_f \tilde{A}}{\rho_f \omega^2} k_x^2 + \frac{g_0}{\rho_f c^2} \right) \frac{h_2}{3} + \lambda_1 \right] p_4 \\
& - \lambda_1 p_s + D_1 \cos(\theta_1 - \alpha) \frac{h_2}{2} u_{bm} + (\lambda_2 + \tilde{B}) u_{tms} + \left(\lambda_3 + \frac{\tilde{B}}{2} \right) u_2^s + \left(\lambda_4 + \frac{\tilde{B}}{2} \right) u_3^s \\
& + \lambda_5 u_{bm} + \lambda_6 (u_{tmb}^0 + w_2^b) + \frac{h_2}{6} [B_{21} u_{bm} + B_{23}(u_{tms} + u_2^s) + B_{24}(u_{tmb}^0 + w_2^b)] \\
& + \frac{L_{Ro}}{6 \ell_{tm}} (2h_2 - 3\ell_{tm}) u_{tmb}^0 - \frac{3h_2}{20} w_2^b - \frac{h_2^2}{30} \phi_2 - \frac{7h_2}{20} w_3^b + \frac{h_2^2}{20} \phi_3 = 0. \tag{E.15}
\end{aligned}$$

APPENDIX F

Integral evaluation

Here we derive the approximation for the integrals I_1 , I_2 , I_3 , I'_2 , and I'_3 in Sec. 4.2.2.2.

Evaluating integrals I_1 , I_2 , and I_3

The integrals are defined on $s' \in [-R_{IHC}, R_{IHC}]$. For approximation, we will evaluate the integrals by taking $(-\infty, \infty)$ as the domain of integration.

The distance in the IHB HC tip gap is

$$g_{IHB} = g_{HS} - h_{IHB} = A(s')^2 + Bs' + C, \quad (\text{F.1})$$

where

$$\begin{aligned} A &= \frac{1}{R_{IHB}}, \quad B = -\frac{g_0 - g_{HS_0}}{d_{HS}}, \\ C &= \frac{g_0 - g_{HS_0}}{d_{HS}} U^s|_{s=L_{IHC}} + W^b|_{s=L_{IHC}} - u_{rl}^b|_{s=L_{IHC}} + \frac{g_0 - g_{HS_0}}{d_{HS}} a_{HS} + g_{HS_0} - h_{IHB_0}. \end{aligned} \quad (\text{F.2})$$

Since g_{IHB} should be positive for all s' , the quadric has two complex roots. Let s'_1 be the root in the upper complex plane, and s'_2 in the lower plane, i.e.,

$$A(s')^2 + Bs' + C = A \left((s')^2 + \frac{B}{A}s' + \frac{C}{A} \right) = A(s' - s'_1)(s' - s'_2), \quad (\text{F.3})$$

with

$$s'_1 - s'_2 = \frac{i\sqrt{4AC - B^2}}{A}, \quad (\text{F.4})$$

where $4AC - B^2 > 0$. Then by the residual theory

$$\begin{aligned} I_3 &= \int_{-\infty}^{\infty} \frac{ds'}{A^3(s' - s'_1)^3(s' - s'_2)^3} = 2\pi i \frac{1}{2} \left[\frac{1}{A^3(s' - s'_2)^3} \right]''_{s'=s'_1} \\ &= \frac{12\pi i}{A^3(s'_1 - s'_2)^5} = \frac{12\pi}{A^3} \left(\frac{A}{\sqrt{4AC - B^2}} \right)^5. \end{aligned} \quad (\text{F.5})$$

Similarly,

$$\begin{aligned} I_2 &= \int_{-\infty}^{\infty} \frac{ds'}{A^2(s' - s'_1)^2(s' - s'_2)^2} = 2\pi i \left[\frac{1}{A^2(s' - s'_2)^2} \right]'_{s'=s'_1} \\ &= \frac{-4\pi i}{A^2(s'_1 - s'_2)^3} = \frac{4\pi}{A^2} \left(\frac{A}{\sqrt{4AC - B^2}} \right)^3, \end{aligned} \quad (\text{F.6})$$

$$I_1 = \int_{-\infty}^{\infty} \frac{ds'}{A(s' - s'_1)(s' - s'_2)} = 2\pi i \left[\frac{1}{A(s' - s'_2)} \right]_{s'=s'_1} = \frac{2\pi}{A} \left(\frac{A}{\sqrt{4AC - B^2}} \right). \quad (\text{F.7})$$

To simplify the algebra, let

$$\begin{aligned} \left(\frac{A}{\sqrt{4AC - B^2}} \right)^n &= \left(\frac{4C}{A} - \frac{B^2}{A^2} \right)^{-\frac{n}{2}} \\ &= (R_{IHB}\sigma)^{-\frac{n}{2}} \left[1 + 4 \frac{g_0 - g_{HS_0}}{d_{HS}\sigma} U^s|_{s=L_{IHC}} + \frac{4}{\sigma} (W^b|_{s=L_{IHC}} - u_{rl}^b|_{s=L_{IHC}}) \right]^{-\frac{n}{2}}, \end{aligned} \quad (\text{F.8})$$

where

$$\sigma = 4 \frac{g_0 - g_{HS_0}}{d_{HS}} a_{HS} + 4(g_{HS_0} - h_{IHB_0}) - R_{IHB} \left(\frac{g_0 - g_{HS_0}}{d_{HS}} \right)^2. \quad (\text{F.9})$$

Therefore,

$$\begin{aligned} I_3 &= \frac{12\pi}{A^3} \left(\frac{A}{\sqrt{4AC - B^2}} \right)^5 \\ &\sim 12\pi R_{IHB}^{\frac{1}{2}} \sigma^{-\frac{5}{2}} \left[1 - 10 \frac{g_0 - g_{HS_0}}{d_{HS}\sigma} U^s|_{s=L_{IHC}} - \frac{10}{\sigma} (W^b|_{s=L_{IHC}} - u_{rl}^b|_{s=L_{IHC}}) \right], \end{aligned} \quad (\text{F.10})$$

$$\begin{aligned} I_2 &= \frac{4\pi}{A^2} \left(\frac{A}{\sqrt{4AC - B^2}} \right)^3 \\ &\sim 4\pi R_{IHB}^{\frac{1}{2}} \sigma^{-\frac{3}{2}} \left[1 - 6 \frac{g_0 - g_{HS_0}}{d_{HS}\sigma} U^s|_{s=L_{IHC}} - \frac{6}{\sigma} (W^b|_{s=L_{IHC}} - u_{rl}^b|_{s=L_{IHC}}) \right], \end{aligned} \quad (\text{F.11})$$

$$\begin{aligned}
I_1 &= \frac{2\pi}{A} \left(\frac{A}{\sqrt{4AC - B^2}} \right) \\
&\sim 2\pi R_{IHB}^{\frac{1}{2}} \sigma^{-\frac{1}{2}} \left[1 - 2 \frac{g_0 - g_{HS_0}}{d_{HS} \sigma} U^s|_{s=L_{IHC}} - \frac{2}{\sigma} (W^b|_{s=L_{IHC}} - u_{rl}^b|_{s=L_{IHC}}) \right]. \quad (F.12)
\end{aligned}$$

By assuming that u_{bm} , U^s , and W^b are much smaller than any geometrical dimension around the TM-RL gap and the Hessen's stripe, we may approximate I_1 , I_2 , and I_3 as

$$I_1 = 2\pi R_{IHB}^{\frac{1}{2}} \sigma^{-\frac{1}{2}}, \quad I_2 = 4\pi R_{IHB}^{\frac{1}{2}} \sigma^{-\frac{3}{2}}, \quad I_3 = 12\pi R_{IHB}^{\frac{1}{2}} \sigma^{-\frac{5}{2}}. \quad (F.13)$$

This approximation is equivalent to linearizing the boundary condition at IHC HB.

Evaluating integrals I'_2 and I'_3

As defined in the text, I'_2 and I'_3 can be directly evaluated as

$$\begin{aligned}
I'_2 &= \int_{R_{IHB}}^{a_{HS}} \frac{ds'}{g_{HS}^2} = \frac{d_{HS}}{(g_0 - g_{HS_0})} \left[\left(\frac{g_0 - g_{HS_0}}{d_{HS}} U^s + g_{HS_0} + W^b - u_{rl}^b|_{s=L_{IHC}} \right)^{-1} \right. \\
&\quad \left. - \left(-\frac{g_0 - g_{HS_0}}{d_{HS}} (R_{IHB} - U^s - a_{HS}) + g_{HS_0} + W^b - u_{rl}^b|_{s=L_{IHC}} \right)^{-1} \right], \quad (F.14)
\end{aligned}$$

$$\begin{aligned}
I'_3 &= \int_{R_{IHB}}^{a_{HS}} \frac{ds'}{g_{HS}^3} = \frac{d_{HS}}{2(g_0 - g_{HS_0})} \left[\left(\frac{g_0 - g_{HS_0}}{d_{HS}} U^s + g_{HS_0} + W^b - u_{rl}^b|_{s=L_{IHC}} \right)^{-2} \right. \\
&\quad \left. - \left(-\frac{g_0 - g_{HS_0}}{d_{HS}} (R_{IHB} - U^s - a_{HS}) + g_{HS_0} + W^b - u_{rl}^b|_{s=L_{IHC}} \right)^{-2} \right]. \quad (F.15)
\end{aligned}$$

By assuming that u_{bm} , U^s , and W^b are much smaller than any geometrical dimension around the TM-RL gap and the Hessen's stripe (infinitesimal assumption), I'_2 and I'_3 can be approximated as

$$I'_2 \sim \frac{d_{HS}}{(g_0 - g_{HS_0})} \left[(g_{HS_0})^{-1} - \left(\frac{g_0 - g_{HS_0}}{d_{HS}} (a_{HS} - R_{IHB}) + g_{HS_0} \right)^{-1} \right], \quad (F.16)$$

$$I'_3 \sim \frac{d_{HS}}{2(g_0 - g_{HS_0})} \left[(g_{HS_0})^{-2} - \left(\frac{g_0 - g_{HS_0}}{d_{HS}} (a_{HS} - R_{IHB}) + g_{HS_0} \right)^{-2} \right]. \quad (\text{F.17})$$

Likewise, this approximation is equivalent to linearizing the boundary condition at IHC HB.

APPENDIX G

Derivation of the reciprocity in the passive cochlea

The following shows the derivation of the reciprocity of two excitation methods in the passive case. The physical boundary of this problem is shown in Fig. G.1. The superscript ‘(1)’ denotes any quantities that are associated with acoustic stimuli (force on the stapes), and ‘(2)’ denotes any quantities associated with the internal force excitation on the basilar membrane.

Under acoustic stimuli, the following relations hold,

$$Z_{\text{BM}}v_{\text{BM}}^{(1)} = \Delta p^{(1)}, \quad -\frac{\partial p_{\text{BM}}^{(1)}}{\partial z} = j\omega\rho v_{\text{BM}}^{(1)}, \quad (\text{G.1})$$

$$Z_{\text{ow}}v_{\text{ow}}^{(1)} = F_{\text{ext}} - \int_{\Gamma_{\text{ow}}} p_{\text{ow}}^{(1)} ds, \quad -\frac{\partial p_{\text{ow}}^{(1)}}{\partial x} = j\omega\rho v_{\text{ow}}^{(1)}, \quad (\text{G.2})$$

$$Z_{\text{rw}}v_{\text{rw}}^{(1)} = - \int_{\Gamma_{\text{rw}}} p_{\text{rw}}^{(1)} \psi_{\text{rw}} ds, \quad -\frac{\partial p_{\text{rw}}^{(1)}}{\partial x} = j\omega\rho v_{\text{rw}}^{(1)}, \quad (\text{G.3})$$

where v is the velocity, p is the pressure, and ρ is the density of the intracochlear fluid. Each Z is a self-adjoint operator. Loosely, you can think of this as the impedance, although

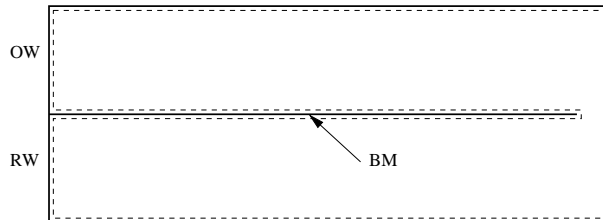


Figure G.1: Schematic showing the boundary (denoted by dashed lines) of the intracochlear fluid.

a lossless elastic dynamic operator will also satisfy the relationship (e.g., $\int v(Zu)ds = \int u(Zv)ds$ for displacement fields u and v). Subscripts ‘BM’, ‘ow’, and ‘rw’ represent quantities that are associated with the BM, the oval window, and the round window, respectively. F_{ext} is the external force from acoustic stimuli. $\Delta p (= p_{\text{ST}}(\text{BM}) - p_{\text{SV}}(\text{BM}))$ is the pressure difference across the BM. ψ_{rw} is the mode shape of the round window.

Similarly, under the internal force excitation, the following relations hold,

$$Z_{\text{BM}}v_{\text{BM}}^{(2)} = \Delta p^{(2)} + f_{\text{BM}}, \quad -\frac{\partial p_{\text{BM}}^{(2)}}{\partial z} = j\omega\rho v_{\text{BM}}^{(2)}, \quad (\text{G.4})$$

$$Z_{\text{ow}}v_{\text{ow}}^{(2)} = -\int_{\Gamma_{\text{ow}}} p_{\text{ow}}^{(2)} ds, \quad -\frac{\partial p_{\text{ow}}^{(2)}}{\partial x} = j\omega\rho v_{\text{ow}}^{(2)}, \quad (\text{G.5})$$

$$Z_{\text{rw}}v_{\text{rw}}^{(2)} = -\int_{\Gamma_{\text{rw}}} p_{\text{rw}}^{(2)} \psi_{\text{rw}} ds, \quad -\frac{\partial p_{\text{rw}}^{(2)}}{\partial x} = j\omega\rho v_{\text{rw}}^{(2)}, \quad (\text{G.6})$$

where f_{BM} is the internal force per unit area applied on the BM.

The governing equations of the intracochlear fluid under the two states are,

$$\nabla^2 p^{(1)} + k^2 p^{(1)} = 0, \quad \nabla^2 p^{(2)} + k^2 p^{(2)} = 0. \quad (\text{G.7})$$

Multiply the first equation by $p^{(2)}$ and the second by $p^{(1)}$, and subtract they two to find

$$p^{(2)}\nabla^2 p^{(1)} - p^{(1)}\nabla^2 p^{(2)} = 0. \quad (\text{G.8})$$

Integrate Eq. G.8 over the whole fluid domain and apply the divergence theorem to get

$$\int_{\Gamma} (p^{(2)}\nabla p^{(1)} - p^{(1)}\nabla p^{(2)}) \cdot \mathbf{n} ds = 0, \quad (\text{G.9})$$

where \mathbf{n} is in the outward-normal direction of the fluid surface. After applying Eqs. G.1 to G.6 along with the rigid boundary conditions at the other walls, Eq. G.9 becomes

$$\int_{\Gamma_{\text{BM}}} f_{\text{BM}} v_{\text{BM}}^{(1)} dx - v_{\text{ow}}^{(2)} F_{\text{ext}} = 0. \quad (\text{G.10})$$

If $f_{\text{BM}}(x)$ is a δ -function applied at $x = x_0$, which is defined as

$$f_{\text{BM}}(x) = F_{\text{BM}}\delta(x - x_0), \quad (\text{G.11})$$

then Eq. G.10 shows the reciprocity

$$\frac{v_{\text{ow}}^{(2)}}{F_{\text{BM}}(x_0)} = \frac{v_{\text{BM}}^{(1)}(x_0)}{F_{\text{ext}}}. \quad (\text{G.12})$$

BIBLIOGRAPHY

BIBLIOGRAPHY

- [1] J. Baumgart, C. Chiaradia, M. Fleischer, Y. Yarin, R. Grundmann, and A. W. Gummer. Fluid mechanics in the subreticular space. In N. P. Cooper and D. T. Kemp, editors, *Concepts and challenges in the biophysics of hearing*, pages 288–293. World Scientific, Singapore, 2009.
- [2] G. V. Bekeesy. *Experiments in hearing*. McGraw Hill, NY, 1960.
- [3] W. M. Beltman, P. J. M. Van der Hoogt, R. M. E. J. Spiering, and H. Tijdeman. Implementation and experimental validation of a new viscothermal acoustic finite element for acousto-elastic problems. *J. Sound Vibr.*, 216(1):159–185, 1998.
- [4] M. Billone and A. Raynor. Transmission of radial shear forces to cochlear hair cells. *J. Acoust. Soc. Am.*, 54(5):1143–1156, 1973.
- [5] R. Bossart, N. Joly, and M. Bruneau. Hybrid numerical and analytical solutions for acoustic boundary problems in thermo-viscous fluids. *J. Sound Vibr.*, 263(1):69–84, 2003.
- [6] D. K. Chan and A. J. Hudspeth. Ca²⁺ current-driven nonlinear amplification by the mammalian cochlea in vitro. *Nat. Neurosci.*, 8(2):149–155, 2005.
- [7] D. K. Chan and A. J. Hudspeth. Mechanical responses of the organ of corti to acoustic and electrical stimulation in vitro. *Biophys. J.*, 89:4382–4395, 2005.
- [8] L. Cheng. *Cochlear-based Transducers: Modeling and Design*. PhD thesis, University of Michigan, 2007.
- [9] L. Cheng, R. D. White, and K. Gosh. Three-dimensional viscous finite element formulation for acoustic fluid-structure interaction. *Comput. Meth. Appl. Mech. Eng.*, 197(49-50):4160–4172, 2008.
- [10] N. P. Cooper. Harmonic distortion on the basilar membrane in the basal turn of the guinea-pig cochlea. *Journal of Physiology-London*, 509(1):277–288, 1998.
- [11] N. P. Cooper and W. S. Rhode. Basilar mechanics in the hook region of the cat and guinea pig cochlea: sharp tuning and nonlinearity in the absence of baseline position shifts. *Hear. Res.*, 63(1-2):163–190, 1992.
- [12] N. P. Cooper and W. S. Rhode. Nonlinear mechanics at the apex of the guinea-pig cochlea. *Hear. Res.*, 82(2):225–243, 1995.

- [13] N. P. Cooper and W. S. Rhode. Fast travelling waves, slow travelling waves and their interactions in experimental studies of apical cochlear mechanics. *Auditory Neuroscience*, 2:289–299, 1996.
- [14] N. P. Cooper and W. S. Rhode. Mechanical responses to two-tone distortion products in the apical and basal turns of the mammalian cochlea. *J. Neurophysiol.*, 78(1):261–270, 1997.
- [15] P. Dallos. The active cochlea. *J. Neurosci.*, 12:4575–4585, 1992.
- [16] P. Dallos. Organ of corti kinematics. *J. Assoc. Res. Otolaryngol.*, 4(3):416–421, 2003.
- [17] E. de Boer. Short waves in three-dimensional cochlea models: Solution for a 'block' model. *Hear. Res.*, 4:53–77, 1981.
- [18] E. de Boer. The sulcus connection. on a mode of participation of outer hair cells in cochlear mechanics. *J. Acoust. Soc. Am.*, 93:2845–2859, 1993.
- [19] E. de Boer. Mechanics of the Cochlea: Modeling efforts. In P. Dallos, A. Popper, and R. Fay, editors, *The Cochlea*, pages 258–317. Springer-Verlag, New York, 1996.
- [20] E. de Boer and A. L. Nuttall. The “inverse problem” solved for a three-dimensional model of the cochlea. III. brushing-up the solution method. *J. Acoust. Soc. Am.*, 105:3410–3420, 1999.
- [21] E. de Boer and A. L. Nuttall. The mechanical waveform of the basilar membrane. III. intensity effects. *J. Acoust. Soc. Am.*, 107(3):1497–1507, 2000.
- [22] E. de Boer and A. L. Nuttall. Spontaneous basilar-membrane oscillation (SBMO) and coherent reflection. *J. Assoc. Res. Otolaryngol.*, 7:26–37, 2006.
- [23] E. de Boer, A. L. Nuttall, and C. A. Shera. Wave propagation patterns in a “classical” three-dimensional model of the cochlea. *J. Acoust. Soc. Am.*, 121(1):352–362, 2007.
- [24] E. de Boer, J. Zheng, E. Porsov, and A. L. Nuttall. Inverted direction of wave propagation (IDWP) in the cochlea. *J. Acoust. Soc. Am.*, 123(3):1513–1521, 2008.
- [25] Egbert de Boer and M. A. Viergever. Validity of the Liouville-Green (or WKB) method for cochlear mechanics. *Hear. Res.*, 8:131–155, 1982.
- [26] O. de La Rochefoucauld and E. S. Olson. The role of organ of corti mass in passive cochlear tuning. *Biophysical Journal*, 93:3434–3450, 2007.
- [27] C. De Souza and M. E. Glasscock. *Otosclerosis and stapedectomy: diagnosis, management, and complications*. Thieme Medical Publishers, 2004.
- [28] N. V. Deo. *Micro and Macro-mechanics of the Mammalian Cochlea*. PhD thesis, University of Michigan, 2006.

- [29] N. V. Deo and K. Grosh. Simplified nonlinear outer hair cell models. *J. Acoust. Soc. Am.*, 117(4):2141–2146, 2005.
- [30] W. Dong and N. P. Cooper. An experimental study into the acousto-mechanical effects of invading the cochlea. *J. R. Soc. Interface*, doi:10.1098/rsif.2006.0117, 2006.
- [31] W. Dong and E. S. Olson. Supporting evidence for reverse cochlear traveling waves. *J. Acoust. Soc. Am.*, 123:222–240, January 2008.
- [32] W. Dong and E. S. Olson. Local cochlear damage reduces local nonlinearity and decreases generator-type cochlear emissions while increasing reflector-type emissions. *J. Acoust. Soc. Am.*, 127:1422–1431, March 2010.
- [33] X. X. Dong, M. Ospeck, and K. H. Iwasa. Piezoelectric reciprocal relationship of the membrane motor in the cochlear outer hair cell. *Biophys. J.*, 82:1254–1259, March 2002.
- [34] G Emadi, CP Richter, and P Dallos. Stiffness of the gerbil basilar membrane: Radial and longitudinal variations. *Jouranal of Neurophysiology*, 91(1):474–488, 2004.
- [35] C. Fernandez. Dimensions of the cochlea (guinea pig). *J. Acoust. Soc. Am.*, 24(5):519–523, 1952.
- [36] C. A. Figueroa, I. E. Vignon-Clementel, K. E. Jansen, T. J. R. Hughes, and C. A. Taylor. A coupled momentum method for modeling blood flow in three-dimensional deformable arteries. *Comput. Meth. Appl. Mech. Eng.*, 195(41-43):5685–5706, 2006.
- [37] J. A. Fisher, F. Nin, T. Reichenbach, Uthaiah R. C., and A. J. Hudspeth. The spatial pattern of cochlear amplification. *Neuron*, 76(5):989–997, 2012.
- [38] A. Fridberger, J. B. de Monvel, and M. Ulfendahl. Internal shearing within the hearing organ evoked by basilar membrane motion. *J. Neurosci.*, 22(22):9850–9857, 2002.
- [39] G. H. Frommer and C. R. Steele. Permeability of fluid flow through hair cell cilla. *J. Acoust. Soc. Am.*, 65:759–764, 1979.
- [40] Henri Gavin. The levenberg-marquardt method for nonlinear least squares curve-fitting problems. September 2011.
- [41] M. P. Gorga, S. T. Neely, B. Ohlrich, B. Hoover, J. Redner, and J. Peters. From laboratory to clinic: A large scale study of distortion product otoacoustic emissions in ears with normal hearing and ears with hearing loss. *Ear Hear.*, 18(6):440–455, 1997.
- [42] D Greenwood. A cochlear frequency-position function for several species - 29 years later. *J. Acoust. Soc. Am.*, 87:2592–2605, 1990.

- [43] B. E. Griffith, R. D. Hornung, D. M. McQueen, and C. S. Peskin. An adaptive, formally second order accurate version of the immersed boundary method. *J. Comput. Phys.*, 223:10–49, 2007.
- [44] J. J. Guinan. How are inner hair cells stimulated? evidence for multiple mechanical drives. *Hear. Res.*, 292(1-2):35–50, 2012.
- [45] A. W. Gummer, B. M. Johnstone, and N. J. Armstrong. Direct measurement of basilar membrane stiffness in guinea pig. *J. Acoust. Soc. Am.*, 70(5):1298–1309, 1981.
- [46] D. Z. Z. He and P. Dallos. Properties of voltage-dependant somatic stiffness of cochlear outer hair cells. *J. Assoc. Res. Otolaryngol.*, 01:64–81, 2000.
- [47] W. He, A. Fridberger, E. Porsov, K. Grosh, and T. Ren. Reverse wave propagation in the cochlea. *Proc. Natl. Acad. Sci. USA.*, 105(7):2729–2733, 2008.
- [48] W. Hemmert, H. P. Zenner, and A. W. Gummer. Three-dimensional motion of the organ of corti. *Biophys. J.*, 78(5):2285–2297, 2000.
- [49] M. H. Holmes and J. D. Cole. Cochlear mechanics: Analysis for a pure tone. *J. Acoust. Soc. Am.*, 76:767–778, 1984.
- [50] M. Homer, A. Champneys, G. Hunt, and N. P. Cooper. Mathematical modeling of the radial profile of basilar membrane vibrations in the inner ear. *J. Acoust. Soc. Am.*, 116(2):1025–1034, 2004.
- [51] T. J. R. Hughes. *The Finite Element Method: Linear Static and Dynamic Finite Element Analysis*. Prentice-Hall Englewood Cliffs, NJ, 1987.
- [52] T. J. R. Hughes. *The Finite Element Method: Linear Static and Dynamic Finite Element Analysis*. Dover, 2000.
- [53] K. H. Iwasa and M. Adachi. Force generation in the outer hair cell of the cochlea. *Biophys. J.*, 73:546–555, July 1997.
- [54] D. T. Kemp. Simulated acoustic emissions from within the human auditory system. *J. Acoust. Soc. Am.*, 64:1386–1391, 1978.
- [55] K. Levenberg. A method for the solution of certain non-linear problems in least squares. *Quart. Appl. Math.*, 2:164C168, 1944.
- [56] Y. Li and K. Grosh. Direction of wave propagation in the cochlea for internally excited basilar membrane. *J. Acoust. Soc. Am.*, 131:4710–4721, 2012.
- [57] K. M. Lim. *Physical and Mathematical Cochlear Models*. PhD thesis, Stanford University, 2000.
- [58] K. M. Lim and C. R. Steele. A three-dimensional nonlinear active cochlear model analyzed by the WKB-numeric method. *Hear. Res.*, 170:190–205, 2002.

- [59] L. M. Lyamshev. A question in connection with the principle of reciprocity in acoustics. *Sov. Phys. Dokl.*, 4:406–409, 1959.
- [60] D. W. Marquardt. An algorithm for least-squares estimation of nonlinear parameters. *J. Soc. Ind. Appl. Math.*, 11(2):431C441, 1963.
- [61] G. K. Martin, B. B. Stagner, and B. L. Lonsbury-Martin. Evidence for basal distortion-product otoacoustic emission components. *J. Acoust. Soc. Am.*, 127(5):2955–2972, 2010.
- [62] J. W. Matthews and C. E. Molnar. Modeling intracochlear and ear canal distortion product 2f1-f2. In J. B. Allen, J. L. Hall, A. Hubbard, S. T. Neely, and A. Tubis, editors, *Peripheral Auditory Mechanisms*, pages 258–266. Springer-Verlag, Berlin, 1985.
- [63] J. Meaud and K. Grosh. The effect of tectorial membrane and basilar membrane longitudinal coupling in cochlear mechanics. *J. Acoust. Soc. Am.*, 127(3):1411–1421, 2010.
- [64] J. Meaud and K. Grosh. Coupling active hair bundle mechanics, fast adaptation, and somatic motility in a cochlear model. *Biophys. J.*, 100(11):2576–2585, 2011.
- [65] S. W. F. Meenderink and M. van der Heijden. Reverse cochlear propagation in the intact cochlea of the gerbil: Evidence for slow traveling waves. *J. Neurophysiol.*, 103:1448–1455, 2010.
- [66] M. Muller. The cochlear place-frequency map of the adult and developing mongolian gerbil. *Hear. Res.*, 94(1-2):148–156, 1996.
- [67] R. C. Naidu and D. C. Mountain. Measurements of the stiffness map challenge a basic tenet of cochlear theories. *Hear. Res.*, 124:124–131, 1998.
- [68] K. E. Nilsen and I. J. Russell. The spatial and temporal representation of a tone on the guinea pig basilar membrane. *Proc. Natl. Acad. Sci. U. S. A.*, 97(22):11751–11758, 2000.
- [69] M. Nowotny and A. W. Gummer. Nanomechanics of the subtectorial space caused by electromechanics of cochlear outer hair cells. *Proc. Natl. Acad. Sci. U. S. A.*, 103(7):2120–2125, 2006.
- [70] A. L. Nuttall and D. Dolan. Steady-state sinusoidal velocity responses of the basilar membrane in guinea pig. *J. Acoust. Soc. Am.*, 99:1556–1565, 1996.
- [71] A. L. Nuttall, K. Grosh, J. Zheng, E. de Boer, Y. Zou, and T. Ren. Spontaneous basilar membrane oscillation and otoacoustic emission at 15 khz in a guinea pig. *J. Assoc. Res. Otolaryngol.*, 5(4):337–348, 2004.
- [72] E. S. Olson. Intracochlear pressure measurements related to cochlear tuning. *J. Acoust. Soc. Am.*, 110:349–367, 2001.

- [73] Ronald L. Panton. *Incompressible Flow*. John Wiley, 1984.
- [74] A. Papoulis. *Signal Analysis*. McGraw-Hill Int. Book Co, 1984.
- [75] A. A. Parthasarathi. *Numerical Modeling and Electro-Acoustic Stimulus Response Analysis for Cochlear Mechanics*. PhD thesis, University of Michigan, 2000.
- [76] A. A. Parthasarathi, K. Grosh, and A. L. Nuttall. Three-dimensional numerical modeling for global cochlear dynamics. *J. Acoust. Soc. Am.*, 107(1):474–485, 2000.
- [77] A. A. Parthasarathi, K. Grosh, J. F. Zheng, and A. L. Nuttall. Effect of current stimulus on in vivo cochlear mechanics. *J. Acoust. Soc. Am.*, 113(1):442–452, 2003.
- [78] L. C. Peterson and B. P. Bogert. A dynamical theory of the cochlea. *J. Acoust. Soc. Am.*, 22:369–381, 1950.
- [79] R. Probst, B. L. Lonsbury-Martin, and G. K. Martin. A review of otoacoustic emissions. *J. Acoust. Soc. Am.*, 89(5):2027–2067, 1991.
- [80] S. Puria, K. O’Connor, H. Yamada, Y. Shimizu, G. Popelka, and C. Steele. Do otoacoustic emissions travel in the cochlea via slow or fast waves? *32nd MidWinter Meeting on Association for Research in Otolaryngology*, Feb. 14-19, 2009.
- [81] W. Rall. Core conductor theory and cable properties of neurons. In E. R. Kandel, J. M. Brookhardt, and V. B. Mountcastle, editors, *Handbook of Physiology: The Nervous System.*, volume 1, chapter 3, pages 39–98. Williams and Wilkins, 1977.
- [82] S. Ramamoorthy, N. V. Deo, and K. Grosh. A mechano-electro-acoustical model for the cochlea: Response to acoustic stimuli. *J. Acoust. Soc. Am.*, 121(5):2758–2773, 2007.
- [83] Y. Raphael and R. A. Altschuler. Structure and innervation of the cochlea. *Brain Res. Bull.*, 60:397–422, 2003.
- [84] T. Y. Ren. Longitudinal pattern of basilar membrane vibration in the sensitive cochlea. *Proc. Natl. Acad. Sci. U. S. A.*, 99:17101–17106, 2002.
- [85] T. Y. Ren. Reverse propagation of sound in the gerbil cochlea. *Nat. Neurosci.*, 7(4):333–334, 2007.
- [86] T. Y. Ren, W. X. He, and P. G. Gillespie. Measurement of cochlear power gain in the sensitive gerbil ear. *Nat. Commun.*, 2:216–223, 2011.
- [87] T. Y. Ren, W. X. He, M. Scott, and A. L. Nuttall. Group delay of acoustic emissions in the ear. *J. Neurophysiol.*, 96:2785–2791, 2006.
- [88] W. S. Rhode and N. P. Cooper. Two-tone suppression and distortion production on the basilar-membrane in the hook region of cat and guinea-pig cochleae. *Hear. Res.*, 66(1):31–45, 1993.

- [89] L. Robles and M. A. Ruggero. Mechanics of the mammalian cochlea. *Physiological Reviews*, 81(3):1305–1352, 2001.
- [90] J. J. Rosowski. Chapt. 2: Models of external and middle ear function. In H. Hawkins, T. McMullen, A. Popper, and R. Fay, editors, *Auditory Computation*, pages 15–61. Springer–Verlag, New York, 1996.
- [91] M. Ruggero, N. C. Rich, S. S. Narayan, and L. Robles. Basilar-membrane responses to tones at the base of the chinchilla cochlea. *J. Acoust. Soc. Am.*, 101:2151–2163, 1997.
- [92] M. A. Ruggero. Comparison of group delays of 2f1-f2 distortion product otoacoustic emissions and cochlear travel times. *Acoustics Research Letters Online*, 5(4):142–147, 2004.
- [93] M. P. Scherer and A. W. Gummer. Vibration pattern of the organ of corti up to 50 khz: Evidence for resonant electromechanical force. *Proc. Natl. Acad. Sci. U. S. A.*, 101(51):17652–17657, 2004.
- [94] C. A. Shera, A. Tubis, and C. L. Talmadge. Coherent reflection in a two-dimensional cochlea: Short-wave versus long-wave scattering in the generation of reflection-source otoacoustic emissions. *J. Acoust. Soc. Am.*, 118(1):287–313, 2005.
- [95] J. H. Siegel, A. J. Cerka1, A. Recio-Spinoso, A. N. Temchin, P. van Dijk, and M. A. Ruggero. Delays of stimulus-frequency otoacoustic emissions and cochlear vibrations contradict the theory of coherent reflection filtering. *J. Acoust. Soc. Am.*, 118(4):2434–2443, 2005.
- [96] R. Sisto, A. Moleti, T. Botti, D. Bertaccini, and C. A. Shera. Distortion products and backward-traveling waves in nonlinear active models of the cochlea. *J. Acoust. Soc. Am.*, 129(5):3141–3152, 2011.
- [97] G. F. Smoorenburg. Combination tones and their origin. *J. Acoust. Soc. Am.*, 52:615–632, 1972.
- [98] C. R. Steele. Stiffness of reissner’s membrane. *J. Acoust. Soc. Am.*, 56:1252–1257, 1974.
- [99] C. R. Steele and S. Puria. Force on inner hair cell cilia. *Int. J. Solids Struct.*, 42:5887–5904, 2005.
- [100] C. R. Steele and L. A. Taber. Comparison of wkb calculations and experimental results for three-dimensional cochlear models. *J. Acoust. Soc. Am.*, 65:1007–1018, 1979.
- [101] M. R. Stinson. The propagation of plane sound waves in narrow and wide circular tubes, and generalization to uniform tubes of arbitrary cross-sectional shape. *J. Acoust. Soc. Am.*, 89(2):550–558, 1991.

- [102] D. Strelhoff. Computer-simulation of generation and distribution of cochlear potentials. *J. Acoust. Soc. Am.*, 54(3):620–629, 1973.
- [103] D. Strelhoff and A. Flock. Stiffness of sensory-cell hair bundles in the isolated guinea-pig cochleas. *Hear. Res.*, 15(1):19–28, 1984.
- [104] M. Sugawara, Y. Ishida, and H. Wada. Local mechanical properties of guinea pig outer hair cells measured by atomic force microscopy. *Hear. Res.*, 174:222–229, 2002.
- [105] K. Sugiyama, S. Ii, S. Takeuchi, S. Takagi, and Y. Matsumoto. A full eulerian finite difference approach for solving fluid-structure coupling problems. *J. Comput. Phys.*, 230(3):596–627, 2011.
- [106] C. L. Talmadge, A. Tubis, G. R. Long, and C. Tong. Experimental confirmation of the two-source interference model for the fine structure of distortion product otoacoustic emissions. *J. Acoust. Soc. Am.*, 105(6):275–292, 1999.
- [107] J. A. Tolomeo and M. C. Holley. Mechanics of microtubule bundles in pillar cells from the inner ear. *Biophys. J.*, 73:2241–2247, 1997.
- [108] A. Vetesnik, R. Nobili, and A. Gummer. How does the inner ear generate distortion product otoacoustic emissions? *J. Otorhinolaryngol. Relat. Spec.*, 68:347–352, 2006.
- [109] L. Watts. The mode-coupling liouville-green approximation for a a two-dimensional cochlear model. *J. Acoust. Soc. Am.*, 108(5):2266–2271, 2000.
- [110] M. Wilson. Interferometry data challenge prevailing view of wave propagation in the cochlea. *Phys. Today*, April:26–27, 2008.
- [111] H. P. Wit, E. O. Thalen, and F. W. J. Albers. Dynamics of inner ear pressure release, measured with a double-barreled micropipette in the guinea pig. *Hear. Res.*, 132:131–139, 1999.
- [112] Y. J. Yoon, S. Puria, and C. R. Steele. Intracochlear pressure and derived quantities from a three-dimensional model. *J. Acoust. Soc. Am.*, 122:952–966, 2007.
- [113] D. E. Zetes and C. R. Steele. Fluid-structure interaction of the stereocilia bundle in relation to mechanotransduction. *J. Acoust. Soc. Am.*, 101:3593–3601, 1997.
- [114] J. F. Zheng, N. Deo, Y. Zou, K. Grosh, and A. L. Nuttall. Chlorpromazine alters cochlear mechanics and amplification: In vivo evidence for a role of stiffness modulation in the organ of corti. *J. Neurophysiol.*, 97(2):994–1004, 2007.
- [115] J. F. Zheng, S. Ramamoorthy, T. Y. Ren, W. X. He, D. J. Zha, F. Y. Chen, A. Magnusson, A. L. Nuttall, and A. Fridberger. Persistence of past stimulations: Storing sounds within the inner ear. *Biophys. J.*, 100(7):1627–1634, 2011.

- [116] C. Zinn, H. Maier, H. P. Zenner, and A. W. Gummer. Evidence for active, nonlinear, negative feedback in the vibration response of the apical region of the in-vivo guinea-pig cochlea. *Hear. Res.*, 142(1-2):159–183, 2000.
- [117] G. Zweig and C. A. Shera. The origin of periodicity in the spectrum of evoked otoacoustic emissions. *J. Acoust. Soc. Am.*, 98(4):2018–2047, 1995.
- [118] J. J. Zwislocki and L. K. Cefaratti. Tectorial membrane ii: Stiffness measurement in vivo. *Hear. Res.*, 42(2-3):211–228, 1989.